THE UNIVERSITY of ADELAIDE

Designing advanced electrode materials for rechargeable magnesium & sodium batteries and spectroscopic investigation

Xin Xu

A thesis submitted for the degree of Doctor of Philosophy

School of Chemical Engineering and Advanced Materials
The University of Adelaide

November 2022

Table of Contents

Abstracts **1**

Declaration **4**

Acknowledgments **5**

Chapter 1: Introduction **7**

1.1 Significance of this project 7

1.2 Research objectives 8

1.3 Thesis outline 8

1.4 References 9

Chapter 2: Literature Review **11**

2.1 Introduction of rechargeable magnesium & sodium batteries 11

2.2 Electrode materials for low-temperature batteries 15

2.3 Spectroscopic study 18

2.4 Conclusions and outlook 23

2.5 References 25

Chapter 3: Revealing the Magnesium Storage Mechanism in Mesoporous Bismuth via Spectroscopy and Ab Initio Simulation **37**

3.1 Introduction and significance 37

3.2 Revealing the Magnesium Storage Mechanism in Mesoporous Bismuth via Spectroscopy and Ab Initio Simulation 41

Chapter 4: Synchrotron X-ray Spectroscopic Investigations of In-Situ Formed Alloy Anodes for Magnesium Batteries **67**

4.1 Introduction and significance 67

4.2 Synchrotron X-ray Spectroscopic Investigations of In-Situ Formed Alloy Anodes for Magnesium Batteries 71

Chapter 5: Initiating Jahn-Teller Effect in Vanadium Diselenide for High Performance

Magnesium-Based Batteries Operated at -40 ºC..... 99

5.1 Introduction and significance 99

5.2 Initiating Jahn-Teller Effect in Vanadium Diselenide for High Performance Magnesium-Based Batteries Operated at -40 ºC.....103

Chapter 6: Modulating Solution-Mediated Kinetics for Sodium-Organic Battery Operated at Ultra-Low Temperature 145

6.1 Introduction and significance 145

6.2 Modulating Solution-Mediated Kinetics for Sodium-Organic Battery Operated at Ultra-Low Temperature 149

Chapter 7: Conclusions and Perspectives 187

7.1 Conclusions 187

7.2 Perspectives 189

Appendix: Publications during PhD Candidature 191

Abstracts

From portable electronics to grid storage, batteries act as important media to store electrical energy. Lithium-ion batteries (LIBs) are taking a dominant role in battery markets. The supply risks associated with Li resources could stimulate the development of practical post-LIBs, especially magnesium (Mg) /sodium (Na)-based batteries. Mg and Na batteries with the advantages of natural abundance and low cost of precursor materials are promising alternatives to LIBs. Rechargeable Mg batteries offer many advantages over the LIBs. The theoretical volumetric capacity of Mg metal anode (3833 mAh cm^{-3}) is approximately two times higher than that of the Li metal (2061 mAh cm^{-3}). Pure Mg-metal anode is dendrite-free with high safety. In addition, Na-ion batteries are one of the fast-growing batteries following LIBs. Recent prototypes of Na-based batteries are competitive with some LIBs and are already being introduced into commercial products. Therefore, the cost-effective post-LIBs (Mg and Na batteries) will be promising and competitive in the future battery market. To broaden the future application of batteries, we further develop electrode materials with good ultra-low temperature tolerance. The design of organic/inorganic electrode materials and an in-depth understanding of the reaction mechanism via spectroscopies are the main objectives of this thesis.

Firstly, we demonstrated a new Mg storage mechanism for Mg/Bi batteries. A latent MgBi intermediate phase is firstly captured via operando synchrotron spectroscopy and *ab initio* methods. We synthesized the mesoporous bismuth nanosheets (p-Bi NS) as a free-standing alternative anode to pure Mg metal. Results demonstrate that p-Bi NS outperforms reported bismuth-based materials in Mg batteries. These findings will advance the

mechanistic understanding and material design principles for Mg batteries.

Secondly, we in-situ constructed a nanostructured Bi anode from bismuth selenide. Through the combination of operando synchrotron X-ray diffraction, ex-situ synchrotron X-ray absorption spectroscopy, and comprehensive electrochemical tests, it is demonstrated that the nanosize of the in-situ formed Bi crystals contributes to the fast Mg^{2+} diffusion kinetics and highly efficient Mg-Bi alloying/de-alloying. The resultant Bi anodes exhibited superior long-term cycling stability with over 600 cycles. We conclude that our findings offer a practical approach to guide the materials design of the alloy anode for highly stable rechargeable Mg batteries.

Thirdly, we reported layer-structured metallic vanadium diselenide (1T-VSe_2) as a cathode material for low-temperature Mg^{2+}/Li^{+} hybrid batteries. We demonstrated the high electronic conductivity and fast ion diffusion kinetics for 1T-VSe_2, and a highly safe 1T-VSe_2/Mg battery for operation under -40 ^{o}C. The Jahn-Teller effect in compressed configuration is initiated in 1T-VSe_2 with the change of electronic state on electrochemical intercalation of alkali metal ions. Using combined experimental results and theoretical studies including operando synchrotron X-ray diffraction, ex-situ X-ray absorption spectroscopy, and density functional theory (DFT) computation, we confirm that the Jahn-Teller effect contributes significantly to the fast overall kinetics and structural stability of the electrode.

Lastly, we reported an organic electrode, nanosized disodium rhodizonate hybridizing with graphene oxide (nDSR/GO) as the highly efficient electrode for sodium-ion batteries with an excellent ultra-low temperature performance, in which the pseudocapacitive

electrochemical behavior of the organic electrode has been fully utilized. By modulating the solution-mediated kinetics of composite electrodes, the Na-nDSR/GO battery exhibits a high capacity of 119 mAh g^{-1} at -50 ºC. The Prussian blue analogue (PBA)-nDSR/GO full cell demonstrates an ultra-long lifespan over 2500 cycles with a capacity of 99 mAh g^{-1} at a high current density of 300 mA g^{-1}. The designed Na-ion batteries perform one of the best performances under an ultra-low temperature. Therefore, this battery is promising in practical use in extreme cold conditions.

Declaration

I certify that this work contains no material which has been accepted for the award of any other degree or diploma in my name, in any university or other tertiary institution and, to the best of my knowledge and belief, contains no material previously published or written by another person, except where due reference has been made in the text. In addition, I certify that no part of this work will, in the future, be used in a submission in my name, for any other degree or diploma in any university or other tertiary institution without the prior approval of the University of Adelaide and where applicable, any partner institution responsible for the joint award of this degree.

The author acknowledges that the copyright of published works contained within the thesis resides with the copyright holder(s) of those works.

I give permission for the digital version of my thesis to be made available on the web, via the University's digital research repository, the Library Search and also through web search engines, unless permission has been granted by the University to restrict access for a period of time.

Name of Candidate: Xin Xu

Signature:

Date: 04/November/2022

Acknowledgments

This thesis would not be accomplished without the support and help of my supervisors, friends, and families. It was a wonderful and pleasure experience working at Qiao's group. Here, I would like to express my gratitude to all of them.

First and foremost, I would like to express my deepest gratitude to my principal supervisor, Professor Shizhang Qiao, for his excellent guidance, supportive encouragement, and trust. I am very grateful to him for providing me with an excellent atmosphere and resources for doing research throughout my PhD candidature. The freedom that I enjoyed in the labs was excellent, and I could work on any projects that interest me and conduct research in some challenging fields. The four years of pursuing research projects shapes my research ability and arms me with strong learning will. And I could not get any achievements without his guidance and support for my PhD study. I will forever benefit from his training as a researcher in my future career.

I sincerely appreciate my co-supervisor Dr. Dongliang Chao, for his insightful suggestions and continuous encouragement. It's lucky to be a student under his supervision. He is such a good mentor and friend. I also thank my co-supervisor Dr. Chao Ye for his patient guidance in research and paper writing, and his encouragement in daily life.

I am also grateful to all members of Qiao's group who give me support and suggestions on pursuing my PhD. Many thanks go to Dr. Huan Li for his great help in experimental discussion, daily help, and being a good friend; many thanks to Dr. Fangxi Xie for helping with synchrotron analysis; many thanks to Dr. Junnan Hao for his friendly guidance and discussion; many thanks to Dr. Cheng Tang for his helpful discussion on material synthesis.

many thanks to Dr. Biao Chen for his assistance on material characterization. I would like to thank all the battery group members Han Wu, Shaojian Zhang, Jiahao Liu, Chun-Chuan Kao, Libei Yuan, and Qianru Chen for their help in discussion and experiments. Also, I would like to thank all the group members from electrocatalysis or photocatalysis group for their interactions and inspiring discussion. For example, Dr. Jiao Yan, Dr. Yao Zheng, Dr. Bo You, Dr. Jingrun Ran, Dr. Huanyu Jin, Dr. Jieqiong Shan, Dr. Xing Zhi, Dr. Laiquan Li, Dr. Pengtang Wang, Mr. Xianlong Zhou, Mr. Dazhi Yao, Mr. Bingquan Xia. Thanks to all of them.

Many thanks go to Prof. Kenneth Davey for his fruitful suggestions for paper writing. I appreciate the support from Dr. Qinfen Gu and Dr. Bernt Johannessen at Australian Synchrotron for their very helpful input. It is a great pleasure to express my appreciation to Professor David Lewis, Mrs. Michelle Fitton, and Mrs. Sarah Flavel from the School of Chemical Engineering and Advanced Materials for their administrative help.

Last, I would like to thank my friends and family who have helped me maintain the ideal balance outside research. I extend my deepest gratitude to my family for their unconditional love and support. Special thanks go to my dear husband Shiying Ren for his understanding, encouragement, and endless support.

I would also like to acknowledge The University of Adelaide for the financial support.

Chapter 1: Introduction

1.1 Significance of this project

Rechargeable Mg and Na batteries with the advantages of natural abundance and low cost are promising alternatives to LIBs.[1-4] However, the practical utilization of them are still hindered by unsatisfactory cycle life, rate capacity, temperature tolerance, and energy density.[5-6] These are due to the bivalent nature of Mg^{2+} and the large radius of Na^{+} (0.102 nm) induced sluggish ion diffusion kinetics in solid electrode. More importantly, there is a lack of mechanism studies to guide the rational design of high-performance electrode materials.[7-12] The redox chemistries of active electrode materials determine the energy density of the battery. This thesis developed several electrode materials with excellent electrochemical performance for Mg and Na-based batteries. And further work on developing ultra-low temperature electrode materials enhanced the temperature tolerance of Mg and Na batteries, which broadened the application of these batteries.

This thesis will contribute to:

- *Innovative guidance* to design materials with boosted Mg^{2+} diffusion kinetics via nanostructure engineering.
- *A novel strategy* on in-situ electrochemical construction of alloy anode, which will benefit the further exploration of high-energy cathode materials for Mg-based batteries.
- *An evidence understanding* at an atomic level of the mechanism that can be further applied to the rational design of novel electrode materials with good low-temperature performance.
- *An exploration of organic electrodes* for sodium-ion batteries operated at ultra-low

temperature. It promotes the development of ultra-low temperature batteries, including monovalent and multivalent ion batteries.

1.2 Research objectives

This thesis aims to develop high-performance electrode materials for rechargeable Mg and Na-based batteries, and design electrode materials with good low-temperature tolerance to broaden the application of energy storage batteries. In particular, the goals of this thesis are:

✧ To design novel electrode materials for Mg batteries with enhanced Mg^{2+} diffusion kinetics and to suggest strategies for synthesizing high-performance electrodes.

✧ To clarify the Mg^{2+} storage mechanism in alloy-type anode materials to guide the development of anodes for rechargeable Mg batteries.

✧ To explore low-temperature electrode materials for Mg-based hybrid batteries with mechanism studies via spectroscopic investigation and to propose strategies in the rational design of high-performance electrode materials for low-temperature operation.

✧ To develop organic electrodes for ultra-low temperature batteries and shed light on the unique energy storage behavior of the organic electrodes.

✧ To inspire applications of in-situ/operando spectroscopic characterization techniques, such as X-ray diffraction, X-ray absorption, Fourier-transform infrared and Raman spectroscopy, and scanning/transmission electron microscopy, in rechargeable batteries.

1.3 Thesis outline

This thesis is presented in the form of journal publications. It includes research results on material syntheses, electrochemical tests (at RT and low temperatures), spectroscopic investigations, and theoretical computations for Mg and Na-based batteries. The challenges

and recent progress were reviewed, followed by the conclusion and perspective of further development of advanced electrode materials for rechargeable Mg and Na batteries. Specifically, the chapters in this thesis are presented as follows:

- ***Chapter 1*** introduces the significance of this project, research objectives, and main contributions to the development of batteries.
- ***Chapter 2*** reviews recent progresses and challenges for Mg and Na batteries, electrode materials for low-temperature batteries, and spectroscopic characterization techniques.
- ***Chapter 3*** exhibits a mesoporous Bi anode and reveals Mg/Bi storage mechanism via spectroscopy and *Ab initio* simulation.
- ***Chapter 4*** demonstrates an in-situ formed alloy anode for rechargeable Mg batteries and uncovering the Mg^{2+} storage mechanism via synchrotron X-ray spectroscopy.
- ***Chapter 5*** unravels the Jahn-Teller effect in vanadium diselenide for high-performance Mg-based batteries operated at -40 ºC.
- ***Chapter 6*** modulates solution-mediated kinetics in the organic electrode for ultra-low temperature Na-ion batteries.
- ***Chapter 7*** gives the conclusion and perspectives on further improvement of energy density for rechargeable Mg and Na batteries.

1.4 References

1. Usiskin, R.; Lu, Y.; Popovic, J.; Law, M.; Balaya, P.; Hu, Y.-S.; Maier, J., Fundamentals, Status and Promise of Sodium-Based Batteries. *Nat. Rev. Mater.* **2021,** *6* (11), 1020-1035.

2. Che, H.; Chen, S.; Xie, Y.; Wang, H.; Amine, K.; Liao, X.-Z.; Ma, Z.-F., Electrolyte Design Strategies and Research Progress for Room-Temperature Sodium-Ion Batteries. *Energy*

Environ. Sci. **2017,** *10* (5), 1075-1101.

3. Attias, R.; Salama, M.; Hirsch, B.; Goffer, Y.; Aurbach, D., Anode-Electrolyte Interfaces in Secondary Magnesium Batteries. *Joule* **2019,** *3* (1), 27-52.

4. Mao, M.; Gao, T.; Hou, S.; Wang, C., A Critical Review of Cathodes for Rechargeable Mg Batteries. *Chem. Soc. Rev.* **2018,** *47* (23), 8804-8841.

5. Choi, J. W.; Aurbach, D., Promise and Reality of Post-Lithium-Ion Batteries with High Energy Densities. *Nature Reviews Materials* **2016,** *1* (4), 1-16.

6. Liu, Q.; Hu, Z.; Chen, M.; Zou, C.; Jin, H.; Wang, S.; Chou, S. L.; Liu, Y.; Dou, S. X., The Cathode Choice for Commercialization of Sodium-Ion Batteries: Layered Transition Metal Oxides versus Prussian Blue Analogs. *Adv. Funct. Mater.* **2020,** *30* (14), 1909530.

7. Chu, S.; Guo, S.; Zhou, H., Advanced cobalt-free cathode materials for sodium-ion batteries. *Chem. Soc. Rev.* **2021,** *50* (23), 13189-13235.

8. Lee, B.; Paek, E.; Mitlin, D.; Lee, S. W., Sodium Metal Anodes: Emerging Solutions to Dendrite Growth. *Chem. Rev.* **2019,** *119* (8), 5416-5460.

9. Regulacio, M. D.; Nguyen, D. T.; Horia, R.; Seh, Z. W., Designing Nanostructured Metal Chalcogenides as Cathode Materials for Rechargeable Magnesium Batteries. *Small* **2021**, e2007683.

10. Guo, Z.; Zhao, S.; Li, T.; Su, D.; Guo, S.; Wang, G., Recent Advances in Rechargeable Magnesium-Based Batteries for High-Efficiency Energy Storage. *Adv. Energy Mater.* **2020**, 1903591.

11. Zhang, Z.; Dong, S.; Cui, Z.; Du, A.; Li, G.; Cui, G., Rechargeable Magnesium Batteries using Conversion-Type Cathodes: A Perspective and Minireview. *Small Methods* **2018,** *2* (10), 1800020.

12. Canepa, P.; Sai Gautam, G.; Hannah, D. C.; Malik, R.; Liu, M.; Gallagher, K. G.; Persson, K. A.; Ceder, G., Odyssey of Multivalent Cathode Materials: Open Questions and Future Challenges. *Chem. Rev.* **2017,** *117* (5), 4287-4341.

Chapter 2: Literature Review

2.1 Introduction of rechargeable magnesium & sodium batteries

Rechargeable magnesium batteries (RMBs). LIBs have powered many electronic devices, which greatly influence our daily life and have increased our demand for energy. However, the unbalanced distribution and resource depletion risk of Li cannot ensure uninterrupted supply and satisfy an ever-increasing requirement for LIBs.[1-3] Unlike LIBs, RMBs draw wide attention due to several advantages, such as abundance in the earth's crust (ranking 7th in all elements), low cost, high volumetric capacity (3833 mAh cm^{-3} *vs.* 2046 mAh cm^{-3} for Li), and high safety because of its dendrite-free deposition, as summarized in **Table 1**.[4-7] Moreover, Mg is air-stable and can be easily recycled as Mg foil. RMBs emerges as highly safe and reliable energy storage technique exhibiting great potential for practical use. However, the development of RMBs is still in its early stage and encountering many challenges.

Table 1. Comparison of key parameters for monovalent/multivalent metal anodes.[2-3, 8]

Metal anode	Standard potential (*vs.* SHE)/V	Volumetric capacity/ mAh cm^{-3}	Gravimetric capacity/ mAh g^{-1}	Ionic radius/Å	Abundance in earth's crust/ wt%	Stability in the air?	Dendrite growth?	Market price/ US$ Kg^{-1} [a]
Li	-3.04	2062	3861	76	0.002	No	Yes	81-85
Na	-2.71	1131	1166	102	2.36	No	Yes	2.5–3.4
K	-2.93	591	685	138	2.09	No	Yes	12.1-13.6
Mg	-2.37	3837	2205	72	2.33	Yes	No	2.32
Al	-1.66	8046	2980	53.5	8.23	Yes	Yes	1.79
Zn	-0.76	5845	820	74	0.007	Yes	Yes	2.55

Notes: data from different literatures. [a] The prices are obtained from "https://www.metal.com/" websites, Shanghai metals market.

The electrochemical behavior of RMBs is different from that of LIBs. Firstly, metallic Mg anode shows a tendency to form an electron-insulated and ion-insulated surface layer, which is different from the solid electrolyte interphase (SEI) in LIBs and makes it difficult to choose compatible electrolytes.[9] The most commonly used electrolytes in RMBs containing Cl^- are air-sensitive and highly corrosive, which presents a potential threat for their practical use. Secondly, the bivalent nature of Mg^{2+} causes a strong electrostatic interaction with the host material and inevitably leads to sluggish ion diffusion kinetics. Previous works have been devoted to developing electrolytes for RMBs.[10-20] Whilst there is still a lack of electrode materials that are compatible with conventional electrolytes and exhibit efficient intercalation and deintercalation of Mg^{2+}. This thesis will mainly focus on the design and development of anode materials to address uncontrollable interfacial electrochemical behaviors of Mg.

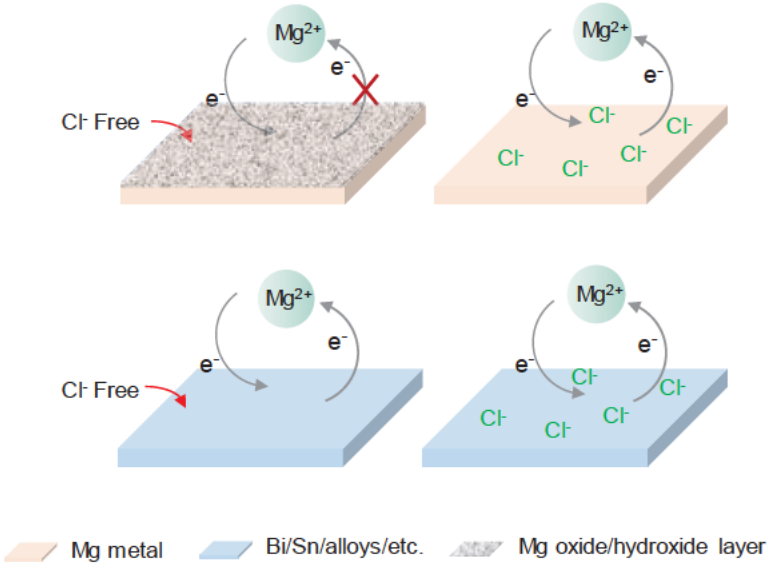

Figure 1 Schematics depicting Mg metal and alloy-type anodes for RMBs in Cl^- containing and Cl^--free electrolytes.

A passivation layer formed when Mg metal is exposed to common Mg-salts ($Mg(TFSI)_2$, $Mg(ClO_4)_2$, $Mg(PF_6)_2$, etc.) or conventional carbonate electrolytes, deteriorates the

reversibility of the battery.[10-11] To overcome the interfacial problems of the Mg anode, Cl^- containing ethereal electrolytes are used. However, these electrolytes, such as Grignard-based electrolytes[21] and magnesium aluminate chloride complex (MACC)[22] in tetrahydrofuran or glyme solvents, are often corrosive, air-sensitive, and suffer from poor anodic stability.[9, 23] Another strategy is to design artificial solid-electrolyte interphase, as reported in LIBs, via ex-situ or in-situ surface modification.[24-29] More practical strategy is applying an alternative Mg^{2+} host anode, as demonstrated in **Figure 1**. Alloy-type anodes such as Bi, Sn, Sb, and their alloy compounds have been intensively investigated in RMBs.[30-32] Among them, Bi is one of the most studied anodes as an alternative to Mg metal because of its relatively high theoretical volumetric capacity (1949 mAh cm^{-3} for Mg_3Bi_2) and stable output with flat and low redox potential plateau.[33] Additionally, Bi is compatible with conventional carbonate electrolytes and has been demonstrated to be applicable in high-voltage systems and Mg-S batteries.[34-35] The structure of Bi active materials has a great influence on the ion transfer in solid materials. Bi and its alloy with various morphologies and components, such as Bi nanotube,[36-37] colloidal Bi nanocrystals,[38] and nanocluster Mg_3Bi_2 alloy,[39] have been developed to reversibly store Mg^{2+}. However, these Bi anodes are still suffering from severe volume change and limited Mg^{2+} diffusion kinetics during the alloy/de-alloy process, and therefore exhibited poor cycling stability.[40] Especially under high-rate conditions, the cycling life of these Bi-based electrodes is limited to 200 cycles, which is much shorter than the cycling requirement for practical applications. Therefore, rational design and precise synthesis of Bi electrodes are urgently needed to achieve high rate and long cycle life of RMBs.

Sodium-based batteries. Na-based batteries are one of the most appealing battery technologies, as alternatives or complement to the prevailing LIBs.[41-43] Increasing utilization of Li in energy storage pushes up the price of lithium compounds, thereby making large-scale energy storage based on LIBs less affordable. Given the high abundance and low cost of elemental Na with relatively low-redox potential, as summarized in **Table 1**, Na-based batteries hold great promise for energy storage, especially for large-scale grid applications as demonstrated in **Figure 2**. Renewable resources, such as solar and wind power, provide intermittent energy to the grid. Off-grid, compact battery systems are well suited to provide energy storage for local solar energy output and backup power during outages for residential use. On-grid, batteries are used to relieve transmission congestion to store the peak load energy, and in return, the stored power can be released to feed the grid for off-peak utilization.[44]

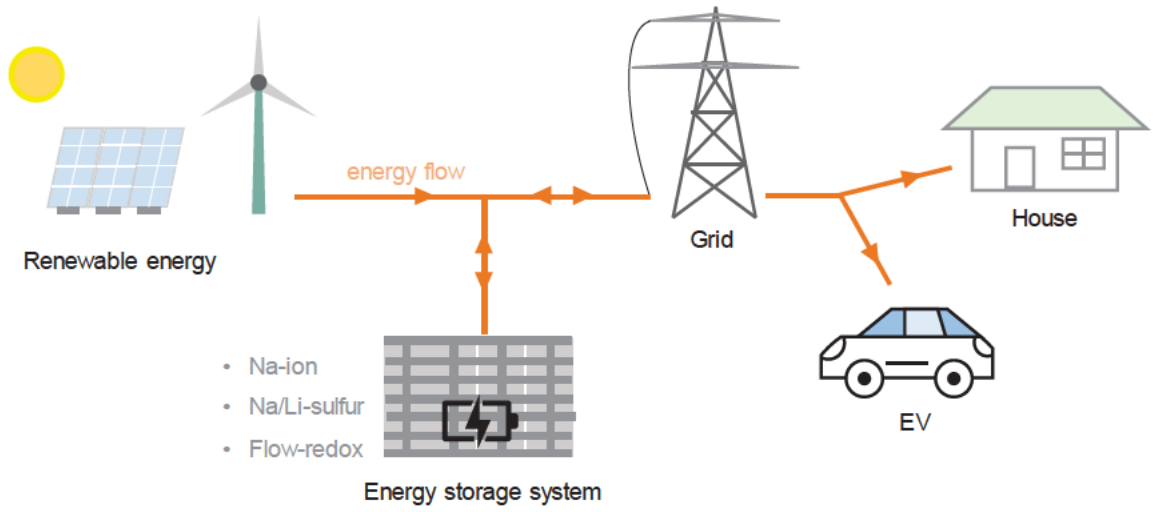

Figure 2 Schematics for large-scale application of Na-based batteries in grid or microgrid. Grid storage enables the integration of renewable energy sources.

Importantly, except for the low cost of Na resources, Na batteries possess the same working principle as LIBs. Therefore, if the energy density and other performances meet the

requirement for practical application, manufacturers can use identical manufacturing protocols and equipment as LIBs to produce Na batteries with significant cost reduction.[45] In addition, the Na battery takes a large cost advantage regarding to the anode current collector.[46] Unlike Li, Na does not form an alloy with Al. Thus, the anode of Na-based batteries can utilize Al foil as the collector, which is much cheaper than Cu foil for the anode of LIBs. Research on Na batteries have made significant progress over the last decades, and some well-famed battery manufacturers, such as CATL (one of the global leaders in battery development and manufacturing), have launched production of commercial Na-ion batteries. Although Na-ion batteries are making strides towards energy storage applications, electrode materials with high power and energy density are still lacking and required to be developed.

2.2 Electrode materials for low-temperature batteries

Over decades of development and practical application of batteries, issues on the significantly decayed electrochemical performance at low temperatures pop up, which largely limit their applications in cold conditions, as depicted in **Figure 3**. Most commercial batteries suffer from severe energy loss when the operation temperature is down to -20 ^{o}C. This is caused by the sluggish ionic conductivity of the electrolyte, significantly increased charge transfer resistance, and slow metal ion transport within solid materials at low temperatures.[47-50] As previously reported, the Pana-sonic 18650 LIBs maintain only around 5% of energy density at -40 ^{o}C due to the high melting point of the solvent.[51] And the common graphite or hard carbon-based commercial batteries suffer severely from capacity and energy loss at temperature below -30 ^{o}C because of poor diffusion kinetics through the carbon layer. More importantly, the easily formed metal dendrites (Li/Na/K/Al) at low temperature bring severe

safety concerns to manufacturers and customers.[52-56] Currently, to overcome the poor function of batteries at low temperature, thermal management systems (TMS) using self-heating accessories are applied to handle the issue. Whilst the extra accessories increased the complexity and reduced the overall energy density of battery systems.[57-58] Therefore, it is more practical to focus on advancing the battery components, including the innovation of electrode materials for the system.

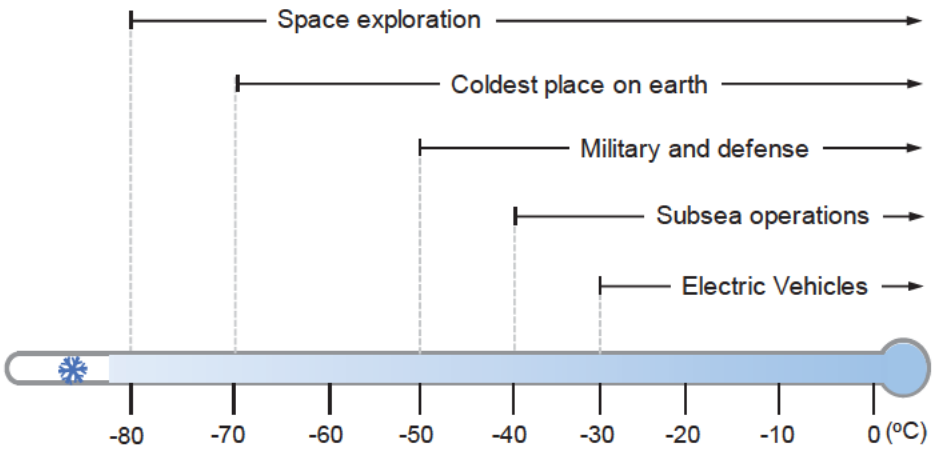

Figure 3 Various task-specific applications of energy storage batteries at low-temperature conditions.

$LiFePO_4$ (LFP) as the most successful and widely utilized cathode for commercial LIBs however possesses inferior low-temperature performance because of poor ionic and electronic conductivity. It exhibits huge overpotential at low temperature on cycling and shows discouraging rate capability.[59-63] To optimize the low-temperature performance of LFP, intensive efforts have focused on improving the overall kinetics of the electrode via nano-sizing and surface modification.[64-65] Another strategy used fluorinated electrolytes to weaken the binding energy between Li^+ and solvent molecules, which enhances the kinetics of Li-LFP batteries at low temperature,[66] as demonstrated in **Table 2**. The commercial graphite

anode faces the same issue of slow ion diffusion kinetics at low temperature. Low discharging potential of the graphite even results in a Li plating on the electrode surface at low temperature.[67] Whilst hard carbon with disordered crystal structure and nanovoids performs relatively better low-temperature performance than the pristine graphite anode.[68] For the intercalation electrode, shortening the diffusion path of metal ions is generally effective to improve the kinetics of the battery at low temperatures. Therefore, alternative battery chemistry beyond intercalation, such as surface-controlled and solution-mediated reactions with shortening ion diffusion path and fast kinetics can be promising to optimize the low-temperature performance of batteries.

Intercalation pseudocapacitive materials combine the high power of capacitors with the high energy of intercalation chemistry, emerging as a type of electrode material with excellent temperature-dependent capacity.[69] Nanosized Nb_2O_5 and its relative compounds are typical materials that perform fast insertion kinetics via intrinsic pseudocapacitive behaviors.[70] Liang et al. employed mesoporous $Ti_{0.88}Nb_{0.88}O_{4-x}$@C as an anode material for Na-ion batteries achieving a high rate and long-cycling performance at -40 ^{o}C.[71] Prussian blue and its analogues are a large family of transition metal hexacyanoferrates with 3D open framework structures. Prussian blue with extrinsic pseudocapacitive behavior has turned out to be an excellent low-temperature electrode material for both LIBs and Na-ion batteries.[72-73] Moreover, as shown in **Table 2**, the work from Wang et al., explored metal-sulfur batteries which demonstrated the highest capacity at a low temperature of -40 ^{o}C.[74] The metal-sulfur batteries with advantage of kinetically fast amorphous conversion reactions is strongly promising in low-temperature operations. Organic compounds are a type of sustainable

material with surface-controlled reactions, which exhibit fast reaction kinetics.[75-77] Therefore, the organic electrodes are promising candidates for low-temperature applications. As previously reported, the metal-organic batteries can withstand temperature down to -70 °C.[78-80] They are encouraging to be introduced in the extreme harsh environment, such as polar explorations and subsea operations. While efforts on improving the cyclability and energy density of the organic electrode are needed to make it viable for practical use.

Table 2. Low-temperature performance of different battery systems.

Battery systems		Specific capacity	Cycling performance	Average discharge voltage (V)	Operating temperature (°C)	Ref.
Sodium batteries	$Ti_{0.88}Nb_{0.88}O_{4-x}$@C//Na	99 mAh g^{-1} at 0.5C	81% retained after 500	~0.7	-40	1[71]
	Prussian blue@CNTs	76 mAh g^{-1} at 2.4C	86% retained after 1000	~2.7	-25	2[73]
Lithium batteries	$LiFePO_4$(LFP)//Li	~80 mAh g^{-1} at 0.5C	89.4% retained after 200	unknown	-40	3[66]
	NMC811//Li	108 mAh g^{-1} at 0.2C	>90% retained after 200	3.7	-40	4[81]
	$LiMn_2O_4$(LMO)// $Li_4Ti_5O_{12}$ (LTO)	~70 mAh g^{-1} at 0.2C	~80% retained after 40	2.4	-40	5[82]
	SPAN//Li	~300 mAh g^{-1} at 0.2 A g^{-1}	86% retained after 100	~1.4	-40	6[83]
	Polyimide (PI)//Li	~70 mAh g^{-1} at 0.2C	~83% retained after 100	2.3	-70	7[79]
	S (SRVCR)//Li	~587 mAh g^{-1} at 0.2C	~80% retained after 50	~1.9	-40	8[74]
Aqueous batteries	MnO_2@GF//MoO_3	171.8 mAh g^{-1} at 0.2 A g^{-1}	>99% retained after 100	~1.0 (vs. Ag/AgBr)	-70	9[84]
	PI//LiBr+ TPABr//PC	56 mAh g^{-1} at 0.5 A g^{-1}	98% retained after 1000 at 1 A g^{-1}	0.8	-40	10[85]
	AC//$NaTi_2(PO_4)_3$@C	~65 mAh g^{-1} at 0.5C	>80% retained after 100	~1.2	-50	11[86]
	α-MnO_2//Zn	~40 mAh g^{-1} at 6 A g^{-1}	>99% retained after 1000	~1.3	-50	12[87]
Full organic battery	PTPAn//PI	103 mAh g^{-1} at 5C	>99% retained after 2000	~1.2	-50	13[78]

Notes: CNTs= carbon nanotubes; NMC 811= $LiNi_{0.8}Mn_{0.1}Co_{0.1}O_2$; SPAN = sulfurized polyacrylonitrile; AC= active carbon; TPBr= tetrapropylammonium bromide; PTPAn= polytrriphenylamine; SRVCR= sulfur-rich vulcanized clay rubber.

2.3 Spectroscopic study

Over the past decade, advanced characterization techniques have been developed to monitor

batteries from various scales to guide the rational design and to improve the electrochemical performance of batteries.[88-90] Especially, many in-situ and operando techniques have been developed to capture the real-time information of the electrochemical process via customized cells.[91-93] The in-depth fundamental understanding on the structure and kinetics of both electrode materials and the electrolyte/electrode interfacial reactions is essential to develop advanced materials for all types of batteries. In this thesis, we present both static (ex-situ) and real-time (in-situ or operando) spectroscopies, which are keys to guide the development of electrode materials.

In-situ/operando X-ray diffraction (XRD). XRD is a well-established technique to characterize the crystal structure and phase composition of electrode materials. In situ/operando XRD techniques are used to capture the structural change and phase transition of electrodes during electrochemical cycling. Unlike other in-situ characterization techniques, in-situ XRD does not require any specially designed cell and the operation is relatively simple, as shown in **Figure 4**a.[94] The coin cell with a hole covered by Kapton tape can be used for operando synchrotron XRD tests. In-situ XRD is commonly applied to monitor the structural change of cathode materials. For example, the research conducted by Liu et al.[95], confirmed that a solid-solution region occurs between $LiFePO_4$ and $FePO_4$. The identified solid-solution phase directly contributes to an outstanding rate performance of LIBs (**Figure 4b**). Such a fast transition process can hardly be captured via ex-situ XRD. Sodium-rich rhombohedral Prussian blue was a typical cathode material studied via synchrotron operando XRD as reported by Wang et al.[41] The operando XRD results exhibited a highly reversible rhombohedral structure for the prepared material. A three-phase transition among

rhombohedral, cubic, and tetragonal appears upon Na^+ insertion/extraction in Prussian blue, which contributes to a stable structural evolution of the electrode with excellent cycling stability, as shown in **Figure 4c-e**. In-situ/operando XRD provides insightful structural information to further guide the design and optimization of the electrode materials.

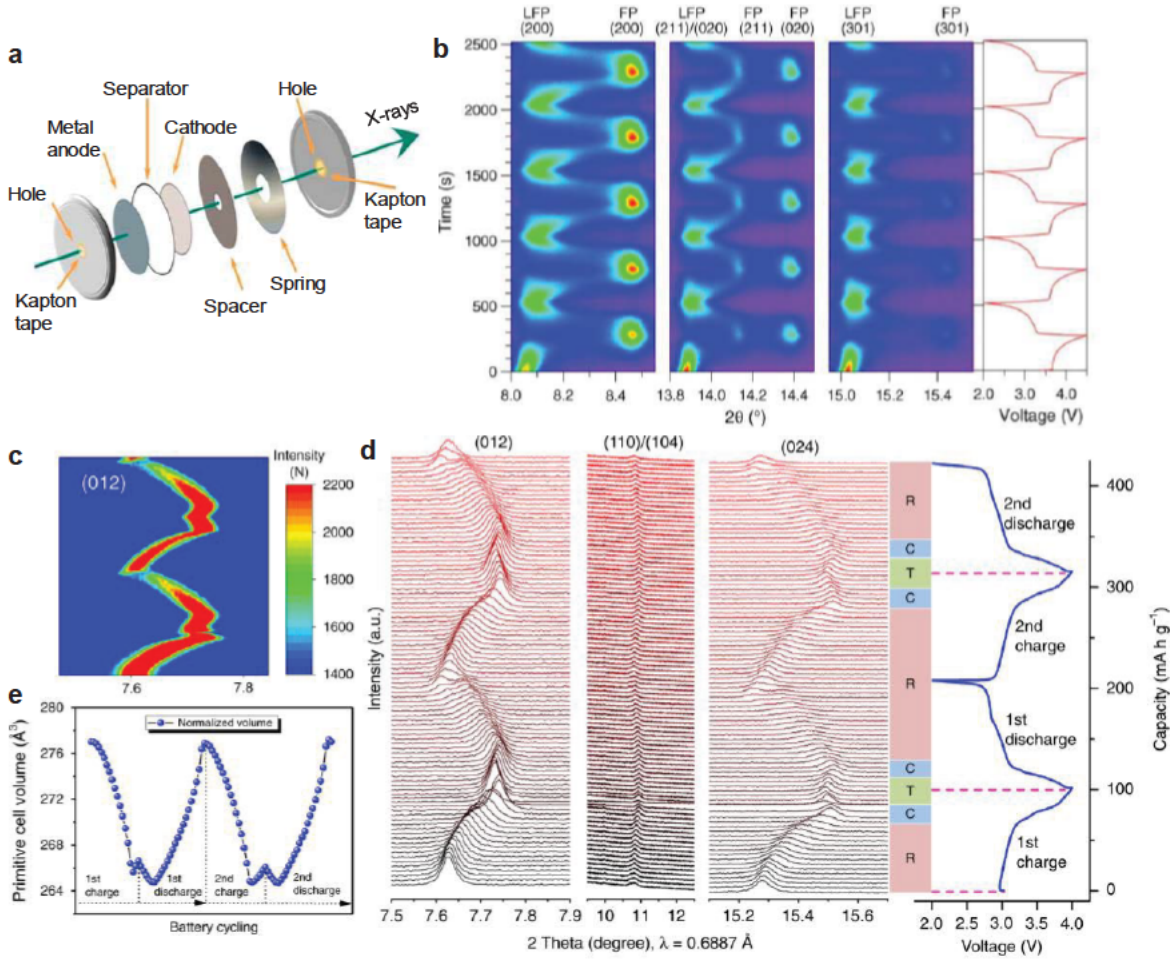

Figure 4 a) Schematic illustration of self-made coin cell for operando XRD testing.[94] b) Contour image of in-situ XRD patterns for Li-$LiFPO_4$ batteries during the initial five cycles.[95] c-e) Operand synchrotron XRD patterns of rhombohedral Prussian blue for Na-ion batteries.[41]

X-ray absorption spectroscopy (XAS). XAS is a powerful technique to investigate the chemical state and local environment of center atoms.[96-99] XAS contains two parts: X-ray absorption near-edge structure (XANES) and extended X-ray absorption fine structure

(EXAFS).[100] XANES is sensitive to the oxidation state and coordination symmetry of the center atom.[101] EXAFS can obtain detailed information on the local environment of atoms,

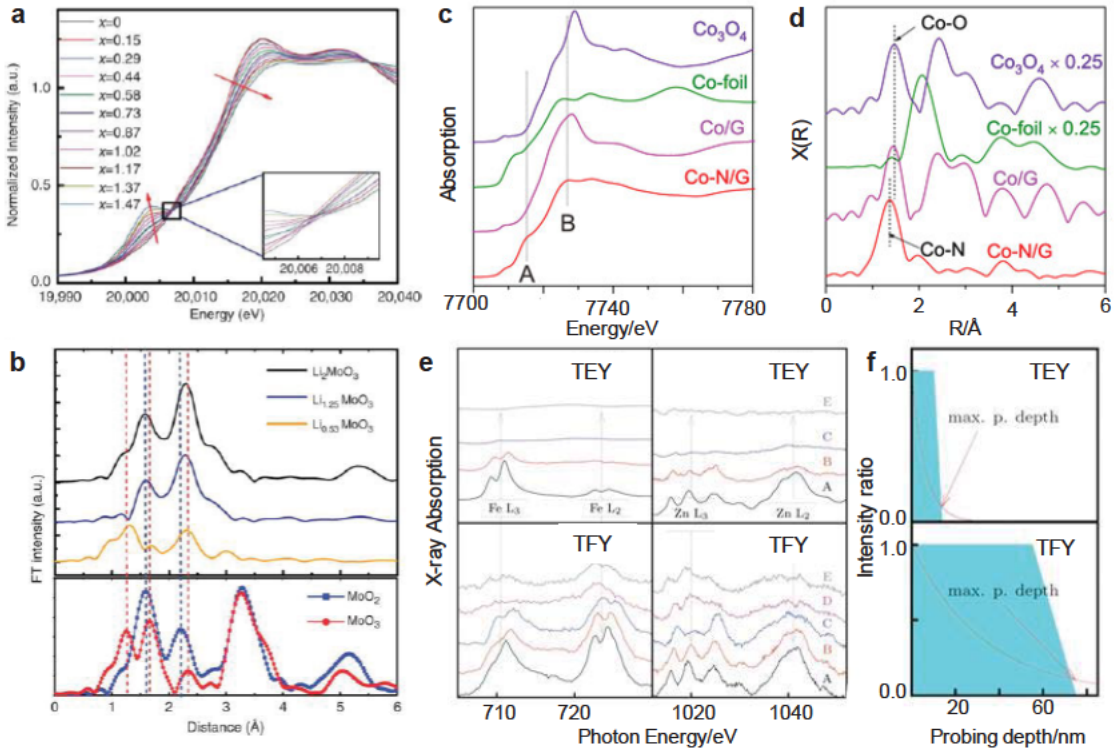

Figure 5 a) In-situ XANES for Mo K-edge, and b) ex-situ FT-EXAFS of $Li_{2-x}MoO_3$ at different charging states.[102] c) XANES and d) FT-EXAFS in R space for cobalt atoms embedded nitrogen-doped graphene (Co-N/G).[103] e) TEY and TFY yield XAS for Fe L_2 and Zn L_2 with different probing depth. f) Schematics of estimated TEY and TFY probing depth.[98]

including the bonding state. Zhou et al.[102] elucidated the electronic and local atomic structure of Mo atoms in Li_2MoO_3. XANES demonstrated an increased valence state of Mo^{4+}, and Fourier-transformed (FT) EXAFS exhibited a varied local coordination environment of Mo (**Figure 5a-b**). The change of Mo-Mo bond length and migration of Mo ions stabilized the structure of the electrode during cycling. The mechanistic study at the atomic level including the electronic structure and local environment change of Mo atoms explained the structural stability and enhanced electrochemical capacity of designed batteries. Du et al.[103] using ex-

situ XAS confirmed that Co atoms in N-doped graphene are coordinated with N atoms forming Co-N-C coordination centers in the designed Li-S battery, which facilitates the formation and decomposition of Li_2S upon cycling with fast reaction kinetics (**Figure 5c-d**). These XAS characterizations at an atomic level provide an in-depth fundamental understanding of materials, and offer strategies on surface modification and hetero dopings, to rationally guide the design of electrodes. For soft-XAS (< 3 keV), the total secondary electrons yield (TEY) and the total fluorescence photon yield (TFY) detection modes are used. The probing depths for them are different, as shown in **Figure 5e-f**.[98] Therefore, soft-XAS can be applied to distinguish the bulk and surface behaviors of active materials simultaneously.

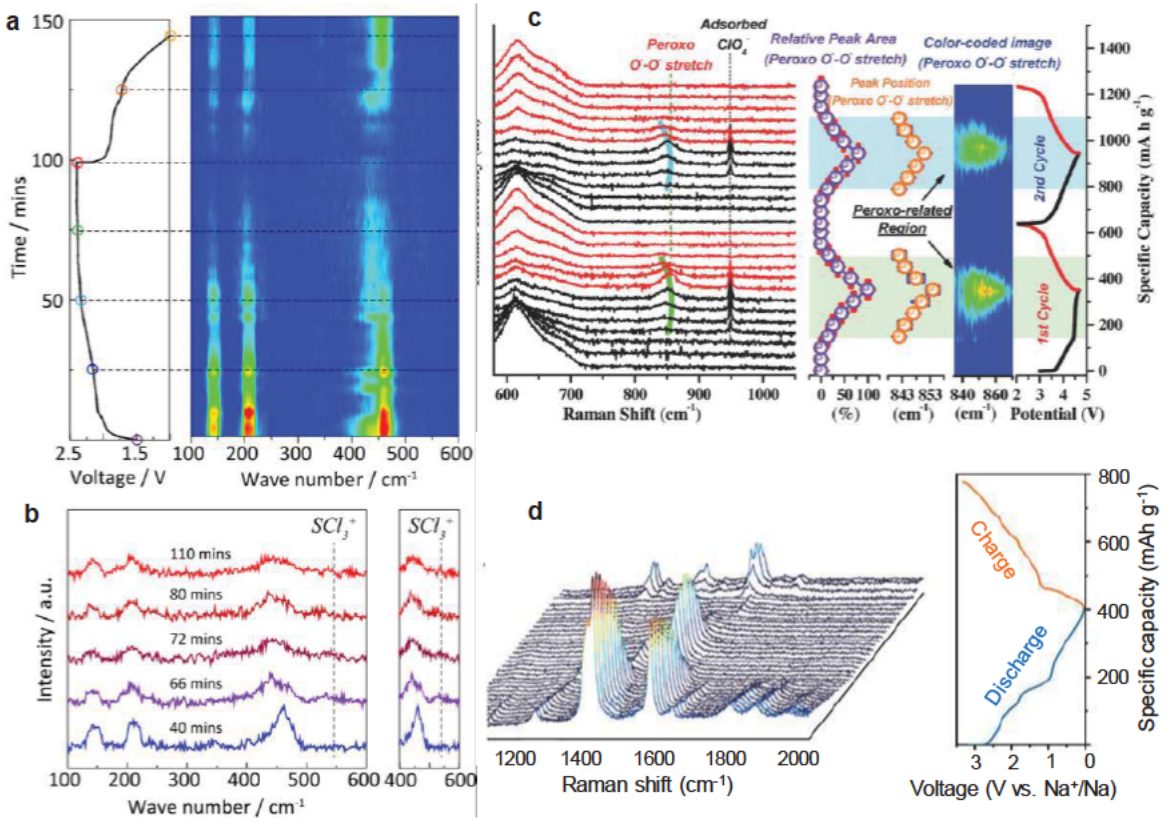

Figure 6 a) In-situ Raman contour map for Al-S/CNT batteries, and b) corresponding Raman spectra extracted from the contour map.[104] c) In-situ Raman spectra recorded for Li-

$Li_{1.2}Ni_{0.2}Mn_{0.6}O_2$ batteries.[105] d) In-situ Raman spectra and corresponding discharge-charge curves for Na-organic($C_6H_2Na_2O_6$) batteries.[106]

In-situ Raman spectroscopy. The Raman spectrum is used to identify the vibrational energy of molecular/crystal bonds within electrode materials. It is sensitive to detect transient species and intermediate phases. The Raman spectroscopy is commonly used to investigate the reaction mechanism of electrode materials.[107] For example, Li et al.[104] applied in-situ Raman spectra to identify the intermediate products in sulfur oxidation processes for Al-S batteries. Via in-situ Raman, they found that the SCl_3^+ intermediate is soluble in the electrolyte, which results in the loss of active sulfur during cycling (**Figure 6a-b**). And further work focusing on promoting transformation kinetics of the SCl_3^+ will benefit the cycling stability of Al-S batteries. Another work from Zhou's group[105] used in-situ Raman to capture an oxygen redox process via the signal of peroxo O-O bonds and identified the origin of the high capacity of the Li-rich ($Li_{1.2}Ni_{0.2}Mn_{0.6}O_2$) cathode (**Figure 6c**). In addition, most organic materials exhibit strong Raman activity. The Raman spectra are especially important to study organic electrodes. Zhang et al.[106] identified the active sites and captured the transformation process of the functional group from C=O to C-O for the organic electrode via in-situ Raman spectroscopy (**Figure 6d**). Apart from detecting changes in electrodes, in-situ Raman also plays an important role in monitoring the liquid electrolytes for rechargeable batteries.[108-110] And more research work will benefit from advances in Raman technique, especially the in-situ/operando characterizations.

2.4 Conclusions and outlook

Following the fast development of renewable energy (solar and wind power, etc.), high-

performance energy storage devices are highly demanded. Post-LIBs with the advantage of low cost and abundant resources are promising in large-scale applications and are intensively studied. In this project, we present an overview of post-LIBs, mainly focusing on rechargeable Mg and Na batteries, and offer strategies for the optimization of electrode materials to achieve high energy density and good temperature tolerance. Despite the current achievements in both Mg and Na-based batteries, there are still great challenges and opportunities in them. The sluggish kinetics of bivalent Mg^{2+}, and the large radius of Na^{+} lead to the lack of suitable electrode materials for fast and efficient intercalation/deintercalation of Mg^{2+} or Na^{+}. Hence, meticulous electrode optimization and cell designs are urgently needed to take full advantage of their material advantage and eventually surpass the state-of-the-art LIBs. Future work on RMBs and Na-based batteries should focus on new approaches for the improvement of the overall kinetics of electrode materials and achieving high energy density close to 500 Wh kg^{-1} for operation at both RT and low temperatures.

Addressing current issues in RMBs and Na-based batteries requires adequate fundamental knowledge of characterization techniques. Characterization techniques are vital for the in-depth fundamental understanding of battery materials. The commonly used techniques are highlighted. In-situ/operando XRD has been illustrated as a powerful tool to offer valuable information on structural evolution and phase transformation of electrode materials during cycling. XAS and Raman spectroscopy techniques provide information on the surface and electronic structure of inorganic/organic materials. More in-situ or operando techniques, such as pair distribution function (PDF), Fourier-transform infrared (FTIR), X-

ray photoelectron spectroscopy (XPS), nuclear magnetic resonance (NMR), and transmission electron microscopy (TEM) are required. New in-situ cells and equipment should be designed to ensure good quality of data and fit into real operation conditions. Overall, new insights from a combination of different characterization techniques contribute to the mechanistic understanding of cell failures and thus benefit the future optimization and innovation of battery materials.

2.5 References

1. Liu, F.; Wang, T.; Liu, X.; Fan, L. Z., Challenges and Recent Progress on Key Materials for Rechargeable Magnesium Batteries. *Adv. Energy Mater.* **2020**, 2000787.

2. Guo, Z.; Zhao, S.; Li, T.; Su, D.; Guo, S.; Wang, G., Recent Advances in Rechargeable Magnesium-Based Batteries for High-Efficiency Energy Storage. *Adv. Energy Mater.* **2020**, 1903591.

3. Zhang, Z.; Dong, S.; Cui, Z.; Du, A.; Li, G.; Cui, G., Rechargeable Magnesium Batteries using Conversion-Type Cathodes: A Perspective and Minireview. *Small Methods* **2018,** *2* (10), 1800020.

4. Muldoon, J.; Bucur, C. B.; Gregory, T., Quest for Nonaqueous Multivalent Secondary Batteries: Magnesium and Beyond. *Chem. Rev.* **2014,** *114* (23), 11683-11720.

5. Canepa, P.; Sai Gautam, G.; Hannah, D. C.; Malik, R.; Liu, M.; Gallagher, K. G.; Persson, K. A.; Ceder, G., Odyssey of Multivalent Cathode Materials: Open Questions and Future Challenges. *Chem. Rev.* **2017,** *117* (5), 4287-4341.

6. Johnson, I. D.; Ingram, B. J.; Cabana, J., The Quest for Functional Oxide Cathodes for Magnesium Batteries: A Critical Perspective. *ACS Energy Lett.* **2021,** *6* (5), 1892-1900.

7. Li, L.; Lu, Y.; Zhang, Q.; Zhao, S.; Hu, Z.; Chou, S. L., Recent Progress on Layered Cathode Materials for Nonaqueous Rechargeable Magnesium Batteries. *Small* **2021,** *17* (9), e1902767.

8. Song, M.; Tan, H.; Chao, D.; Fan, H. J., Recent Advances in Zn-Ion Batteries. *Adv. Funct. Mater.* **2018,** *28* (41), 1802564.

9. Attias, R.; Salama, M.; Hirsch, B.; Goffer, Y.; Aurbach, D., Anode-Electrolyte Interfaces in Secondary Magnesium Batteries. *Joule* **2019,** *3* (1), 27-52.

10. Yoo, H. D.; Shterenberg, I.; Gofer, Y.; Gershinsky, G.; Pour, N.; Aurbach, D., Mg Rechargeable Batteries: An on-going Challenge. *Energy Environ. Sci.* **2013,** *6* (8), 2265-2279.

11. Song, J.; Sahadeo, E.; Noked, M.; Lee, S. B., Mapping the Challenges of Magnesium Battery. *J. Phys. Chem. Lett.* **2016,** *7* (9), 1736-1749.

12. Muldoon, J.; Bucur, C. B.; Gregory, T., Fervent Hype behind Magnesium Batteries: An Open Call to Synthetic Chemists-Electrolytes and Cathodes Needed. *Angew. Chem. Int. Ed.* **2017,** *56* (40), 12064-12084.

13. Lu, Y.; Wang, C.; Liu, Q.; Li, X.; Zhao, X.; Guo, Z., Progress and Perspective on Rechargeable Magnesium-Sulfur Batteries. *Small Methods* **2021,** *5* (5), 2001303.

14. Kopac Lautar, A.; Bitenc, J.; Rejec, T.; Dominko, R.; Filhol, J. S.; Doublet, M. L., Electrolyte Reactivity in the Double Layer in Mg Batteries: An Interface Potential-Dependent DFT Study. *J. Am. Chem. Soc.* **2020,** *142* (11), 5146-5153.

15. Du, A.; Zhang, H.; Zhang, Z.; Zhao, J.; Cui, Z.; Zhao, Y.; Dong, S.; Wang, L.; Zhou, X.; Cui, G., A Crosslinked Polytetrahydrofuran-Borate-Based Polymer Electrolyte Enabling Wide-Working-Temperature-Range Rechargeable Magnesium Batteries. *Adv. Mater.* **2019,** *31* (11), 1805930.

16. Zhao-Karger, Z.; Liu, R.; Dai, W.; Li, Z.; Diemant, T.; Vinayan, B. P.; Bonatto Minella, C.; Yu, X.; Manthiram, A.; Behm, R. J.; Ruben, M.; Fichtner, M., Toward Highly Reversible Magnesium–Sulfur Batteries with Efficient and Practical $Mg[B(hfip)_4]_2$ Electrolyte. *ACS Energy Lett.* **2018,** *3* (8), 2005-2013.

17. Zhao-Karger, Z.; Zhao, X.; Wang, D.; Diemant, T.; Behm, R. J.; Fichtner, M., Performance Improvement of Magnesium Sulfur Batteries with Modified Non-Nucleophilic Electrolytes. *Adv. Energy Mater.* **2015,** *5* (3), 1401155.

18. Shterenberg, I.; Salama, M.; Yoo, H. D.; Gofer, Y.; Park, J.-B.; Sun, Y.-K.; Aurbach, D., Evaluation of $(CF_3SO_2)_2N^-$ (TFSI) Based Electrolyte Solutions for Mg Batteries. *J. Electrochem. Soc.* **2015,** *162* (13), A7118-A7128.

19. Kim, H. S.; Arthur, T. S.; Allred, G. D.; Zajicek, J.; Newman, J. G.; Rodnyansky, A. E.; Oliver, A. G.; Boggess, W. C.; Muldoon, J., Structure and Compatibility of a Magnesium

Electrolyte with a Sulphur Cathode. *Nat. Commun.* **2011,** *2*, 427.

20. Mohtadi, R.; Matsui, M.; Arthur, T. S.; Hwang, S. J., Magnesium Borohydride: From Hydrogen Storage to Magnesium Battery. *Angew. Chem. Int. Ed.* **2012,** *51* (39), 9780-9783.

21. Mizrahi, O.; Amir, N.; Pollak, E.; Chusid, O.; Marks, V.; Gottlieb, H.; Larush, L.; Zinigrad, E.; Aurbach, D., Electrolyte Solutions with a Wide Electrochemical Window for Rechargeable Magnesium Batteries. *J. Electrochem. Soc.* **2008,** *155* (2), A103-A109.

22. Doe, R. E.; Han, R.; Hwang, J.; Gmitter, A. J.; Shterenberg, I.; Yoo, H. D.; Pour, N.; Aurbach, D., Novel, Electrolyte Solutions Comprising Fully Inorganic Salts with High Anodic Stability for Rechargeable Magnesium Batteries. *Chem. Commun.* **2014,** *50* (2), 243-245.

23. Li, Y. Q.; Guan, S. L.; Huo, H.; Ma, Y. L.; Gao, Y. Z.; Zuo, P. J.; Yin, G. P., A Review of Magnesium Aluminum Chloride Complex Electrolytes for Mg Batteries. *Adv. Funct. Mater.* **2021,** *31* (24), 2100650.

24. Liang, Z.; Ban, C., Strategies to Enable Reversible Magnesium Electrochemistry: From Electrolytes to Artificial Solid-Electrolyte Interphases. *Angew. Chem. Int. Ed.* **2021,** *60* (20), 11036-11047.

25. Son, S. B.; Gao, T.; Harvey, S. P.; Steirer, K. X.; Stokes, A.; Norman, A.; Wang, C.; Cresce, A.; Xu, K.; Ban, C., An Artificial Interphase Enables Reversible Magnesium Chemistry in Carbonate Electrolytes. *Nat. Chem.* **2018,** *10* (5), 532-539.

26. Dou, H.; Zhao, X.; Zhang, Y.; Zhao, W.; Yan, Y.; Ma, Z.-F.; Wang, X.; Yang, X., Revisiting the Degradation of Solid/Electrolyte Interfaces of Magnesium Metal Anodes: Decisive Role of Interfacial Composition. *Nano Energy* **2021,** *86*, 106087.

27. Li, X.; Gao, T.; Han, F.; Ma, Z.; Fan, X.; Hou, S.; Eidson, N.; Li, W.; Wang, C., Reducing Mg Anode Overpotential via Ion Conductive Surface Layer Formation by Iodine Additive. *Adv. Energy Mater.* **2018,** *8* (7), 1701728.

28. Tang, K.; Du, A.; Dong, S.; Cui, Z.; Liu, X.; Lu, C.; Zhao, J.; Zhou, X.; Cui, G., A Stable Solid Electrolyte Interphase for Magnesium Metal Anode Evolved from a Bulky Anion Lithium Salt. *Adv. Mater.* **2019**, e1904987.

29. Li, Y.; Yang, G.; Sun, S.; Zhang, C.; Lim, C. Y. J.; Wong, A. J. Y.; Lieu, W. Y.; Sofer, Z.; Ng, M. F.; Liu, W.; Seh, Z. W., High Utilization of Composite Magnesium Metal Anodes

Enabled by a Magnesiophilic Coating. *Nano Lett.* **2022,** *22* (16), 6808-6815.

30. Niu, J. Z.; Zhang, Z. H.; Aurbach, D., Alloy Anode Materials for Rechargeable Mg Ion Batteries. *Adv. Energy Mater.* **2020,** *10* (23), 2000697.

31. Bella, F.; De Luca, S.; Fagiolari, L.; Versaci, D.; Amici, J.; Francia, C.; Bodoardo, S., An Overview on Anodes for Magnesium Batteries: Challenges towards a Promising Storage Solution for Renewables. *Nanomaterials* **2021,** *11* (3), 810.

32. Yaghoobnejad Asl, H.; Fu, J.; Kumar, H.; Welborn, S. S.; Shenoy, V. B.; Detsi, E., In Situ Dealloying of Bulk Mg_2Sn in Mg-ion Half Cell as an Effective Route to Nanostructured Sn for High Performance Mg-ion Battery Anodes. *Chem. Mater.* **2018,** *30* (5), 1815-1824.

33. Benmayza, A.; Ramanathan, M.; Singh, N.; Mizuno, F.; Prakash, J., Electrochemical and Thermal Studies of Bismuth Electrodes for Magnesium-Ion Cells. *J. Electrochem. Soc.* **2015,** *162* (8), A1630-A1635.

34. Meng, Z.; Foix, D.; Brun, N.; Dedryvere, R.; Stievano, L.; Morcrette, M.; Berthelot, R., Alloys to Replace Mg Anodes in Efficient and Practical Mg-Ion/Sulfur Batteries. *ACS Energy Lett.* **2019,** *4* (9), 2040-2044.

35. Arthur, T. S.; Singh, N.; Matsui, M., Electrodeposited Bi, Sb and $Bi_{1-x}Sb_x$ Alloys as Anodes for Mg-ion Batteries. *Electrochem. Commun.* **2012,** *16* (1), 103-106.

36. Shao, Y.; Gu, M.; Li, X.; Nie, Z.; Zuo, P.; Li, G.; Liu, T.; Xiao, J.; Cheng, Y.; Wang, C.; Zhang, J. G.; Liu, J., Highly Reversible Mg Insertion in Nanostructured Bi for Mg Ion Batteries. *Nano Lett.* **2014,** *14* (1), 255-260.

37. Liu, Z.; Lee, J.; Xiang, G.; Glass, H. F.; Keyzer, E. N.; Dutton, S. E.; Grey, C. P., Insights into the Electrochemical Performances of Bi Anodes for Mg Ion Batteries Using ^{25}Mg Solid State NMR Spectroscopy. *Chem. Commun.* **2017,** *53* (4), 743-746.

38. Kravchyk, K. V.; Piveteau, L.; Caputo, R.; He, M.; Stadie, N. P.; Bodnarchuk, M. I.; Lechner, R. T.; Kovalenko, M. V., Colloidal Bismuth Nanocrystals as a Model Anode Material for Rechargeable Mg-ion Batteries: Atomistic and Mesoscale Insights. *ACS Nano* **2018,** *12* (8), 8297-8307.

39. Tan, Y. H.; Yao, W. T.; Zhang, T.; Ma, T.; Lu, L. L.; Zhou, F.; Yao, H. B.; Yu, S. H., High Voltage Magnesium-ion Battery Enabled by Nanocluster Mg_3Bi_2 Alloy Anode in Noncorrosive Electrolyte. *ACS Nano* **2018,** *12* (6), 5856-5865.

40. Xu, X.; Chao, D.; Chen, B.; Liang, P.; Li, H.; Xie, F.; Davey, K.; Qiao, S. Z., Revealing the Magnesium-Storage Mechanism in Mesoporous Bismuth via Spectroscopy and Ab-Initio Simulations. *Angew. Chem. Int. Ed.* **2020,** *59* (48), 21728-21735.

41. Wang, W.; Gang, Y.; Hu, Z.; Yan, Z.; Li, W.; Li, Y.; Gu, Q. F.; Wang, Z.; Chou, S. L.; Liu, H. K.; Dou, S. X., Reversible Structural Evolution of Sodium-Rich Rhombohedral Prussian Blue for Sodium-Ion Batteries. *Nat. Commun.* **2020,** *11* (1), 980.

42. Zhang, H.; Gao, Y.; Liu, X. H.; Yang, Z.; He, X. X.; Li, L.; Qiao, Y.; Chen, W. H.; Zeng, R. H.; Wang, Y.; Chou, S. L., Organic Cathode Materials for Sodium-Ion Batteries: From Fundamental Research to Potential Commercial Application. *Adv. Funct. Mater.* **2021,** *32* (4), 2107718.

43. Rui, X.; Zhang, X.; Xu, S.; Tan, H.; Jiang, Y.; Gan, L. Y.; Feng, Y.; Li, C. C.; Yu, Y., A Low-Temperature Sodium-Ion Full Battery: Superb Kinetics and Cycling Stability. *Adv. Funct. Mater.* **2020,** *31* (11), 2009458.

44. Kundu, D.; Talaie, E.; Duffort, V.; Nazar, L. F., The Emerging Chemistry of Sodium Ion Batteries for Electrochemical Energy Storage. *Angew. Chem. Int. Ed.* **2015,** *54* (11), 3431-3448.

45. Rudola, A.; Rennie, A. J. R.; Heap, R.; Meysami, S. S.; Lowbridge, A.; Mazzali, F.; Sayers, R.; Wright, C. J.; Barker, J., Commercialisation of High Energy Density Sodium-ion Batteries: Faradion's Journey and Outlook. *J. Mater. Chem. A* **2021,** *9* (13), 8279-8302.

46. Usiskin, R.; Lu, Y.; Popovic, J.; Law, M.; Balaya, P.; Hu, Y.-S.; Maier, J., Fundamentals, Status and Promise of Sodium-Based Batteries. *Nat. Rev. Mater.* **2021,** *6* (11), 1020-1035.

47. Zhang, N.; Deng, T.; Zhang, S.; Wang, C.; Chen, L.; Wang, C.; Fan, X., Critical Review on Low-Temperature Li-Ion/Metal Batteries. *Adv. Mater.* **2022,** *34* (15), e2107899.

48. Cho, Y.-G.; Li, M.; Holoubek, J.; Li, W.; Yin, Y.; Meng, Y. S.; Chen, Z., Enabling the Low-Temperature Cycling of NMC||Graphite Pouch Cells with an Ester-Based Electrolyte. *ACS Energy Lett.* **2021,** *6* (5), 2016-2023.

49. Gao, Y.; Rojas, T.; Wang, K.; Liu, S.; Wang, D.; Chen, T.; Wang, H.; Ngo, A. T.; Wang, D., Low-Temperature and High-Rate-Charging Lithium Metal Batteries Enabled by an Electrochemically Active Monolayer-Regulated Interface. *Nat. Energy* **2020,** *5* (7), 534-542.

50. Wu, X.-L.; Guo, Y.-G.; Su, J.; Xiong, J.-W.; Zhang, Y.-L.; Wan, L.-J., Carbon-Nanotube-

Decorated Nano-$LiFePO_4$@C Cathode Material with Superior High-Rate and Low-Temperature Performances for Lithium-Ion Batteries. *Adv. Energy Mater.* **2013,** *3* (9), 1155-1160.

51. Nagasubramanian, G., Electrical Characteristics of 18650 Li-Ion Cells at Low Temperatures. *J. Appl. Electrochem.* **2001,** *31* (1), 99-104.

52. Hubble, D.; Brown, D. E.; Zhao, Y.; Fang, C.; Lau, J.; McCloskey, B. D.; Liu, G., Liquid Electrolyte Development for Low-Temperature Lithium-Ion Batteries. *Energy Environ. Sci.* **2022,** *15* (2), 550-578.

53. Zhang, J.; Zhang, J.; Liu, T.; Wu, H.; Tian, S.; Zhou, L.; Zhang, B.; Cui, G., Toward Low-Temperature Lithium Batteries: Advances and Prospects of Unconventional Electrolytes. *Adv. Energy Sustainability Res.* **2021,** *2* (10), 2100039.

54. Li, Q.; Liu, G.; Cheng, H.; Sun, Q.; Zhang, J.; Ming, J., Low-Temperature Electrolyte Design for Lithium-Ion Batteries: Prospect and Challenges. *Chemistry* **2021,** *27* (64), 15842-15865.

55. Lin, X.; Zhou, G.; Liu, J.; Yu, J.; Effat, M. B.; Wu, J.; Ciucci, F., Rechargeable Battery Electrolytes Capable of Operating over Wide Temperature Windows and Delivering High Safety. *Adv. Energy Mater.* **2020,** *10* (43), 2001235.

56. Hou, J.; Yang, M.; Wang, D.; Zhang, J., Fundamentals and Challenges of Lithium Ion Batteries at Temperatures between -40 and 60 °C. *Adv. Energy Mater.* **2020,** *10* (18), 1904152.

57. Gupta, A.; Manthiram, A., Designing Advanced Lithium-Based Batteries for Low-Temperature Conditions. *Adv Energy Mater* **2020,** *10* (38), 2001972.

58. Hu, X.; Zheng, Y.; Howey, D. A.; Perez, H.; Foley, A.; Pecht, M., Battery Warm-up Methodologies at Subzero Temperatures for Automotive Applications: Recent Advances and Perspectives. *Prog. Energy Combust. Sci.* **2020,** *77*, 100806.

59. Xue, J. J.; Zhang, Z. L.; Guo, H. Y.; Liu, R. X.; Wang, Y.; Wen, L. Z.; Liang, G. C., Primary Particles with Ultra-Thin Carbon Layer Combined with Loose Secondary Particles to Jointly Promote the Low-Temperature Performance of $LiFePO_4$. *Ionics* **2022,** *28* (9), 4229-4237.

60. Ren, W.; Zhang, Y.; Lv, R.; Guo, S.; Wu, W.; Liu, Y.; Wang, J., In-Situ Formation of Quasi-Solid Polymer Electrolyte for Improved Lithium Metal Battery Performances at Low

Temperatures. *J. Power Sources* **2022,** *542*, 231773.

61. Wu, X.; Wang, W.; Du, J., Effect of Charge Rate on Capacity Degradation of $LiFePO_4$ Power Battery at Low Temperature. *Int. J. Energy Res.* **2019,** *44* (3), 1775-1788.

62. Huang, C.; Zhao, S.-X.; Peng, H.; Lin, Y.-H.; Nan, C.-W.; Cao, G.-Z., Hierarchical Porous $Li_4Ti_5O_{12}$–TiO_2 Composite Anode Materials with Pseudocapacitive Effect for High-Rate and Low-Temperature Applications. *J. Mater. Chem. A* **2018,** *6* (29), 14339-14351.

63. Qin, R.; Wei, Y.; Zhai, T.; Li, H., LISICON Structured $Li_3V_2(PO_4)_3$ with High Rate and Ultralong Life for Low-Temperature Lithium-Ion Batteries. *J. Mater. Chem. A* **2018,** *6* (20), 9737-9746.

64. Wang, X.; Wen, L.; Zheng, Y.; Ren, X.; Li, Y.; Liang, G., Effect of $FeSO_4$ Purity on Low Temperature Performance of $LiFePO_4$/C. *Ionics* **2020,** *26* (9), 4433-4442.

65. Zhou, Y.; Gu, C. D.; Zhou, J. P.; Cheng, L. J.; Liu, W. L.; Qiao, Y. Q.; Wang, X. L.; Tu, J. P., Effect of Carbon Coating on Low Temperature Electrochemical Performance of $LiFePO_4$/C by Using Polystyrene Sphere as Carbon Source. *Electrochim. Acta* **2011,** *56* (14), 5054-5059.

66. Zhang, D.; Zhu, D.; Guo, W.; Deng, C.; Xu, Q.; Li, H.; Min, Y., The Fluorine-Rich Electrolyte as an Interface Modifier to Stabilize Lithium Metal Battery at Ultra-Low Temperature. *Adv. Funct. Mater.* **2022,** *32* (23), 2112764.

67. Hu, D.; Chen, L.; Tian, J.; Su, Y.; Li, N.; Chen, G.; Hu, Y.; Dou, Y.; Chen, S.; Wu, F., Research Progress of Lithium Plating on Graphite Anode in Lithium-Ion Batteries. *Chin. J. Chem.* **2020,** *39* (1), 165-173.

68. Liu, Y.; Yang, B.; Dong, X.; Wang, Y.; Xia, Y., A Simple Prelithiation Strategy To Build a High-Rate and Long-Life Lithium-Ion Battery with Improved Low-Temperature Performance. *Angew. Chem. Int. Ed.* **2017,** *56* (52), 16606-16610.

69. Dong, X.; Wang, Y. G.; Xia, Y., Promoting Rechargeable Batteries Operated at Low Temperature. *Acc Chem Res* **2021,** *54* (20), 3883-3894.

70. Dong, X.; Yang, Y.; Li, P.; Fang, Z.; Wang, Y.; Xia, Y., A High-Rate and Long-Life Rechargeable Battery Operated at -75 °C. *Batteries & Supercaps* **2020,** *3* (10), 1016-1020.

71. Liang, H.; Liu, L.; Wang, N.; Zhang, W.; Hung, C. T.; Zhang, X.; Zhang, Z.; Duan, L.; Chao, D.; Wang, F.; Xia, Y.; Li, W.; Zhao, D., Unusual Mesoporous Titanium Niobium

Oxides Realizing Sodium-Ion Batteries Operated at -40 degrees C. *Adv. Mater.* **2022,** *34* (28), e2202873.

72. Dong, X.; Yang, Y.; Wang, B.; Cao, Y.; Wang, N.; Li, P.; Wang, Y.; Xia, Y., Low-Temperature Charge/Discharge of Rechargeable Battery Realized by Intercalation Pseudocapacitive Behavior. *Adv. Sci. (Weinh.)* **2020,** *7* (14), 2000196.

73. You, Y.; Yao, H. R.; Xin, S.; Yin, Y. X.; Zuo, T. T.; Yang, C. P.; Guo, Y. G.; Cui, Y.; Wan, L. J.; Goodenough, J. B., Subzero-Temperature Cathode for a Sodium-Ion Battery. *Adv. Mater.* **2016,** *28* (33), 7243-7248.

74. Wang, Z.; Shen, X.; Li, S.; Wu, Y.; Yang, T.; Liu, J.; Qian, T.; Yan, C., Low-Temperature Li-S Batteries Enabled by All Amorphous Conversion Process of Organosulfur Cathode. *J. Energy Chem.* **2022,** *64*, 496-502.

75. Liang, Y.; Yao, Y., Positioning Organic Electrode Materials in the Battery Landscape. *Joule* **2018,** *2* (9), 1690-1706.

76. Poizot, P.; Gaubicher, J.; Renault, S.; Dubois, L.; Liang, Y.; Yao, Y., Opportunities and Challenges for Organic Electrodes in Electrochemical Energy Storage. *Chem. Rev.* **2020,** *120* (14), 6490-6557.

77. Qin, K.; Huang, J.; Holguin, K.; Luo, C., Recent Advances in Developing Organic Electrode Materials for Multivalent Rechargeable Batteries. *Energy Environ. Sci.* **2020,** *13* (11), 3950-3992.

78. Qin, J.; Lan, Q.; Liu, N.; Zhao, Y.; Song, Z.; Zhan, H., A Metal-Free Battery Working at -80 °C. *Energy Storage Mater.* **2020,** *26*, 585-592.

79. Dong, X.; Lin, Y.; Li, P.; Ma, Y.; Huang, J.; Bin, D.; Wang, Y.; Qi, Y.; Xia, Y., High-Energy Rechargeable Metallic Lithium Battery at -70 ºC Enabled by a Cosolvent Electrolyte. *Angew. Chem. Int. Ed.* **2019,** *58* (17), 5623-5627.

80. Dong, X.; Guo, Z.; Guo, Z.; Wang, Y.; Xia, Y., Organic Batteries Operated at -70°C. *Joule* **2018,** *2* (5), 902-913.

81. Holoubek, J.; Kim, K.; Yin, Y.; Wu, Z.; Liu, H.; Li, M.; Chen, A.; Gao, H.; Cai, G.; Pascal, T. A.; Liu, P.; Chen, Z., Electrolyte Design Implications of Ion-Pairing in Low-Temperature Li Metal Batteries. *Energy Environ. Sci.* **2022,** *15* (4), 1647-1658.

82. Zhang, W.; Xia, H.; Zhu, Z.; Lv, Z.; Cao, S.; Wei, J.; Luo, Y.; Xiao, Y.; Liu, L.; Chen, X.,

Decimal Solvent-Based High-Entropy Electrolyte Enabling the Extended Survival Temperature of Lithium-Ion Batteries to −130 °C. *CCS Chemistry* **2021,** *3* (4), 1245-1255.

83. Cai, G.; Holoubek, J.; Xia, D.; Li, M.; Yin, Y.; Xing, X.; Liu, P.; Chen, Z., An Ester Electrolyte for Lithium-Sulfur Batteries Capable of Ultra-Low Temperature Cycling. *Chem. Commun.* **2020,** *56* (64), 9114-9117.

84. Yan, L.; Huang, J.; Guo, Z.; Dong, X.; Wang, Z.; Wang, Y., Solid-State Proton Battery Operated at Ultralow Temperature. *ACS Energy Lett.* **2020,** *5* (2), 685-691.

85. Wang, M.; Li, T.; Yin, Y.; Yan, J.; Zhang, H.; Li, X., A -60 °C Low-Temperature Aqueous Lithium Ion-Bromine Battery with High Power Density Enabled by Electrolyte Design. *Adv. Energy Mater.* **2022,** *12* (25), 2200728.

86. Nian, Q.; Wang, J.; Liu, S.; Sun, T.; Zheng, S.; Zhang, Y.; Tao, Z.; Chen, J., Aqueous Batteries Operated at -50 degrees C. *Angew. Chem. Int. Ed.* **2019,** *58* (47), 16994-16999.

87. Yang, G.; Huang, J.; Wan, X.; Liu, B.; Zhu, Y.; Wang, J.; Fontaine, O.; Luo, S.; Hiralal, P.; Guo, Y.; Zhou, H., An Aqueous Zinc-Ion Battery Working at -50°C Enabled by Low-Concentration Perchlorate-Based Chaotropic Salt Electrolyte. *EcoMat* **2022,** *4* (2), e12165.

88. Shadike, Z.; Zhao, E.; Zhou, Y. N.; Yu, X.; Yang, Y.; Hu, E.; Bak, S.; Gu, L.; Yang, X. Q., Advanced Characterization Techniques for Sodium-Ion Battery Studies. *Adv. Energy Mater.* **2018,** *8* (17), 1702588.

89. Lu, J.; Wu, T. P.; Amine, K., State-of-the-Art Characterization Techniques for Advanced Lithium-Ion Batteries. *Nat. Energy* **2017,** *2* (3), 1-13.

90. Pu, J.; Zhong, C.; Liu, J.; Wang, Z.; Chao, D., Advanced In-Situ Technology for Li/Na Metal Anodes: An In-Depth Mechanistic Understanding. *Energy Environ. Sci.* **2021,** *14* (7), 3872-3911.

91. Li, H.; Guo, S.; Zhou, H., In-Situ/Operando Characterization Techniques in Lithium-Ion Batteries and Beyond. *J. Energy Chem.* **2021,** *59*, 191-211.

92. Bak, S.-M.; Shadike, Z.; Lin, R.; Yu, X.; Yang, X.-Q., In Situ/Operando Synchrotron-Based X-ray Techniques for Lithium-Ion Battery Research. *NPG Asia Mater.* **2018,** *10* (7), 563-580.

93. Lin, F.; Liu, Y.; Yu, X.; Cheng, L.; Singer, A.; Shpyrko, O. G.; Xin, H. L.; Tamura, N.; Tian, C.; Weng, T. C.; Yang, X. Q.; Meng, Y. S.; Nordlund, D.; Yang, W.; Doeff, M. M.,

Synchrotron X-ray Analytical Techniques for Studying Materials Electrochemistry in Rechargeable Batteries. *Chem. Rev.* **2017,** *117* (21), 13123-13186.

94. Lou, S.; Sun, N.; Zhang, F.; Liu, Q.; Wang, J., Tracking Battery Dynamics by Operando Synchrotron X-ray Imaging: Operation from Liquid Electrolytes to Solid-State Electrolytes. *Accounts of Materials Research* **2021,** *2* (12), 1177-1189.

95. Liu, H.; Strobridge, F. C.; Borkiewicz, O. J.; Wiaderek, K. M.; Chapman, K. W.; Chupas, P. J.; Grey, C. P., Batteries. Capturing Metastable Structures during High-Rate Cycling of $LiFePO_4$ Nanoparticle Electrodes. *Science* **2014,** *344* (6191), 1252817.

96. Fu, Q.; Sarapulova, A.; Trouillet, V.; Zhu, L.; Fauth, F.; Mangold, S.; Welter, E.; Indris, S.; Knapp, M.; Dsoke, S.; Bramnik, N.; Ehrenberg, H., In Operando Synchrotron Diffraction and in Operando X-ray Absorption Spectroscopy Investigations of Orthorhombic V_2O_5 Nanowires as Cathode Materials for Mg-Ion Batteries. *J. Am. Chem. Soc.* **2019,** *141* (6), 2305-2315.

97. Wu, Y. A.; Yin, Z.; Farmand, M.; Yu, Y. S.; Shapiro, D. A.; Liao, H. G.; Liang, W. I.; Chu, Y. H.; Zheng, H., In-situ Multimodal Imaging and Spectroscopy of Mg Electrodeposition at Electrode-Electrolyte Interfaces. *Sci. Rep.* **2017,** *7*, 42527.

98. Di Cicco, A.; Giglia, A.; Gunnella, R.; Koch, S. L.; Mueller, F.; Nobili, F.; Pasqualini, M.; Passerini, S.; Tossici, R.; Witkowska, A., SEI Growth and Depth Profiling on ZFO Electrodes by Soft X-Ray Absorption Spectroscopy. *Adv. Energy Mater.* **2015,** *5* (18), 1500642.

99. Zhang, L.; Sun, D.; Kang, J.; Wang, H. T.; Hsieh, S. H.; Pong, W. F.; Bechtel, H. A.; Feng, J.; Wang, L. W.; Cairns, E. J.; Guo, J., Tracking the Chemical and Structural Evolution of the TiS_2 Electrode in the Lithium-Ion Cell Using Operando X-ray Absorption Spectroscopy. *Nano Lett.* **2018,** *18* (7), 4506-4515.

100. Ravel, B.; Newville, M., ATHENA, ARTEMIS, HEPHAESTUS: Data Analysis for X-ray Absorption Spectroscopy Using IFEFFIT. *J. Synchrotron Radiat.* **2005,** *12* (4), 537-541.

101. Yamamoto, T., Assignment of Pre-Edge Peaks in K-edge X-ray Absorption Spectra of 3d Transition Metal Compounds: Electric Dipole or Quadrupole? *X-Ray Spectrom.* **2008,** *37* (6), 572-584.

102. Zhou, Y. N.; Ma, J.; Hu, E.; Yu, X.; Gu, L.; Nam, K. W.; Chen, L.; Wang, Z.; Yang, X.

Q., Tuning Charge-Discharge Induced Unit Cell Breathing in Layer-Structured Cathode Materials for Lithium-Ion Batteries. *Nat. Commun.* **2014,** *5*, 5381.

103. Du, Z.; Chen, X.; Hu, W.; Chuang, C.; Xie, S.; Hu, A.; Yan, W.; Kong, X.; Wu, X.; Ji, H.; Wan, L. J., Cobalt in Nitrogen-Doped Graphene as Single-Atom Catalyst for High-Sulfur Content Lithium-Sulfur Batteries. *J. Am. Chem. Soc.* **2019,** *141* (9), 3977-3985.

104. Li, H.; Meng, R.; Guo, Y.; Chen, B.; Jiao, Y.; Ye, C.; Long, Y.; Tadich, A.; Yang, Q. H.; Jaroniec, M.; Qiao, S. Z., Reversible Electrochemical Cxidation of Sulfur in Ionic Liquid for High-Voltage Al-S Batteries. *Nat. Commun.* **2021,** *12* (1), 5714.

105. Sarycheva, A.; Gogotsi, Y., Raman Spectroscopy Analysis of the Structure and Surface Chemistry of $Ti_3C_2T_x$ MXene. *Chem. Mater.* **2020,** *32* (8), 3480-3488.

106. Zhang, H.; Gao, Y.; Chen, M.; Li, L.; Li, L.; Qiao, Y.; Li, W.; Wang, J.; Chou, S. L., Organic Small Molecules with Electrochemical-Active Phenolic Enolate Groups for Ready-to-Charge Organic Sodium-Ion Batteries. *Small Methods* **2022,** *6* (7), 2200455.

107. Flores, E.; Novák, P.; Berg, E. J., In situ and Operando Raman Spectroscopy of Layered Transition Metal Oxides for Li-ion Battery Cathodes. *Front. Energy Res.* **2018,** *6*, 82.

108. Ren, W.; Wu, D.; NuLi, Y. N.; Zhang, D.; Yang, Y.; Wang, Y.; Yang, J.; Wang, J. L., An Efficient Bulky $Mg[B(Otfe)_4]_2$ Electrolyte and Its Derivatively General Design Strategy for Rechargeable Magnesium Batteries. *ACS Energy Lett.* **2021,** *6* (9), 3212-3220.

109. Vestfried, Y.; Chusid, O.; Goffer, Y.; Aped, P.; Aurbach, D., Structural Analysis of Electrolyte Solutions Comprising Magnesium-Aluminate Chloro-Organic Complexes by Raman Spectroscopy. *Organometallics* **2007,** *26* (13), 3130-3137.

110. Pour, N.; Gofer, Y.; Major, D. T.; Aurbach, D., Structural Analysis of Electrolyte Solutions for Rechargeable Mg Batteries by Stereoscopic Means and DFT Calculations. *J. Am. Chem. Soc.* **2011,** *133* (16), 6270-6278.

Chapter 3: Revealing the Magnesium Storage Mechanism in Mesoporous Bismuth via Spectroscopy and Ab Initio Simulation

3.1 Introduction and significance

Bismuth is a promising alternative to magnesium metal anode. It permits non-corrosive magnesium electrolytes with high oxidation stability and encourages the investigation of high-voltage cathode materials for magnesium ion batteries (MIBs). An in-depth understanding of the mechanism of Mg storage in bismuth is crucial for the search for reliable approaches to boost the electrochemical performance of MIBs. Here, we present mesoporous bismuth nanosheets as a model to study the charge storage mechanism of Mg/Bi system. Using a systematic spectroscopy investigation of combined synchrotron-based operando X-ray diffraction, near-edge X-ray absorption fine structure and Raman, for the first time, we demonstrate a reversible two-step alloying reaction mechanism of $Bi \leftrightarrow MgBi \leftrightarrow Mg_3Bi_2$. Ab initio simulation methods disclose the formation of the MgBi intermediate and confirm its high electronic conductivity. This intermediate serves as a buffer for the significant volume expansion (204 %) and acts to regulate Mg storage kinetics. The mesoporous bismuth nanosheets, as an ideal material for the investigation of Mg charge storage mechanism, effectively alleviate volume expansion and endow significant electrochemical performance in the lithium-free electrolyte. These findings will benefit mechanistic understandings and advance material designs for MIBs. The highlights of this work include:

- **New Mg-ion storage mechanism** – We propose for the first time a two-step alloying reaction in Mg/Bi battery systems i.e. reversible charge storage of $Bi \leftrightarrow MgBi \leftrightarrow Mg_3Bi_2$. The

storage mechanism is comprehensively investigated by synchrotron-based operando X-ray diffraction and near-edge X-ray absorption fine structure, together with theoretical computations.

- **Boosted kinetics** – The electrochemical process and Mg-ion migration kinetics are theoretically simulated. The MgBi intermediate phase is modelled with a low volume expansion ratio, fast kinetics and high electronic conductivity to accelerate electrochemical kinetics.

- **Nano-engineering with excellent performance** – The electrochemical process and Mg-ion migration kinetics are theoretically simulated. A free-standing mesoporous Bi nanosheet is firstly applied as an advanced anode for Mg-ion storage. As a result, the p-Bi NS mitigates volume expansion to provide a record cycling stability when compared with other Bi-based materials in Li-free electrolytes.

3.2 Revealing the Magnesium Storage Mechanism in Mesoporous Bismuth via Spectroscopy and Ab Initio Simulation

This Chapter is included as it appears as a journal paper published by **Xin Xu**, Dongliang Chao, Biao Chen, Pei Liang, Huan Li, Fangxi Xie, Kenneth Davey, and Shi-Zhang Qiao*. Revealing the Magnesium‐Storage Mechanism in Mesoporous Bismuth via Spectroscopy and Ab‐Initio Simulations. ***Angewandte Chemie International Edition*** 2020, 59(48): 21728-21735.

Statement of Authorship

Title of Paper	Revealing the Magnesium-Storage Mechanism in Mesoporous Bismuth via Spectroscopy and Ab-Initio Simulations
Publication Status	☑ Published ☐ Accepted for Publication ☐ Submitted for Publication ☐ Unpublished and Unsubmitted work written in manuscript style
Publication Details	Xin Xu, Dongliang Chao, Biao Chen, Pei Liang, Huan Li, Fangxi Xie, Kenneth Davey, and Shi-Zhang Qiao. Angewandte Chemie International Edition 2020, 59(48): 21728-21735.

Principal Author

Name of Principal Author (Candidate)	Xin Xu		
Contribution to the Paper	Conducted experiments, data curation, formal analysis, investigation, and writing–original draft.		
Overall percentage (%)	70		
Certification:	This paper reports on original research I conducted during the period of my Higher Degree by Research candidature and is not subject to any obligations or contractual agreements with a third party that would constrain its inclusion in this thesis. I am the primary author of this paper.		
Signature		Date	20 October 2022

Co-Author Contributions

By signing the Statement of Authorship, each author certifies that:

i. the candidate's stated contribution to the publication is accurate (as detailed above);

ii. permission is granted for the candidate in include the publication in the thesis; and

iii. the sum of all co-author contributions is equal to 100% less the candidate's stated contribution.

Name of Co-Author	Dongliang Chao		
Contribution to the Paper	Supervision, formal analysis, writing–review and editing		
Signature		Date	20 October 2022

Name of Co-Author	Biao Chen		
Contribution to the Paper	Assisted with material characterizations		
Signature		Date	20 October 2022

Name of Co-Author	Pei Liang		
Contribution to the Paper	Conducted theoretical computations		
Signature		Date	20 October 2022

Name of Co-Author	Huan Li		
Contribution to the Paper	Helped with data analysis		
Signature		Date	20 October 2022

Name of Co-Author	Fangxi Xie		
Contribution to the Paper	Assisted with synchrotron characterization and analysis		
Signature		Date	20 October 2022

Name of Co-Author	Kenneth Davey		
Contribution to the Paper	Analysis, writing–review and editing		
Signature		Date	20 October 2022

Name of Co-Author	Shi-Zhang Qiao		
Contribution to the Paper	Supervision, resources, conceptualization and writing–review and editing		
Signature		Date	20 October 2022

Name of Co-Author			
Contribution to the Paper			
Signature		Date	

How to cite: *Angew. Chem. Int. Ed.* **2020**, *59*, 21728 21735
International Edition: doi.org/10.1002/anie.202009528
German Edition: doi.org/10.1002/ange.202009528

VIP **Mg/Bi Batteries** **Very Important Paper**

Revealing the Magnesium-Storage Mechanism in Mesoporous Bismuth via Spectroscopy and Ab-Initio Simulations

*Xin Xu[+], Dongliang Chao[+], Biao Chen, Pei Liang, Huan Li, Fangxi Xie, Kenneth Davey, and Shi-Zhang Qiao**

Abstract: *We present mesoporous bismuth nanosheets as a model to study the charge storage mechanism of Mg/Bi systems in magnesium ion batteries (MIBs). Using a systematic spectroscopy investigation of combined synchrotron based operando X ray diffraction, near edge X ray absorption fine structure and Raman, we demonstrate a reversible two step alloying reaction mechanism $Bi \leftrightarrow MgBi \leftrightarrow Mg_3Bi_2$. Ab initio simulation methods disclose the formation of a MgBi intermediate and confirm its high electronic conductivity. This intermediate serves as a buffer for the significant volume expansion (204%) and acts to regulate Mg storage kinetics. The mesoporous bismuth nanosheets, as an ideal material for the investigation of the Mg charge storage mechanism, effectively alleviate volume expansion and enable significant electrochemical performance in a lithium free electrolyte. These findings will benefit mechanistic understandings and advance material designs for MIBs.*

Introduction

Due to low cost, high volumetric energy density and, intrinsic dendrite free behaviour, magnesium (Mg) ion batteries appear practical for energy storage systems.[1] However, application has been hindered by the uncontrolled electrochemical interfacial behaviour between the metal and the electrolyte. The formation of a passivation layer on the surface of Mg metal deteriorates reversibility when exposed to conventional carbonate electrolytes.[2] To be compatible with Mg anode, ethereal electrolytes that are stable in metallic Mg have been developed. However these electrolytes, such as Grignard based,[3] borohydride based[4] and magnesium aluminate chloride complex (MACC)[5] in tetrahydrofuran or glyme solvents, are often corrosive, air sensitive, and suffer from poor anodic stability.[6] Therefore, an alternative Mg^{2+} host anode is practically desirable.

Alloy type anodes such as Bi,[7] Sn,[8] Sb[9] and Ga[10] have been investigated in Mg based batteries. Bismuth is attractive because of its relatively high theoretical volumetric capacity (1949 $mAh\,cm^{-3}$ for Mg_3Bi_2).[11] Additionally, Bi can be coupled with conventional carbonate electrolyte, and has been demonstrated to be applicable in high voltage MIBs due to the flat and low redox potential of Bi/Bi^{3+}.[12] Authur et al.[9] first demonstrated the electrochemical activity of Bi model in Mg battery and achieved a capacity of 222 $mAh\,g^{-1}$ in Grignard based electrolyte. The Mg^{2+} storage mechanism was depicted as:

$$2\,Bi + 3\,Mg^{2+} + 6\,e \leftrightarrow Mg_3Bi_2 \quad (1)$$

This is accepted for the Mg/Bi system.[12,13] Charge storage mechanisms for Bi have been systematically investigated in Li/Bi, Na/Bi and K/Bi batteries. Findings from early studies on Li/Bi system imply that Li reversibly alloys with Bi by forming intermediate phases of LiBi and Li_3Bi.[14] In Na/Bi the alloying reaction follows a process of Bi NaBi Na_3Bi, with a two step reversible reaction.[15] A more complicated K ion storage mechanism of Bi KBi_2 K_3Bi_2 K_3Bi in K/Bi system has been confirmed.[16] However, current achievements on Mg/Bi battery system were not aware of any intermediate states as aforementioned alloying process. The formation of intermediate phases not addressed in Equation (1) might be exploited to positively impact the mechanics,[17] physical properties and kinetics of the electrode.[18] A thorough investigation of the Mg^{2+} storage mechanism in Mg/Bi is therefore timely.

The past ten years development of Mg/Bi batteries has actually been sluggish, with materials developed exhibiting poor rate and cycling performance in lithium (Li) free electrolyte (*see* Table S1). This because of a significant volume change and poor kinetics of Mg^{2+} during magnesiation/demagnesiation. Here, a mesoporous bismuth nanosheet (p Bi NS) electrode is used as a model to investigate Mg^{2+} transfer kinetics and charge storage mechanism of Mg/Bi. Endowed by this mesoporous feature, the p Bi NS exhibits record cycling stability compared with other Bi based materials in Li free electrolytes. Through combining spectroscopy technologies of synchrotron based operando X ray diffraction (XRD) and near edge X ray absorption fine structure (NEXAFS), and ab initio simulation, we systematically investigate the Mg storage mechanism. Strong intensity of

[*] X. Xu,[+] Dr. D. Chao,[+] H. Li, Dr. F. Xie, Dr. K. Davey, Prof. S. Z. Qiao
School of Chemical Engineering & Advanced Materials, The University of Adelaide
Adelaide, SA 5005 (Australia)
E mail: s.qiao@adelaide.edu.au
Dr. B. Chen
School of Materials Science and Engineering and Tianjin Key Laboratory of Composite and Functional Materials, Tianjin University
Tianjin, 300350 (P. R. China)
P. Liang
College of Optical and Electronic Technology, China Jiliang University
Hangzhou, 310038 (P. R. China)
[+] These authors contributed equally to this work.
Supporting information and the ORCID identification number(s) for the author(s) of this article can be found under: https://doi.org/10.1002/anie.202009528.

X ray techniques with high temporal and spatial resolution allows more accurate disclosure of electrochemical evolution of batteries.[19] An intermediate phase MgBi, is firstly captured during magnesiation. Theoretical computations based on density functional theory (DFT) confirm high electronic conductivity of MgBi, and low energy barrier of the two step reaction (Bi MgBi Mg_3Bi_2). The formation of this intermediate phase is well aligned with significant Mg^{2+} storage performance. These findings aid understanding of alloy type anodes to advance the development and practical application in MIBs.

Results and Discussion

Proposal of Two-Step Charge-Storage Mechanism

The alloying/de alloying of Bi was firstly investigated by ex situ Raman, NEXAFS and synchrotron based operando XRD. Figure 1a shows the Raman spectra of p Bi NS at different stages of the initial discharge/charge. The corre sponding discharge/charge profile with successively marked stages is shown. Two clear characteristic peaks at 70 and 94 cm^{-1} are indexed, respectively, to the vibrational modes of Bi Bi (E_g) and the lattice (A_{1g}).[20] The disappearance and re appearance of two Raman peaks imply a reversible reaction of Bi anode with Mg. Metallic Mg alloying with Bi in different atomic ratios should possess different local electronic struc ture. As is shown in Figure 1b, Mg K edge NEXAFS spectra provide reliable information on electronic and chemical states of central atoms. The position shift of the main edge of Mg K edge suggests a variation of the electronic structure of Mg atoms. The main edge values acquired from the Athena software based on first derivative results (Figure S1) are shown as the inset of Figure S2. During discharge, the photon energies move continuously to a lower position from stage 1, 2 to 3, indicating different electronic structures of Mg atoms between stage 2 and 3. This implies an intermediate state before full discharge. When fully charged to stage 6, the photon energy returns to a higher position, suggesting a reversible alloying/de alloying process. The variation of the main edge points to the existence of an intermediate phase.

To confirm the phase evolution upon cycling, synchrotron based operando X ray diffraction was applied. The contour maps in the initial cycle are shown in Figure 1c. The results

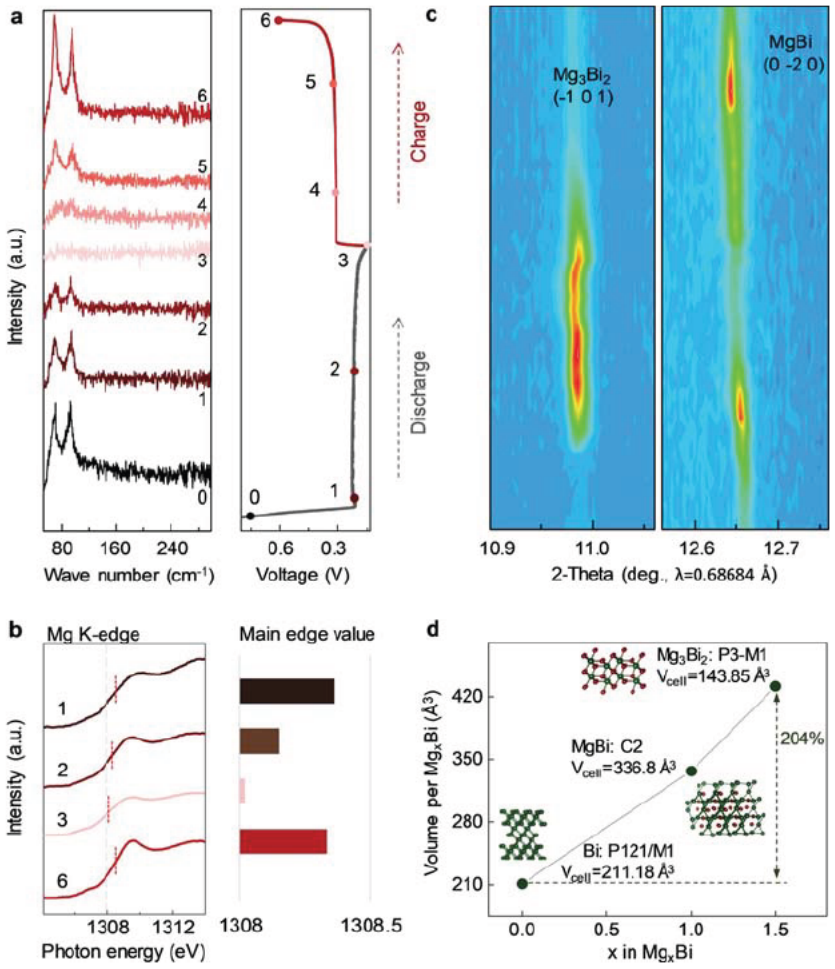

Figure 1. Proposal of two step Mg ion storage mechanism in Bi. a) The ex situ Raman spectra of p Bi NS in the initial cycle and the corresponding discharge/charge profile. b) Normalized Mg K edge NEXAFS spectra. c) Contour maps of synchrotron based operando XRD analyses in the initial cycle. d) DFT calculation of volume change of Mg Bi alloys. Insets show corresponding crystal structures and detailed crystal parameters.

involve a two step reaction process that has not previously been reported. At the beginning of discharge (stage 1), a peak at 12.65° indexed to monoclinic MgBi (0 20) is detected, and intensity gradually increases. Further discharging to stage 2, the peak at 10.99° (101) assigned to trigonal Mg_3Bi_2 emerges, accompanying the weakened peak of MgBi. Following full discharge to 0.05 V vs. Mg/Mg^{2+} (stage 3), MgBi phase all but vanishes to transform to Mg_3Bi_2. During the following charge process, the peak intensity of Mg_3Bi_2 decreases gradually and finally disappears concomitantly with the re appearance of MgBi. Here, the MgBi acts as the intermediate phase that transforms between Bi and Mg_3Bi_2. Therefore the electrochemical reaction mechanism of Bi anode can be reliably described by two successive steps:

$$Bi + Mg^{2+} + 2e \leftrightarrow MgBi \quad (3)$$

$$2MgBi + Mg^{2+} + 2e \leftrightarrow Mg_3Bi_2 \quad (4)$$

As computational results shown in Figure 1 d, the reaction from Mg/Bi to Mg_3Bi_2 via MgBi intermediate gives good mechanical properties. This is due to the volume buffer effect of the intermediate phase.[17] The volume expansion ratio to form MgBi is less than the direct formation of Mg_3Bi_2. The intermediate phase serves as a buffer to lower mechanical disruptions. Whilst the estimated volume expansion from Bi to Mg_3Bi_2 is still high and up to 204%. The computed result highlights the importance of rational structural design of Bi anode, which can accommodate the mechanical stress and significant volume expansion.

Structural Evolution and Electrochemical Performance

Bismuth is a promising anode for alkali metal ion batteries based on the alloying reaction mechanism. However, poor kinetics associated with the high diffusion barrier of metal ions, and the severe volume variations originated from alloying/de alloying process, are two key obstacles that prevent wide application of this alloy anode.[21] Delicate structures, such as yolk shell nanospheres for Na^+ storage,[22] colloidal nanocrystals for Mg ion battery[13a] and dual shell boxes for K ion storage[23] can significantly enhance electro chemical performance by shortening the ion diffusion length. Here, for the first time, mesoporous Bi nanosheets were loaded onto flexible substrate forming a free standing Mg^{2+} storage anode. As is illustrated in Figure S3 and S4, bismuth oxyiodide nanosheet was grown on carbon matrix via a facile hydrothermal approach. It was reduced to Bi nanosheets in sodium borohydride solution to form a highly porous structure (Figure 2 a,b and Figure S5) through removal of oxygen and iodine. The XRD pattern confirms the crystal structure of hexagonal Bi (JCPDS #44 1246, Figure S6). The N_2 adsorption desorption isotherm of Figure 2 c provides detailed pore information for p Bi NS. This is ascribed to type IV with typical mesoporous attributions. The average

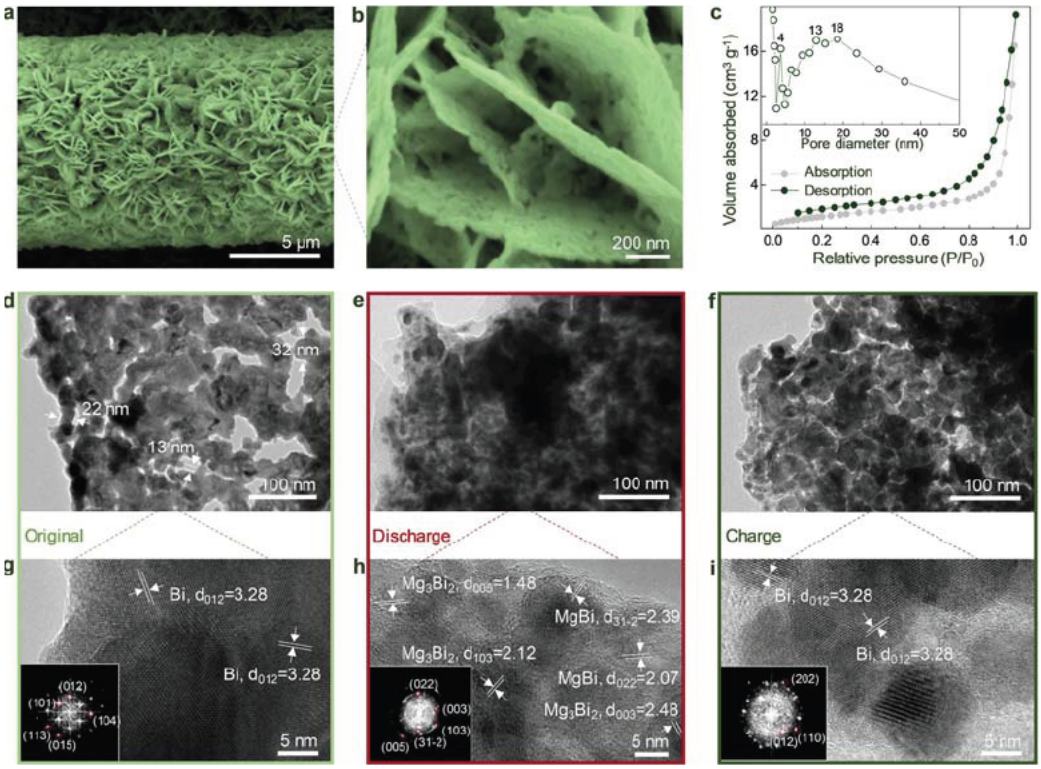

Figure 2. Morphology and structural/crystal evolution of p Bi NS. a) SEM images of mesoporous Bi nanosheets on single carbon fiber. b) Enlarge SEM image of mesoporous Bi nanosheets. c) N_2 absorption desorption isothermsm (77 K) of p Bi NS and corresponding pore size distribution (inset). d f) TEM images of p Bi NS of the original (d), fully discharged (e) and charged (f) states. g i) HRTEM images of p Bi NS of the original (g), fully discharged (h) and charged (i) states (Insets are the relevant fast Fourier transformation images).

pore diameter of p Bi NS is 17.6 nm. The Bi bulk sample does not show any obvious characteristics of mesopores (Figure S7a and S8). This porous structure in p Bi NS functions as efficient transport channels for both ions and electrolytes, and offers efficient buffering space for the 204% volume change during alloying/de alloying process.

The volume buffering effect from the mesopores was recorded via transmission electron microscopy (TEM) images, Figure 2d f, which correspond, respectively, to the original, discharge and, charge state of p Bi NS. The original p Bi NS exhibits an interconnected nanocrystalline feature with grain size ranging from 10 to 40 nm (Figure 2d). The high resolution transmission electron microscopy (HRTEM), and corresponding fast Fourier transformation patterns (inset) of original p Bi NS are shown as Figure 2g. These confirm the pure phase of Bi metal. The as prepared material shows excellent crystallinity with a lattice spacing of 3.28 Å. This agrees very well with hexagonal Bi (012) facets. After full alloying with Bi, the volume expansion extends inwardly and occupies the available voids. The result is that this leads to continuous nanosheets, rather than pulverization of the material (Figure 2e and S7b). The HRTEM and corresponding Fourier transformation (inset) of fully discharged p Bi NS in Figure 2h disclose d spacing of 1.48, 2.12, 2.48, 2.39 and 2.07 Å that correspond, respectively, to trigonal Mg_3Bi_2 (005) (103) (003) and remaining monoclinic MgBi (31 2) (022) facets. The incomplete magnesiation of MgBi after full discharge is supposed to be related to activation of the Mg/Bi. It can be deduced from Figure 2f that the general morphology of p Bi NS recovers to its mesoporous feature after full charge. The measured lattice spacing of the de magnesiation electrode in Figure 2i is 3.28 Å, corresponding to Bi (012) plane. These results from ex situ HRTEM substantiate reversibility of p Bi NS in Mg^{2+} storage, and the existence of a MgBi intermediate phase. This structural design of p Bi NS will boost electrochemical performance and is suitable for the study of charge storage mechanism.

The p Bi NS sample was directly used as a flexible and binder free anode for MIBs in all phenyl complex (APC) electrolytes. Cyclic voltammetry (CV) was conducted at a scan rate of 0.1 $mV s^{-1}$ between 0.6 0.05 V to investigate electrode reactions. Figure 3a shows the CV curves of p Bi NS and bulk Bi. In comparison p Bi NS anode shows a couple of symmetric and narrower cathodic/anodic peaks, indicating a highly reversible electrochemical process. Bi bulk sample exhibits greater polarization, with a lower cathodic peak voltage. Figure 3b illustrates the galvanostatic discharge/charge profiles of p Bi NS and Bi bulk at a current density of 0.2 $A g^{-1}$ for the first cycle. Ultra flat voltage plateaus for both samples at about 0.2 V were observed. These correspond to the stable phase change process of Mg/Bi alloying reaction. The discharge voltage plateaus for the subsequent cycles are maintained at about 0.25 V (Figure S9). As is shown in the inset of Figure 3b, a highly significant alloying nucleation over potential was observed for the Bi bulk electrode (0.14 V, vs. 0.01 V for p Bi NS). This is because of poor kinetics. The nucleation over potential was defined as the difference between the bottom of voltage tip and the stable section of voltage plateau.[24] More energy is required for Bi bulk to overcome the alloying barrier and form an alloy compound

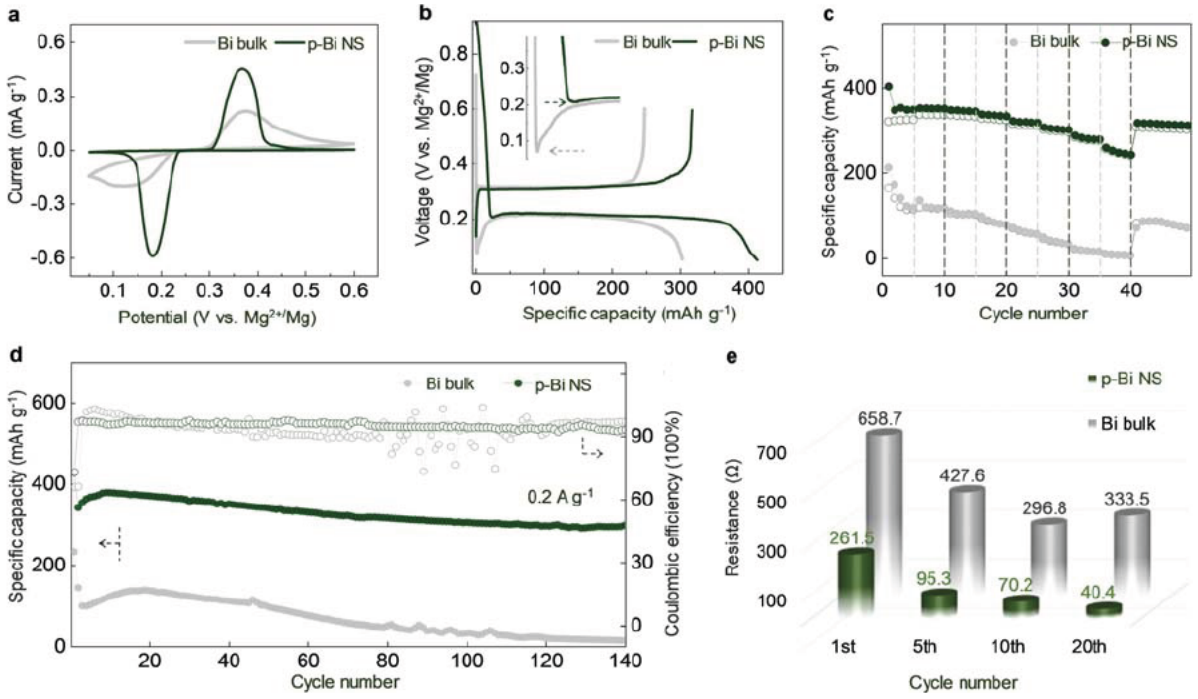

Figure 3. Electrochemical performances of Bi bulk and p Bi NS. a) CV curves at a scan rate of 0.1 mV s ^{1} between 0.6 0.05 V. b) Galvanostatic discharge/charge profiles of the first cycle. Inset is the enlarged curves with alloying nucleation overpotential. c) Rate performance at the current density of 0.08, 0.1, 0.2, 0.3, 0.5, 0.8, 1.2, 2.0 and 0.2 A g ^{1}. d) Cycling performance at 0.2 A g ^{1}. e) EIS fitted results for resistance after different cycles.

phase with Mg. The structural design of p Bi NS highlights the advantage of a low activation barrier. The rate performance in Figure 3c confirms the fast kinetics of p Bi NS which is capable of delivering specific capacities of 351 mAh g^{-1} at 0.1 A g^{-1} and 247 mAh g^{-1} at high current densities of 2.0 A g^{-1}. The corresponding discharge/charge rate profiles are shown as Figure S10. p Bi NS exhibited a lower polar ization voltage at a greater rate. This finding suggests faster alloy reaction kinetics and lower electrode resistance of p Bi NS.

To further investigate Mg^{2+} migration kinetics in bismuth based electrodes, CVs were measured at various scan rates (Figure S11) to evaluate the diffusion coefficients (D) of p Bi NS and Bi bulk. Figure S12 shows a linear relationship between I_p and $v^{1/2}$ A. According to the Randles Sevcik equation (equation (S1)), the square root of diffusion coefficient of Mg ions is proportional to the slop of $I_p/v^{1/2}$ A. Based on linear fitting results of $I_p/v^{1/2}$ A values, the average diffusion coefficient for p Bi NS is 2.61×10^{-15} $cm^2 s^{-1}$. This is one order of magnitude greater than that for Bi bulk of 2.87×10^{-16} $cm^2 s^{-1}$. The fast Mg ions migration kinetics of p Bi NS are attributed to the mesoporous nanocrystalline feature. The p Bi NS exhibits excellent cycling stability in Mg/Bi and is superior to those of Bi based materials in Li free electrolyte as previously reported (*see* Table S1). The cycling perform ances at a current density of 0.2 A g^{-1} are shown as Figure 3d. The p Bi NS exhibits high specific capacity of 297 mAh g^{-1} after 140 cycles. The initial Coulombic efficiencies of both samples are not high. This is due to the formation of solid electrolyte interphase layer, as is demonstrated in Figure S13. It is seen that both electrodes undergo a period of activation process for the initial cycles with increasing capacities. Compared with Bi bulk, p Bi NS electrode presents relatively shorter activating cycles, which contributes to the fast kinetics of p Bi NS with delicate structure design. The discharge capacity of p Bi NS reached 378 mAh g^{-1} following activa tion. Significantly, this is comparable to the theoretical capacity of 385 mAh g^{-1} calculated based on the three electron reaction [Eq. (3) & (4)]. The p Bi NS, with high reactivity and fast ion diffusion kinetics, is more suitable for investigation of the electrode reaction mechanism.

Electrochemical impedance spectroscopy (EIS) was ap plied to characterize the interfacial resistance between electrode and electrolyte. Figure S14 shows the Nyquist plots for both p Bi NS and Bi bulk after 5 cycles. These plots comprise a flattened semicircle from high frequency to medium frequency and an inclined line at the low frequency region. These two parts associate with a sum resistance (R) including internal (R_Ω) and charge transfer (R_{ct}) resistances, and the Warburg resistance. Notably, the R for p Bi NS of 95.3 Ω is significantly less than that for Bi bulk of 427.6 Ω. Materials grown directly on a conductive carbon matrix with a strong affinity are expected to exhibit high electronic conductivity.[25] EIS was also conducted after different cycles (Figure S15). Fitted results are presented as Figure 3e. With increased cycling, the R value of p Bi NS remains low and decreases continually after 20 cycles (40.4 Ω). The R of Bi bulk reduces gradually in the initial 10 cycles, but returns to a high value of 333.5 Ω after 20 cycles. This continuously decreasing R value during initial cycles is associated with the activation process that results in a growing capacity for both samples, as is demonstrated in Figure 3d. The increased resistance of Bi bulk after 20 cycles corresponds to the deteriorated cycling performance. This is generated by structural collapse of the Bi bulk because of the highly significant volume change during alloying/de alloying process as is shown in Figure S7. p Bi NS with porous structure is beneficial therefore to release internal stress and mitigate pulverization to give robust mechanical stability. Compared with conventional copper/nickel metal current collectors, this robust carbon matrix electrode is favored to increase chem ical resistance to corrosive magnesium electrolyte. We inves tigated the electrochemical performance of pure mesoporous bismuth nanosheets without carbon matrix, as is shown in Figure S16 18. The electrochemical performance of the sample without carbon matrix is inferior to the p Bi NS, but is significantly better than the Bi bulk. Importantly, the free standing p Bi NS design demonstrates a new concept in nanoengineering to achieve good ionic/electronic conductiv ity and concomitant high chemical resistance in corrosive Mg electrolyte. This makes it an excellent alternative anode to metallic Mg and a highly qualified model for the investigation of the Mg^{2+} charge storage mechanism.

Kinetic Analyses and Theoretical Modelling

Magnesium storage behaviour of Bi in APC electrolytes was studied. It is reported that APC electrolyte prepared from PhMgCl and $AlCl_3$ in tetrahydrofuran (THF) is a complicated chemical system.[26] As is demonstrated in Figure S19, it is believed that Mg ions in organometallic electrolytes are accompanied with Cl^- and THF molecules to form tetracoordinated or hexacoordinated oligomer in THF containing electrolyte.[26b,27] Based on theoretical and exper imental studies, an $MgCl^+$ intercalation mechanism was proposed by Yao et al.[28] and Mai et al.[29] Instead of Mg^{2+}, the intercalation of electro active species $MgCl^+$ into ex panded layer materials can lower the polarity and increase ion diffusion kinetics. In order to confirm the active species in the charge storage process of Mg/Bi, X ray photoelectron spectra (XPS) of p Bi NS at the original and fully discharged states were analysed, Figure S20. The atomic ratios of Mg to Cl at different stages are presented in Table S2. After alloying, the atomic ratio of Mg to Cl at the fully discharged state is 17.24, which is greater than that of $MgCl^+$ (equals to 1) species intercalation. In order to rule out influences from surface side reactions, argon ion sputtering was applied to study the possibility of $MgCl^+$ intercalation. As a result, the ratio of Mg to Cl increased to 20.17 after sputtering. This underscores that the active species for the alloying reaction is Mg^{2+} rather than $MgCl^+$. The intercalating Mg^{2+} ions are produced by breaking the Mg Cl bond.

The theoretical computations and ab initio molecular dynamics (AIMD) modelling were conducted to evaluate the Mg^{2+} intercalation kinetics at the atomic level. To estimate the energy barrier of Mg^{2+} migration in Bi matrix, we computed diffusion pathways along [110] (path 1) and [100]

(path 2). Figure 4a is the top and side view of the Mg migration pathway. As is shown in Figure 4b, the energy barriers for Mg^{2+} migration along path 1 and path 2 are 1.61 eV and 1.84 eV, respectively. This suggests that Mg^{2+} is more favoured to diffuse along [110] in the Bi crystal matrix. Snapshots of the AIMD simulation at different states from 0 2000 fs are presented as Figure 4c. Mg diffuses onto the surface of the crystal matrix and rapidly interacts with Bi atoms, implying fast reaction dynamics. H is defined as the statistical difference in height between the Mg atomic layer closest to Bi and the top layer of Bi. The H values at different states are shown as Figure S21. Over time the layer of Mg atoms approaches the top layer of Bi with decreasing H values. At 2000 fs the height of the Mg layer is almost the same as the top layer of Bi atoms, indicating the formation of Mg/Bi alloy on the surface because of Mg interaction. The ab initio simulation results demonstrate that Bi based material with fast Mg^{2+} ion diffusion kinetics is a practically promising alternative to Mg metal anode.

To determine the electrochemical reaction mechanism, theoretical computations based on DFT were carried out to predict the voltage profile, energy barrier for different reaction pathways and the density of states (DOS) of Mg Bi alloy. Figure 5a displays comparison between theoretical and experimental voltage profiles. The calculated voltage profile demonstrates two plateaus, corresponding to Bi MgBi and MgBi Mg_3Bi_2 at 0.25 V and 0.21 V, respectively. For the experimental results, the initial consistent plateau at 0.25 V is associated with Bi MgBi. The plateau declines smoothly near the end of the discharge, corresponding to the computed lower plateau of MgBi Mg_3Bi_2 at 0.21 V. The theoretical electrochemical profile agrees well with the experimental, this result supports the two step Bi MgBi Mg_3Bi_2 reaction mechanism. The climbing image nudged elastic band (CL NEB) method was used to compute the energy barrier between two different reaction pathways of Bi Mg_3Bi_2 and Bi MgBi Mg_3Bi_2. As is shown in Figure 5b, the phase change energy barriers forming MgBi and Mg_3Bi_2 from Bi + Mg are 0.245 and 0.468 eV, respectively. The total energy barrier for the pathway Bi MgBi Mg_3Bi_2 is less than that for Bi Mg_3Bi_2. This result indicates that the alloying process is more likely to form MgBi intermediate phase, and then convert it to Mg_3Bi_2. This benefits the magnesiation kinetics.

To estimate the electronic conductivity of Bi alloy anode, the bandstructure and total/partial density of states (TDOS/PDOS) were computed. From the band structures of Mg_3Bi_2 and MgBi in Figure S22 it is evident that MgBi exhibits metallic behaviour, whilst Mg_3Bi_2 exhibits semi metallic properties. The computed TDOS of Mg_3Bi_2 and MgBi and the PDOS projected on Mg and Bi atoms are shown as Figure 5c and Figure S23. When compared with Mg_3Bi_2, MgBi is more metallic with increased DOS at the Fermi level. As is demonstrated by the PDOS the main contribution to electronic states of MgBi at the Fermi level is from Bi 6p. It is concluded therefore the formation of MgBi intermediate enhances the electronic conductivity of the electrode in both charge and discharge. As is summarized in Figure 5d, Bi anode undergoes a reversible two step alloying reaction process of Bi↔MgBi↔Mg_3Bi_2 during discharge/charge. The formation of MgBi intermediate accelerates the electrochemical kinetics of Mg/Bi system and boosts the electronic conductivity of the electrode.

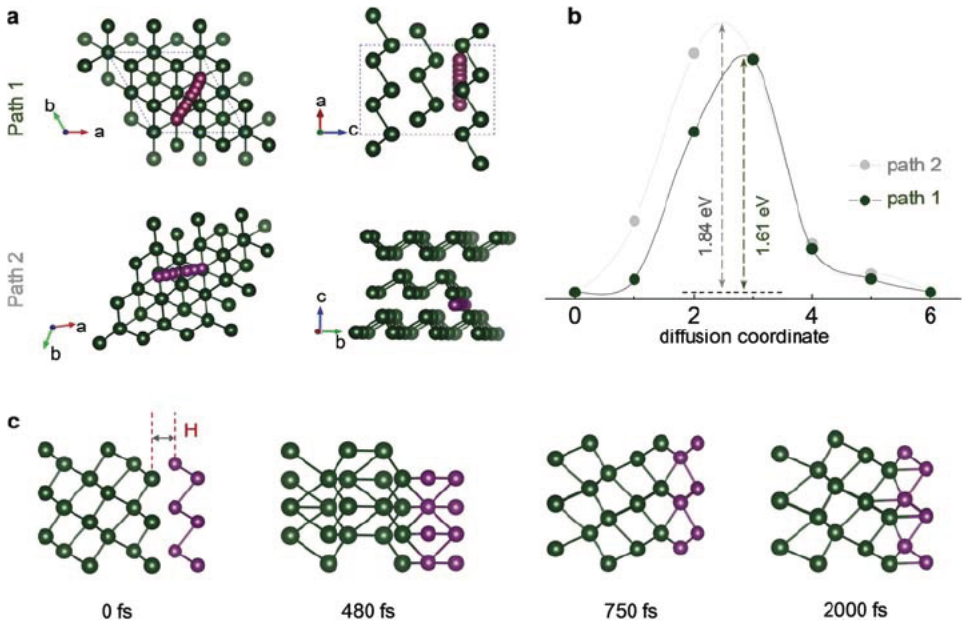

Figure 4. Ab initio molecular dynamics simulation and kinetics of electro active species of Mg. a) Mg migration pathway along Bi [110] (path 1) and [100] (path 2), top view (left), side view (right). b) The corresponding energy barrier profiles for two different diffusion pathways. c) AIMD simulation, the configuration of Mg Bi along [110] direction at 0, 480, 750, and 2000 fs. The green and red balls represent, respectively, Bi and Mg atoms. H is an average value, and is the difference in height between the Mg atomic layer closest to Bi and the top layer of Bi.

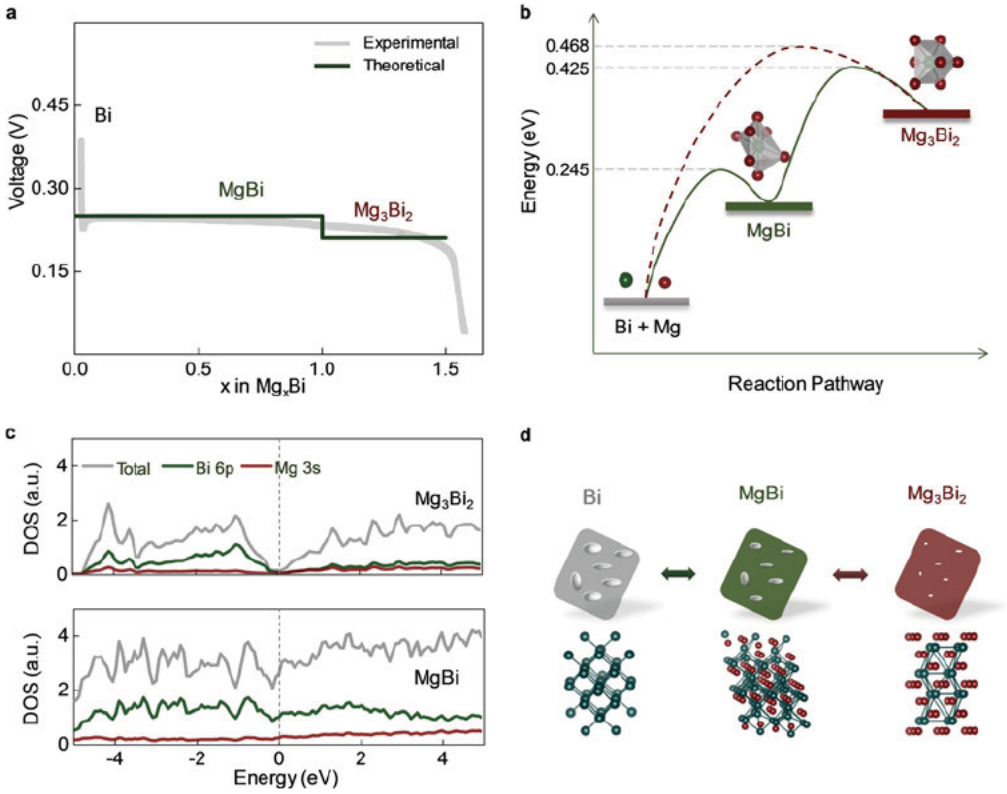

Figure 5. Computational modelling of charge storage mechanism. a) Computed voltage profile in comparison with the experimental discharge curve of p Bi NS during the 3rd cycle. b) Illustration of computed energy barrier in different reaction pathways with or without an intermediate state. c) TDOS of Mg_3Bi_2 and MgBi and, corresponding PDOS of Mg 3s and Bi 6p. The Fermi level (vertical dashed line) is shifted to zero. d) Schematic of magnesiation and relevant crystal structures of Bi (hexagonal), MgBi (monoclinic) and Mg_3Bi_2 (trigonal).

Conclusion

In summary, we propose a new alloying reaction mechanism for Mg/Bi batteries via an elaborated electrode design of mesoporous Bi nanosheets. The p Bi NS with record electrochemical performance in lithium free electrolyte is ideal for the investigation of Mg charge storage mechanism. MgBi intermediate phase is firstly detected via spectroscopy technologies of synchrotron based operando X ray diffraction and near edge X ray absorption fine structure. The alloying/de alloying process can be depicted as a reversible two step reaction of $Bi \leftrightarrow MgBi \leftrightarrow Mg_3Bi_2$. The ab initio method underscores the energy barrier priority in forming MgBi intermediate, and confirms the high electronic conductivity of MgBi. The intermediate phase accelerates reaction kinetics and acts as a buffer to mitigate disruption of significant volume expansion (204%). The nanoengineering design of p Bi NS offers a practically new means for application in corrosive Mg based electrolyte, and concomitantly, to mitigate volume variation. This strategy should be promising for investigation of advanced MIBs for next generation energy storage.

Acknowledgements

This research was financially supported by the Australian Research Council Discovery Projects DP160104866, DE20010124 and FL170100154. The authors acknowledge support from the Powder Diffraction and X ray Absorption Spectroscopy beamlines at the Australian Synchrotron, ANSTO, Melbourne.

Conflict of interest

The authors declare no conflict of interest.

Keywords: mesoporous bismuth · Mg/Bi batteries · Mg^{2+} storage mechanism · operando synchrotron · theoretical computations

[1] a) H. D. Yoo, I. Shterenberg, Y. Gofer, G. Gershinsky, N. Pour, D. Aurbach, *Energy Environ. Sci.* **2013**, *6*, 2265 2279; b) M. Matsui, *J. Power Sources* **2011**, *196*, 7048 7055.

[2] S. B. Son, T. Gao, S. P. Harvey, K. X. Steirer, A. Stokes, A. Norman, C. Wang, A. Cresce, K. Xu, C. Ban, *Nat. Chem.* **2018**, *10*, 532 539.

[3] D. Aurbach, Z. Lu, A. Schechter, Y. Gofer, H. Gizbar, R. Turgeman, Y. Cohen, M. Moshkovich, E. Levi, *Nature* **2000**, *407*, 724 727.

[4] R. Mohtadi, M. Matsui, T. S. Arthur, S. J. Hwang, *Angew. Chem. Int. Ed.* **2012**, *51*, 9780 9783; *Angew. Chem.* **2012**, *124*, 9918 9921.
[5] K. A. See, K. W. Chapman, L. Zhu, K. M. Wiaderek, O. J. Borkiewicz, C. J. Barile, P. J. Chupas, A. A. Gewirth, *J. Am. Chem. Soc.* **2016**, *138*, 328 337.
[6] a) R. Attias, M. Salama, B. Hirsch, Y. Goffer, D. Aurbach, *Joule* **2019**, *3*, 27 52; b) J. Muldoon, C. B. Bucur, A. G. Oliver, T. Sugimoto, M. Matsui, H. S. Kim, G. D. Allred, J. Zajicek, Y. Kotani, *Energy Environ. Sci.* **2012**, *5*, 5941 5950.
[7] Y. Shao, M. Gu, X. Li, Z. Nie, P. Zuo, G. Li, T. Liu, J. Xiao, Y. Cheng, C. Wang, J. G. Zhang, J. Liu, *Nano Lett.* **2014**, *14*, 255 260.
[8] a) L. R. Parent, Y. Cheng, P. V. Sushko, Y. Shao, J. Liu, C. M. Wang, N. D. Browning, *Nano Lett.* **2015**, *15*, 1177 1182; b) H. Yaghoobnejad Asl, J. Fu, H. Kumar, S. S. Welborn, V. B. Shenoy, E. Detsi, *Chem. Mater.* **2018**, *30*, 1815 1824.
[9] T. S. Arthur, N. Singh, M. Matsui, *Electrochem. Commun.* **2012**, *16*, 103 106.
[10] L. Wang, S. S. Welborn, H. Kumar, M. Li, Z. Wang, V. B. Shenoy, E. Detsi, *Adv. Energy Mater.* **2019**, *9*, 1902086.
[11] M. Hattori, K. Yamamoto, M. Matsui, K. Nakanishi, T. Mandai, A. Choudhary, Y. Tateyama, K. Sodeyama, T. Uchiyama, Y. Orikasa, Y. Tamenori, T. Takeguchi, K. Kanamura, Y. Uchimoto, *J. Phys. Chem. C* **2018**, *122*, 25204 25210.
[12] Y. H. Tan, W. T. Yao, T. Zhang, T. Ma, L. L. Lu, F. Zhou, H. B. Yao, S. H. Yu, *ACS Nano* **2018**, *12*, 5856 5865.
[13] a) K. V. Kravchyk, L. Piveteau, R. Caputo, M. He, N. P. Stadie, M. I. Bodnarchuk, R. T. Lechner, M. V. Kovalenko, *ACS Nano* **2018**, *12*, 8297 8307; b) Z. Liu, J. Lee, G. Xiang, H. F. Glass, E. N. Keyzer, S. E. Dutton, C. P. Grey, *Chem. Commun.* **2017**, *53*, 743 746; c) F. Murgia, L. Stievano, L. Monconduit, R. Berthelot, *J. Mater. Chem. A* **2015**, *3*, 16478 16485.
[14] a) J. Wang, I. Raistrick, R. A. Huggins, *J. Electrochem. Soc.* **1986**, *133*, 457 460; b) C. M. Park, S. Yoon, S. I. Lee, H. J. Sohn, *J. Power Sources* **2009**, *186*, 206 210.
[15] a) C. Wang, L. Wang, F. Li, F. Cheng, J. Chen, *Adv. Mater.* **2017**, *29*, 1702212; b) C. H. Lim, B. Selvaraj, Y. F. Song, C. C. Wang, J. T. Jin, S. S. Huang, C. H. Chuang, H. S. Sheu, Y. F. Liao, N. L. Wu, *J. Mater. Chem. A* **2017**, *5*, 21536 21541; c) H. Gao, W. S. Ma, W. F. Yang, J. W. Wang, J. Z. Niu, F. K. Luo, Z. Q. Peng, Z. H. Zhang, *J. Power Sources* **2018**, *379*, 1 9.
[16] a) J. Q. Huang, X. Y. Lin, H. Tan, B. Zhang, *Adv. Energy Mater.* **2018**, *8*, 1703496; b) K. Lei, C. Wang, L. Liu, Y. Luo, C. Mu, F. Li, J. Chen, *Angew. Chem. Int. Ed.* **2018**, *57*, 4687 4691; *Angew. Chem.* **2018**, *130*, 4777 4781.
[17] W. Xianming, T. Nishina, I. Uchida, *J. Power Sources* **2002**, *104*, 90 96.
[18] T. Yoshinari, T. Mori, K. Otani, T. Munesada, K. Yamamoto, T. Uchiyama, K. Fukuda, Y. Koyama, R. Hagiwara, Y. Orikasa, Y. Uchimoto, *Chem. Mater.* **2019**, *31*, 7160 7166.
[19] a) Z. Gong, Y. Yang, *J. Energy Chem.* **2018**, *27*, 1566 1583; b) F. Lin, Y. Liu, X. Yu, L. Cheng, A. Singer, O. G. Shpyrko, H. L. Xin, N. Tamura, C. Tian, T. C. Weng, X. Q. Yang, Y. S. Meng, D. Nordlund, W. Yang, M. M. Doeff, *Chem. Rev.* **2017**, *117*, 13123 13186; c) S. M. Bak, Z. Shadike, R. Lin, X. Yu, X. Q. Yang, *NPG Asia Mater.* **2018**, *10*, 563 580.
[20] a) L. Wang, C. Wang, F. Li, F. Cheng, J. Chen, *Chem. Commun.* **2018**, *54*, 38 41; b) J. S. Lannin, J. M. Calleja, M. Cardona, *Phys. Rev. B* **1975**, *12*, 585 593; c) E. Haro Poniatowski, M. Jouanne, J. F. Morhange, M. Kanehisa, R. Serna, C. N. Afonso, *Phys. Rev. B* **1999**, *60*, 10080 10085; d) L. Q. Li, C. Tang, B. Q. Xia, H. Y. Jin, Y. Zheng, S. Z. Qiao, *ACS Catal.* **2019**, *9*, 2902 2908.
[21] a) M. Lao, Y. Zhang, W. Luo, Q. Yan, W. Sun, S. X. Dou, *Adv. Mater.* **2017**, *29*, 1700622; b) J. Z. Niu, Z. H. Zhang, D. Aurbach, *Adv. Energy Mater.* **2020**, *10*, 2000697.
[22] H. Yang, L. W. Chen, F. He, J. Zhang, Y. Feng, L. Zhao, B. Wang, L. He, Q. Zhang, Y. Yu, *Nano Lett.* **2020**, *20*, 758 767.
[23] F. X. Xie, L. Zhang, B. Chen, D. L. Chao, Q. F. Gu, B. Johannessen, M. Jaroniec, S. Z. Qiao, *Matter* **2019**, *1*, 1681 1693.
[24] K. Yan, Z. D. Lu, H. W. Lee, F. Xiong, P. C. Hsu, Y. Z. Li, J. Zhao, S. Chu, Y. Cui, *Nat. Energy* **2016**, *1*, 1 8.
[25] a) D. Chao, W. Zhou, C. Ye, Q. Zhang, Y. Chen, L. Gu, K. Davey, S. Z. Qiao, *Angew. Chem. Int. Ed.* **2019**, *58*, 7823 7828; *Angew. Chem.* **2019**, *131*, 7905 7910; b) D. Chao, C. Ye, F. Xie, W. Zhou, Q. Zhang, Q. Gu, K. Davey, L. Gu, S. Z. Qiao, *Adv. Mater.* **2020**, *32*, 2001894.
[26] a) O. Mizrahi, N. Amir, E. Pollak, O. Chusid, V. Marks, H. Gottlieb, L. Larush, E. Zinigrad, D. Aurbach, *J. Electrochem. Soc.* **2008**, *155*, A103 A109; b) N. Pour, Y. Gofer, D. T. Major, D. Aurbach, *J. Am. Chem. Soc.* **2011**, *133*, 6270 6278.
[27] a) A. Benmayza, M. Ramanathan, T. S. Arthur, M. Matsui, F. Mizuno, J. Guo, P. A. Glans, J. Prakash, *J. Phys. Chem. C* **2013**, *117*, 26881 26888; b) L. F. Wan, D. Prendergast, *J. Am. Chem. Soc.* **2014**, *136*, 14456 14464; c) Y. Nakayama, Y. Kudo, H. Oki, K. Yamamoto, Y. Kitajima, K. Noda, *J. Electrochem. Soc.* **2008**, *155*, A754 A759; d) P. Canepa, S. Jayaraman, L. Cheng, N. N. Rajput, W. D. Richards, G. S. Gautam, L. A. Curtiss, K. A. Persson, G. Ceder, *Energy Environ. Sci.* **2015**, *8*, 3718 3730.
[28] H. D. Yoo, Y. Liang, H. Dong, J. Lin, H. Wang, Y. Liu, L. Ma, T. Wu, Y. Li, Q. Ru, Y. Jing, Q. An, W. Zhou, J. Guo, J. Lu, S. T. Pantelides, X. Qian, Y. Yao, *Nat. Commun.* **2017**, *8*, 339.
[29] L. Zhou, Q. Liu, Z. Zhang, K. Zhang, F. Xiong, S. Tan, Q. An, Y. M. Kang, Z. Zhou, L. Mai, *Adv. Mater.* **2018**, *30*, 1801984.

Manuscript received: July 11, 2020
Revised manuscript received: August 12, 2020
Accepted manuscript online: August 13, 2020
Version of record online: September 17, 2020

Angewandte Chemie
Eine Zeitschrift der Gesellschaft Deutscher Chemiker

Supporting Information

Revealing the Magnesium-Storage Mechanism in Mesoporous Bismuth via Spectroscopy and Ab-Initio Simulations

*Xin Xu[+], Dongliang Chao[+], Biao Chen, Pei Liang, Huan Li, Fangxi Xie, Kenneth Davey, and Shi-Zhang Qiao**

anie 202009528 sm miscellaneous information.pdf

Experimental Methods

Synthesis of mesoporous bismuth nanosheets. Carbon-cloth was treated with concentrated acid (HNO_3: H_2SO_4=1:3) overnight, and rinsed with deionized (DI) water and ethanol 3 x times. In synthesizing the bismuth oxyiodide (BiOI) nanosheets, 0.407 g bismuth nitrate pentahydrate (Sigma-Aldrich) and 0.418 g potassium iodide (Sigma-Aldrich) were dissolved in 35 mL ethylene glycol (Fluka), and then transferred to a 50 mL autoclave together with the acid-treated carbon-cloth (2 x 3, cm). The autoclave was held at 160 ℃ for 6 h. The obtained BiOI nanosheets on carbon-cloth (BiOI-CC) were washed with DI water and ethanol to remove any residual solvent. Porous Bi nanosheets (p-Bi NS) were obtained by reduction of BiOI with a solution method. Specifically, BiOI-CC was immersed in 20 mL of 0.25 M sodium borohydride ($NaBH_4$, Sigma-Aldrich) aqueous solution for 20 min and then washed with DI water and ethanol in turn. Porous Bi nanosheet are obtained due to the strong etching effect of $NaBH_4$. The control sample of porous bismuth nanosheets without carbon-cloth was prepared in this same way by commercial bismuth powder (100 mesh, Sigma-Aldrich).

Material characterization. The morphology of the sample was obtained on FEI Quanta 450 FEG scanning electron microscopy (SEM) and transmission electron microscopy (TEM, JEOL JEM-2100f). Crystal structures examined by *ex-situ* X-ray diffraction were collected on a Rigaku Mini Flex 600 X-Ray Diffractometer. N_2 adsorption-desorption isotherm (77 K) was measured by a Micromeritics ASAP 2460. The micro Raman spectra were collected using Labram HR Evolution (Horiba Scientific) in the range 20 - 2000 cm^{-1} and recorded by 532 nm laser beam with a 50X objective lens. X-ray photoelectron spectra (XPS) measurements were conducted on a PHI Quantera X-ray photoelectron spectrometer with a spatial resolution of 30 mm and Al Kα radiation. All samples prepared for the *ex-situ* testing were rinsed with tetrahydrofuran (THF) solution to remove soluble species on the surface, and sealed within Ar protection. The *ex-situ* NEXAFS spectra were characterized by soft X-ray spectroscopy (XAS) beamline in the Australian Synchrotron (ANSTO), Melbourne. The data energy were calibrated with standard Mg foil and processed with the Athena program.[1] Synchrotron operando X-ray diffraction (XRD) data were collected continuously in 30 s acquisitions by the powder diffraction beamline of ANSTO with a wavelength (λ) of 0.68684 Å. Home-made 2032 coin-cells were used for synchrotron operando XRD data collection. Both sides of the cell cases were punched with holes and sealed with Kapton films to allow X-ray transmission.

Electrochemical measurements. 0.25 M all phenyl complex (APC) in THF solution was prepared in argon-filled glove box following the method of Aurbach and co-authors.[2] Specifically, 0.2 g aluminium chloride powder ($AlCl_3$, anhydrous, Sigma-Aldrich) was added slowly into 4.5 mL THF (> 99.9 %, anhydrous, Sigma-Aldrich) and stirred overnight. 1.5 mL phenylmagnesium chloride solution (PhMgCl,

2 M in THF, Sigma-Aldrich) was added slowly into $AlCl_3$/THF solution and stirred overnight. The obtained APC solution was used as the electrolyte for the test of the battery. Electrochemical performance was evaluated in the 2032 type coin-cell. P-Bi NS was directly used as a binder-free working electrode. The mass loading was weighted ~ 2.15 mg cm^{-2}, based on the mass difference before and after Bi loading on the clean carbon-cloth. The control sample of Bi bulk and Bi nanosheets without carbon matrix were prepared by grinding active materials, carbon black (> 99 %, Alfa Aesar) and poly(vinylidene fluoride) (PVDF, Sigma-Alrich) in a mass ratio of 70:20:10, and then the slurry pasted on copper foil to form the electrodes. Mg foil and glass fiber were applied as anode and separator, respectively. Galvanostatic cycling tests between 0.6 - 0.05 V were performed on a Land CT2001A battery testing system at different rates. The cyclic voltammetry (CV) and electrochemical impedance spectroscopy (EIS) data were collected by Zahner IM6 electrochemical station.

Calculation of diffusion coefficient based on CV profiles. The diffusion coefficient of Mg ions was calculated by the Randles-Sevcik equation (at 25 ℃).

$$I_p = 2.686\times10^5 n^{3/2} A D^{1/2} v^{1/2} C \qquad (S1)$$

in which I_p is the current peak value (A) shown in CV curves, n is the number of electrons transferred (assuming six electrons transfer), A is the electrode area (cm^2), D is the diffusion coefficient (cm^2 s^{-1}), v is the scan rate (V s^{-1}), and C is the concentration (mol cm^{-3}) of Mg ions. The value of D can be calculated from the slope of I_p- $v^{1/2}$ lines. It should be noted that samples were tested from different electrode areas. Each p-Bi NS sample was cut into squares of ~ 0.35 cm^{-2} for use. The electrode area for control sample was 1.13 cm^{-2}. The value of D can be extracted from the slope of I_p- $v^{1/2}$ A.

Computational details. The package of Vienna *ab initio* simulation was adopted in all computations.[3] Electron-ion interactions were tested by projector augmented wave (PAW), whilst the electron exchange-related interactions were processed through the Perdew-Burke-Ernzerhof (PBE) exchange in the generalized gradient approximation (GGA) scheme.[4] Additionally, in our calculations, we used plane wave set with energy cutoff of 550 eV, which was adequate to achieve energy convergence. For optimization and static calculations, the Brillouin zone was sampled using a 8 x 8 x 8 Monkhorst-Pack special k-point grid centered on Γ.[5] Conjugate gradient was used to optimize all atom positions until all Hellmann-Feynman forces on each atom were < 0.01 eV / Å. The total energy difference between two consecutive steps is less than 10^{-7} eV / unit. In computing the density of states, the denser grid was set to 15 x 15 x 15. When computing the energy band, the high symmetry points were set to G (0,0,0), K(0,0.5,0), M(0,0.5,0.5) and Z (0,0,0.5), respectively. The Fermi level was shifted to 0 eV. The valence states were $3s^2 3p^0$ for Mg and $6s^2 6p^3$ for Bi. The width of smearing was 0.1 eV.

Supplementary Results

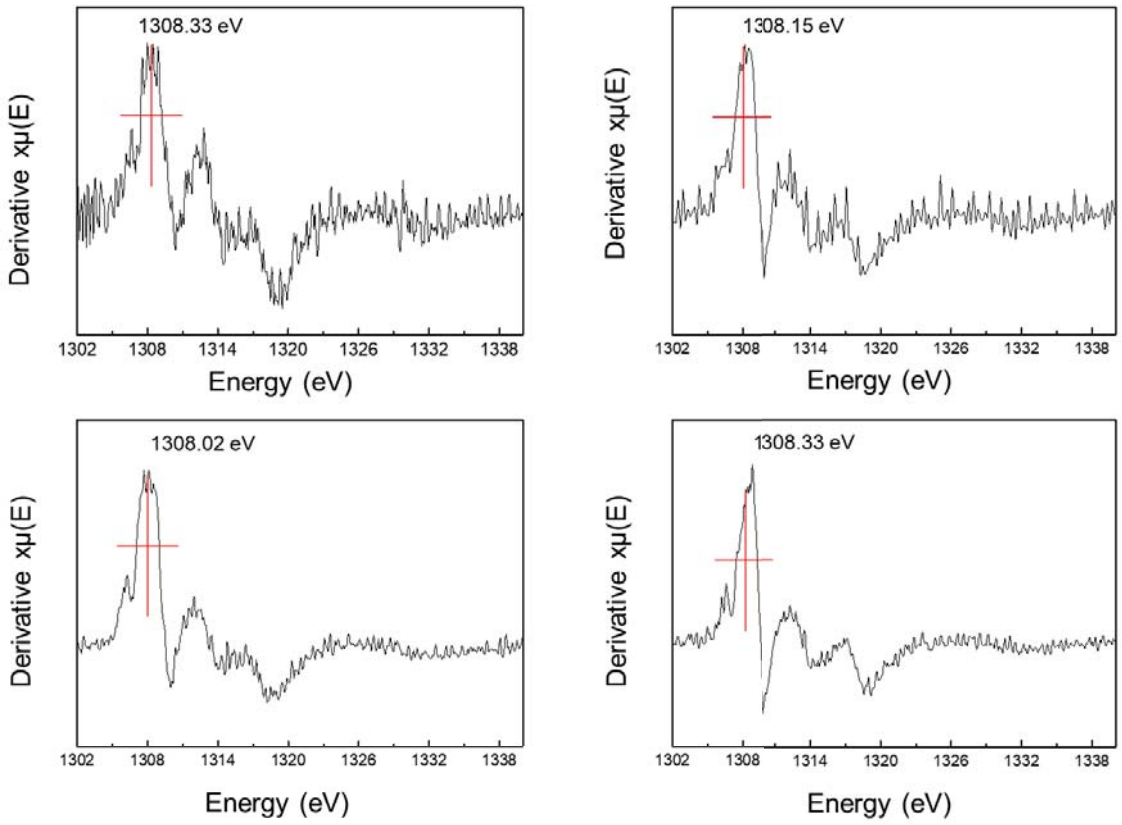

Figure S1. First-order derivative curves from NEXAFS for Mg K-edge of p-Bi NS, and corresponding main edge values extracted from half-peak energy with Athena.

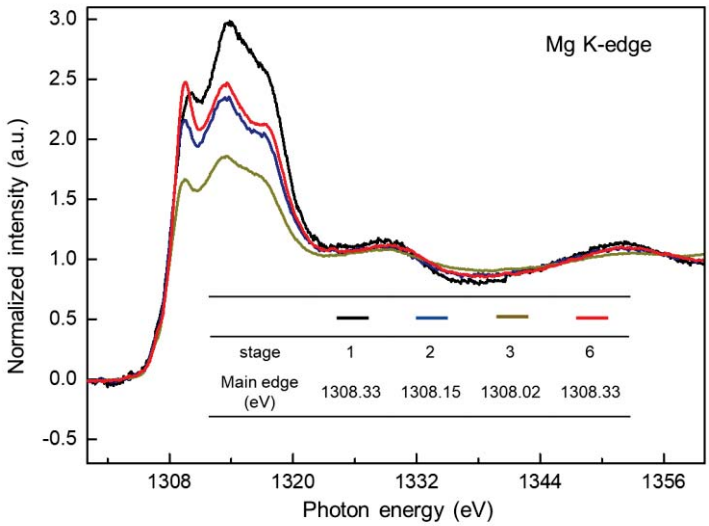

Figure S2. Normalized NEXAFS at Mg K-edge of p-Bi NS. Inset shows the extracted main edge values of p-Bi NS, corresponding to different electrochemical reaction stages for the initial cycle.

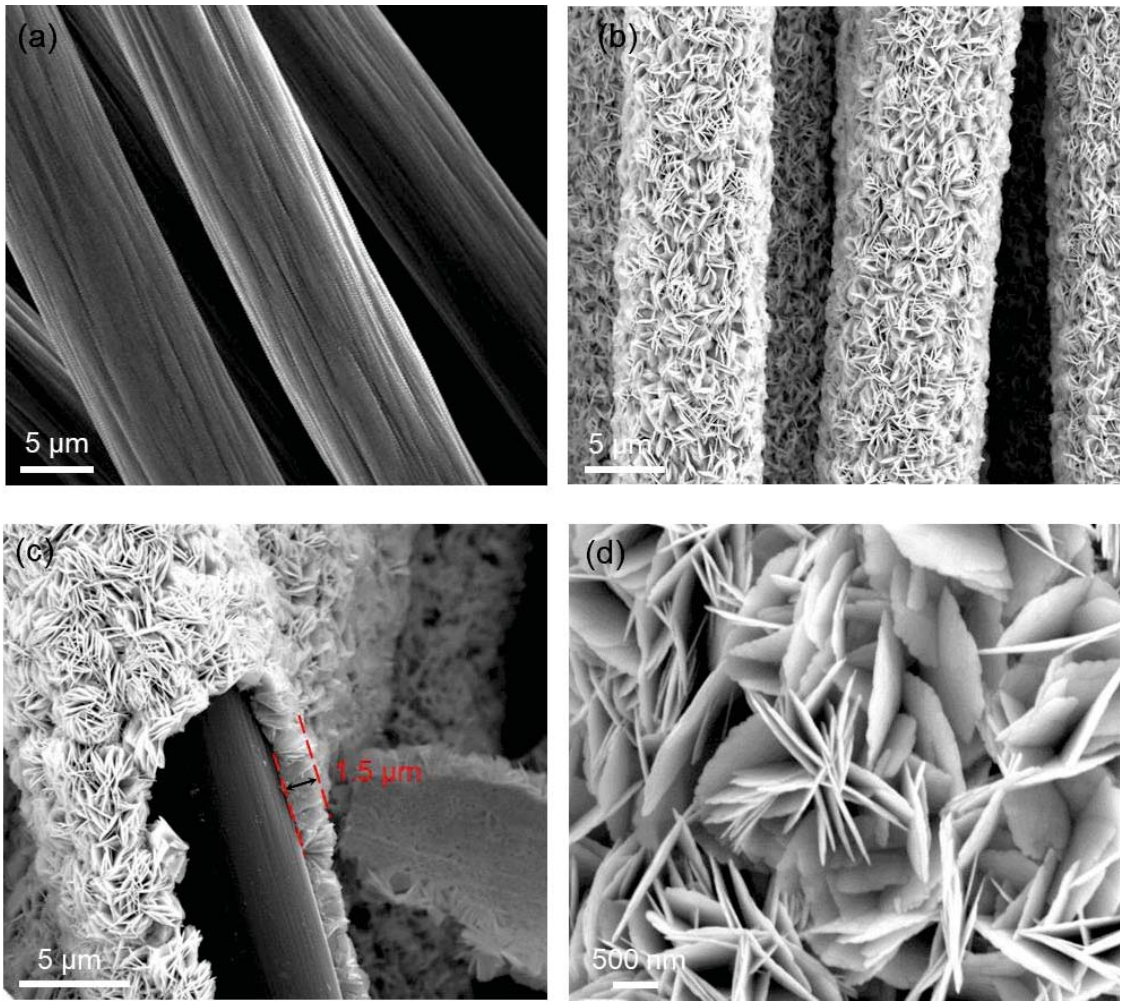

Figure S3. Morphology of BiOI-CC. SEM images of **a**) pure carbon-cloth, **b**) BiOI nanosheets directly grown on carbon-cloth, **c**) a piece of 'stripped off' BiOI. The lateral size of BiOI nanosheet is ~ 1.5 μm. **d**) Enlarged SEM image.

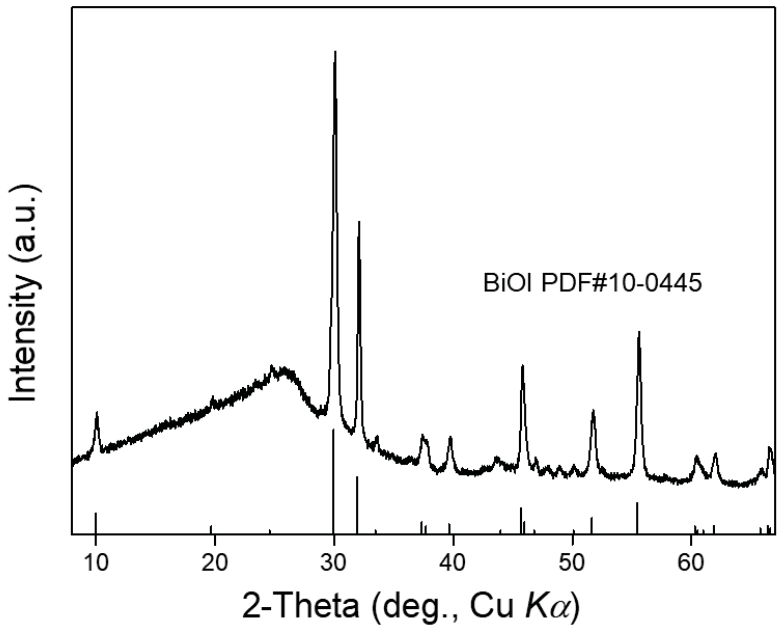

Figure S4. XRD spectrum for BiOI-CC corresponding to tetragonal BiOI.

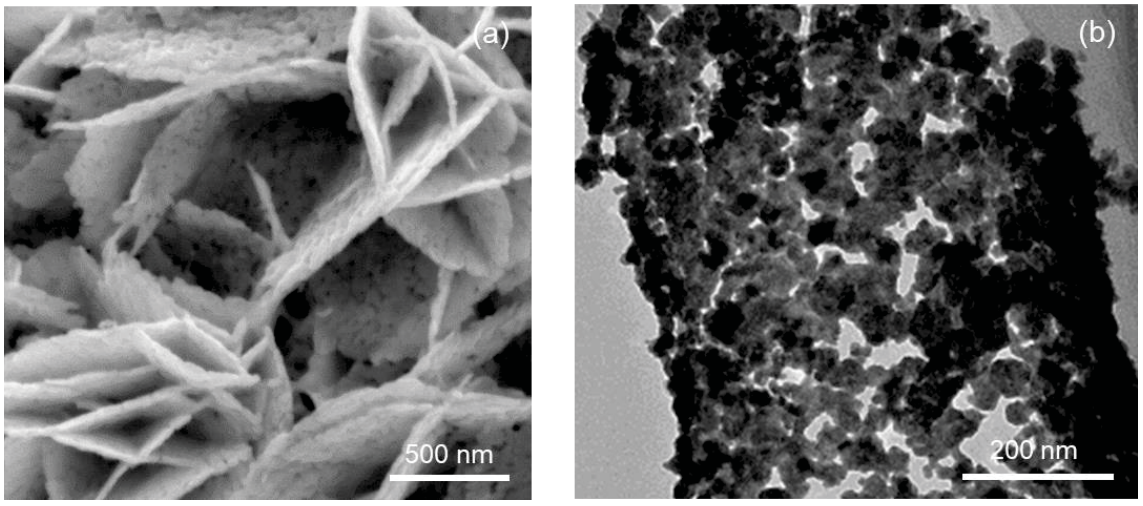

Figure S5. a) SEM and **b**) TEM images of mesoporous bismuth nanosheets.

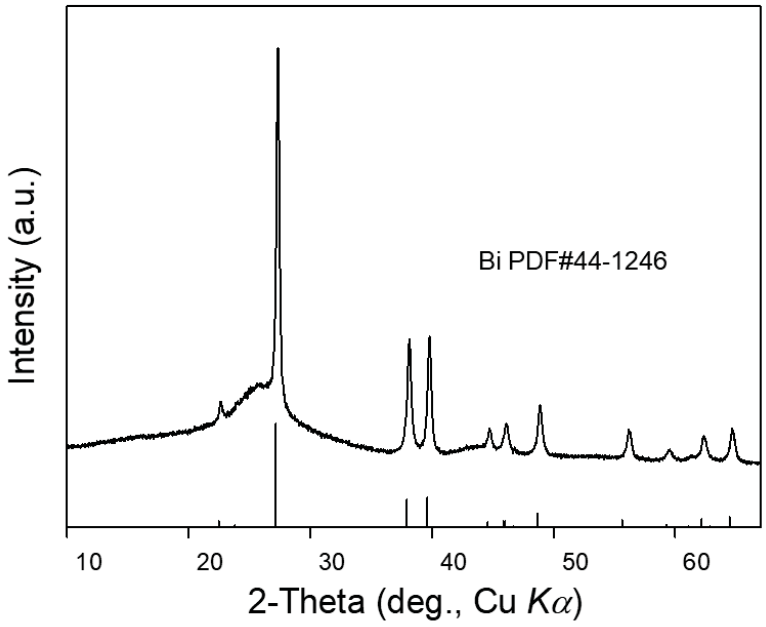

Figure S6. XRD pattern for p-Bi NS corresponding to hexagonal Bi.

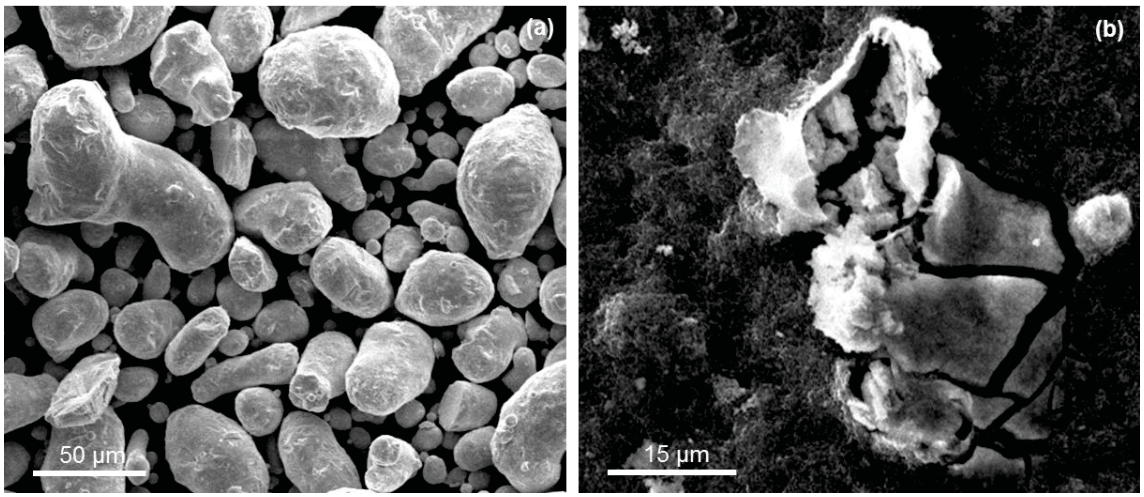

Figure S7. SEM image of **a**) commercial bismuth powder and **b**) Bi bulk electrode after 50 cycles.

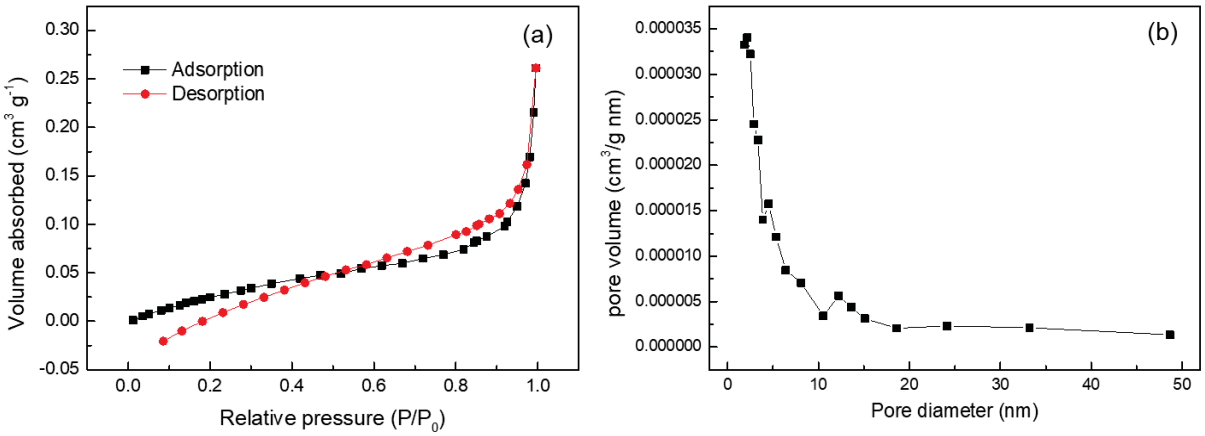

Figure S8. a) N_2 absorption−desorption isotherms for Bi bulk and **b**) corresponding distribution of pore size.

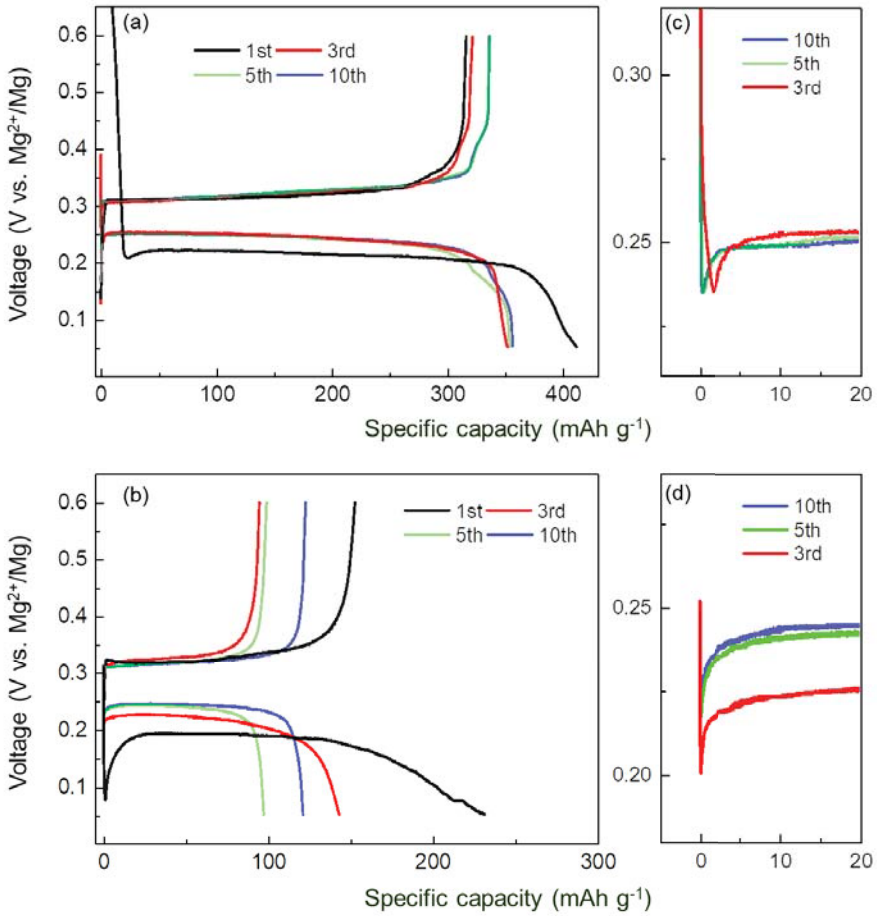

Figure S9. Galvanostatic discharge/charge profiles and corresponding partially-enlarged discharge profiles for **a**) **c**) p-Bi NS and **b**) **d**) Bi bulk after different cycles.

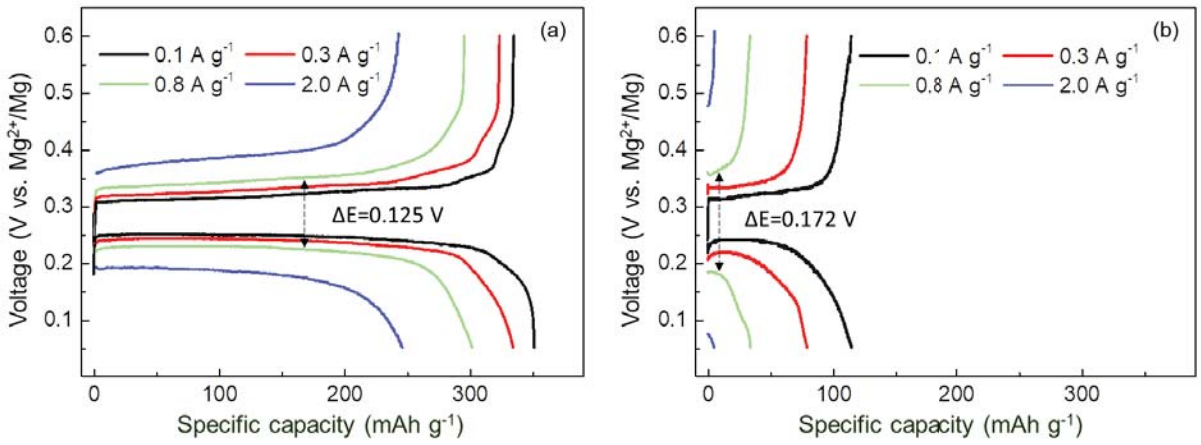

Figure S10. Galvanostatic discharge/charge profiles for **a**) p-Bi NS and **b**) Bi bulk at different rates. (ΔE is the polarization voltage-plateau gap)

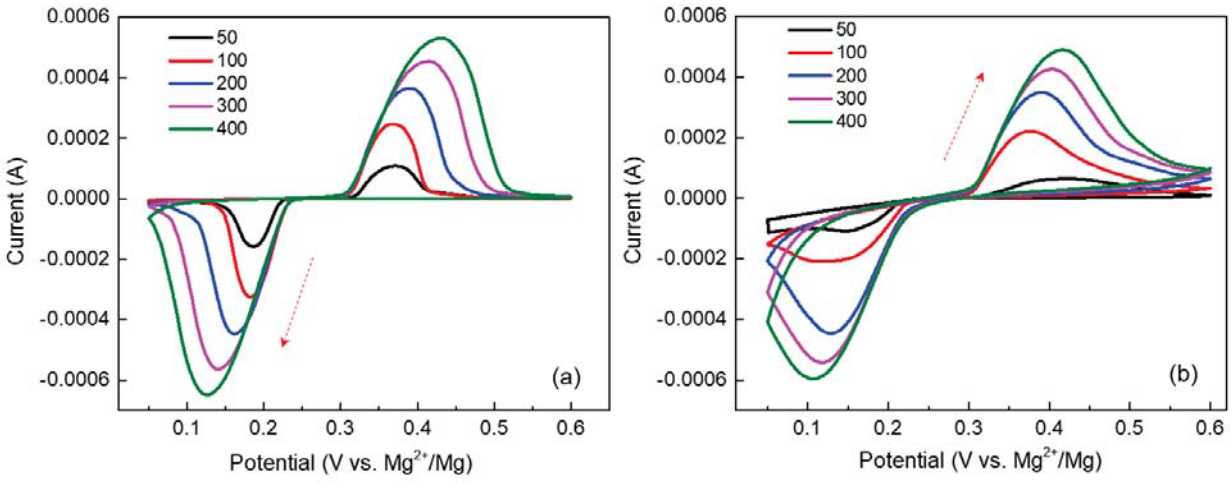

Figure S11. CV curves for **a**) p-Bi NS and **b**) Bi bulk at different scan rates of 50, 100, 200, 300 and 400 $\mu V\ s^{-1}$.

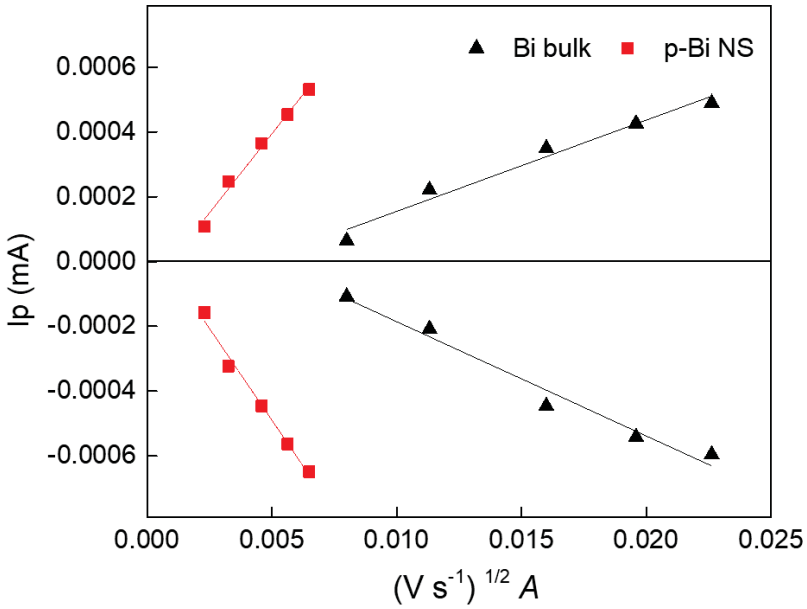

Figure S12. Fitted linear curve between I_p and $v^{1/2}A$ for measuring diffusion coefficient. (I_p is the current peak value as shown in CV curves, A is the electrode area (cm^2) and v is the scan rate ($V\ s^{-1}$)).

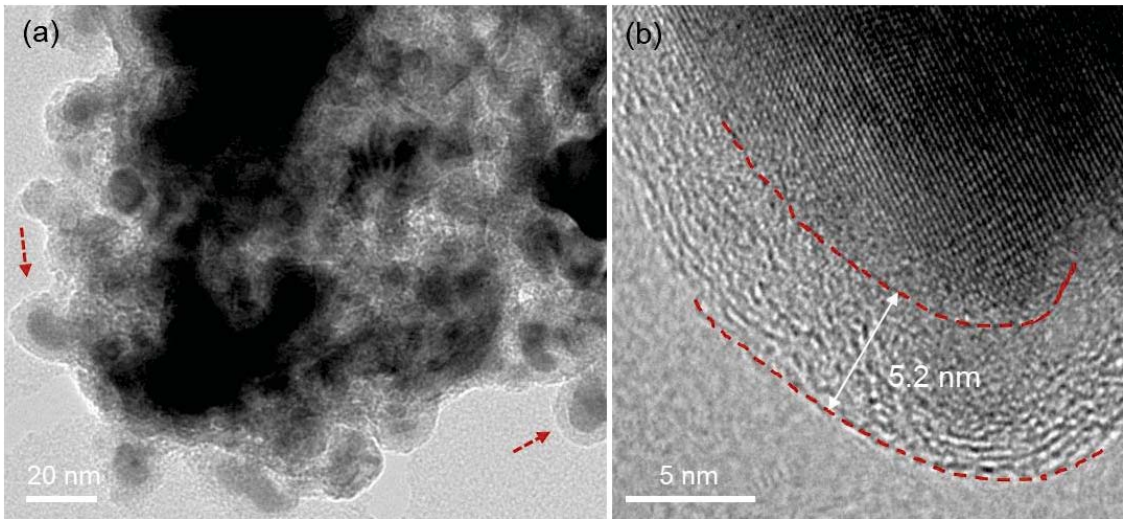

Figure S13. a) TEM images of p-Bi NS at full discharge and **b**) enlarged image. A solid-electrolyte interphase layer is formed during discharge. The thickness of the layer is about 5.2 nm.

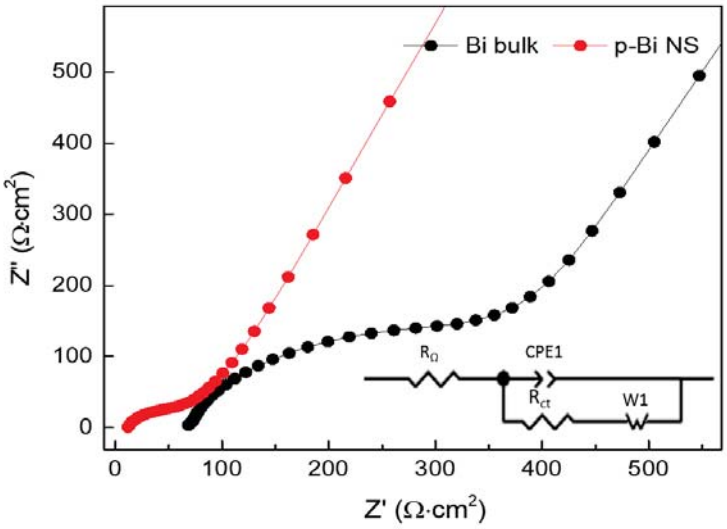

Figure S14. Nyquist plots for p-Bi NS and Bi bulk after 5 cycles. Inset is the equivalent circuit for the fitting of impedance. (R_{Ω} is the internal/ohmic resistance, R_{ct} is the interfacial resistance).

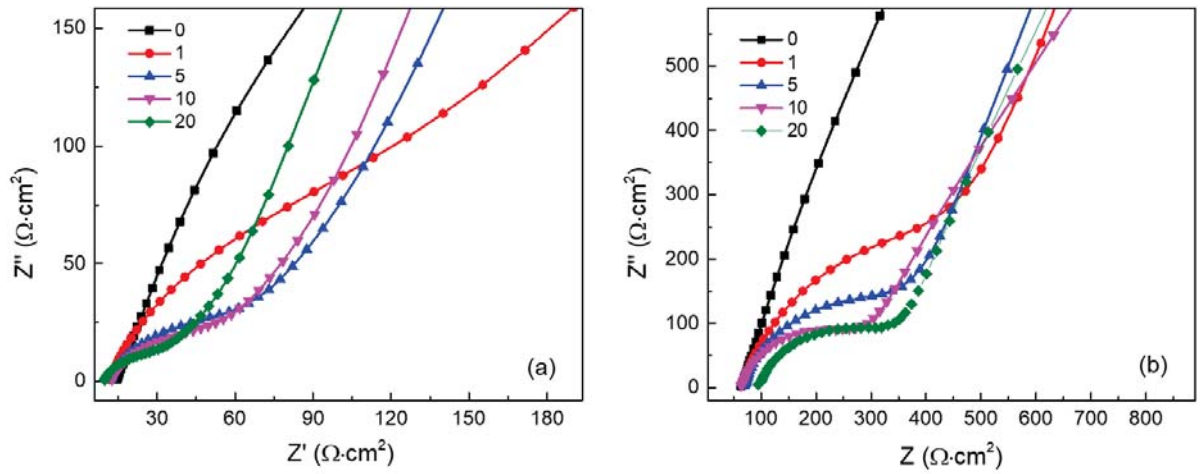

Figure S15. EIS spectra for **a**) p-Bi NS, **b**) Bi bulk original and after 1, 5, 10 and 20 charge/discharge cycles.

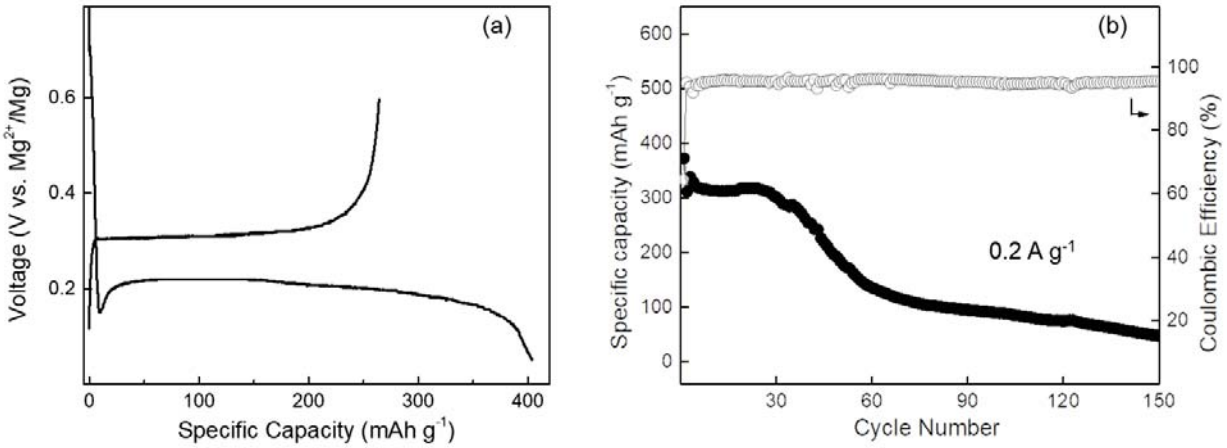

Figure S16. Electrochemical performance of porous bismuth nanosheet without carbon matrix. **a**) Galvanostatic discharge-charge profile. **b**) Cycling performance at 0.2 A g^{-1}.

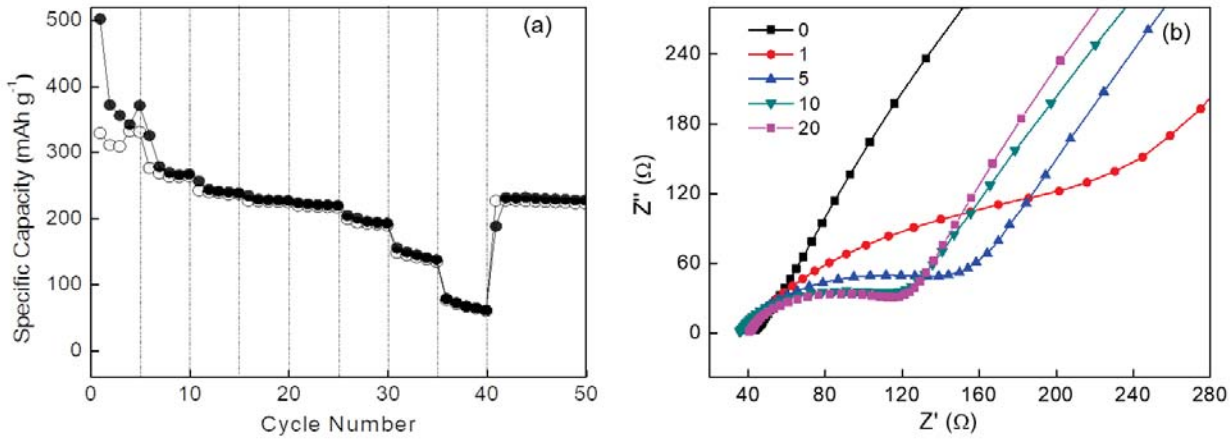

Figure S17. Electrochemical performance of porous bismuth nanosheet without carbon matrix. **a**) Rate performance at current density of 0.08, 0.1, 0.2, 0.3, 0.5, 0.8, 1.2, 2.0 and 0.2 A g^{-1}. **b**) Nyquist plots.

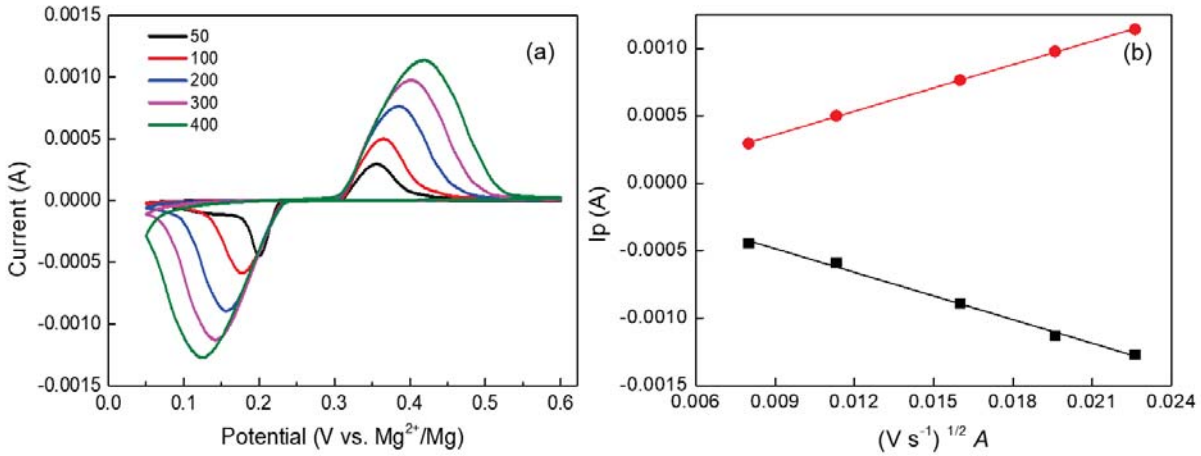

Figure S18. Electrochemical performance of porous bismuth nanosheet without carbon matrix. **a**) CV curves at different scan rates 50, 100, 200, 300 and 400 μV s^{-1} between 0.6 - 0.05 V. **b**) Fitted linear curve between Ip and $v^{1/2}A$.

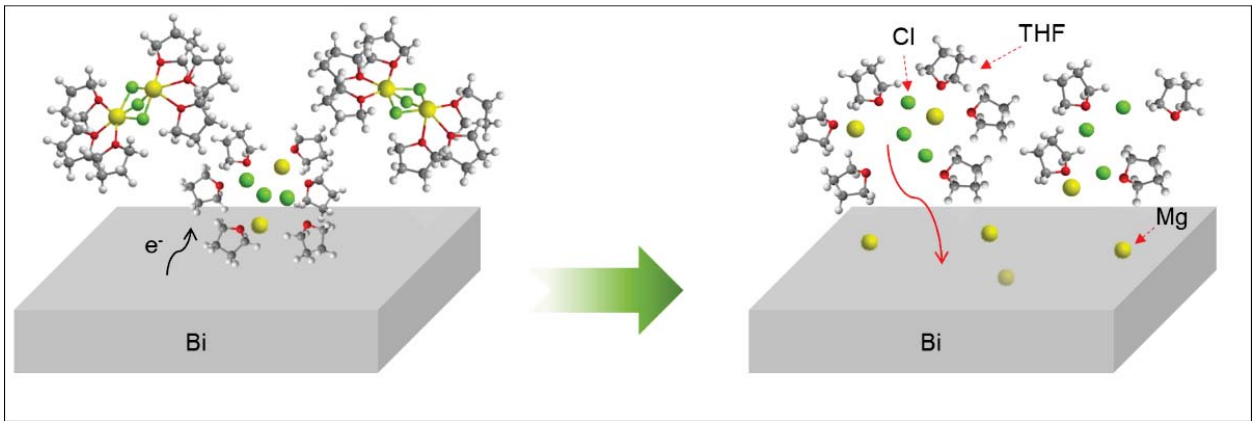

Figure S19. Schematic of the interfacial reaction between APC electrolyte and bismuth electrode.

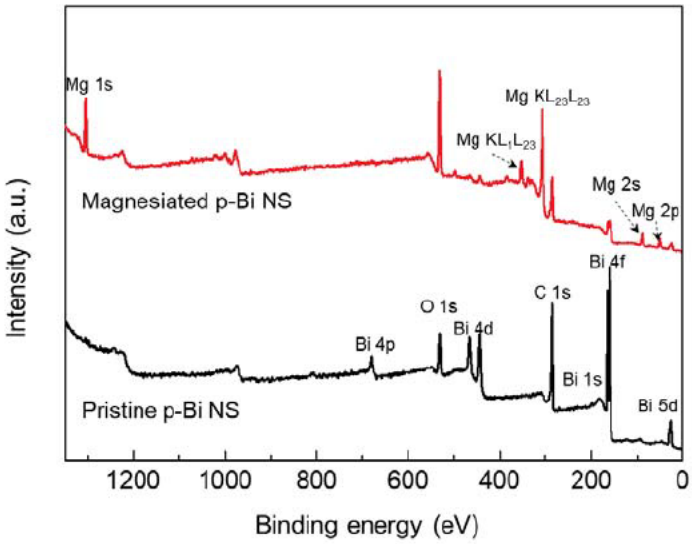

Figure S20. XPS spectra of original and fully magnesiated (stage 3) p-Bi NS.

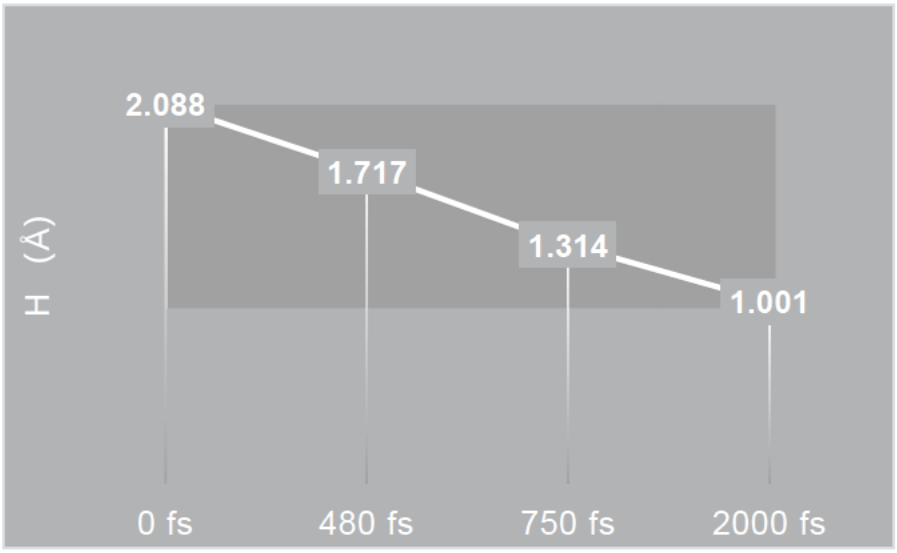

Figure S21. AIMD simulated values at the configuration of Mg-Bi along [110] direction at 0, 480, 750, and 2000 fs. (H is an average value, the statistical difference in height between the Mg atomic layer closest to Bi and the top layer of Bi.)

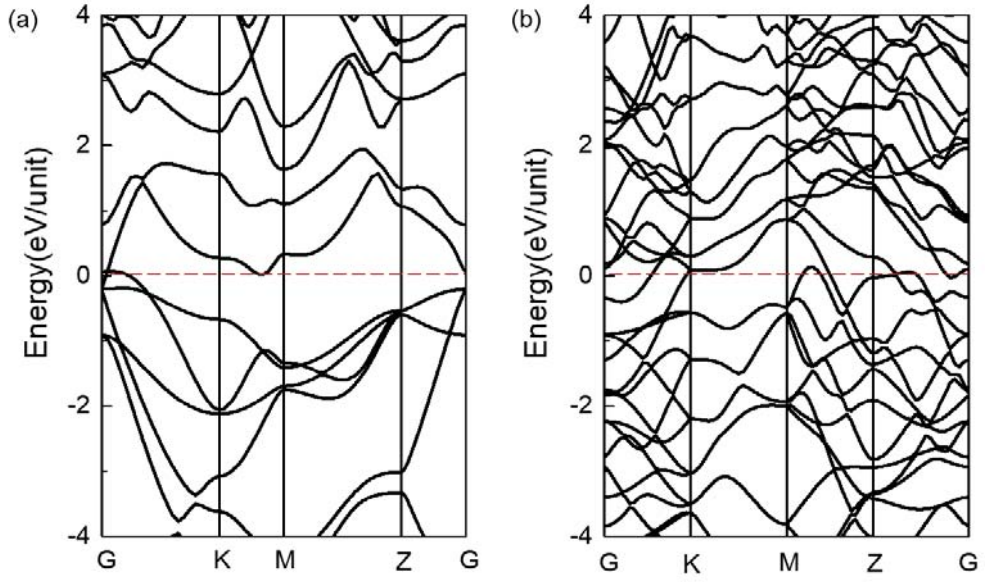

Figure S22. Band structures near the Fermi level for **a**) Mg_3Bi_2, **b**) MgBi. The Fermi level (horizontal dashed line) is shifted to zero.

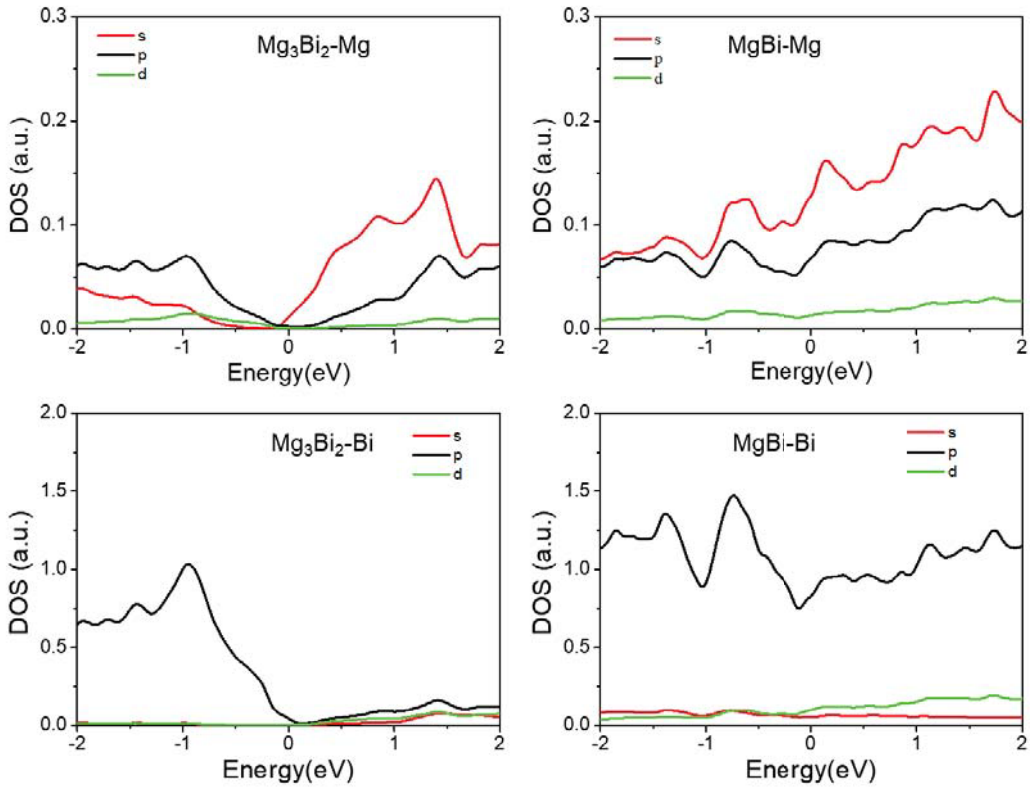

Figure S23. Comparison of the partial density of states for various Mg and Bi in Mg_3Bi_2 and MgBi.

Table S1. Summary comparison of performance of Mg/Bi systems in Li-free electrolytes.

Sample	*Rate (mA g^{-1})*	*Cycles*	*Capacity (mAh g^{-1})*	*Electrolyte (in THF)*	*Ref.*
p-Bi NS	200	140	297	$PhMgCl/AlCl_3$	This work
Bi	385	100	222	$Mg(AlCl_2EtBu)_2$	[6]
Micrometric Bi	770	50	300	$Mg(AlCl_2EtBu)_2$	[7]
Bi nanowires	193	100	207	$Mg(AlCl_2EtBu)_2$	[8]
Bi	19	50	285	$Mg(EtCl_2)$	[9]
Bi	300	100	260	$Mg(AlCl_2EtBu)_2$	[10]

Table S2. Atomic ratios of Mg to Cl extracted from the XPS.

Sample	Electrochemical reaction stage					
	1	2	3	4	5	3 - After sputtering
p-Bi NS	5.58	5.50	17.24	5.58	5.2	20.17

Supplementary References

[1] B. Ravel, M. Newville, *J. Synchrotron Radiat.* **2005**, *12*, 537-541.

[2] O. Mizrahi, N. Amir, E. Pollak, O. Chusid, V. Marks, H. Gottlieb, L. Larush, E. Zinigrad, D. Aurbach, *J. Electrochem. Soc.* **2008**, *155*, A103-A109.

[3] G. Kresse, J. Furthmuller, *Phys. Rev. B Condens. Matter* **1996**, *54*, 11169-11186.

[4] a) J. P. Perdew, K. Burke, M. Ernzerhof, *Phys. Rev. Lett.* **1996**, *77*, 3865-3868; b) J. P. Perdew, M. Ernzerhof, K. Burke, *J. Chem. Phys.* **1996**, *105*, 9982-9985.

[5] H. J. Monkhorst, J. D. Pack, *Phys. Rev. B* **1976**, *13*, 5188-5192.

[6] T. S. Arthur, N. Singh, M. Matsui, *Electrochem. Commun.* **2012**, *16*, 103-106.

[7] F. Murgia, L. Stievano, L. Monconduit, R. Berthelot, *J. Mater. Chem. A* **2015**, *3*, 16478-16485.

[8] Z. Liu, J. Lee, G. Xiang, H. F. Glass, E. N. Keyzer, S. E. Dutton, C. P. Grey, *Chem. Commun.* **2017**, *53*, 743-746.

[9] T. R. Penki, G. Valurouthu, S. Shivakumara, V. A. Sethuraman, N. Munichandraiah, *New J. Chem.* **2018**, *42*, 5996-6004.

[10] W. Wang, L. Liu, P. F. Wang, T. T. Zuo, Y. X. Yin, N. Wu, J. M. Zhou, Y. Wei, Y. G. Guo, *Chem. Commun.* **2018**, *54*, 1714-1717.

Chapter 4: Synchrotron X-ray Spectroscopic Investigations of In-Situ Formed Alloy Anodes for Magnesium Batteries

4.1 Introduction and significance

Magnesium batteries present high volumetric energy density and dendrite-free deposition of Mg, drawing wide attention in energy storage devices. However, its further development remains stagnated due to relevant interfacial issues between Mg anode and the electrolyte, and sluggish solid-state diffusion kinetics of Mg^{2+} ions. Herein, for the first time, we propose in-situ conversion chemistry to construct a nanostructured Bi anode from bismuth selenide driven by Li^{+}. Through the combination of operando synchrotron X-ray diffraction, ex-situ synchrotron X-ray absorption spectroscopy and comprehensive electrochemical tests, we demonstrate that the nanosize of the in-situ formed Bi crystals contribute to the fast Mg^{2+} diffusion kinetics and highly efficient Mg-Bi alloy/de-alloy. The resultant Bi anodes exhibit superior long-term cycling stability with over 600 cycles under a high current density of 1.0 A g^{-1}. This work provides a new approach to construct alloy anode and paves the way for exploring novel electrode materials for magnesium batteries. The highlights of this work include:

- **In-situ constructing anode -** The nanostructured Bi alloy anode has been prepared through an in-situ electrochemical conversion from bismuth selenide. Based on a series of electrochemical tests and operando synchrotron X-ray diffraction and DFT calculations, the fast Mg^{2+} diffusion kinetics and high electrochemical activity of BS-Bi electrode are proved to be evoked by the in-situ conversion driven by Li^{+}.

- **Mg^{2+} storage mechanism -** We demonstrate a highly reversible Mg alloy/de-alloy reaction in in-situ formed nanosized Bi crystals through combining ex-situ synchrotron X-ray absorption spectroscopy and X-ray photoelectron spectroscopy.

- **Superior performance -** We demonstrate that in-situ constructed BS-Bi anode exhibits an excellent rate performance (335 mAh g^{-1} at 1 A g^{-1}) and long cycling stability over 600 cycles. This performance is amongst the best-reported bismuth-based alloy anode materials in RMBs.

4.2 Synchrotron X-ray Spectroscopic Investigations of In-Situ Formed Alloy Anodes for Magnesium Batteries

This Chapter is included as it appears as a journal paper published by **Xin Xu**, Chao Ye, Dongliang Chao, Biao Chen, Huan Li, Cheng Tang, Xiongwei Zhong, and Shi-Zhang Qiao. "Synchrotron X-ray Spectroscopic Investigations of In-Situ-Formed Alloy Anodes for Magnesium Batteries." ***Advanced Materials*** **2022**, 34(8): 2108688.

Statement of Authorship

Title of Paper	Synchrotron X-ray Spectroscopic Investigations of In-Situ-Formed Alloy Anodes for Magnesium Batteries
Publication Status	☑ Published ☐ Accepted for Publication ☐ Submitted for Publication ☐ Unpublished and Unsubmitted work written in manuscript style
Publication Details	Xin Xu, Chao Ye, Dongliang Chao, Biao Chen, Huan Li, Cheng Tang, Xiongwei Zhong, and Shi-Zhang Qiao. Advanced Materials 2022, 34(8): 2108688

Principal Author

Name of Principal Author (Candidate)	Xin Xu		
Contribution to the Paper	Conducted experiments, data curation, formal analysis, investigation, and writing–original draft.		
Overall percentage (%)	70		
Certification:	This paper reports on original research I conducted during the period of my Higher Degree by Research candidature and is not subject to any obligations or contractual agreements with a third party that would constrain its inclusion in this thesis. I am the primary author of this paper.		
Signature		Date	20 October 2022

Co-Author Contributions

By signing the Statement of Authorship, each author certifies that:

i. the candidate's stated contribution to the publication is accurate (as detailed above);

ii. permission is granted for the candidate in include the publication in the thesis; and

iii. the sum of all co-author contributions is equal to 100% less the candidate's stated contribution.

Name of Co-Author	Chao Ye		
Contribution to the Paper	Supervision, formal analysis, writing–review and editing		
Signature		Date	20 October 2022

Name of Co-Author	Dongliang Chao		
Contribution to the Paper	Supervision, writing–review and editing		
Signature		Date	20 October 2022

Name of Co-Author	Biao Chen		
Contribution to the Paper	Assisted with material characterizations		
Signature		Date	20 October 2022

Name of Co-Author	Huan Li		
Contribution to the Paper	Conducted theoretical computations		
Signature		Date	20 October 2022

Name of Co-Author	Cheng Tang		
Contribution to the Paper	Helped with material synthesis		
Signature		Date	20 October 2022

Name of Co-Author	Xiongwei Zhong		
Contribution to the Paper	Assisted with material characterizations		
Signature		Date	20 October 2022

Name of Co-Author	Shi-Zhang Qiao		
Contribution to the Paper	Supervision, resources, conceptualization and writing–review and editing		
Signature		Date	20 October 2022

Name of Co-Author			
Contribution to the Paper			
Signature		Date	

ADVANCED MATERIALS
www.advmat.de

Synchrotron X-ray Spectroscopic Investigations of In-Situ-Formed Alloy Anodes for Magnesium Batteries

*Xin Xu, Chao Ye, Dongliang Chao, Biao Chen, Huan Li, Cheng Tang, Xiongwei Zhong, and Shi-Zhang Qiao**

Magnesium batteries present high volumetric energy density and dendrite-free deposition of Mg, drawing wide attention in energy-storage devices. However, their further development remains stagnated due to relevant interfacial issues between the Mg anode and the electrolyte and sluggish solid-state diffusion kinetics of Mg^{2+} ions. Herein, an in situ conversion chemistry to construct a nanostructured Bi anode from bismuth selenide driven by Li^+ is proposed. Through the combination of operando synchrotron X-ray diffraction, ex situ synchrotron X-ray absorption spectroscopy, and comprehensive electrochemical tests, it is demonstrated that the nanosize of the in-situ-formed Bi crystals contributes to the fast Mg^{2+} diffusion kinetics and highly efficient Mg–Bi alloingy/de-alloying. The resultant Bi anodes exhibit superior long-term cycling stability with over 600 cycles under a high current density of 1.0 A g^{-1}. This work provides a new approach to construct alloy anode and paves the way for exploring novel electrode materials for magnesium batteries.

1. Introduction

Rechargeable magnesium batteries (RMBs) with advantages of abundant resources, high volumetric capacity (3833 mAh cm^{-3}/Mg vs 2046 mAh cm^{-3}/Li), and dendrite-free deposition of Mg are potentially taking an important role in practical energy-storage technologies.[1] However, the practical use of the RMBs is hindered by the severe interfacial issues of forming the ion-block layer on the surface of metallic Mg, which leads to limited choices of conventional electrolytes based on $Mg(TFSI)_2$, $Mg(PF_6)_2$, $Mg(BF_4)_2$, etc.[2–4] One promising way to address the interfacial issues is the application of Mg alloy anode instead of Mg metal anode. In this case, efforts have been made to explore alloy anodes including Bi, Sn, Sb, Pb, etc., that allow the application of conventional electrolytes and development of high-voltage cathode materials for RMBs.[5–13]

Among them, Bi is the most investigated alloy anode in RMBs.[14] Based on six-electron transfer, the volumetric capacity of metallic Bi reaches 3783 mAh cm^{-3}, which is comparable to that of the Mg metal. The prototype of reversible alloying/de-alloying of Mg in Bi was achieved in $Mg(N(SO_2CF_3)_2)_2$/acetonitrile electrolyte by Arthur et al.,[6] demonstrating the compatibility of Bi with the conventional electrolyte. Bi anodes with various morphologies and components such as Bi nanotubes,[7] colloidal Bi nanocrystals,[8] nanocluster Mg_3Bi_2 alloy,[9] and mesoporous Bi nanosheets[15] have been developed to reversibly store Mg^{2+}. However, these Bi anodes suffered from severe volume change and limited Mg^{2+} diffusion kinetics during alloying/de-alloying processes, and therefore exhibited poor cycling stability. Especially under high-rate conditions, the cycling life of these Bi-based electrodes is only 200 cycles, which is much shorter than the cycling requirement for practical battery application. Therefore, rational design and synthesis of Bi electrodes to further buffer its volume change and simultaneously promote Mg^{2+} diffusion kinetics are desperately needed to achieve high rate and long cycling performance.

In this work, we prepared the in-situ-formed Bi anode from layered bismuth selenide (Bi_2Se_3) driven by Li^+. The combination of operando synchrotron X-ray diffraction (XRD) and ex situ X-ray absorption spectroscopy (XAS) demonstrates that the resultant nanostructured Bi in selenium compound matrix significantly increases Mg^{2+} diffusion kinetics. This greatly improves the efficiency of the Mg–Bi alloying/de-alloying reaction and the cycling stability of RMBs under high current densities. As a result, such Bi anode achieves a high reversible capacity of 252 mAh g^{-1} over 600 cycles at the current density of 1.0 A g^{-1}, which represents a significant improvement compared to the state-of-the-art Bi anode. Our findings offer a practical approach to address the kinetic issues and guide the design of novel electrode materials in RMBs.

X. Xu, C. Ye, H. Li, C. Tang, S.-Z. Qiao
School of Chemical Engineering and Advanced Materials
The University of Adelaide
Adelaide, SA 5005, Australia
E-mail: s.qiao@adelaide.edu.au
D. Chao
Laboratory of Advanced Materials
Shanghai Key Laboratory of Molecular Catalysis and Innovative Materials
Fudan University
Shanghai 200433, P. R. China
B. Chen, X. Zhong
Shenzhen Geim Graphene Center
Tsinghua-Berkeley Shenzhen Institute & Tsinghua Shenzhen International Graduate School
Tsinghua University
Shenzhen 518055, P. R. China
The ORCID identification number(s) for the author(s) of this article can be found under https://doi.org/10.1002/adma.202108688.

DOI: 10.1002/adma.202108688

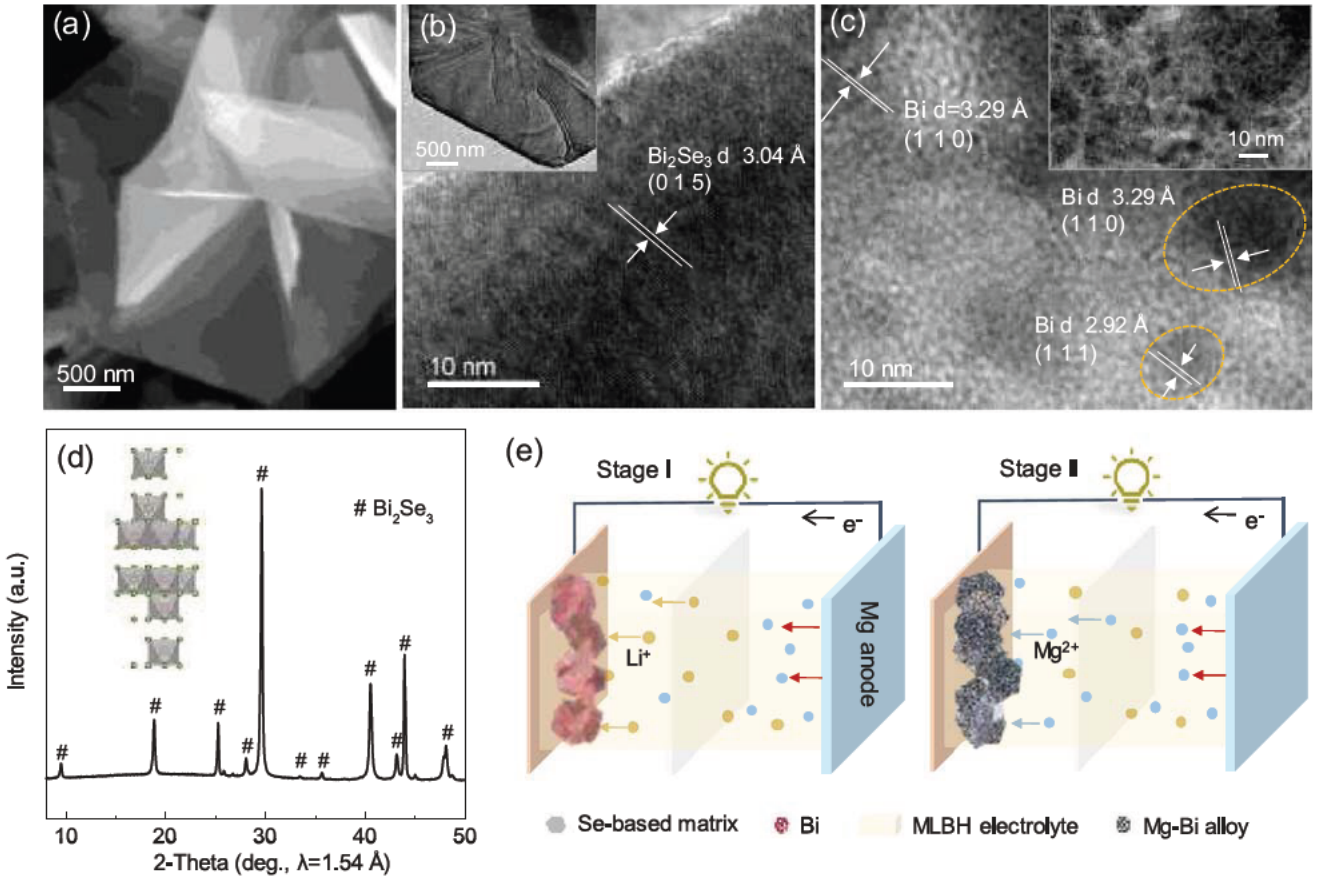

Figure 1. a) SEM image of Bi_2Se_3 nanosheets. b) HRTEM images of Bi_2Se_3. The inset shows the corresponding TEM image on a relatively large scale. c) HRTEM image of nanostructured m-Bi obtained from the initial discharge of Bi_2Se_3 at a cut-off voltage of 0.75 V. The inset shows the corresponding TEM image. d) XRD pattern of the Bi_2Se_3. The inset shows the scheme of the corresponding crystal structure in which the green and red spheres represent Se and Bi atoms, respectively. e) Schematic illustration of the two-stage working mechanism. I) The BS-Bi electrode with nanosized Bi crystals was constructed through an in situ conversion from Bi_2Se_3 precursor. II) The electrode further undergoes an alloying/de-alloying process with Mg.

2. Results and Discussion

Bi_2Se_3 nanosheets with hexagonal $R\bar{3}m$ space group crystal structure were synthesized via a facile solvothermal route and utilized as a precursor to construct the Bi anode (BS-Bi). The morphology and crystal structure of Bi_2Se_3 nanosheets were investigated by scanning electron microscopy (SEM) and transmission electron microscopy (TEM). As shown in **Figure 1**a and Figure S1a in the Supporting Information, the SEM images show that the as-prepared Bi_2Se_3 are randomly stacked hexagonal nanosheets. This is also confirmed with TEM image of the Bi_2Se_3 shown in the inset of Figure 1b. High-resolution transmission electron microscopy (HRTEM) image (Figure 1b) displays distinct lattice fringes with *d*-spacing of 3.04 Å, which can be assigned to the (0 1 5) plane of Bi_2Se_3. Figure S1b in the Supporting Information shows the selected-area electron diffraction (SAED) pattern of the Bi_2Se_3 whose zone axis is indexed along the [1 2 $\bar{1}$] direction. Three sets of diffraction spots with hexagonal configuration further confirm the hexagonal phase (PDF#33-0214) as demonstrated in the XRD pattern (Figure 1d). The HRTEM images of the BS-Bi at the discharge state of 0.75 V in Figure 1c display lattice fringes with the spacing of 3.29 and 2.92 Å which can be assigned to the (1 1 0) and (1 1 1) planes of monoclinic Bi (m-Bi), respectively. These results demonstrate an in situ conversion process of Bi_2Se_3 to Bi nanocrystals. This in situ conversion process can be ascribed to the layered structure of Bi_2Se_3 with a periodical arrangement of five atomic layers (Se–Bi–Se–Bi–Se) connected with weak van der Waals forces (Figure 1d). This layered structure provides sufficient space for extraneous ions, and thus benefits the intercalation and diffusion of metal ions for electrochemical energy storage.[16,17] Here, the two-stage working mechanism is proposed as shown in the scheme (Figure 1e). In stage I, the BS-Bi electrode with nanosized Bi crystals was constructed through an in situ conversion from the Bi_2Se_3 precursor. Then BS-Bi electrode further undergoes an alloying/de-alloying process with Mg in stage II.

The electrochemical performance of BS-Bi electrode was investigated in coin cells with Mg metal anode and 0.1 M $Mg(BH_4)_2$–1.5 M $LiBH_4$ in diglyme (MLBH) hybrid electrolyte. To demonstrate the inert nature of Bi_2Se_3 in this electrolyte, the pristine electrode soaked in the electrolyte for a week was tested by XRD. All diffraction peaks in Figure S2 in the Supporting Information are indexed to pure Bi_2Se_3, demonstrating the stability of Bi_2Se_3 in MLBH electrolyte. **Figure 2**a shows the discharge/charge profiles of the BS-Bi electrode in a voltage range

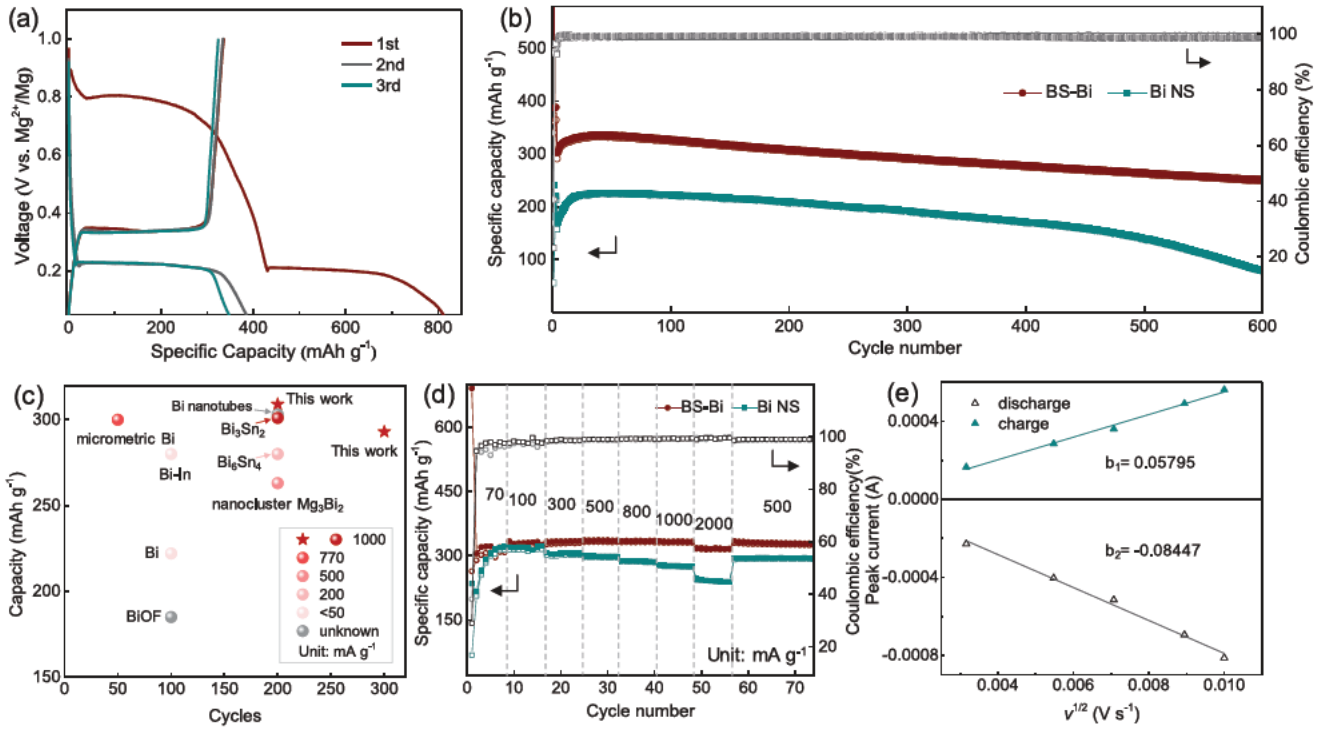

Figure 2. a) Discharge/charge curves of BS-Bi electrode at the current density of 0.1 A g^{-1}. b) Long-cycle stability comparison at the high current density of 1.0 A g^{-1} with three pre-activation cycles at 0.1 A g^{-1}. c) Comparison of the cycling stability and specific capacity between BS-Bi and previously reported Bi-based materials. The cycling current densities are presented with different colors. d) Rate capability from 0.07 to 2.0 A g^{-1}. e) A linear fitting for the relationship between the peak current (I_p) and the square root of scan rate ($v^{1/2}$).

of 0.05–1.0 V at the current density of 0.1 A g^{-1}. In the first cycle, two obvious discharge plateaus at ≈0.8 and ≈0.2 V are observed. Here, to clarify the effectiveness of the MLBH system, electrochemical tests using various control electrolytes were conducted. As shown in Figure S3a in the Supporting Information, the capacity is negligible with no addition of $LiBH_4$ which is in line with previous reports,[18,19] because the Bi_2Se_3 is hardly activated by divalent Mg^{2+} with a low solid-diffusion rate. Another dual-ion electrolyte system containing 0.25 M all phenyl complex (APC) (with or without 1.0 M LiCl) was studied. In both hybrid systems, the addition of Li-salt largely expands the initial discharge capacity of BS-Bi with the appearance of a flat plateau at ≈0.8 V (Figures S3b and S4, Supporting Information). The electrochemical stability of BS-Bi in MLBH electrolyte is superior to those in APC (Figure S5, Supporting Information). Moreover, as shown in Figure S6 in the Supporting Information, the reversible capacities with 1.5 M $LiBH_4$ are significantly higher than those with 0.6 M $LiBH_4$. These results suggest that the first discharge plateau of BS-Bi is related to Li^+ instead of Mg^{2+} and the $LiBH_4$ plays a vital role in MLBH hybrid electrolyte to activate pristine BS-Bi electrode. This is consistent with previous reports that the conversion reaction in Li^+/Mg^{2+} hybrid battery system was usually driven by Li^+ instead of Mg^{2+},[18,20–22] while the alloying reactions are involving with a Mg chemistry.[7–9] Here, the first and the lower plateaus correspond to a conversion and an alloying reaction, respectively. To demonstrate the high alloying/de-alloying efficiency of the BS-Bi, a control sample bismuth nanosheets (Bi NS) was prepared via a hydrothermal method (Figures S7 and S8, Supporting Information). Figure 2b shows the long cycling performance of the BS-Bi and the Bi NS at the current density of 1.0 A g^{-1}. For the BS-Bi anode, a high discharge specific capacity of 335 mAh g^{-1} is achieved. And after 600 cycles, the capacity maintains at 252 mAh g^{-1} with high Coulombic efficiency of 99.2%. The high specific capacity with long-term cycling performances of the BS-Bi electrode outperforms most of the previously reported Bi-based materials for RMBs (Figure 2c and Table S1, Supporting Information).[6,7,9,23–27] While the highest capacity of Bi NS in MLBH electrolyte is 240 mAh g^{-1} with poor initial Coulombic efficiency (23.1%) and high polarization (Figure S9, Supporting Information). In addition, only 79 mAh g^{-1} is maintained after 600 cycles for Bi NS. The high rate performance of BS-Bi is demonstrated in Figure 2d. When the current densities increased, the capacities of BS-Bi exhibit slight decay with specific discharge capacities of 322, 330, 333, 335, 335, 333, and 318 mAh g^{-1} at 0.07, 0.1, 0.3, 0.5, 0.8, 1.0, and 2.0 A g^{-1}, respectively. When the current density is switched back to 0.5 A g^{-1}, a high discharge capacity of 332 mAh g^{-1} can be attained, exhibiting good electrochemical stability at high rates. By comparison, the capacities of Bi NS dramatically decrease from 322 to 240 mAh g^{-1} when the current density increased from 0.1 to 2.0 A g^{-1}. These results demonstrate that the BS-Bi exhibits faster Mg^{2+} diffusion kinetics and better structural stability than Bi NS.

To reveal the reasons for the good rate performance of BS-Bi, the kinetic analysis via cyclic voltammetry curves was carried out under scan rates from 0.01 to 0.1 mV s^{-1} to confirm the fast Mg^{2+} diffusion kinetics of the BS-Bi electrode (Figure S10,

Supporting Information). The linear relationship between the peak current (I_p) and the square root of the scan rate ($v^{1/2}$) is plotted in Figure 2e. Plugging the slope of the linear fitting in the Randles–Sevcik equation (Equation (S1), Supporting Information), the diffusion coefficients of Mg^{2+} are calculated to be 2.41×10^{-11} and 1.13×10^{-11} cm^2 s^{-1} for the alloying and de-alloying processes, respectively. The resultant diffusion coefficients exhibit orders of magnitude higher than previously reported ones in RMBs such as 3.35×10^{-14} cm^2 s^{-1} for the Pb–Bi alloy system and 7.00×10^{-12} cm^2 s^{-1} for insertion-type VS_2,[28,29] demonstrating an extremely fast Mg^{2+} diffusivity in BS-Bi. Further, in situ electrochemical impedance spectroscopy was carried out during the 1st cycle at different cut-off voltages to monitor the change of interfacial impedance. Figure S11 in the Supporting Information shows the Nyquist plot with high impedance at an open-circuit voltage. Then the impedance immediately decreases to a low value after the initial Li^+ insertion (Figure S12 in the Supporting Information dark gray line at 0.8 V), which can be attributed to the activation of interfaces by Li^+ insertion.[30] At a fully charge state (red line at 1.0 V), the electrode exhibits a low impedance with enhanced conductivity. These electrochemical tests demonstrate that the superior rate performances of the BS-Bi anode benefit from the high ionic and electronic conductivity.

To investigate the reaction mechanism of the BS-Bi anode in MLBH hybrid electrolyte, operando synchrotron XRD and electron microscopies were performed for the first cycle. The diffraction patterns and corresponding discharge/charge profile are shown in **Figure 3**a. Two distinct peaks at 21.90° and 36.73° correspond to the copper current collector. The discharge curve presents two plateaus (stages I and II) during the initial discharge. For a pristine electrode, two major peaks at 11.07° and 12.97° correspond to the (1 0 1) and (0 1 5) planes of Bi_2Se_3, respectively. An enlarged portion of the patterns at

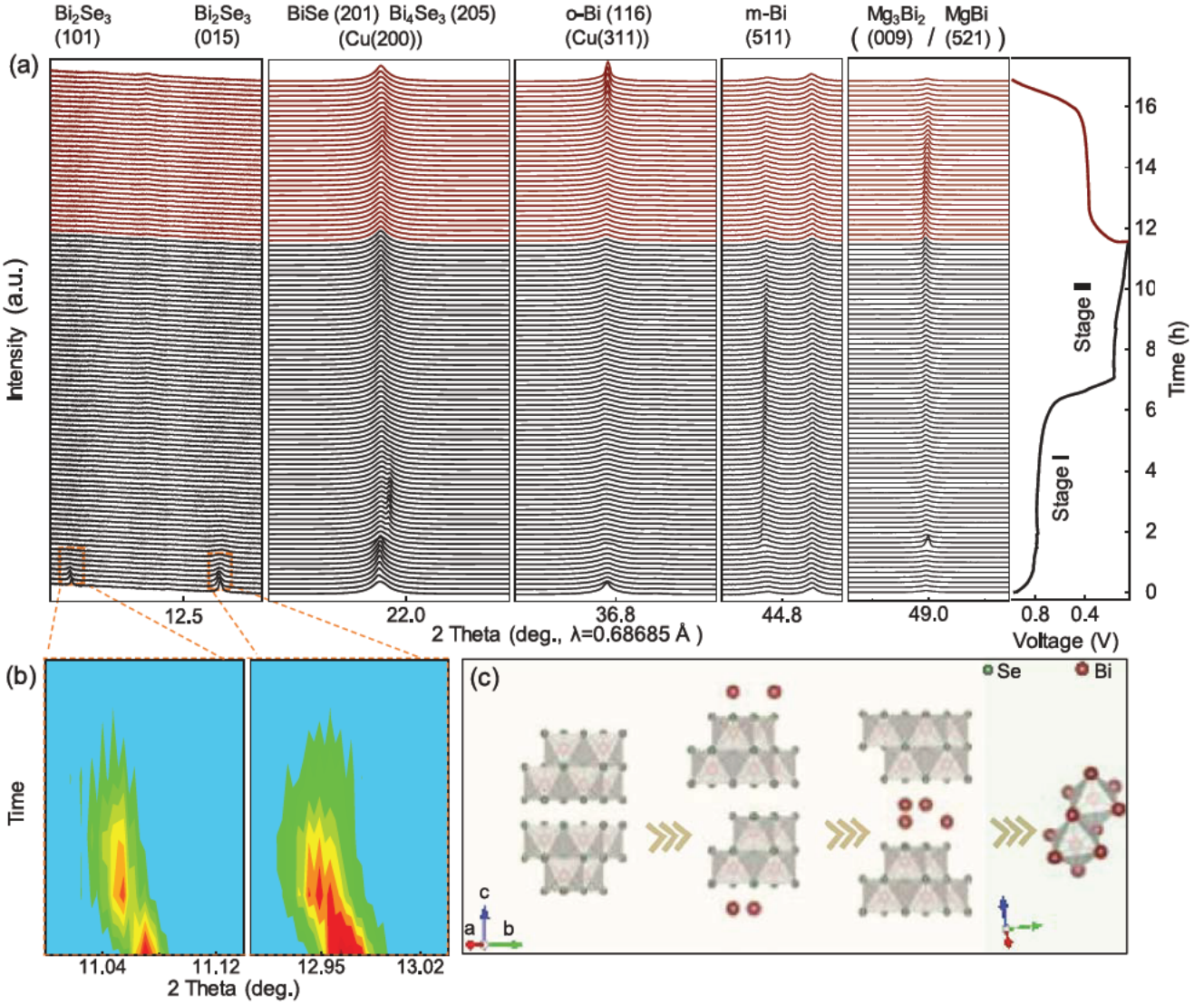

Figure 3. a) Operando synchrotron XRD patterns of the BS-Bi electrode and the corresponding discharge/charge curve. The black and red lines correspond to the discharge and charge processes, respectively. b) Contour plots of the partial synchrotron XRD data in the early state of the initial discharge. c) The crystal structural evolution of the phase conversion of Bi_2Se_3 (from left to right: Bi_2Se_3, BiSe, Bi_4Se_3, and m-Bi).

the very beginning of the discharge (Figure 3b) reveals that the two peaks shift to the low-angle direction. This results from the insertion of Li^+ in Bi_2Se_3, leading to the expansion of the (1 0 1) and (0 1 5) planes of Bi_2Se_3. The expanded planes further enhance the diffusion kinetics of extraneous cations in the host material. During further discharge, the intensities of these two peaks gradually decrease and disappear at ≈0.8 V. At the same time, the peak emerges at 21.90° ascribing to the (2 0 1) plane of BiSe, which indicates the appearance of the BiSe phase. The overlapped phase of BiSe and Cu can only be identified by the variation of the intensity and is hardly distinguished from lab-based XRD results. In addition, the SAED pattern of BS-Bi during the first discharge plateau demonstrates the existence of BiSe and Li_2Se phases as shown in Figure S13 in the Supporting Information. Then, BiSe completely transforms to Bi_4Se_3 (21.97°). At the end of stage I, m-Bi at 44.72° is formed, which is consistent with the HRTEM image of nanostructured Bi crystals formed in Se-based matrix, as shown in Figure 1c. These findings reveal that stage I in the initial discharge process is attributed to Li^+-driven in situ conversion from Bi_2Se_3 to metallic Bi. The crystal structure evolution and lattice parameters of relevant phases from the electrochemical conversion of Bi_2Se_3 are summarized in Figure 3c and Table S2 in the Supporting Information. In stage II, the emerged peak at 48.99° can be assigned to the overlap of MgBi (5 2 1) and Mg_3Bi_2 (0 0 9) with the gradual vanishing of m-Bi. At the end of the discharge state, HRTEM images of the electrode materials show the spacing of 2.36 and 2.12 Å which can be indexed to the (1 1 0) and (0 1 $\bar{3}$) planes of the trigonal Mg_3Bi_2 (Figure S14, Supporting Information). The appearance of intermediate monoclinic MgBi demonstrates a highly efficient alloying process from the in-situ-formed Bi nanocrystals to Mg_3Bi_2. In addition, the morphology of the BS-Bi is maintained as an integral nanosheet with the integration of Mg_3Bi_2 nanoparticles after full alloy (Figures S15–S17, Supporting Information). During the charge process, a reversible phase transition from Mg_3Bi_2 to MgBi occurs as demonstrated in the previous report.[15] Importantly, approaching the end of the charge process, a new bismuth phase of orthorhombic Bi (o-Bi) appears at 36.73° with a gradual disappearance of MgBi phase. During the initial alloying/de-alloying process, the phase transition from m-Bi to o-Bi results from the highly efficient alloying/de-alloying processes owing to the nanosize of the in-situ-formed Bi crystals, and similar observations have been reported in tin alloy anode.[31,32] The conversion from Bi to Bi_2Se_3 is difficultly proceed, as shown in Figure S18 in the Supporting Information, even with high upper cut-off voltage in both MLBH and APC-LiCl hybrid systems, and here only Mg–Bi alloying/de-alloying reactions are considered and utilized. The Li^+-driven in situ conversion and the following alloying reaction for BS-Bi in MLBH hybrid electrolyte can be concluded as follows

Initial discharge stage I

$$Bi_2Se_3 + 2Li^+ + 2e^- \rightarrow 2BiSe + Li_2Se \quad (1\text{-}1)$$

$$4BiSe + 2Li^+ + 2e^- \rightarrow Bi_4Se_3 + Li_2Se \quad (1\text{-}2)$$

$$Bi_4Se_3 + 6Li^+ + 6e^- \rightarrow 4m\text{-}Bi + 3Li_2Se \quad (1\text{-}3)$$

Initial discharge stage II

$$m\text{-}Bi + Mg^{2+} + 2e^- \rightarrow MgBi \quad (2\text{-}1)$$

$$2MgBi + Mg^{2+} + 2e^- \rightarrow Mg_3Bi_2 \quad (2\text{-}2)$$

Initial charge

$$Mg_3Bi_2 \leftrightarrow 2MgBi + Mg^{2+} + 2e^- \quad (3\text{-}1)$$

$$MgBi \leftrightarrow o\text{-}Bi + Mg^{2+} + 2e^- \quad (3\text{-}2)$$

To gain more insight into the reaction mechanism of the BS-Bi electrode, electronic states of discharge/charge products were investigated through combining density functional theory (DFT) calculations and a series of ex situ spectroscopic analyses. To investigate the metallic properties of Bi_2Se_3, BiSe, and Bi_4Se_3, the total density of state (DOS) of these samples was calculated and the curves are shown in **Figure 4**a. Compared to Bi_2Se_3, the formed reaction products BiSe and Bi_4Se_3 exhibit increased DOS at the Fermi level, which demonstrates significantly improved electrical conductivities of these phases in Li^+-driven conversion process.[33] For ex situ spectroscopic characterizations, different discharge/charge states are marked in Figure 4b. For example, d_0.75 and c_1.00 represent the discharge state of 0.75 V and the charge state of 1.00 V, respectively. First, ex situ Bi 4f X-ray photoelectron spectroscopy (XPS) spectra were collected to probe the Bi chemical states as shown in Figure 4c. For pristine BS-Bi, the doublet peaks of Bi $4f_{5/2}$ and Bi $4f_{7/2}$ appear at 163.4 and 158.1 eV, respectively. XPS results of the d_0.75 reveal that the Bi $4f_{5/2}$ peak shifts to high binding energy of 163.8 eV after the insertion of Li^+, which is consistent with previous reports.[34] The XPS deconvolution of Bi 4f doublet peaks (Figure S19, Supporting Information) of d_0.75 confirms the presence of Bi (II), Bi (0), and a mid-valence state of Bi (II-0), and the relative percent of Bi (II), Bi (II-0), and Bi (0) is 30.1%, 55.8%, and 14.1%, respectively (Table S3, Supporting Information). With an increased discharge depth from d_0.75, d_0.20 to d_0.05, the peaks of Bi $4f_{5/2}$ continually shift to a lower angle from 163.8, 163.6 to 163.5 eV. These results demonstrated the efficient reduction of Bi from Bi_2Se_3. The energy shift of the spectrum from d_0.20 to d_0.05 indicates the existence of an intermediate phase, MgBi. When recharging back to 1.0 V, the spectrum shows a blueshift toward high energy values of 163.7 eV, which suggests good reversibility of the alloying/de-alloying process. Second, Raman spectra of the pristine BS-Bi exhibit three typical active modes including two A_{1g} modes (≈69 and ≈172 cm^{-1}) and an E_g mode (≈128 cm^{-1}) as shown in Figure S20 in the Supporting Information. In the state of d_0.75, the E_g peak correlating with in-plane bond vibrations vertical to the *c*-axis showed a slight redshift, demonstrating a strong interaction between inserted Li^+ and the host materials.[16] When further discharged to 0.5 V, the peaks of Bi_2Se_3 almost disappear accompanying by two new peaks at around 71 and 94 cm^{-1}, assigning to metallic Bi. At fully discharge state, vanishing of these two peaks indicates that the Bi was fully converted. The shape of the XAS spectrum is sensitive to the local geometric structure around the central atom.[35] The line shape of Bi L3 at the state of d_0.50 has dramatically changed from two broad

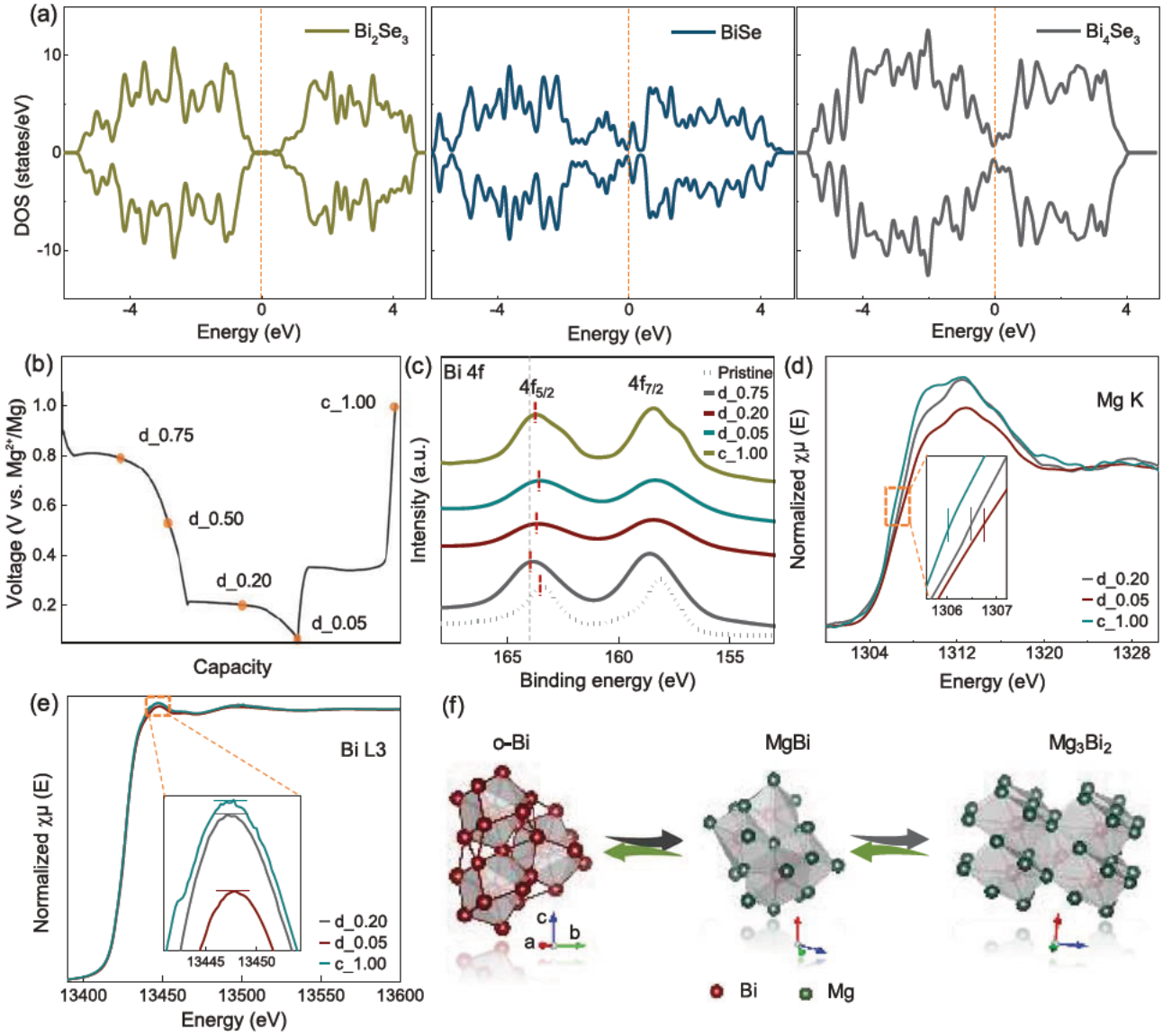

Figure 4. a) The total DOS of Bi_2Se_3, BiSe, and Bi_4Se_3 phases. The dashed yellow line represents the position of the Fermi level. b) The discharge/charge states were tested by the spectroscopic characterizations. c) Ex situ XPS spectra of Bi 4f at discharge state of 0.75, 0.50, and 0.05 V, and fully charge state of 1.00 V. d,e) XAS spectra of Mg K-edge (d) and Bi L_3-edge (e) of the BS-Bi electrode under various discharge/charge states. f) Schematic illustration of crystal structure evolution of the BS-Bi during electrochemical alloying process after the initial cycle.

peaks to a single peak influenced by Li^+ insertion, which suggests a totally different local geometric structure of Bi center atoms over phase evolution (Figure S21, Supporting Information). All these spectroscopic results match well with operando synchrotron XRD and electron microscopy analysis, revealing a valence change of Bi center atoms from Bi_2Se_3, and a highly efficient and reversible alloying process of Mg–Bi.

To further reveal the origin of high alloying/de-alloying efficiency, ex situ synchrotron XAS and XPS were collected to further probe electron transfer behavior between Mg and Bi during the alloying/de-alloying process.[36] The absorption energies of Mg K-edge at the d_0.20 and d_0.05 states exhibit an increase from 1306.4 to 1306.7 eV, and then decrease back to 1306.0 eV at the state c_1.00 as shown in Figure 4d. The increased energy is attributed to the decreased electron density of Mg in Mg_3Bi_2 compared with that in the MgBi, and a reversed trend can be observed in the de-alloying process. The Bi atom has the electronic configuration of $4f^{14}5d^{10}6s^26p^3$. The Bi L3 is used to probe 6s and 5d electrons, due to the excitation of 2p3/2 electron to unfilled s or d orbitals.[37] The decreasing peak intensity of Bi L3 from the d_0.20 to d_0.05 states demonstrates an increasing electron density of Bi during the alloying process while the electron density decreased when charged back to 1.0 V (Figure 4e). In addition, compared with the XPS spectrum of pristine BS-Bi, the electrode at the state of d_0.05 V exhibits strong Mg 2s and Mg KLL Auger peaks, suggesting integration of Mg in BS-Bi electrode to form a Mg–Bi alloy phase (Figures S22 and S23, Supporting Information). All these results demonstrate that the

dynamic evolution of the Bi and Mg electronic states leads to a highly efficient alloying/de-alloying reaction with MgBi as an intermediate (Figure 4f).

3. Conclusion

A nanostructured Bi anode has been constructed through an in situ electrochemical reaction from bismuth selenide. Coupled with Mg^{2+}/Li^{+} hybrid electrolyte, the electrochemical activity and alloying/de-alloying efficiency of the nanostructured Bi anode are exclusively evoked by Li-salt. The in-situ-formed Bi anode with nanosized Bi active crystals exhibits the advantages of short Mg^{2+} diffusion length and extremely high ion-diffusivity. As a result, it demonstrates an excellent rate performance (335 mAh g^{-1} at 1 A g^{-1}) and long cycling stability over 600 cycles, which surpasses the state-of-the-art Bi-based anodes in RMBs. A Li^{+}-driven conversion reaction followed by a reversible Mg alloying/de-alloying process is verified via synchrotron XAS and operando synchrotron XRD together with a series of spectroscopic analyses. The Li^{+}-driven battery chemistry can be extended to other multivalent-ion battery systems and promotes the exploration of novel materials through an in situ electrochemical reaction.

4. Experimental Section

Experimental details can be found in the Supporting Information.

Supporting Information

Supporting Information is available from the Wiley Online Library or from the author.

Acknowledgements

X.X. and C.Y. contributed equally to this work. This work was financially supported by the Australian Research Council (ARC) through Discovery Project FL170100154. The authors acknowledge support from the Powder Diffraction and X-ray Absorption Spectroscopy beamlines at the Australian Synchrotron, ANSTO, Melbourne. DFT computations within this research were undertaken with the assistance of resources and services from the National Computational Infrastructure (NCI) and Phoenix High Performance Computing, which are supported by the Australian Government and the University of Adelaide. The authors thank Fangxi Xie and Junnan Hao from the University of Adelaide for the helpful discussions.

Conflict of Interest

The authors declare no conflict of interest.

Data Availability Statement

The data that support the findings of this study are available from the corresponding author upon reasonable request.

Keywords

bismuth anodes, in situ conversion, layered bismuth selenide, magnesium batteries

Received: October 28, 2021
Revised: November 18, 2021
Published online: January 20, 2022

[1] M. Mao, T. Gao, S. Hou, C. Wang, *Chem. Soc. Rev.* **2018**, *47*, 8804.
[2] I. Shterenberg, M. Salama, H. D. Yoo, Y. Gofer, J.-B. Park, Y.-K. Sun, D. Aurbach, *J. Electrochem. Soc.* **2015**, *162*, A7118.
[3] E. N. Keyzer, H. F. Glass, Z. Liu, P. M. Bayley, S. E. Dutton, C. P. Grey, D. S. Wright, *J. Am. Chem. Soc.* **2016**, *138*, 8682.
[4] R. Attias, M. Salama, B. Hirsch, Y. Goffer, D. Aurbach, *Joule* **2019**, *3*, 27.
[5] Z. Meng, D. Foix, N. Brun, R. Dedryvere, L. Stievano, M. Morcrette, R. Berthelot, *ACS Energy Lett.* **2019**, *4*, 2040.
[6] T. S. Arthur, N. Singh, M. Matsui, *Electrochem. Commun.* **2012**, *16*, 103.
[7] Y. Shao, M. Gu, X. Li, Z. Nie, P. Zuo, G. Li, T. Liu, J. Xiao, Y. Cheng, C. Wang, J. G. Zhang, J. Liu, *Nano Lett.* **2014**, *14*, 255.
[8] K. V. Kravchyk, L. Piveteau, R. Caputo, M. He, N. P. Stadie, M. I. Bodnarchuk, R. T. Lechner, M. V. Kovalenko, *ACS Nano* **2018**, *12*, 8297.
[9] Y. H. Tan, W. T. Yao, T. Zhang, T. Ma, L. L. Lu, F. Zhou, H. B. Yao, S. H. Yu, *ACS Nano* **2018**, *12*, 5856.
[10] N. Singh, T. S. Arthur, C. Ling, M. Matsui, F. Mizuno, *Chem. Commun.* **2013**, *49*, 149.
[11] H. Yaghoobnejad Asl, J. Fu, H. Kumar, S. S. Welborn, V. B. Shenoy, E. Detsi, *Chem. Mater.* **2018**, *30*, 1815.
[12] L. R. Parent, Y. Cheng, P. V. Sushko, Y. Shao, J. Liu, C. M. Wang, N. D. Browning, *Nano Lett.* **2015**, *15*, 1177.
[13] K. Periyapperuma, T. T. Tran, M. I. Purcell, M. N. Obrovac, *Electrochim. Acta* **2015**, *165*, 162.
[14] J. Z. Niu, Z. H. Zhang, D. Aurbach, *Adv. Energy Mater.* **2020**, *10*, 2000697.
[15] X. Xu, D. Chao, B. Chen, P. Liang, H. Li, F. Xie, K. Davey, S. Z. Qiao, *Angew. Chem., Int. Ed.* **2020**, *59*, 21728.
[16] K. P. Chen, F. R. Chung, M. Wang, K. J. Koski, *J. Am. Chem. Soc.* **2015**, *137*, 5431.
[17] J. Ni, X. Bi, Y. Jiang, L. Li, J. Lu, *Nano Energy* **2017**, *34*, 356.
[18] Y. Zhang, J. Xie, Y. Han, C. Li, *Adv. Funct. Mater.* **2015**, *25*, 7300.
[19] R. Mohtadi, M. Matsui, T. S. Arthur, S. J. Hwang, *Angew. Chem., Int. Ed.* **2012**, *51*, 9780.
[20] S. Su, Y. NuLi, Z. Huang, Q. Miao, J. Yang, J. Wang, *ACS Appl. Mater. Interfaces* **2016**, *8*, 7111.
[21] H. Yuan, N. Wang, Y. NuLi, J. Yang, J. Wang, *Electrochim. Acta* **2018**, *261*, 503.
[22] X. Zhou, J. Tian, J. Hu, C. Li, *Adv. Mater.* **2018**, *30*, 1704166.
[23] F. Murgia, L. Stievano, L. Monconduit, R. Berthelot, *J. Mater. Chem. A* **2015**, *3*, 16478.
[24] F. Murgia, L. Monconduit, L. Stievano, R. Berthelot, *Electrochim. Acta* **2016**, *209*, 730.
[25] J. Niu, H. Gao, W. Ma, F. Luo, K. Yin, Z. Peng, Z. Zhang, *Energy Storage Mater.* **2018**, *14*, 351.
[26] W. Wang, L. Liu, P. F. Wang, T. T. Zuo, Y. X. Yin, N. Wu, J. M. Zhou, Y. Wei, Y. G. Guo, *Chem. Commun.* **2018**, *54*, 1714.
[27] J. Niu, K. Yin, H. Gao, M. Song, W. Ma, Z. Peng, Z. Zhang, *Nanoscale* **2019**, *11*, 15279.
[28] M. Song, J. Niu, H. Gao, T. Kou, Z. Wang, Z. Zhang, *J. Mater. Chem. A* **2020**, *8*, 13572.

[29] X. Xue, R. Chen, C. Yan, P. Zhao, Y. Hu, W. Kong, H. Lin, L. Wang, Z. Jin, *Adv. Energy Mater.* **2019**, *9*, 1900145.
[30] F. Mizuno, N. Singh, T. S. Arthur, P. T. Fanson, M. Ramanathan, A. Benmayza, J. Prakash, Y. S. Liu, P. A. Glans, J. H. Guo, *Front. Energy Res.* **2014**, *2*, 46.
[31] L. Xu, C. Kim, A. K. Shukla, A. Dong, T. M. Mattox, D. J. Milliron, J. Cabana, *Nano Lett.* **2013**, *13*, 1800.
[32] Z. Wang, Q. Su, J. Shi, H. Deng, G. Q. Yin, J. Guan, M. P. Wu, Y. L. Zhou, H. L. Lou, Y. Q. Fu, *ACS Appl. Mater. Interfaces* **2014**, *6*, 6786.
[33] B. Chen, T. Wang, S. Zhao, J. Tan, N. Zhao, S. P. Jiang, Q. Zhang, G. Zhou, H. M. Cheng, *Adv. Mater.* **2021**, *33*, 2007090.
[34] B. Pradhan, A. Dalui, S. Paul, D. Roy, S. Acharya, *Mater. Res. Express* **2020**, *6*, 124005.
[35] F. Lin, Y. Liu, X. Yu, L. Cheng, A. Singer, O. G. Shpyrko, H. L. Xin, N. Tamura, C. Tian, T. C. Weng, X. Q. Yang, Y. S. Meng, D. Nordlund, W. Yang, M. M. Doeff, *Chem. Rev.* **2017**, *117*, 13123.
[36] C. Ye, Y. Jiao, D. Chao, T. Ling, J. Shan, B. Zhang, Q. Gu, K. Davey, H. Wang, S. Z. Qiao, *Adv. Mater.* **2020**, *32*, 1907557.
[37] A. A. Mistonov, A. P. Chumakov, R. P. Ermakov, L. D. Iskhakova, A. V. Zakharova, A. V. Chumakova, K. O. Kvashnina, *J. Alloys Compd.* **2018**, *753*, 646.

ADVANCED MATERIALS

Supporting Information

for *Adv. Mater.,* DOI: 10.1002/adma.202108688

Synchrotron X-ray Spectroscopic Investigations of In-Situ-Formed Alloy Anodes for Magnesium Batteries

*Xin Xu, Chao Ye, Dongliang Chao, Biao Chen, Huan Li, Cheng Tang, Xiongwei Zhong, and Shi-Zhang Qiao**

Supporting Information

Synchrotron X-ray Spectroscopic Investigations of In-Situ-Formed Alloy Anodes for Magnesium Batteries

*Xin Xu[#], Chao Ye[#], Dongliang Chao, Biao Chen, Huan Li, Cheng Tang, Xiongwei Zhong, and Shi-Zhang Qiao**

Experimental Section

Materials synthesis. The Bi_2Se_3 nanosheets were prepared via a solvothermal method. Firstly, 0.126 g bismuth chloride (Sigma, 98%) and 0.104 g sodium selenite (Sigma, 99%) were dissolved in 50 ml ethylene glycol (EG, Sigma, 99%) to obtain a precursor solution. Then, an alkaline EG solution containing 0.240 g sodium hydroxide (Sigma, 98%) and 10 ml EG was prepared for adjusting the pH values of the precursor solution. The 10 ml alkaline EG solution was added dropwise into the precursor solution under vigorous stirring at room temperature. After further stirring for 30 min, the mixture was transferred into a 100 ml Teflon-lined autoclave and kept at 160 °C for 12 h. The obtained precipitates were centrifuged and washed thoroughly with deionized water and ethanol for several times. Bismuth nanosheets (Bi NS) as the control sample were obtained through the reduction of bismuth oxyiodide (BiOI) with 0.25 M $NaBH_4$ (Sigma, 98%) solution. The BiOI sample was prepared following our previous reports with modifications.[1] In a typical procedure, 0.388 g bismuth nitrate pentahydrate (Sigma, 98%) was firstly dissolved in 80 mL of 1.2 M acetic acid and stirred for 30 min, followed by addition of 0.160 g 1,10-phenanthroline (Sigma, 99%) and 0.133 g potassium iodide (Sigma, 99.5%). The pH of the above mixture solution was then adjusted to 6 using 3 M NaOH. After stirring for another 30 min, the solution was then transferred to a 100 mL Teflon-lined autoclave and heated at 160 ℃ for 2h. The BiOI nanosheets were finally obtained after collecting by centrifugation, washing by deionized water and freezing drying.

Preparation of electrolytes. To prepare the hybrid electrolyte, 1.5 M (0.163 g) lithium borohydride ($LiBH_4$, Sigma, 90%) was firstly dissolved in 5 mL diethylene glycol dimethyl ether (Diglyme, Sigma, anhydrous, 99.5%) under stirring. After stirring for 2 h, 0.1 M (0.027 g) magnesium borohydride ($Mg(BH_4)_2$, Sigma, 95%) was added to prepare the final solution and stirred overnight

before use. The electrolyte with 0.6 M $LiBH_4$ was prepared via same method. The control electrolyte, all-phenyl complex (APC), was prepared by adding 0.25 M (0.200 g) $AlCl_3$ (Sigma, anhydrous, 99.99%) slowly into 4.5 mL tetrahydrofuran (THF, Sigma, anhydrous, 99.9%) under stirring. Afterwards, the obtained $AlCl_3$ solution was slowly added into 1.5 ml phenylmagnesium chloride solution (Sigma, 2.0 M in THF), stirring for another 12 h to obtain the APC electrolyte. The APC-LiCl hybrid electrolyte was prepared by dissolving 1.0 M anhydrous LiCl (Sigma, anhydrous, 99.9%) in above APC solution. All procedures were carried out in an Ar-filled glove box (H_2O< 0.5 ppm and O_2< 0.5 ppm).

Material characterizations. The SEM and TEM images of samples were obtained on FEI Quanta 450 FEG SEM and JEOL JEM-2100f TEM, respectively. Lab-based XRD data were collected on a Rigaku Mini Flex 600 X-Ray Diffractometer (Cu Ka λ=1.5418 Å). XPS measurements were conducted on the PHI-5000 Versa Probe X-ray photoelectron spectrometer with Al Kα radiation. All samples prepared for ex-situ testing were thoroughly rinsed with diglyme solution to remove soluble species on the surface and sealed within Ar protection before testing. The ex-situ XPS data were collected after Ar sputtering to a depth of 10 nm. The ex-situ XAS was obtained from XAS beamline of Australian Synchrotron (ANSTO, Melbourne) and processed with the Athena program.[2] The synchrotron XRD data were collected continuously in 30 s acquisitions from the powder diffraction beamline of ANSTO with a wavelength (λ) of 0.68685 Å. To fully take advantage of facility time for data collection, the four-position cells arrangement are employed where high-rate discharge/charge are not required. These cells are connected with a Neware battery tester which enable the control of electrochemistry for each cell while cell is tested through the beam and a data set is collected. Home-made 2032 coin-cells were used for operando synchrotron

XRD data collection. Both sides of the cell cases were punched with d=0.3 cm holes and sealed with Kapton films to allow X-ray transmission.

Electrochemical measurements. The electrochemical performance was evaluated in 2032 type coin-cell. To fabricate electrodes, the active materials (Bi_2Se_3 nanosheets or Bi NS), carbon black (> 99 %, Alfa Aesar) and poly(vinylidene fluoride) (PVDF, Sigma) were mixed with a mass ratio of 7:2:1 in N-methyl-2-pyrrolidone (NMP, Sigma, anhydrous, 99.5%). The mixture was stirred overnight to obtain a homogeneous slurry, pasted on a copper foil with a diameter of 1.2 cm, and dried at 80 °C in a vacuum oven overnight. The mass loading was weighted around 1.0 mg. The as-prepared electrodes, polished Mg foils (MTI, 99.9%) and glass microfibre separators (Whatman, GF/C) were used as the cathodes, anodes and separators, respectively. Galvanostatic cycling tests were performed on Land CT2001A battery testing system at different current densities in the voltage range of 1.0 - 0.05 V. Three initial discharge/charge cycles at a low current density of 0.1 A g^{-1} were performed for the activation of electrodes. The specific capacities of the BS-Bi were calculated based on the mass of Bi. CV tests were carried out among 0.05 and 1.0 V. The EIS plots were obtained from CHI760E electrochemical workstation with an AC amplitude of 5 mV in a frequency range of 100 kHz - 0.01 Hz.

Calculation of diffusion coefficient based on CV profiles. The diffusion coefficient of Mg ions was calculated by the Randles-Sevcik equation (at 25 ℃).

$$I_p = 2.686\times10^5 n^{3/2} A D^{1/2} v^{1/2} C \qquad \text{(S-1)}$$

in which I_p is the current peak value (A) shown in CV curves, n is the number of electrons transferred (assuming six electrons transfer), *A* is the electrode area (electrode area for all samples is 1.131 cm^2), D is the diffusion coefficient (cm^2 s^{-1}) which can be calculated from the slope of I_p-

$v^{1/2}$ lines and v is the scan rate (V s^{-1}). C is the solid concentration in mol cm^{-3} and calculated to be 3.848×10^{-3} mol cm^{-3} in Mg_3Bi_2.

Computational details. All calculations in this work were carried out using the density functional theory (DFT) method as implemented in the VASP code. For the structure optimization and density of states (DOS) computation, the electronic exchange-correlation energy was modeled using the Perdew-Burke-Ernzerhof (PBE) functional within the generalized gradient approximation (GGA). The projector augmented wave (PAW) method was used to describe the ionic cores. A 500 eV kinetic energy cut-off was used for the plane-wave expansion. Monkhorst-Pack 5×5×1, 7×7×1, 9×9×1 k-point grids were used to describe the Brillouin zone for BiSe, Bi_2Se_3, Bi_4Se_3, respectively. The convergence criterion for the electronic structure iteration was set to be 10^{-4} eV, and that for geometry optimizations was set to be 0.01 eV $Å^{-1}$ on force. A Gaussian smearing of 0.1 eV was applied during the geometry optimization.

Supplementary Results

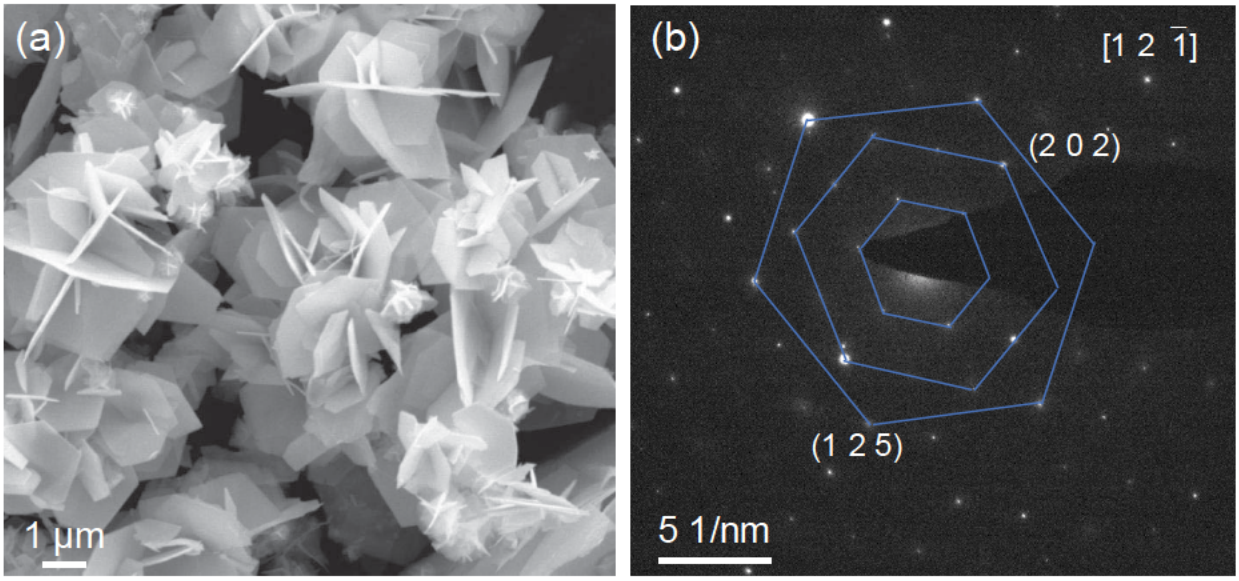

Figure S1. (a) SEM image and (b) SAED pattern of Bi_2Se_3 nanosheets.

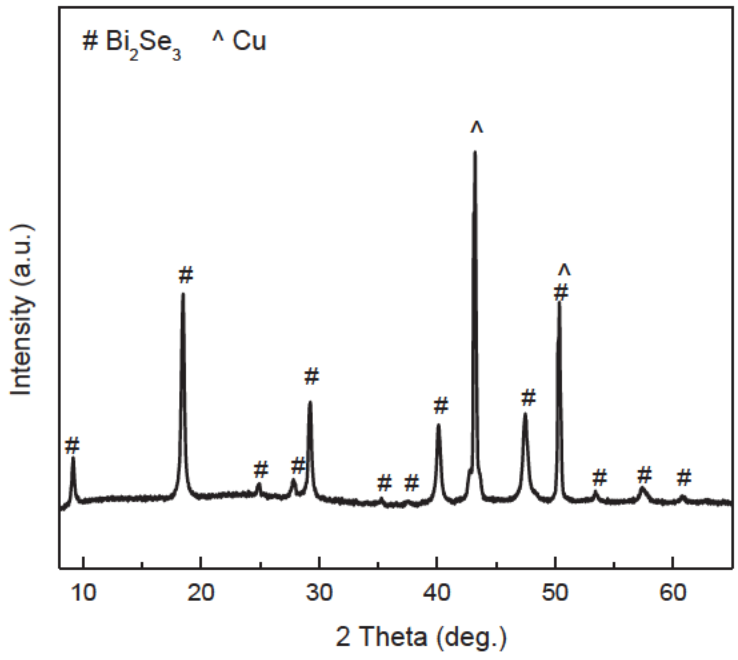

Figure S2. The XRD pattern of BS-Bi electrode after soaking in MLBH electrolyte for a week.

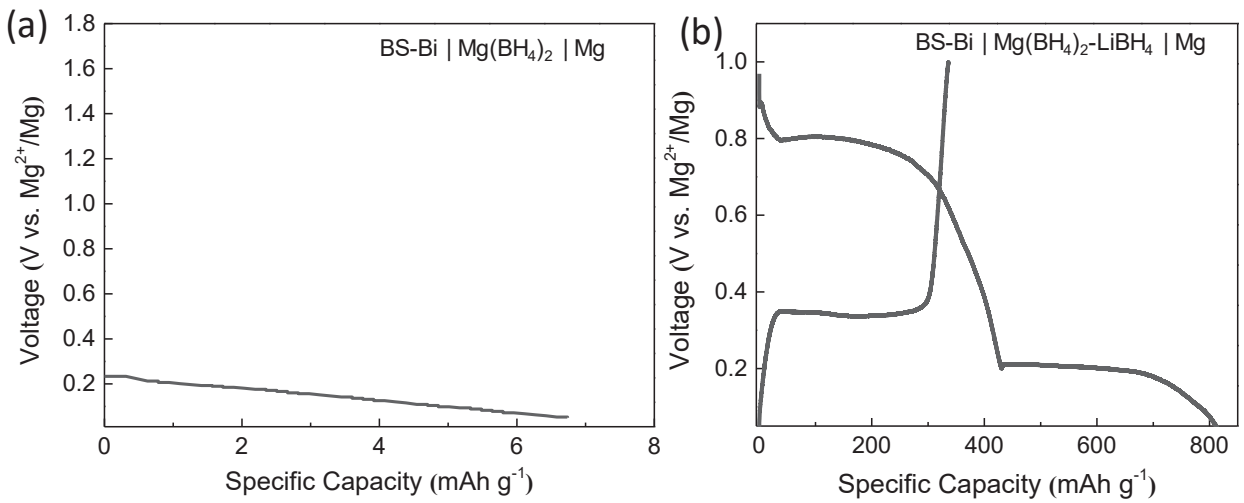

Figure S3. (a) The discharge curve of BS-Bi in single $Mg(BH_4)_2$ salt electrolyte. The capacity is negligible with no addition of $LiBH_4$. (b) Discharge/charge curves of BS-Bi in MLBH hybrid electrolyte.

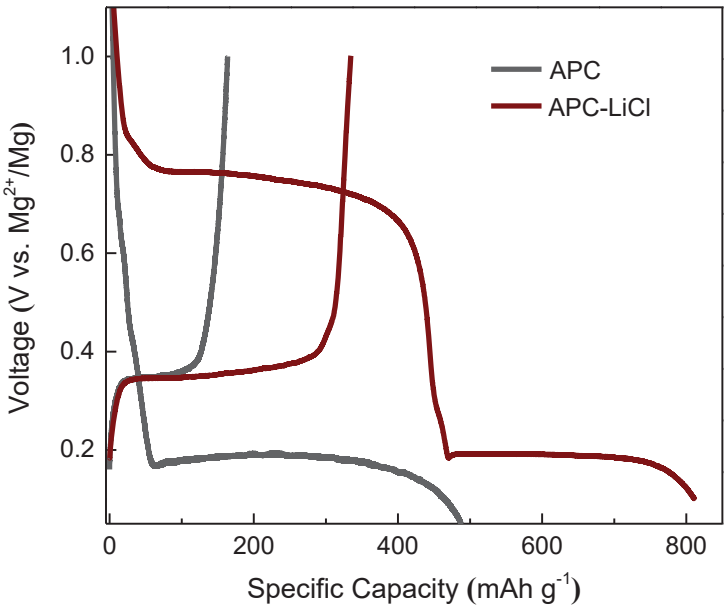

Figure S4. The discharge/charge curves of BS-Bi in APC and APC-LiCl hybrid electrolytes.

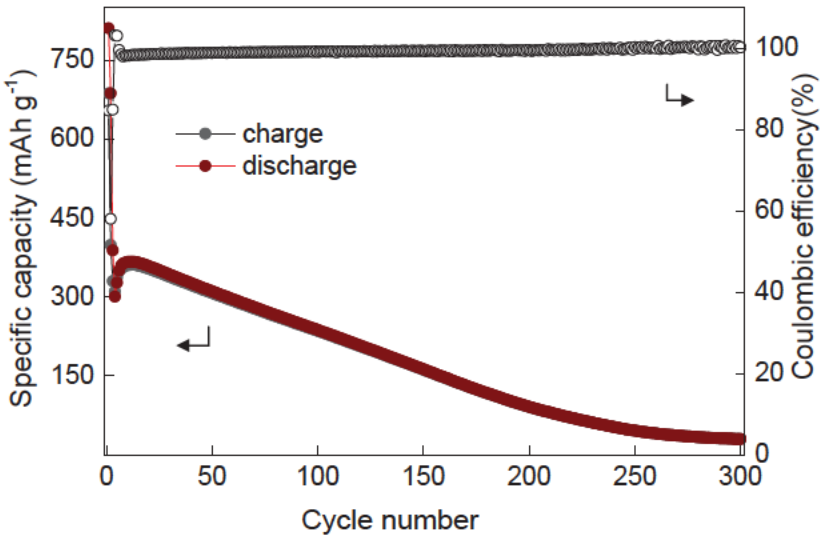

Figure S5. The cycling performance of BS-Bi in APC-LiCl hybrid electrolyte.

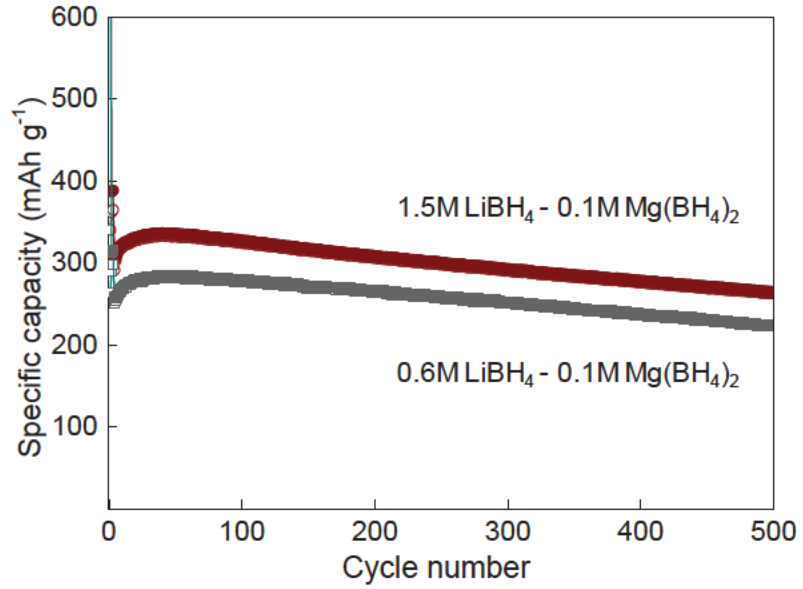

Figure S6. Cycling performances of BS-Bi in MLBH electrolytes with 0.6 M or 1.5 M $LiBH_4$.

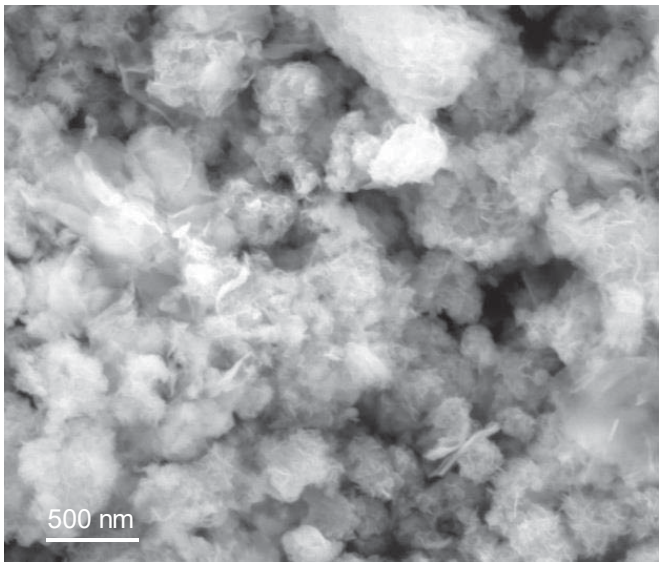

Figure S7. The SEM image of the control sample Bi NS.

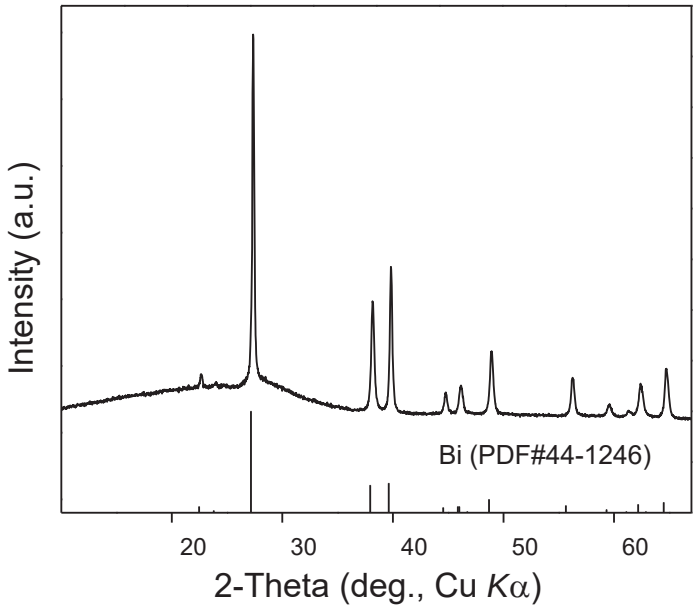

Figure S8. The XRD pattern of the control sample Bi NS.

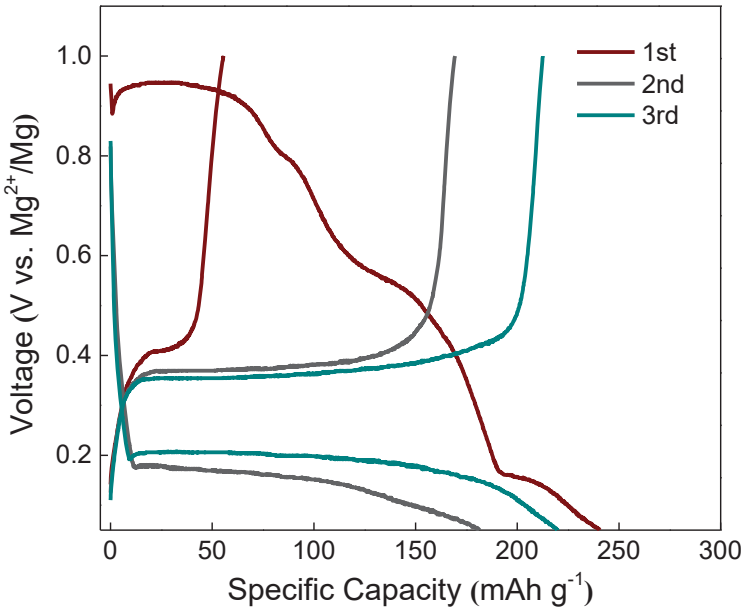

Figure S9. The initial three cycles of discharge/charge curves of Bi NS electrode in MLBH electrolyte.

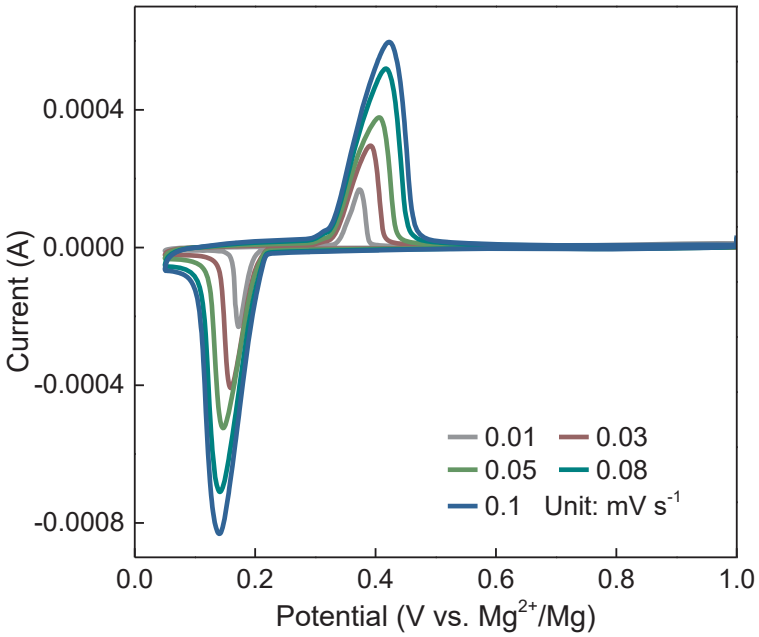

Figure S10. CV curves of BS-Bi electrode at different scan rates after the 1st cycle.

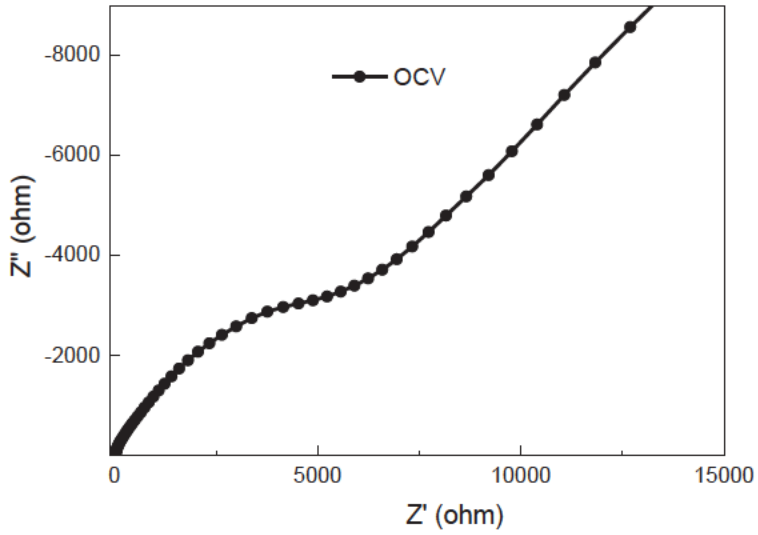

Figure S11. EIS plot of the BS-Bi electrode at open-circuit voltage.

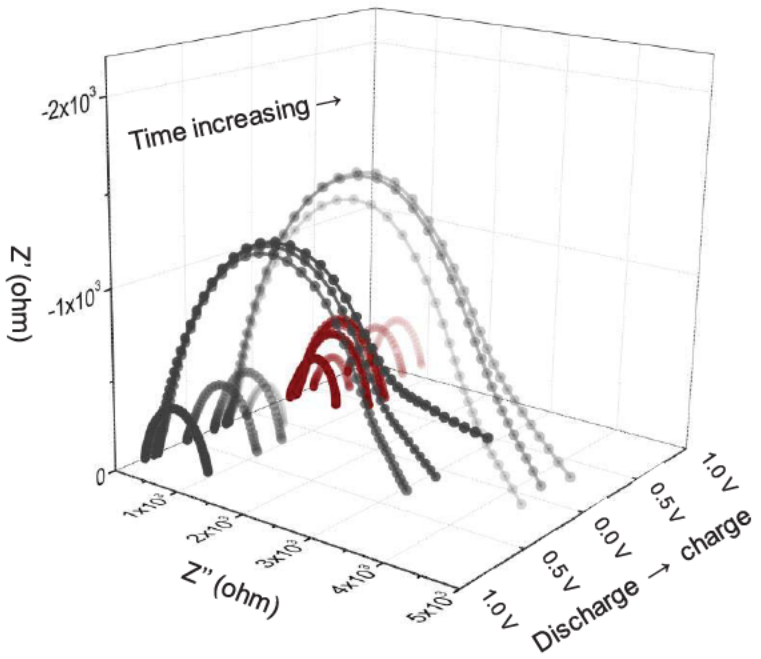

Figure S12. *In-situ* EIS plots of BS-Bi for the 1st cycle. The discharge/charge range among 1.0 - 0.05 V at current density of 0.1 A g^{-1}. The lines in dark grey and red colors correspond to the discharge and charge process, respectively.

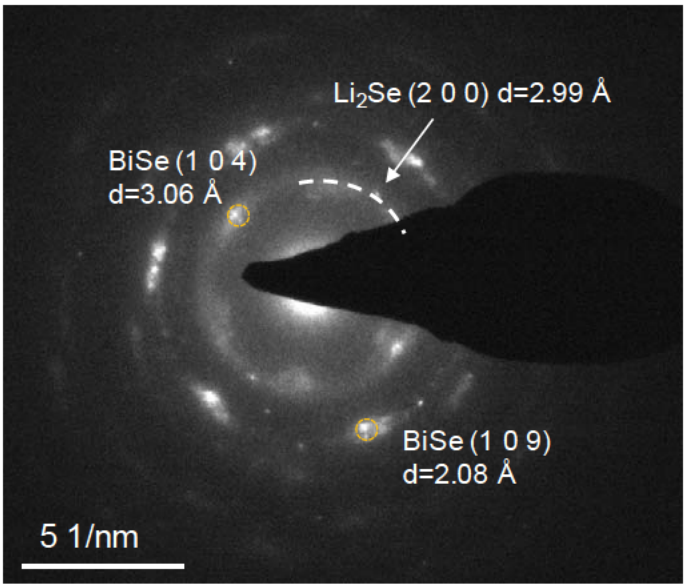

Figure S13. The SAED pattern of BS-Bi electrode during the first discharge plateau of the initial cycle.

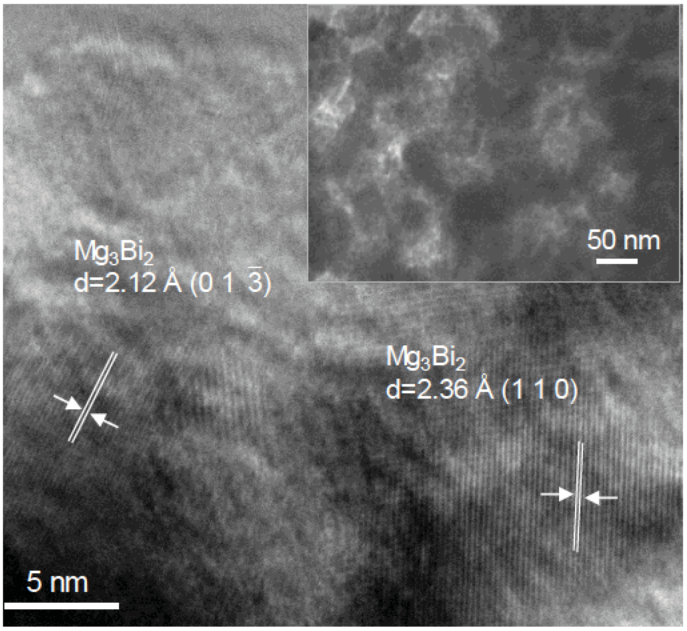

Figure S14. HRTEM image of BS-Bi electrode at fully discharge state of 0.05 V.

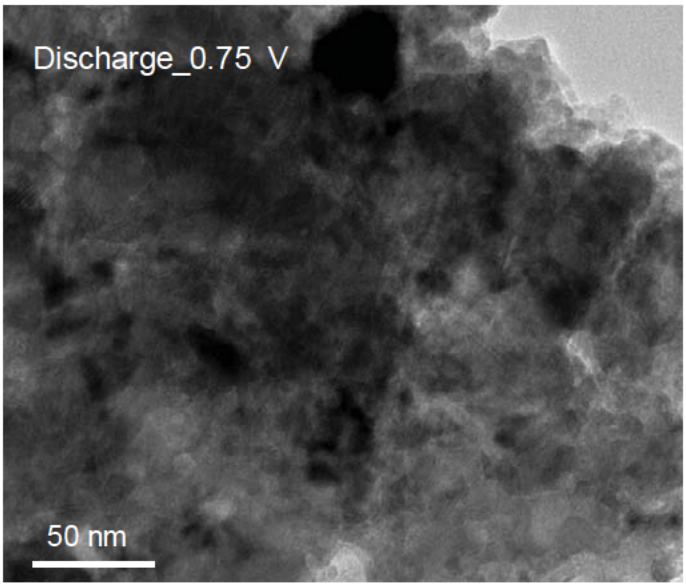

Figure S15. TEM image of BS-Bi electrode under 0.75 V during the initial discharge.

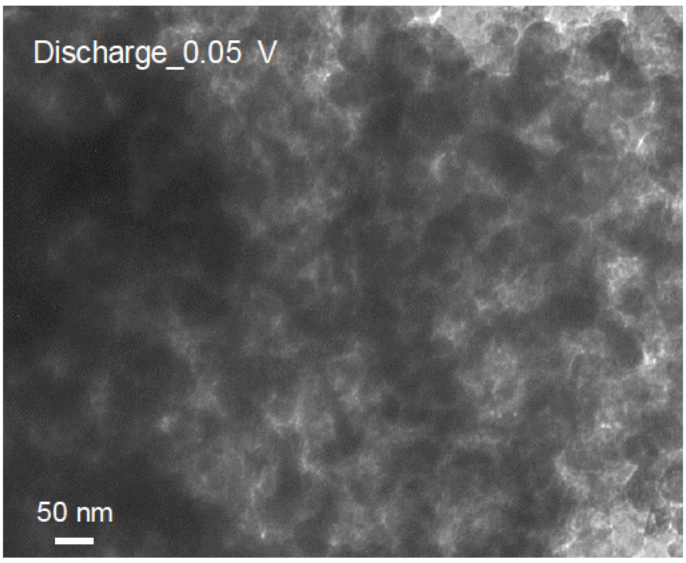

Figure S16. TEM image of BS-Bi electrode under 0.05 V during the initial discharge.

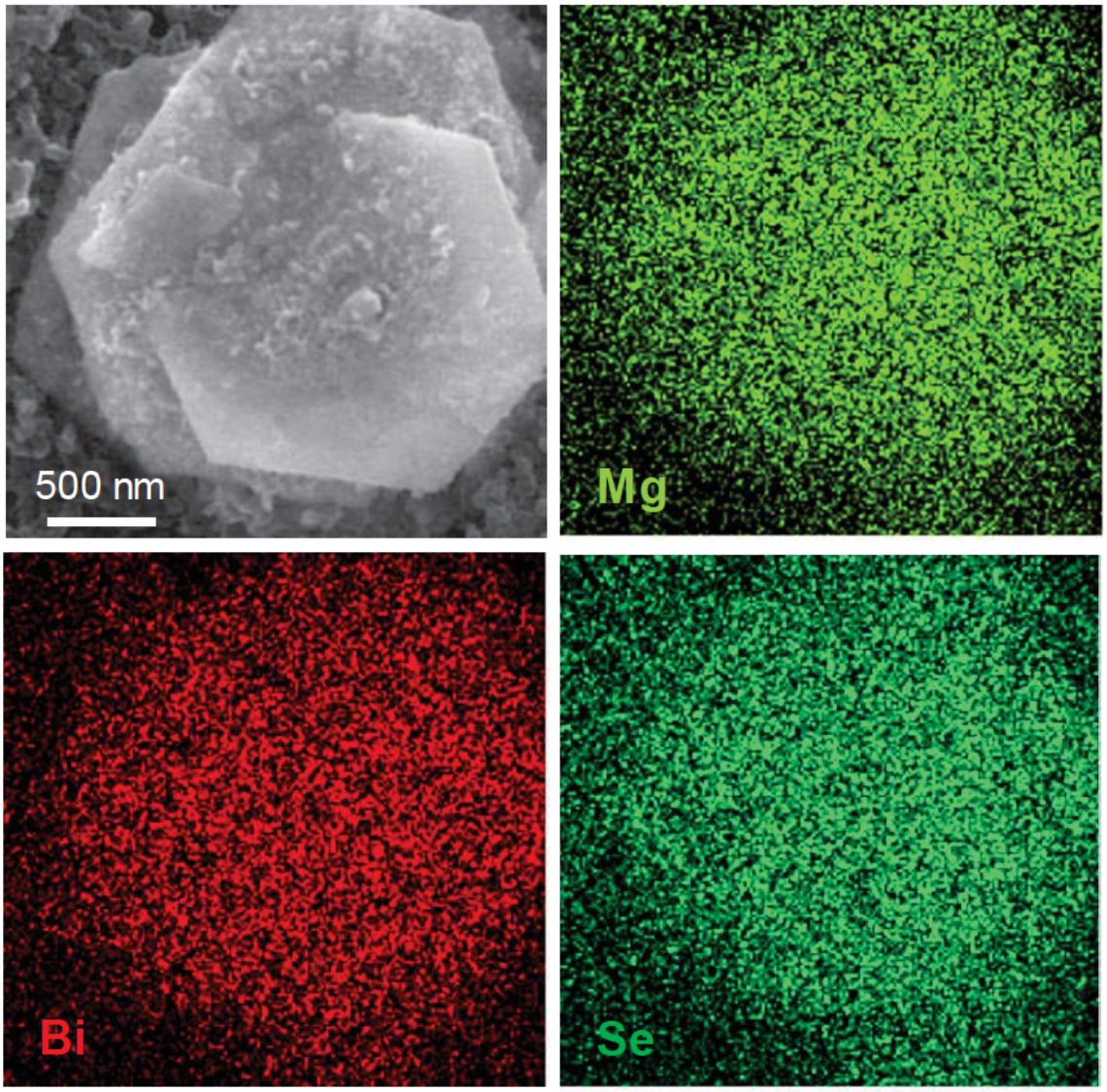

Figure S17. SEM image and the corresponding element mappings of Mg, Bi and Se for BS-Bi electrode at fully discharge state.

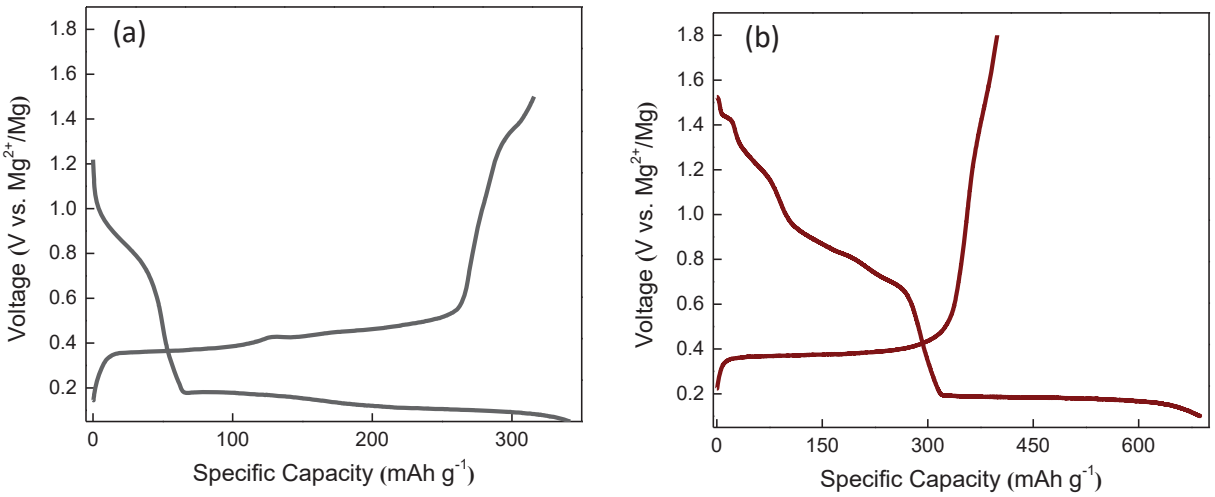

Figure S18. The discharge/charge profile of BS-Bi in (a) MLBH and (b) APC-LiCl hybrid electrolyte at current density of 0.1 A g^{-1} with different cut-off voltage for the second cycle. The reversible phase evolution from Bi to Bi_2Se_3 is difficultly proceed in hybrid system even with high upper cut-off voltage.

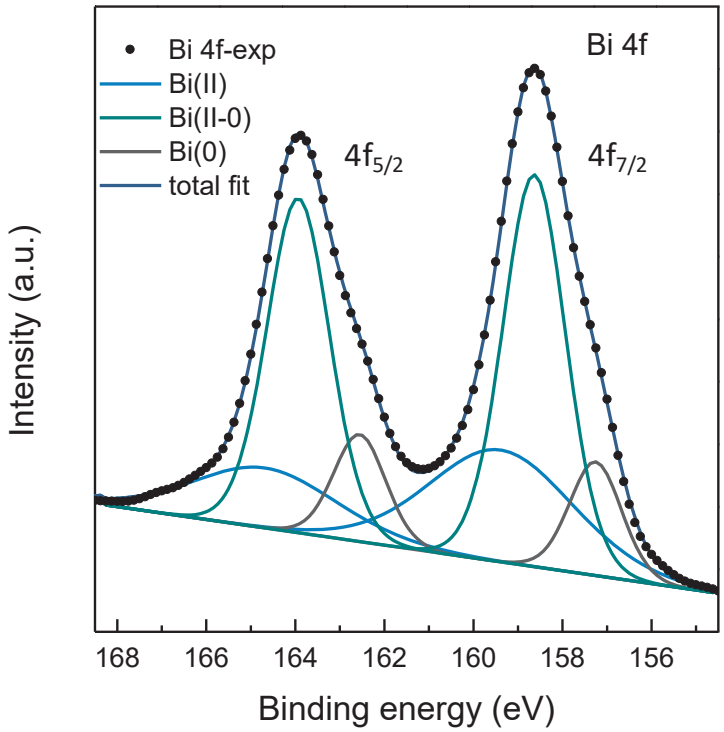

Figure S19. XPS deconvolution of Bi 4f doublet peak at the discharge state of 0.75 V.

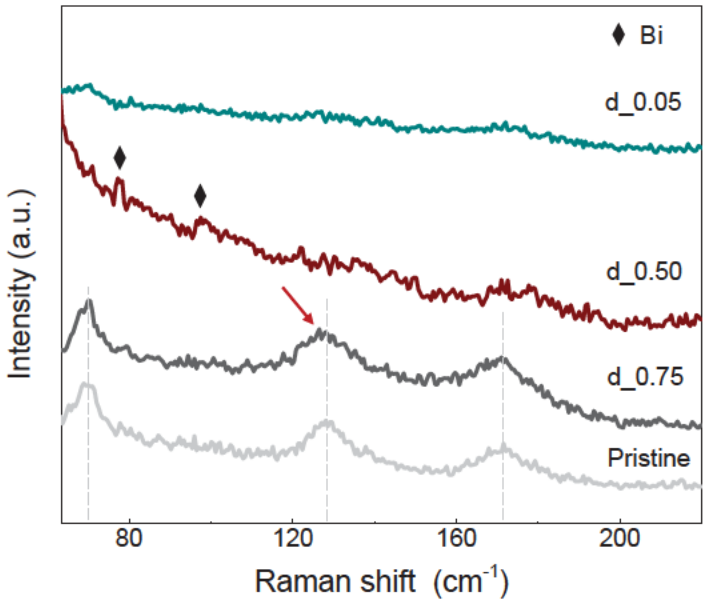

Figure S20. Ex-situ Raman spectrums of the BS-Bi electrode at pristine and discharge states of 0.75 V, 0.50 V, and 0.05 V for the first cycle.

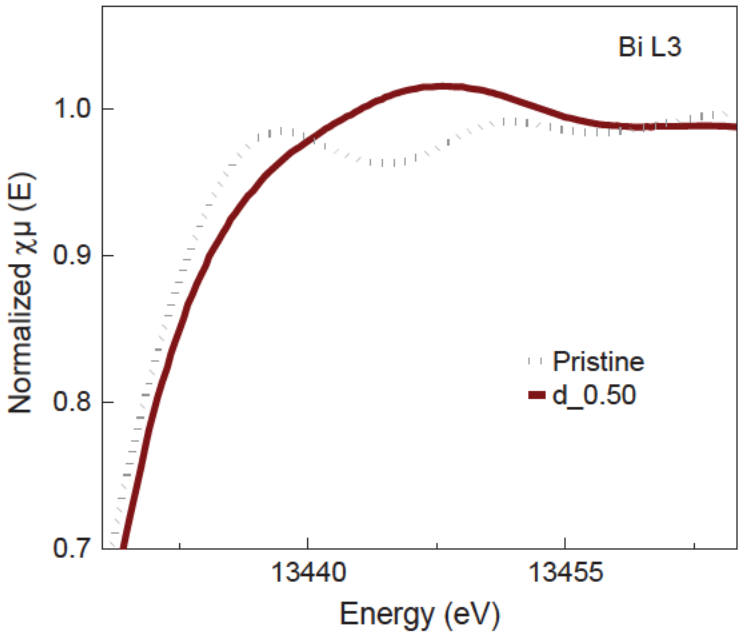

Figure S20. XAS spectrums (Bi L3) of pristine BS-Bi electrode and at discharging states of 0.50 V.

Figure S21. Bi L3-edge XAS of the BS-Bi electrode at pristine and discharge state of 0.50 V.

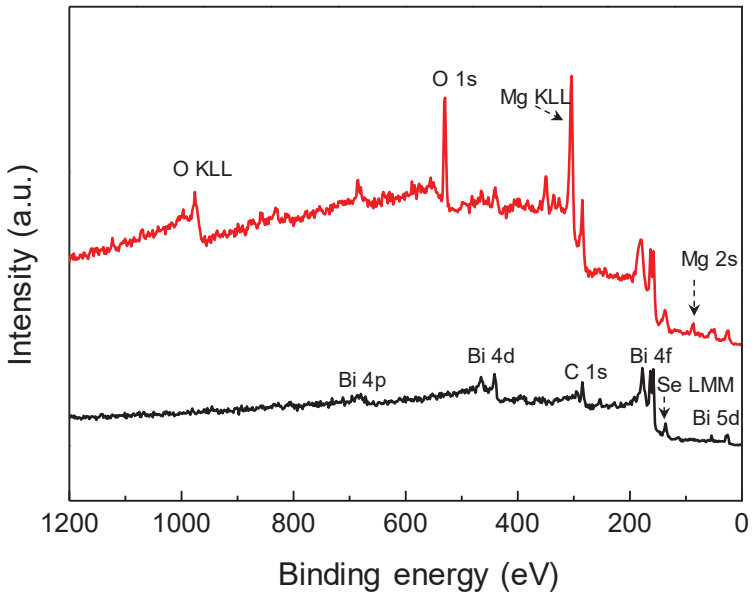

Figure S22. Full XPS of the pristine (black) and fully discharge (red) BS-Bi electrode.

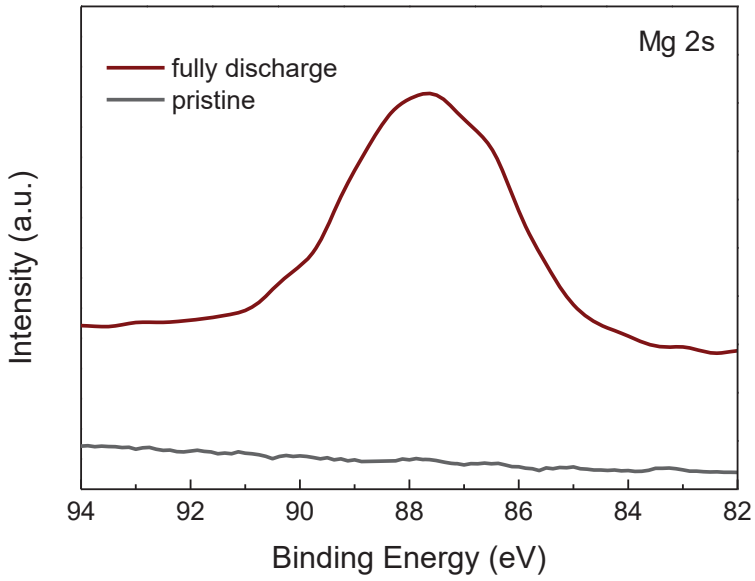

Figure S23. High-resolution XPS of Mg 2s for pristine and fully discharge BS-Bi electrode.

Table S1. Comparison of the cycling stability and specific capacity of bismuth-based materials for RMBs

Anode materials	Capacity (mAh g^{-1})	Cycles	Rate	Reference
BS-Bi	309	200	1000 mA g^{-1}	This work
BS-Bi	293	300	1000 mA g^{-1}	This work
Bi	222	100	0.01C	[3]
Bi nanotubes	303	200	unknown	[4]
Micrometric Bi	300	50	790 mA g^{-1}	[5]
InBi	280	100	C/20	[6]
Nanoporous Bi_6Sn_4	280	200	200 mA g^{-1}	[7]
Nanocluster Mg_3Bi_2	263	200	500 mA g^{-1}	[8]
BiOF	185	100	unknown	[9]
Porous Bi_3Sn_2	301	200	1000 mA g^{-1}	[10]

Table S2. Lattice parameters for the DFT models and the compounds from initial electrochemical conversion.

	Lattice parameters (Å)			Crystal system	Band gap (eV)
	a	b	c		
Bi_2Se_3	4.14	4.14	28.63	hexagonal	0
BiSe	4.27	4.27	23.85	hexagonal	0
Bi_4Se_3	4.32	4.32	41.04	hexagonal	0
m-Bi	4.659	4.659	6.457	monoclinic	0

Table S3. Quantitative analysis results of deconvolution of the Bi 4f doublet peak at discharge state of 0.75 V for the initial cycle.

State	Bi (II)	Bi (II-0)	Bi (0)
Content (%)	30.1	55.8	14.1

Supplemental References

[1] L. Q. Li, C. Tang, B. Q. Xia, H. Y. Jin, Y. Zheng, S. Z. Qiao, *ACS Catal.* **2019**, 9, 2902.

[2] B. Ravel, M. Newville, *J. Synchrotron Radiat.* **2005**, 12, 537.

[3] T. S. Arthur, N. Singh, M. Matsui, *Electrochem. Commun.* **2012**, 16, 103.

[4] Y. Shao, M. Gu, X. Li, Z. Nie, P. Zuo, G. Li, T. Liu, J. Xiao, Y. Cheng, C. Wang, J. G. Zhang, J. Liu, *Nano Lett.* **2014**, 14, 255.

[5] F. Murgia, L. Stievano, L. Monconduit, R. Berthelot, *J. Mater. Chem. A* **2015**, 3, 16478.

[6] F. Murgia, L. Monconduit, L. Stievano, R. Berthelot, *Electrochim. Acta* **2016**, 209, 730.

[7] J. Niu, H. Gao, W. Ma, F. Luo, K. Yin, Z. Peng, Z. Zhang, *Energy Storage Mater.* **2018**, 14, 351.

[8] Y. H. Tan, W. T. Yao, T. Zhang, T. Ma, L. L. Lu, F. Zhou, H. B. Yao, S. H. Yu, *ACS Nano* **2018**, 12, 5856.

[9] W. Wang, L. Liu, P. F. Wang, T. T. Zuo, Y. X. Yin, N. Wu, J. M. Zhou, Y. Wei, Y. G. Guo, *Chem. Commun.* **2018**, 54, 1714.

[10] J. Niu, K. Yin, H. Gao, M. Song, W. Ma, Z. Peng, Z. Zhang, *Nanoscale* **2019**, 11, 15279.

Chapter 5: Initiating Jahn-Teller Effect in Vanadium Diselenide for High Performance Magnesium-Based Batteries Operated at -40 ºC

5.1 Introduction and significance

Poor electronic and ionic conductivity of electrode materials at low temperature of -20 ºC and below has significantly impeded the development of batteries for cold conditions. Here, we report for the first time that layer-structured metallic vanadium diselenide (1T-VSe_2) as a cathode material for low-temperature Mg^{2+}/Li^{+} hybrid batteries. We demonstrate a high electronic conductivity and fast ion diffusion kinetics for 1T-VSe_2 at selected temperatures, and a highly safe 1T-VSe_2/Mg battery for operation at temperature to -40 ºC. The battery exhibited 97 % capacity retention over 500 cycles, which is amongst the best performances in reported Mg-based batteries. The Jahn-Teller effect in compressed configuration is initiated in 1T-VSe_2 with the change of electronic state on electrochemical intercalation of alkali metal ions. Using combined experiment and theory via operando synchrotron X-ray diffraction, ex situ X-ray absorption spectroscopy and density functional theory (DFT) computation, we confirm that the effect contributes significantly to fast-overall kinetics and structural stability of the electrode. We evidence understanding at an atomic level of the mechanism, which provides valuable guidance in designing high-performance electrode materials for low-temperature batteries. The highlights of this work include:

- **Electronic-state change and Jahn-Teller effect in 1T-VSe_2 -** Metallic 1T-VSe_2 as an electrode for Mg-based hybrid batteries exhibits excellent electronic and ionic conductivity at an ultra-low temperature because intercalation of Li^{+} induces a change in the electronic state of the system, resulting in Jahn-Teller compression in 1T-VSe_2. This

significantly improves the structural stability, electronic conductivity and overall kinetics of the electrode. This is demonstrated *via operando* synchrotron X-ray diffraction, EXAFS and density functional theory (DFT) computation.

- **Excellent electrochemical performance at an ultra-low temperature in Mg-based battery** - A highly-safe 1T-VSe_2/Mg battery was operational at low temperature of -40 ^oC. The battery exhibited a long-term cycling capability with a capacity retention of 97 % over 500 cycles, which is better than present state-of-the-art Mg-based batteries, and outperforms many reported lithium and sodium batteries for low-temperature performance.

5.2 Initiating Jahn-Teller Effect in Vanadium Diselenide for High Performance Magnesium-Based Batteries Operated at -40 ^{o}C

This Chapter is included as it appears as a journal paper submitted by **Xin Xu**, Chao Ye, Dongliang Chao, Kenneth Davey, and Shi-Zhang Qiao. "Initiating Jahn-Teller Effect in Vanadium Diselenide for High Performance Magnesium-Based Batteries Operated at -40 ^{o}C." ***Advanced Energy Materials*, Under review**.

Statement of Authorship

Title of Paper	Initiating Jahn-Teller Effect in Vanadium Diselenide for High Performance Magnesium-Based Batteries Operated at -40 °C
Publication Status	☐ Published ☐ Accepted for Publication ☑ Submitted for Publication ☐ Unpublished and Unsubmitted work written in manuscript style
Publication Details	

Principal Author

Name of Principal Author (Candidate)	Xin Xu		
Contribution to the Paper	Conducted experiments, data curation, formal analysis, investigation, and writing–original draft.		
Overall percentage (%)	70		
Certification:	This paper reports on original research I conducted during the period of my Higher Degree by Research candidature and is not subject to any obligations or contractual agreements with a third party that would constrain its inclusion in this thesis. I am the primary author of this paper.		
Signature		Date	20 October 2022

Co-Author Contributions

By signing the Statement of Authorship, each author certifies that:

i. the candidate's stated contribution to the publication is accurate (as detailed above);

ii. permission is granted for the candidate in include the publication in the thesis; and

iii. the sum of all co-author contributions is equal to 100% less the candidate's stated contr bution.

Name of Co-Author	Chao Ye		
Contribution to the Paper	Supervision, writing–review and editing		
Signature		Date	20 October 2022

Name of Co-Author	Dongliang Chao		
Contribution to the Paper	Supervision, writing–review and editing		
Signature		Date	20 October 2022

Name of Co-Author	Kenneth Davey		
Contribution to the Paper	Analysis, writing–review and editing		
Signature		Date	20 October 2022

Name of Co-Author	Shi-Zhang Qiao		
Contribution to the Paper	Supervision, resources, conceptualization and writing–review and editing		
Signature		Date	20 October 2022

Name of Co-Author			
Contribution to the Paper			
Signature		Date	

Name of Co-Author			
Contribution to the Paper			
Signature		Date	

Name of Co-Author			
Contribution to the Paper			
Signature		Date	

Name of Co-Author			
Contribution to the Paper			
Signature		Date	

Initiating Jahn-Teller Effect in Vanadium Diselenide for High Performance Magnesium-based Batteries Operated at -40 ºC

Xin Xu,[a‡] Chao Ye,[a‡] Dongliang Chao,[b] Kenneth Davey,[a] Shi-Zhang Qiao[a]*

X. Xu, Dr. C. Ye, A/Prof. K. Davey, Prof. S. Z. Qiao
School of Chemical Engineering & Advanced Materials, The University of Adelaide, Adelaide, SA 5005, Australia
E-mail: s.qiao@adelaide.edu.au

Dr. D. L. Chao
Laboratory of Advanced Materials, Shanghai Key Laboratory of Molecular Catalysis and Innovative Materials, Fudan University, Shanghai, 200433, China.
‡ These authors contributed equally to this work.

Abstract: Poor electronic and ionic conductivity of electrode materials at low temperature of -20 ºC and below, has significantly impeded development of batteries for cold conditions. Here however, we report for the first time layer-structured metallic vanadium diselenide (1T-VSe_2) as a cathode material for low-temperature Mg^{2+}/Li^+ hybrid batteries. We demonstrate a high electronic conductivity and fast ion diffusion kinetics for 1T-VSe_2 at selected temperatures, and a highly safe 1T-VSe_2/Mg battery for operation at temperature to -40 ºC. The battery exhibited 97 % capacity retention over 500 cycles, which is better performance than reported Mg-based batteries. The Jahn-Teller effect in compressed configuration is initiated in 1T-VSe_2 with the change of electronic state on electrochemical intercalation of alkali metal ions. Using combined experiment and theory via operando synchrotron X-ray diffraction, ex situ X-ray absorption spectroscopy and density functional theory (DFT) computation, we confirm that the weak Jahn-Teller distortion contributes significantly to fast-overall kinetics, structural stability, and high

electronic conductivity of the electrode. We evidence understanding at an atomic level of the mechanism, that provides valuable guidance in designing high-performance electrode materials for low-temperature batteries.

Keywords: weak Jahn-Teller effect, layered 1T-VSe_2, synchrotron spectroscopy, magnesium-based battery, low-temperature battery

1. Introduction

Batteries are significantly important in 'green energy' as a power source for electronic devices. Highly significant capacity loss at sub-zero temperature limits application. This is a result of poor electronic and ionic conductivity because of sluggish charge transfer and slow metal-ion mobility in the bulk materials. Research has therefore focused on electrode materials for low-temperature (low-temp) battery performance.[1-3] There are however limited electrode materials without modifications that are suitable for operating temperature less than -20 ^{o}C. Methods including, surface engineering and molecular structural design have been proposed. However, modified electrode materials, such as Prussian blue analogues (PBAs), layer oxide $LiNi_{1-x-y}Co_xMn_yO_2$ and spinel-type $LiMn_2O_4$ are still with unsatisfied performance at a temperature less than -25 ^{o}C.[4-7] This is caused mainly by insufficient electronic/ionic conductivity, and structural degradation of electrode materials. An improved understanding of the mechanism at atomic level is therefore needed.

The Jahn-Teller (J-T) effect, a geometric distortion of a non-linear molecular system, has been reported with practical consequence in electrode materials with rechargeable lithium, sodium and potassium batteries.[8-11] J-T effect is associated with electronic states and arrangement of atoms in molecular complexes, or ionic lattices, which significantly impacts structural stability,

electronic conductivity and ion diffusion kinetics of electrode materials.[12] The electrode materials, including the complexes of Mn^{3+} (d^4), Cr^{2+} (d^4) in high-spin configurations and Ni^{3+} (d^7), Co^{2+} (d^7) in low-spin configurations, exhibit strong J-T distortion. The strong distortion causes severe structural deformation and results in poor cycling stability.[13, 14] The occurrence of a weak J-T distortion can not only maintain a stable structure but also adjust electronic and ionic conductivity of electrode materials during cycling. Therefore, a weak J-T effect is expected to enhance the low-temperature performance of the battery with good temperature tolerance.

Vanadium diselenide (VSe_2) is a typical member of transition metal dichalcogenides (TMDs) with sandwich-structured Se-V-Se layers stacking together *via* van der Waals interaction, and exhibits a metallic-character in 1T phase (1T-VSe_2).[15-17] The conductivity of 1T-VSe_2 nanosheets is up to 10^6 S m^{-1}, a value comparable with metals.[18] Importantly, 1T-VSe_2 exhibits reduced electrical resistivity (Ω) with decreasing temperature.[19, 20] These properties make it a promising electrode material for low temperature. 1T-VSe_2 has been reported with a distorted crystal structure on electrochemical intercalation of Li^+.[21] The complexes of V^{4+} (V^{3+}) with d^1 (d^2) electronic configuration exhibit a weak J-T distortion. However, unlike the strong distortion in the complexes of Mn^{3+} and Ni^{3+}, the weak J-T distortion in 1T-VSe_2 remains poorly understood, and, significantly, 1T-VSe_2 as a cathode at low temperature is rarely reported.

Here, we report for the first time 1T-VSe_2 as the cathode for low-temp Mg-based hybrid (Mg^{2+}/Li^+) batteries. The Mg-based hybrid battery combines the tetrahydrofuran (THF)-containing electrolyte which has a low melting point (-108 ^oC) and viscosity with a Mg metal anode. Mg-foil is used as the pure metal anode, that can be readily recycled and is dendrite-free.[22] It is acknowledged that lithium metal batteries usually exhibit poor electrochemical capabilities and safety risks due to the formation of Li dendrites at low temperature. Mg-based hybrid batteries

outperform conventional lithium metal batteries with better safety and low-temp performance. The designed 1T-VSe_2/Mg hybrid battery in this work exhibits long-term cyclability with capacity retention of 97 % over 500 cycles and 92.2 % of its room temperature (RT, 25 ^oC) capacity at -20 ^oC. The 1T-VSe_2 electrode without special modification can withstand low temperature to -40 ^oC. Significantly, this is the reported 'best' cycling and low-temp capabilities with Mg-based batteries. Findings from combined *operando* synchrotron X-ray powder diffraction (XRD), *ex-situ* X-ray absorption spectroscopy (XAS), density functional theory (DFT) computations and electrochemical spectroscopies confirm, 1) occurrence of J-T compression and 2) an ultra-stable lattice structure in 1T-VSe_2 on electrochemical intercalation of Li^+, 3) high electronic and ionic conductivity of the electrode, and 4) excellent low-temp performance of the newly designed battery.

2. Results and discussion

Synthesis and structural characterization of 1T-VSe_2. VSe_2 was synthesized *via* direct reaction of vanadium and selenium powders at 550 ^oC in a vacuum-sealed, borosilicate glass tube (**Fig. S1**). XRD patterns presented in **Fig. 1a** are indexed to the single-phase of hexagonal VSe_2 with a space group of P-3m1 (JCPDS card No. 89-1641). The lattice parameters, a(b) = 3.356 Å and c = 6.108 Å were obtained through the Rietveld refinement using TOPAS software. VSe_2 as a typical layered TMDs material has a single, sandwich repeat-unit with V atoms in an octahedral configuration. The sandwiched Se-V-Se layers are perpendicular to the c-axis, whilst V-V chains along the a and b axis form a network structure of the ab-plane (**Fig. S2**). Scanning electron microscopy (SEM) images of VSe_2 are presented in **Fig. 1b** (and **Figs. S3a-S3c**). The layered structure is observed from the cross-section of the bulk material. The transmission electron microscopy (TEM) images, **Fig. 1c** (and **Fig. S3d**) show a lattice fringe of 0.26 nm, assigned to the (0 1 1) crystallographic

plane of VSe_2. The configuration of the material is verified by the Raman spectrum, **Fig. 1d**. A distinct Raman peak at *ca*. 205 cm^{-1} corresponds to the out-of-plane active A_{1g} mode for 1T-VSe_2.[19, 23] These findings evidence that the as-synthesized bulk VSe_2 is of high quality and an 1T (octahedral) phase with metallic character. Following electrode fabrication, the XRD pattern of the prepared 1T-VSe_2 electrode exhibited an enhanced intensity of (0 0 *l*) peaks, **Fig. 1e**, confirming the formation of a layer-by-layer assembled 1T-VSe_2 thin film with preferred crystalline orientation along [0 0 1] axis.

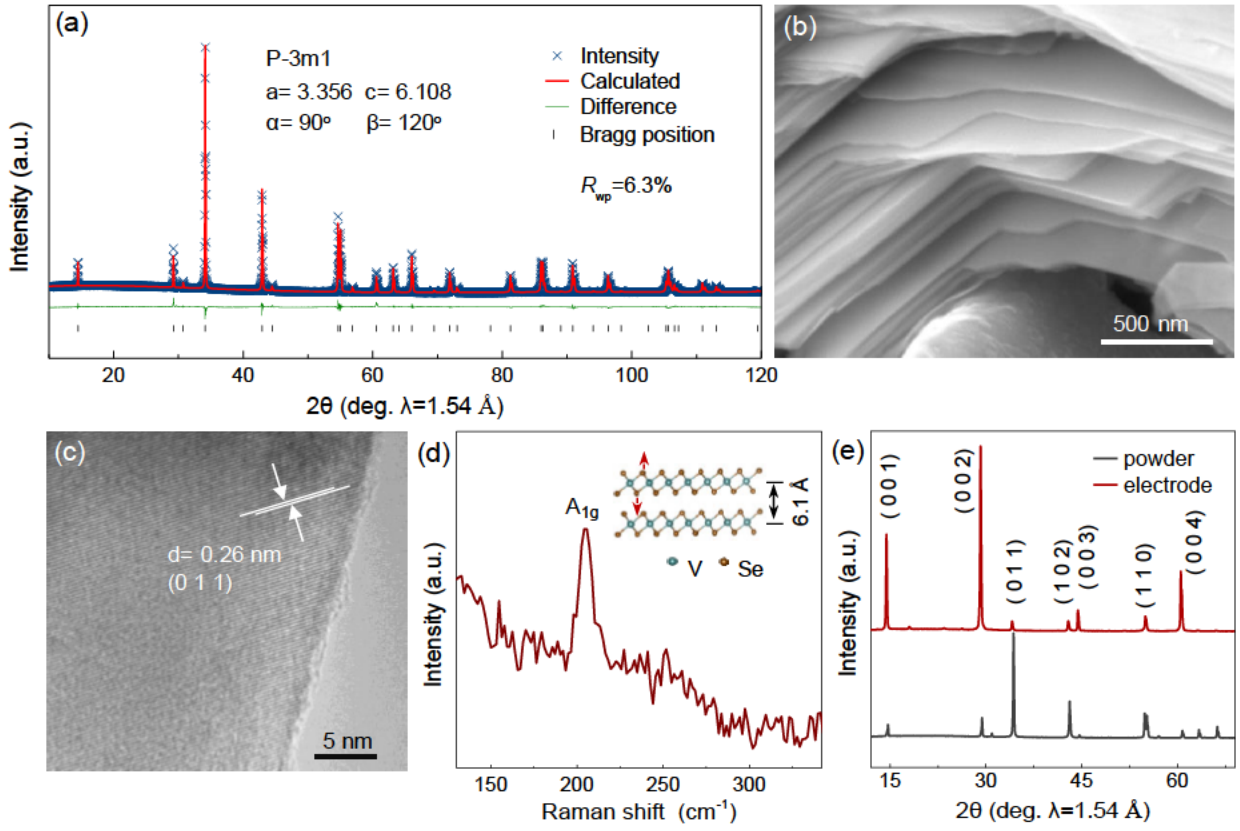

Figure 1. Crystal structure and morphology for 1T-VSe_2. (a) Rietveld refinement X-ray diffraction data (laboratory-based) for 1T-VSe_2 powder with reliability factor (R_{wp}) of 6.3 %. (b) SEM and HRTEM (c) images of 1T-VSe_2. (d) Raman spectrum for 1T-VSe_2 powder. (Inset is schematic for A_{1g} vibrational mode of 1T-VSe_2, blue and red coloured spheres represent V and Se atoms, respectively. (e) XRD pattern for powder sample and prepared electrode of 1T-VSe_2.

Jahn-Teller compression captured via extended X-ray absorption fine structure (EXAFS) spectroscopy. J-T effect is typically observed in octahedral complexes, where two z (axial) bonds can be either longer (J-T elongation) or shorter (J-T compression) than those of the x and y (equatorial) bonds (**Fig. S4**). An atomic structural analysis *via ex situ* XAS was used to determine the J-T effect. **Fig. 2a** shows the X-ray absorption near edge structure (XANES) of the V K-edge for electrodes at different cut-off potentials, namely L0, L1, L2, and L3, as marked on the inset of the discharge-charge curve. Pristine 1T-VSe_2 electrode (L0) exhibited a weak pre-edge, evidencing a slightly distorted octahedral symmetry of V atoms in the prepared sample.[24] The spectrum changed highly significantly following Li^+ intercalation. As the depth of discharge increased, the intensity of the pre-edge peak from L0, L1 to fully discharged L2, progressively increased, evidencing a growing distortion of V-Se octahedra and promoting a dipole-allowed absorption. **Fig. 2b** and **S5** present the enlarged image of the pre-edge area for L0 and L2, and vanadium oxide references. The increased pre-edge of 1T-VSe_2 on electrochemical intercalation of Li^+ is similar to the vanadium oxide because of decreased coordinate symmetry of centre V atoms.[25] The electrochemical intercalation of alkali metal cations accompanied by the electron transfer, induces a local structural distortion of 1T-VSe_2 in which V coordination symmetry decreases.

Fig. 2c shows the Fourier-transformed (FT) EXAFS spectra for V K-edge for L0 and L2. The pristine electrode exhibits a dominant feature at 2.13 Å that corresponds to the V-Se distance, whilst the peak at 2.74 Å is because of scattering from the nearest V atom. The least-square fit for the FT-EXAFS spectra for L0 are given in **Fig. S6**, and the phase-corrected structural parameters obtained are listed in **Table S1** to show that the original V-Se bond length in pristine 1T-VSe_2 is *ca*. 2.47 Å. The actual distance is 0.3-0.5 Å longer than the observed distance in FT-EXAFS spectra.[26] When discharged to 0.4 V (L2), the spectrum changes significantly and a new dominant

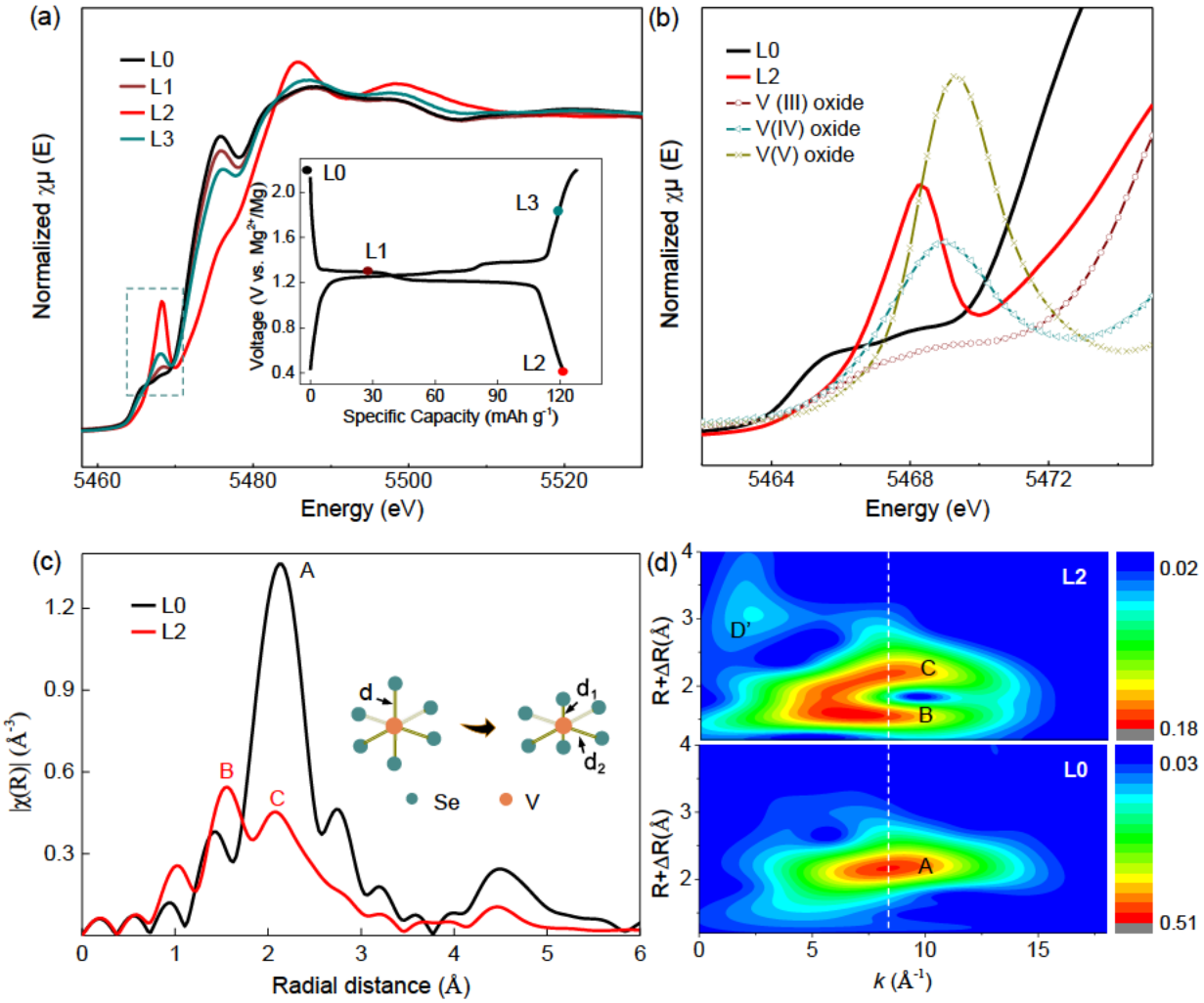

Figure 2. Local structure analysis for V via XAS spectra. (a) XANES spectra for V K-edge at differing potential states during first cycle. Inset is discharge-charge curve. (b) Enlarged pre-edge spectra with reference to vanadium oxides. (c) FT-EXAFS spectra. (Inset: Schematic for 1T-VSe_2 lattice distortion before and following Li^+ intercalation). (d) Wavelet transforms for k^2-weighted EXAFS signals for pristine (L0) and fully discharged (L2) 1T-VSe_2.

peak at 1.55 Å appears. Both peaks at 1.55 and 2.08 Å for the L2 spectrum are assigned to V-Se scattering. To boost the sensitivity of EXAFS analyses, the wavelet transform (WT) was applied to provide a high resolution of the signal features in both *k* and R spaces. The backscattering amplitude factors F(*k*) in *k* space are significantly sensitive to the scattering coordinate atomic

number (Z).[27-29] As is illustrated in **Fig. 2d**, the A, B and C lobs in WT-EXAFS contour plots locate almost at the same *k* value, which is assigned to Se atoms. These findings all evidence that the original V-Se bond splits into two different V-Se bond lengths following electrochemical intercalation of Li^+, as is depicted in the inset of **Fig. 2c**. The newly appeared, shorter V-Se bonds correspond to the shorter z bonds, appearing as a compressed octahedral complex (**Fig. S4**). Therefore, we conclude the electrochemical intercalation of Li^+ initiates J-T compression in 1T-VSe_2.

Phase change with ultra-stable structure identified via operando synchrotron XRD. For the hybrid system, the superior Li^+ mobility takes place in the 1T-VSe_2 cathode, whereas Mg stripping /plating proceeds in the anode (**Fig. S7**). The structural evolution of the 1T-VSe_2 electrode was monitored *via operando* synchrotron XRD, **Fig. 3a** and **S8**. The corresponding discharge-charge curve is shown in the right of **Fig. 3a**, in which an apparent flat plateau is exhibited. The XRD peaks for the pristine electrode (L0) are assigned to 1T-VSe_2 with a space group of P-3m1. The extra peaks, as marked with an asterisk, are from Mg-foil. The Rietveld refinement for the synchrotron data using GSAS II package[30] is based mainly on three major peaks. The peaks from Mg-foil and current collector are excluded. The diffraction pattern for the fully discharged state (L2) is indexed to the $LiVSe_2$ phase that is captured *in situ* during cycling. The 1T-VSe_2 host lattice undergoes a first-order phase transition on Li^+ intercalation which corresponds to the flat plateau of the discharge-charge curve. The newly formed $LiVSe_2$ has almost the same hexagonal structure as for 1T-VSe_2, but exhibits increased lattice parameters in a, b and c, as all peaks shift toward lower angles following Li^+ intercalation. **Fig. 3b** and **S9** show selected individual XRD patterns including, pristine, fully discharged and fully charged states of the electrode. The peaks corresponding to (0 1 1), (1 0 2) and (1 0 3) planes are shifted back to the original position

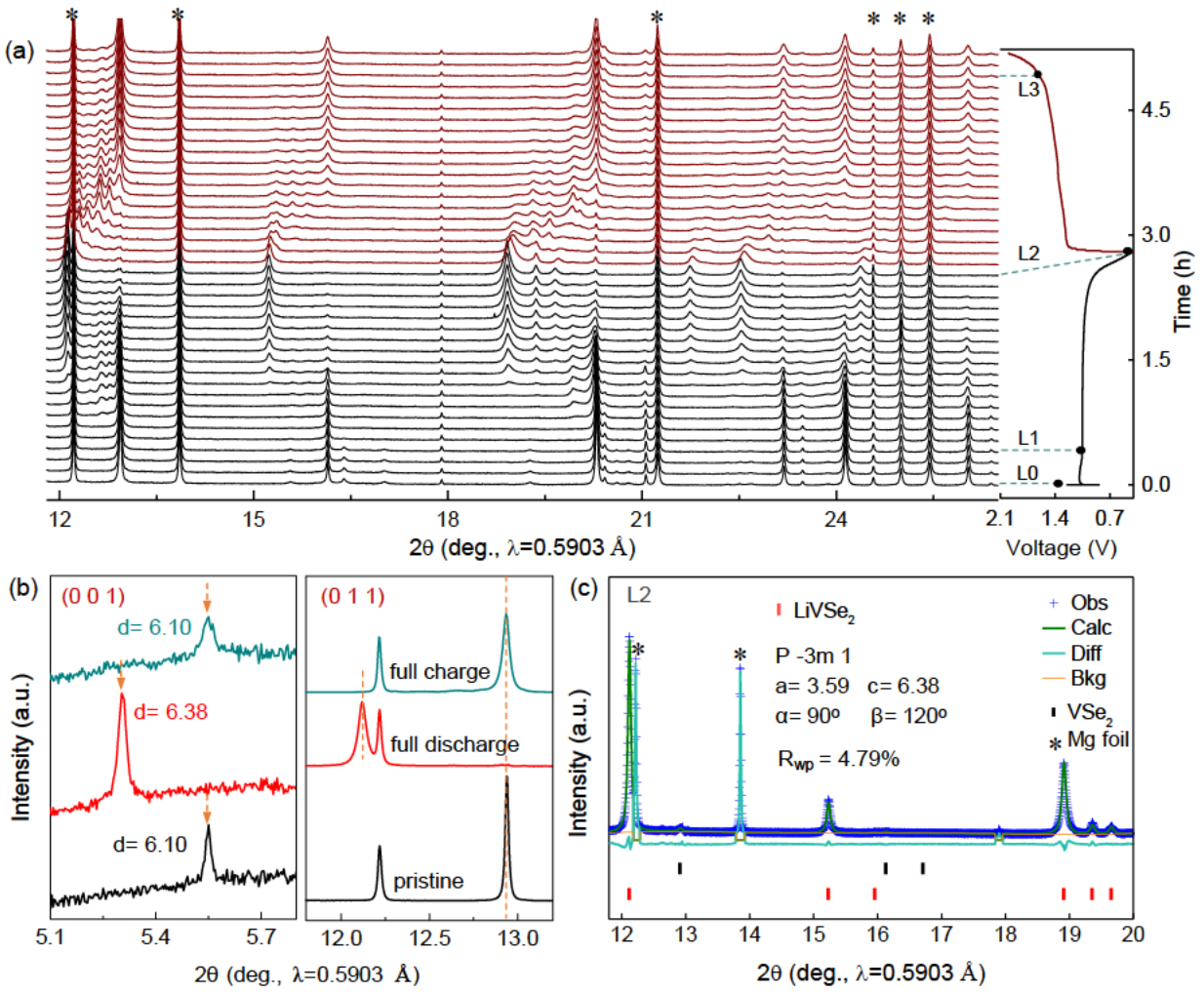

Figure 3. Structural evolution of 1T-VSe_2 electrode. (a) Operando synchrotron diffraction pattern for 1T-VSe_2 and corresponding discharge-charge profile (Peaks marked with an asterisk belong to Mg-foil). (b) Selected individual diffraction pattern and corresponding interlayer distance (Å) were calculated via the Bragg equation. (c) Rietveld refinement from synchrotron XRD data for fully discharged state of 1T-VSe_2 electrode.

following a full cycle, demonstrating a highly reversible process. The interlayer distance change with 1T-VSe_2 was calculated from Bragg's formula ($d = 0.5\lambda / \sin(\theta)$). The calculated distance for pristine 1T-VSe_2 is 6.10 Å, a value that is in line with the Rietveld refinement as c = 6.10 Å (**Fig. S10**). With electrochemical intercalation of Li^+, the calculated interlayer distance has increased to

6.38 Å, corresponding to the refinement result of c = 6.38 Å for a fully discharged state, **Fig. 3c**. The parameter a(b) corresponding to the basal dimension, also increases with Li^+ intercalation, as depicted in **Fig. S11**. The increased a(b) is attributed to the elongated V-V distance because of the electron transfer from intercalated Li^+.[31] The unit cell parameters from the Rietveld refinement for pristine and fully discharged electrodes are summarized in **Table S2**.

It is noteworthy that the percentage expansion value for parameter c following intercalation of Li^+ is less than parameter a(b) in 1T-VSe_2. **Table S3** presents the lattice parameters for 1T-VSe_2 before and following Li^+ intercalation and a summary of lattice parameters for other TMDs. The c/a ratio for 1T-VSe_2 decreases following Li^+ intercalation, which is different from those for other dichalcogenides in groups IV and V with increased c/a ratio. The Δc (difference in c value following and before Li^+ intercalation) for other dichalcogenides, except 2H-MoS_2,[32] is > 0.42 Å (*vs.* 0.28 Å for 1T-VSe_2). As is acknowledged the structure degradation of layered electrode materials is a major obstacle to long-term cyclability. The highly significant difference in Δc can cause irreversible structural damage and capacity fading with foreign ion intercalation. The lattice stability in 1T-VSe_2 with small Δc is achieved *via* the weak J-T (compressed) distortions resulting in the rearrangement of atoms in V-Se complexes with the intercalation of alkali Li^+. The small expansion of the host lattice in the c direction suppresses possible structural collapse and determines the long-term cycling performance of the 1T-VSe_2 electrode.

1T-VSe_2/Mg batteries operated at ultra-low temperature. 1T-VSe_2 was assessed as a cathode for Mg^{2+}/Li^+ hybrid batteries at selected temperatures. The magnesium-aluminium chloride complex (MACC) with the addition of LiCl in THF was used as the hybrid electrolyte. 1T-VSe_2 exhibits a negligible capacity in electrolyte without Li-salt (**Fig. S12**). It confirms that the cathode is dominated by Li^+ intercalation/de-intercalation. The electrochemical performance for 1T-VSe_2

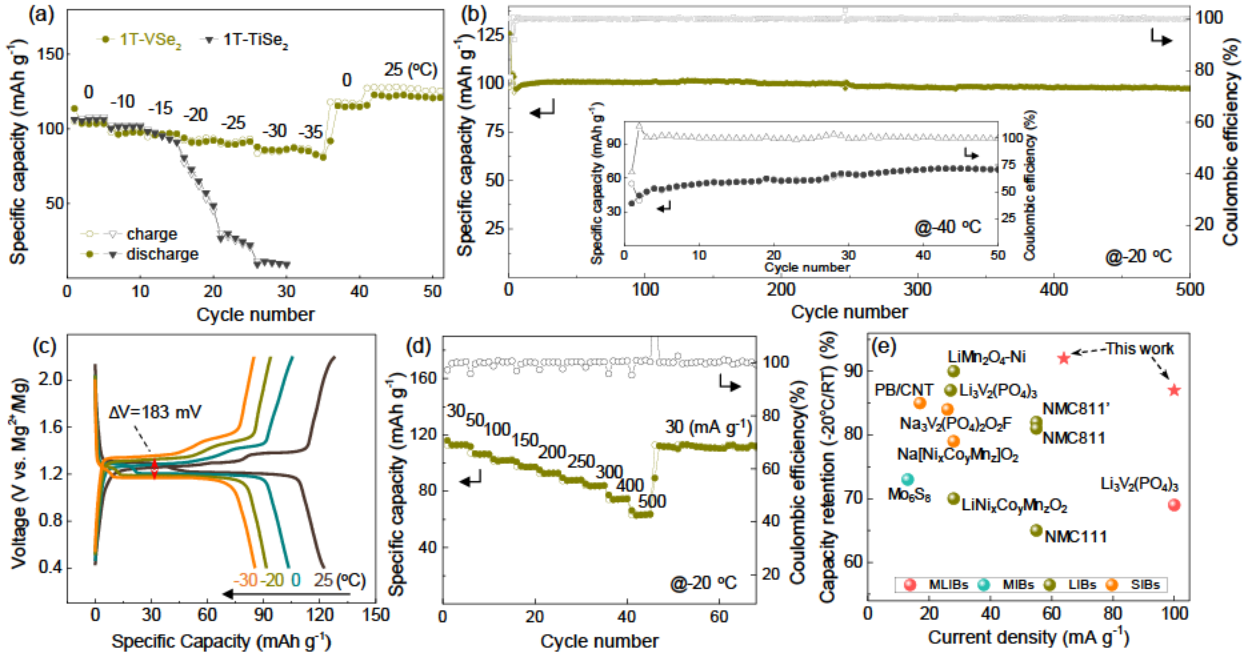

Figure 4. Electrochemical performance for 1T-VSe_2 over a temperature range -40 to 25 °C. (a) Temperature-dependent rate capability for 1T-VSe_2 and 1T-$TiSe_2$. (b) Cycling performance at current density 100 mA g^{-1} at -20 °C. The initial three cycles were activated at current density 50 mA g^{-1}. Inset is cycling performance at a temperature -40 °C and current density 50 mA g^{-1}. (c) Discharge-charge curves for 1T-VSe_2 at selected temperatures. (d) Rate capability for 1T-VSe_2 at -20 °C. (e) Comparison of capacity retention at -20 °C (normalized to that for RT) between 1T-VSe_2 and reported cathode materials for different battery systems, namely, Mg^{2+}/Li^+ hybrid batteries (MLIBs), magnesium-ion batteries (MIBs), lithium-ion batteries (LIBs) and sodium-ion batteries (SIBs).

with hybrid electrolyte at RT is shown in **Figs. S13-S14**. The galvanostatic discharge-charge curves exhibit a stable capacity output, little polarization together with a flat discharge plateau at high current density 500 mA g^{-1}. The flat curves correspond to a two-phase behaviour that is significantly different from other members of TMDs,[33] (**Fig. S15**). With 1T-$TiSe_2$ as the control sample, its detailed structural information and electrochemical properties at RT are given in **Figs. S16-S17**. Because of the low melting point of THF (-108 °C, **Table S4**), the hybrid electrolyte

remains fluid, even as low as -80 ^{o}C (**Fig. S18**). **Fig. 4a** shows the temperature-dependent rate performance for 1T-VSe_2 and 1T-$TiSe_2$. 1T-VSe_2 is operational at temperature to -35 ^{o}C. In contrast, with temperature decreasing the capacity of 1T-$TiSe_2$ decreases significantly at -20 ^{o}C. At low temperature -20 ^{o}C, **Fig. 4b**, (and **Fig. S19**), 1T-VSe_2 exhibited a high initial discharge capacity of 126 mAh g^{-1} and a low capacity decay rate of 0.007 % per cycle (101 – 97.5 mAh g^{-1} over 500 cycles) at 100 mA g^{-1}. The battery exhibited 92.2 % of the RT capacity at 64 mA g^{-1} (0.5C, 1C as 128 mA g^{-1}) (**Fig. S20**). At an ultra-low temperature of -40 ^{o}C, 1T-VSe_2 retained a discharge capacity of 68.5 mAh g^{-1}, inset **Fig. 4b**. The discharge-charge curves for 1T-VSe_2, **Fig. 4c**, (and **Fig. S21**) exhibit a flat discharge plateau even at -30 ^{o}C, together with a significantly low polarization of 183 mV. The high rate performance for 1T-VSe_2 at -20 ^{o}C is confirmed as is presented in **Fig. 4d**. The electrode material without modification is capable of operation at a high current density 500 mA g^{-1} (~ 4C) at -20 ^{o}C, evidencing excellent low-temp kinetics. The designed 1T-VSe_2/Mg battery exhibited best electrochemical performance in rechargeable Mg batteries for stability and low-temp rate performance. Importantly, it outperforms most reported lithium and sodium batteries at -20 ^{o}C, **Fig. 4e** (**Table S5**).

To establish the origin of the electrochemical performance of 1T-VSe_2 at low temperature, the electronic conductivity and ion diffusion kinetics of the electrode was assessed *via* electrochemical spectroscopies at selected temperatures. Electrochemical impedance spectroscopy (EIS) was used to monitor battery impedance from 40 to -30 ^{o}C, **Fig. 5a**. Fitted results with corresponding equivalent circuit for 1T-VSe_2 are presented in **Fig. S22** and **Table S6**. R_s is the series ohmic resistance of the battery, involving resistance of the electrolyte, and other ohmic contacts and elements in the battery. R_{ct} is the resistance of charge transfer corresponding to the semicircle of

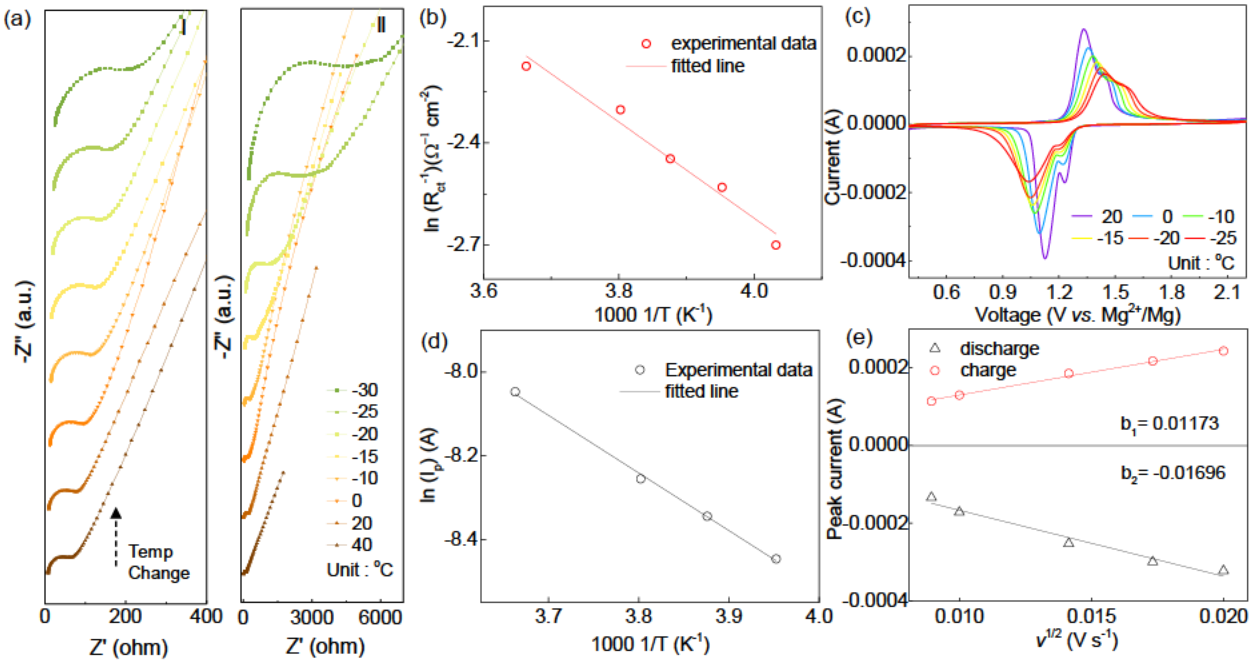

Figure 5. Electronic conductivity and ion diffusion kinetics for 1T-VSe_2 at low temperature. (a) Electrochemical impedance spectroscopy for (I) 1T-VSe_2 and (II) 1T-$TiSe_2$ at selected temperatures. (b) Arrhenius plot for charge transfer resistance of 1T-VSe_2. (c) CV curves at differing temperature, and (d) Arrhenius plot for peak current for 1T-VSe_2. (e) Linear relationship between peak current and square root of scan rate based on CV curves for 1T-VSe_2 at -20 °C.

the high-frequency portion in EIS. As is presented in **Fig. 5a** (I), with temperature decreasing, R_{ct} for 1T-VSe_2 undergoes an increase from 45 Ω (20 °C) to 136 Ω (-30 °C). However, R_{ct} for 1T-$TiSe_2$ highly significantly increases, to some thousands of ohms, and R_s increases significantly to 230.2 Ω (*vs.* 24.6 Ω for 1T-VSe_2) at -30 °C (**Fig. 5a** (II) and **Fig. S23**). Although 1T-$TiSe_2$ shares the character of 1T phase and layered structure of 1T-VSe_2, it exhibits a semi-metallic-character.[34, 35] 1T-$TiSe_2$ as a semi-metal exhibits increasing resistance with decreasing temperature in the range 300-165 K.[36] At low temperature, the increased resistance of 1T-$TiSe_2$ significantly limits charge transfer of the reaction, resulting in a significantly increased value for R_{ct}. When temperature is switched back to 20 °C, the electrical resistance of both samples returns to a low value (**Fig. S24**).

1T-$TiSe_2$ is more susceptible to the temperature change than 1T-VSe_2. The inferior low-temp performance for 1T-$TiSe_2$ is caused by rapidly increased overall resistance with temperature decrease. Whilst 1T-VSe_2 as metallic material reduces resistivity when cooled.[18-20, 37] And the varied electronic states perform high electronic conductivity on cycling with the initiation of J-T effect.

The change in charge transfer resistance with temperature is largely determined by the activation energy (E_a). According to the Arrhenius relationship (Eq. S1), the E_a for the charge transfer of 1T-VSe_2 derives from the slope of the $\ln(1/R_{ct})$ *versus* the inverse of temperature (1/T). As is shown in **Fig. 5b**, the calculated value for E_a from charge transfer resistance is 0.12 eV. *Via* another method, by fitting the peak current (I_p), which is measured from cyclic voltammetry (CV) curves (**Fig. 5c**) at varying temperature into the Arrhenius equation (Eq. S2), the same value for E_a of 0.12 eV is obtained, **Fig. 5d**. Importantly, the calculated value for E_a in this work is significantly less than reported with Li^+ intercalation.[2, 38] The low threshold energy barrier for the charge transfer for 1T-VSe_2 evidences the fast reaction kinetics of the electrode that significantly boosts low-temp performance. The excellent cyclability and rate capability of the electrode at different temperatures is expected from high ion diffusion kinetics. The ion diffusion coefficients for 1T-VSe_2 are calculated based on the Randles-Sevcik equation (Eq. S3). CV measurements, for scanning rates from 0.08 to 0.4 mV s^{-1} were conducted at both RT (**Fig. S25**) and -20 ^oC (**Fig. S26**). The calculated diffusion coefficient at RT is 1.67×10^{-9} cm^2 s^{-1} which is *ca*. two orders of magnitude greater than reported.[39-42] At a low temperature of -20 ^oC (**Fig. 5e**), 1T-VSe_2 continues to exhibit a high diffusion coefficient of 1.7×10^{-10} cm^2 s^{-1}. The fast ion diffusion kinetics and high electronic conductivity of 1T-VSe_2 are directly associated with the J-T effect because of the change in electronic states and local atomic structures to give the excellent low-temp performance of the

battery. It is concluded therefore that 1) 1T-VSe_2 is a practically promising low-temp electrode material, and 2) weak J-T compression with a change in local atomic structures, exhibits a highly significant impact on physical properties of the complex to boost stability, overall kinetics and electronic conductivity of the electrode for excellent performance.

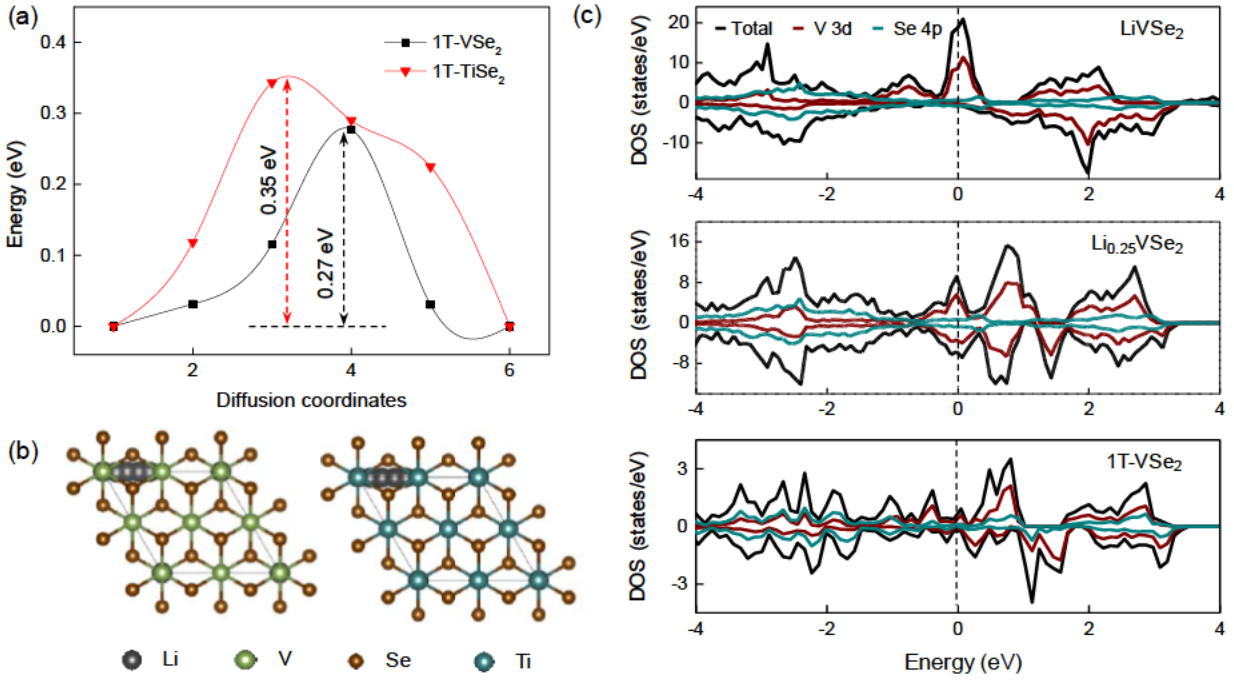

Figure 6. Theoretical computation for 1T-VSe_2 with intercalation of Li^+. (a) Li^+ migration energy barrier profiles for 1T-VSe_2 and 1T-$TiSe_2$. (b) Corresponding Li^+ migration pathways. (c) TDOS for 1T-VSe_2, $Li_{0.25}VSe_2$ and $LiVSe_2$, and corresponding PDOS for V 3d and Se 4p.

Elucidating electronic states and Jahn-Teller effect via theoretical computation. Theoretical computations were performed to confirm kinetics and electronic properties of 1T-VSe_2 on the electrochemical intercalation of Li^+. Li atoms prefer to occupy the octahedral sites in the crystal structure.[21] The computed lowest diffusion energy barriers for both 1T-VSe_2 and 1T-$TiSe_2$ are plotted as **Fig. 6a**, and corresponding migration pathways shown in **Fig. 6b**. 1T-VSe_2 exhibits a lower migration barrier energy of 0.27 eV compared with 1T-$TiSe_2$ 0.35 eV, evidencing a more

ready migration of Li^+ in 1T-VSe_2. **Fig. 6c** presents the computed total density of states (TDOS) for 1T-VSe_2 at varying Li-containing states, together with the partial density of states (PDOS) projected on V and Se atoms. The electrochemical intercalation for each Li^+ is accompanied by one electron transfer to the host, that significantly changes the electronic states of the host, resulting in a weak J-T compression in 1T-VSe_2. Importantly, the product gets more metallic on Li^+ intercalation with significantly increased electronic states around the Fermi level. The improved electronic conductivity of the electrode from 1T-VSe_2 to $LiVSe_2$ results the fast electron transfer and as consequence, boosts two-phase transition with high rate capability at varying temperature. The weak J-T distortion with the change of electronic state boosts electronic conductivity, produces fast overall kinetics, and maintains ultra-stable lattice structures in 1T-VSe_2 to result in excellent low-temp performance of our designed battery.

3. Conclusions

1T-VSe_2 has been demonstrated for the first time as a low-temp cathode in a Mg^{2+}/Li^+ hybrid cell configuration. A 1T-VSe_2/Mg battery is operational at an ultra-low temperature of -40 ^oC. It exhibits a long-term cycling performance with a low capacity decay rate of 0.007 % and performs over 500 cycles. This performance is better than reported Mg-based batteries and many lithium and sodium batteries. Combined *operando* synchrotron X-ray diffraction, *ex situ* X-ray absorption spectroscopy and DFT computations confirm that weak J-T compression occurs and contributes significantly to fast-overall kinetics, structural stability, and high electronic conductivity of 1T-VSe_2 on intercalation/de-intercalation of Li^+. Therefore, electrochemical performance at low temperature is boosted. Using 1T-VSe_2 as a model, evidenced understanding at an atomic level of the J-T effect inspires rational design of new, and optimization of existing electrode materials for low-temp batteries.

Supporting Information

Supporting Information is available from the Wiley Online Library, or from the author.

Acknowledgement

This work was financially supported by the Australian Research Council (ARC) through Discovery and Linkage projects (FL170100154, DP220102596, LP210301397). The authors acknowledge support from the Powder Diffraction and X-ray Absorption Spectroscopy beamline at the Australian Synchrotron, ANSTO, Melbourne. DFT computations were undertaken with the assistance of resources and services from the National Computational Infrastructure (NCI) and Phoenix High Performance Computing, that are supported by the Australian Government and The University of Adelaide. The authors thank Drs. Bernt Johannessen and Qinfen Gu for, respectively, assistance with XAS and PD. We also thank Junnan Hao, Shiying Ren, Chun-Chuan Kao, Huan Li and Gemeng Liang from The University of Adelaide for helpful discussion.

Conflict of Interest

The authors declare no conflict of interest.

Received: ((will be filled in by the editorial staff))
Revised: ((will be filled in by the editorial staff))
Published online: ((will be filled in by the editorial staff))

References

[1] X. Dong, Y. Yang, B. Wang, Y. Cao, N. Wang, P. Li, Y. Wang, Y. Xia, *Adv. Sci. (Weinh.)* **2020**, 7, 2000196.

[2] W. Zhang, X. Sun, Y. Tang, H. Xia, Y. Zeng, L. Qiao, Z. Zhu, Z. Lv, Y. Zhang, X. Ge, S. Xi, Z. Wang, Y. Du, X. Chen, *J. Am. Chem. Soc.* **2019**, 141, 14038.

[3] X. Dong, Z. Guo, Z. Guo, Y. Wang, Y. Xia, *Joule* **2018**, 2, 902.

[4] Y. You, H. R. Yao, S. Xin, Y. X. Yin, T. T. Zuo, C. P. Yang, Y. G. Guo, Y. Cui, L. J. Wan, J. B. Goodenough, *Adv. Mater.* **2016**, 28, 7243.

[5] Z. Sun, Z. Li, L. Gao, X. Zhao, D. Han, S. Gan, S. Guo, L. Niu, *Adv. Energy Mater.* **2018**, 9, 1802946.

[6] R. Qin, Y. Wei, T. Zhai, H. Li, *J. Mater. Chem. A* **2018**, 6, 9737.

[7] X. Zheng, Z. Gu, J. Fu, H. Wang, X. Ye, L. Huang, X. Liu, X. Wu, W. Luo, Y. Huang, *Energy Environ. Sci.* **2021**, 14, 4936.

[8] Y. Shang, X. Li, J. Song, S. Huang, Z. Yang, Z. J. Xu, H. Y. Yang, *Chem* **2020**, 6, 1804.

[9] G. Azzolina, H. Tokoro, K. Imoto, M. Yoshikiyo, S. I. Ohkoshi, E. Collet, *Angew. Chem. Int. Ed.* **2021**, 60, 23267.

[10] Z. Xiao, F. Xia, L. Xu, X. Wang, J. Meng, H. Wang, X. Zhang, L. Geng, J. Wu, L. Mai, *Adv. Funct. Mater.* **2021**, 32, 2108244.

[11] X. Li, X. Ma, D. Su, L. Liu, R. Chisnell, S. P. Ong, H. Chen, A. Toumar, J. C. Idrobo, Y. Lei, J. Bai, F. Wang, J. W. Lynn, Y. S. Lee, G. Ceder, *Nat Mater* **2014**, 13, 586.

[12] H. A. Jahn, E. Teller, *Proc. R. Soc. A* **1997**, 161, 220.

[13] Y. Shang, X. Li, J. Song, S. Huang, Z. Yang, Z. J. Xu, H. Y. Yang, *Chem* **2020**, 6, 1804.

[14] A. Choi, T. Kim, M. H. Kim, S. W. Lee, Y. H. Jung, H. W. Lee, *Adv. Funct. Mater.* **2022**, 32, 2111901.

[15] R. Shao, S. Chen, Z. Dou, J. Zhang, X. Ma, R. Zhu, J. Xu, P. Gao, D. Yu, *Nano Lett.* **2018**, 18, 6094.

[16] C. Yang, J. Feng, F. Lv, J. Zhou, C. Lin, K. Wang, Y. Zhang, Y. Yang, W. Wang, J. Li, S. Guo, *Adv. Mater.* **2018**, 30, 1800036.

[17] Y. Yi, X. Du, Z. Zhao, Y. Liu, H. Guan, X. Liu, X. Pei, S. Zhang, D. Li, *ACS Nano* **2022**, 16, 7772.

[18] Z. Zhang, J. Niu, P. Yang, Y. Gong, Q. Ji, J. Shi, Q. Fang, S. Jiang, H. Li, X. Zhou, L. Gu, X. Wu, Y. Zhang, *Adv. Mater.* **2017**, 29, 1702359.

[19] K. Xu, P. Chen, X. Li, C. Wu, Y. Guo, J. Zhao, X. Wu, Y. Xie, *Angew. Chem. Int. Ed.* **2013**, 52, 10477.

[20] M. Hossain, J. Wu, W. Wen, H. Liu, X. Wang, L. Xie, *Adv. Mater. Interfaces* **2018**, 5, 1800528.

[21] M. S. Whittingham, *Mater. Res. Bull.* **1978**, 13, 959.

[22] R. Attias, M. Salama, B. Hirsch, Y. Goffer, D. Aurbach, *Joule* **2019**, 3, 27.

[23] D. Li, X. Wang, C. M. Kan, D. He, Z. Li, Q. Hao, H. Zhao, C. Wu, C. Jin, X. Cui, *ACS Appl. Mater. Interfaces* **2020**, 12, 25143.

[24] L. Zhang, D. Sun, J. Kang, H. T. Wang, S. H. Hsieh, W. F. Pong, H. A. Bechtel, J. Feng, L. W. Wang, E. J. Cairns, J. Guo, *Nano Lett.* **2018**, 18, 4506.

[25] J. Wong, F. W. Lytle, R. P. Messmer, D. H. Maylotte, *Phys. Rev. B.* **1984**, 30, 5596.

[26] Y. N. Zhou, J. Ma, E. Hu, X. Yu, L. Gu, K. W. Nam, L. Chen, Z. Wang, X. Q. Yang, *Nat. Commun.* **2014**, 5, 5381.

[27] J. Timoshenko, A. Kuzmin, *Comput. Phys. Commun.* **2009**, 180, 920.

[28] V. L. Sushkevich, O. V. Safonova, D. Palagin, M. A. Newton, J. A. van Bokhoven, *Chem. Sci.* **2020**, 11, 5299.

[29] J. Hao, L. Yuan, B. Johannessen, Y. Zhu, Y. Jiao, C. Ye, F. Xie, S. Z. Qiao, *Angew. Chem* **2021**, 133, 25318.

[30] B. H. Toby, R. B. Von Dreele, *J. Appl. Crystallogr.* **2013**, 46, 544.

[31] A. Thompson, J. Scanlon, C. Symon, *Solid State Ion.* **1980**, 1, 47.

[32] M. S. Whittingham, F. R. Gamble, *Mater. Res. Bull.* **1975**, 10, 363.

[33] M. S. Whittingham, *Prog. Solid State Chem.* **1978**, 12, 41.

[34] O. Anderson, R. Manzke, M. Skibowski, *Phys. Rev. Lett.* **1985**, 55, 2188.

[35] Y. Gu, Y. Katsura, T. Yoshino, H. Takagi, K. Taniguchi, *Sci. Rep.* **2015**, 5, 12486.

[36] F. J. Di Salvo, D. E. Moncton, J. V. Waszczak, *Phys. Rev. B.* **1976**, 14, 4321.

[37] A. H. Thompson, B. G. Silbernagel, *Phys. Rev. B.* **1979**, 19, 3420.

[38] X. H. Rui, Y. Jin, X. Y. Feng, L. C. Zhang, C. H. Chen, *J. Power Sources* **2011**, 196, 2109.

[39] X. Xu, C. Ye, D. Chao, B. Chen, H. Li, C. Tang, X. Zhong, S. Z. Qiao, *Adv. Mater.* **2021**, 34, 2108688.

[40] A. V. Churikov, A. V. Ivanishchev, I. A. Ivanishcheva, V. O. Sycheva, N. R. Khasanova, E. V. Antipov, *Electrochim. Acta* **2010**, 55, 2939.

[41] H. Xia, L. Lu, G. Ceder, *J. Power Sources* **2006**, 159, 1422.

[42] C. Huang, S.-X. Zhao, H. Peng, Y.-H. Lin, C.-W. Nan, G.-Z. Cao, *J. Mater. Chem. A* **2018**, 6, 14339.

Table of contents

A highly-safe 1T-VSe_2/Mg battery was operational at low temperature of -40 °C. Metallic 1T-VSe_2 as an electrode for Mg-based hybrid batteries exhibits excellent electronic and ionic conductivity at an ultra-low temperature because intercalation of Li^+ induces change in the electronic state of the system, resulting in weak Jahn-Teller compression in 1T-VSe_2. This significantly improves structural stability, electronic conductivity and overall kinetics of the electrode. This is demonstrated via operando synchrotron X-ray diffraction, extended X-ray absorption fine structure (EXAFS) and density functional theory (DFT) computation.

Xin Xu,[a‡] Chao Ye,[a‡] Dongliang Chao,[b] Kenneth Davey,[a] Shi-Zhang Qiao[a*]

Initiating Jahn-Teller Effect in Vanadium Diselenide for High Performance Magnesium-based Batteries Operated at -40 °C

ToC figure

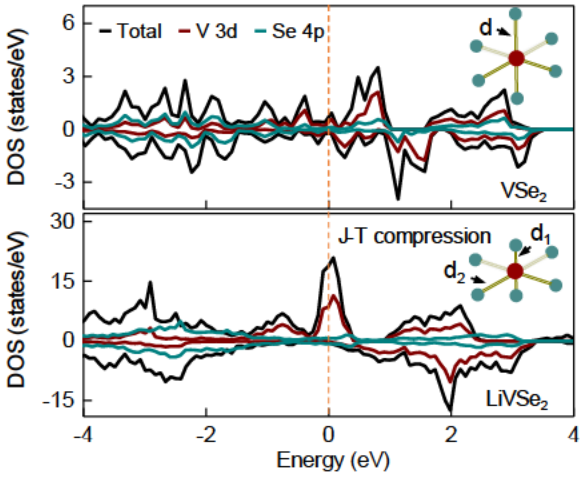

Supporting Information

Initiating Jahn-Teller Effect in Vanadium Diselenide for High Performance Magnesium-based Batteries Operated at -40 ºC

Xin Xu,[1] Chao Ye,[1] Dongliang Chao,[2] Kenneth Davey,[1] Shi-Zhang Qiao[1]*

[1] School of Chemical Engineering and Advanced Materials, The University of Adelaide, SA 5005, Australia. Email: s.qiao@adelaide.edu.au

[2] Laboratory of Advanced Materials Shanghai Key Laboratory of Molecular Catalysis and Innovative Materials, Fudan University, Shanghai 200433, China

Experimental Section

Synthesis of 1T-VSe_2 and 1T-$TiSe_2$. 1T-VSe_2 was prepared *via* direct reaction of vanadium (V) and selenium (Se) powders at a high temperature in a vacuum-sealed glass tube. In a typical synthesis, V (48 mg) and Se (150 mg) powders in molar ratio 1:2 were sealed in a borosilicate glass tube under vacuum and calcined at 550 ^oC for 8 h. The heating rate was 2 $^oC\ min^{-1}$. The calcined sample may contain trace V_2O_3 and unreacted selenium caused by relatively low vacuum. To obviate residual selenium, the sample was heat-treated at 400 ^oC for 0.5 h in Ar with a flow rate of 120 cc min^{-1} in a tube-furnace. The sample was thoroughly washed with 20 % (v/v) diluted nitric acid for 30 min at room temperature (RT, 25 ^oC) to obtain a single phase 1T-VSe_2. 1T-$TiSe_2$ was prepared using thin Ti-foil (99.9 %, 3 mm thick) and Se powder and applying the same vacuum calcination method as preparation for 1T-VSe_2.

Preparation of electrolyte. All chemicals for electrolyte preparation were purchased from Sigma Aldrich. The solvent tetrahydrofuran (THF, anhydrous, ≥ 99.9 %) was dried with activated 3 Å molecular sieves over 12 h before use. Anhydrous $MgCl_2$, $AlCl_3$, and LiCl were purchased and used as received. Typically, $MgCl_2$ (19 mg) was added to 1 ml THF and stirred overnight at RT. $AlCl_3$ (26.7 mg) powder was slowly added to another 1 ml THF to minimize formation of poly-THF. The $AlCl_3$/THF solution was added, dropwise, into $MgCl_2$/THF solution with stirring overnight at 40 ^oC to obtain a clear solution. Five (5) mg Mg powder was added and stirred for an additional 2 h at RT to obtain 0.1 M magnesium-aluminium chloride complex (MACC) electrolyte. With addition of 1.0 M LiCl (84.8 mg) with stirring at RT to complete dissolution, the Mg^{2+}/Li^+ hybrid electrolyte was prepared, and was ready to be used. All procedures were carried out in an Ar-filled glove box (H_2O < 0.5 ppm and O_2 < 0.5 ppm).

Characterization. The morphology of the sample was analysed *via* FEI Quanta 450 FEG scanning electron microscopy (SEM) and transmission electron microscopy (TEM, Philips, CM200). X-ray diffraction (XRD) patterns for sample powders were collected from the X-ray diffractometer (Bruker, D8 ADVANCE ECO) at 40 kV and 25 mA using Cu-Kα radiation (λ = 0.15418 nm). The diffraction data from D8 were analysed with the Rietveld method using TOPAS (Bruker) software package. Raman spectroscopy was performed using a confocal Raman microscope (Horiba Scientific, LabRAM HR evolution) with a 50X objective, and signals were recorded *via* a 532 nm laser. *Ex situ* synchrotron X-ray absorption spectroscopy (XAS) measurements were conducted at the Australian Synchrotron (ANSTO), Melbourne. The data obtained were analysed and processed with Athena and Artemis software. All samples

for *ex situ* characterizations were thoroughly rinsed with THF to remove soluble species on the surface of the electrode.

***Operando* synchrotron X-ray diffraction.** *Operando* synchrotron XRD for the first cycle was collected with an exposure time of 30 s from the powder diffraction beamline, Australia Synchrotron, with a wavelength (λ) 0.5903 Å. Home-made 2032 coin cells were used for data collection. Both sides of the cell cases were punched with a 5 mm hole in the centre, and sealed with Kapton film as the beam entrance. To fully take advantage of facility time for data collection, the four-position cells arrangement is employed where high-rate discharge/charge are not required. These cells are connected with a Neware battery tester which enables the control of electrochemistry for each cell while the cell is tested through the beam and a data set is collected. XRD data from the synchrotron were refined with the Rietveld method using GSAS II software.[1]

Electrochemical test. Electrochemical performance was determined in the 2032 type coin-cell. To fabricate electrodes, the synthesized 1T-VSe_2 powder (or 1T-$TiSe_2$), carbon black (> 99 %, Alfa Aesar) and polytetrafluoroethylene (PTFE) binder (6 % aqueous solution, Sigma-Aldrich) were mixed with a mass ratio 80:10:10. The mixture was ground in an agate mortar with several drops of ethanol and rolled into a free-standing film. Following drying in vacuum at 80 °C for 10 h, the sample was cut into (small) pieces with a mass loading *ca*. 1.0 mg, and pasted on stainless steel mesh. Polished Mg-foil and Whatman™ glass fibre were used as, respectively, anode and separator. Galvanostatic cycling tests between 0.4 - 2.2 V were performed on Neware and Land battery testing systems. The coin-cell was rested for 12 h prior to testing. A thermal test chamber (GWS) was used to carry out variable temperature tests. Batteries were pre-cycled for 3 cycles at RT prior to cycling at -40 °C. Cyclic voltammetry (CV) and electrochemical impedance spectroscopy (EIS) data were collected *via* an electrochemical workstation (CHI 760E). EIS test was conducted in the frequency range 1 MHz to 0.01 Hz, with an amplitude of 5 mV.

Determination of diffusion coefficient and activation energy. The activation energy for the electrode was calculated based on the thermally activated process.[2]

$$\frac{1}{R_{ct}} = A_0\, e^{\frac{-E_a}{RT}} \qquad \text{(S1)}$$

$$I_p = A_0\, e^{\frac{-E_a}{RT}} \qquad \text{(S2)}$$

where A_0 is a constant, R the gas constant, T temperature in Kelvin and E_a activation energy. The charge transfer resistance (R_{ct}) and peak current (I_p) were obtained from fitting of data from, respectively, EIS and CV profiles.

The diffusion coefficient for ions was calculated from the Randles-Sevcik equation based on CV profiles, namely:

$$i_p = 0.4463\ nFAC\ (\frac{nFvD}{RT})^{\frac{1}{2}}$$

$$= (4.644 \times 10^6)\ n^{\frac{3}{2}}\ A\ D^{\frac{1}{2}}\ C\ v^{\frac{1}{2}}\ T^{-\frac{1}{2}} \qquad \text{(S3)}$$

in which i_p is the current peak value (A) in CV curves, n number of electrons transferred (one-electron transfer), A the electrode area (cm^2), D diffusion coefficient ($cm^2\ s^{-1}$), v scan rate ($V\ s^{-1}$), R is the gas constant ($8.314\ J\ K^{-1}\ mol^{-1}$), T temperature (K) and C solid concentration ($2.78 \times 10^{-2}\ mol\ cm^{-3}$). The value for D was computed from the slope of I_p- $v^{1/2}$ lines. The electrode area for all samples was 0.16 cm^2.

Computational methods. DFT computations were carried out using the Vienna *Ab-initio* Simulation Package (VASP).[3, 4] The exchange-correlation interaction was described by generalized gradient approximation (GGA) with the Perdew-Burke-Ernzerhof (PBE) functional.[5] The DFT-TS method of Grimme was employed to treat the VDW interaction.[6] All computations were carried out using a plane wave kinetic energy cut-off of 600 eV. All structures in the computations were spin-polarized and relaxed until the convergence tolerance of force on each atom was < 0.01 eV. Energy convergence criteria were set to 10^{-4} eV for self-consistent computations with a Gamma-centred 3 × 3 × 3 K-points. The energy barrier was located *via* searching for transition states by climbing image, nudged-elastic band (CI-NEB) method implemented in VASP. Transition states were obtained *via* relaxing the force < 0.05 eV $Å^{-1}$. Denser 10 × 10 × 10 K-points were used for density of states (DOS) computations.

Supplementary Figures

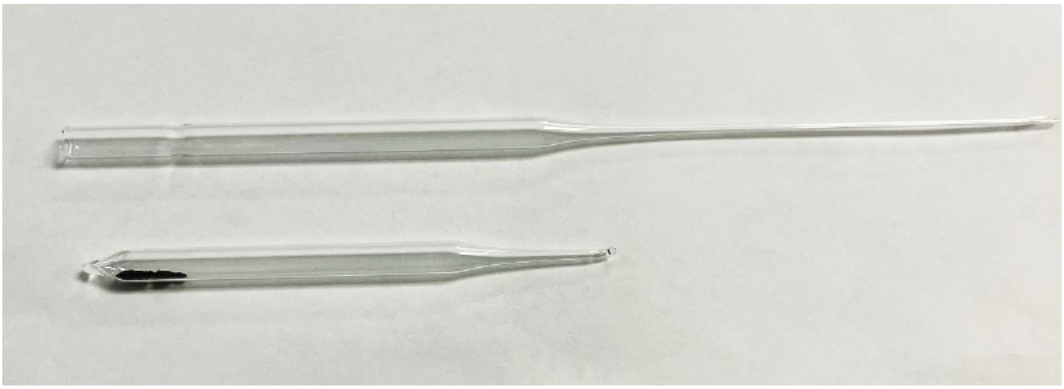

Figure S1. Digital image of vacuum-sealed borosilicate glass tube.

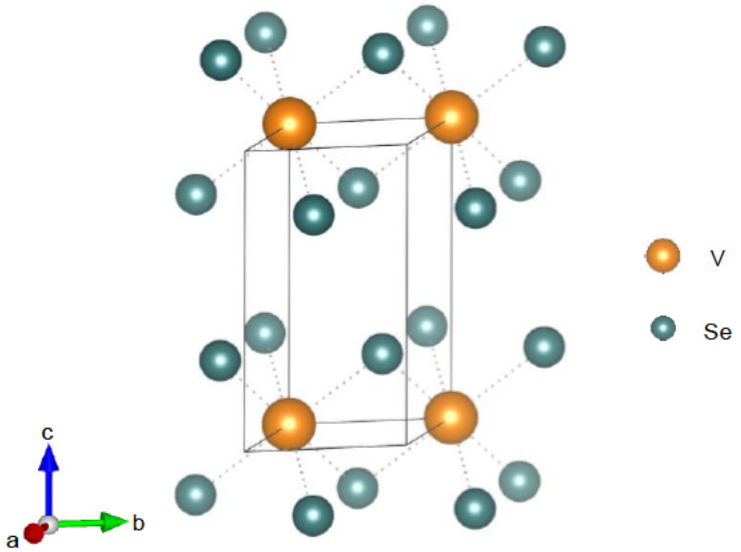

Figure S2. Unit cell structure for 1T-VSe_2.

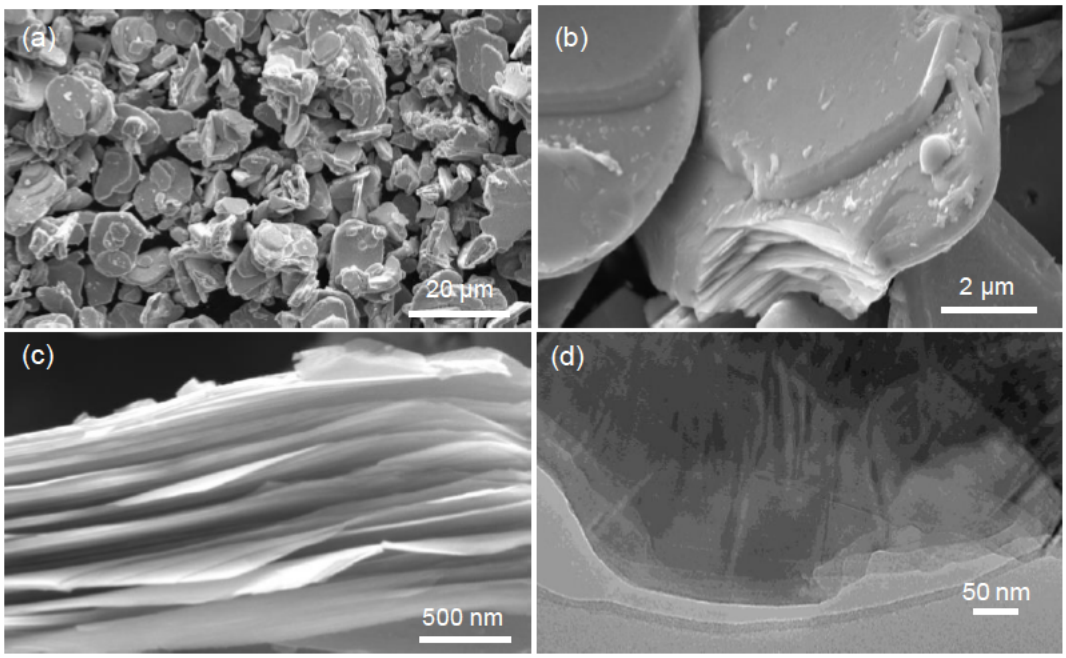

Figure S3. (a-c) SEM images of 1T-VSe_2 at differing magnification. (d) TEM image of 1T-VSe_2.

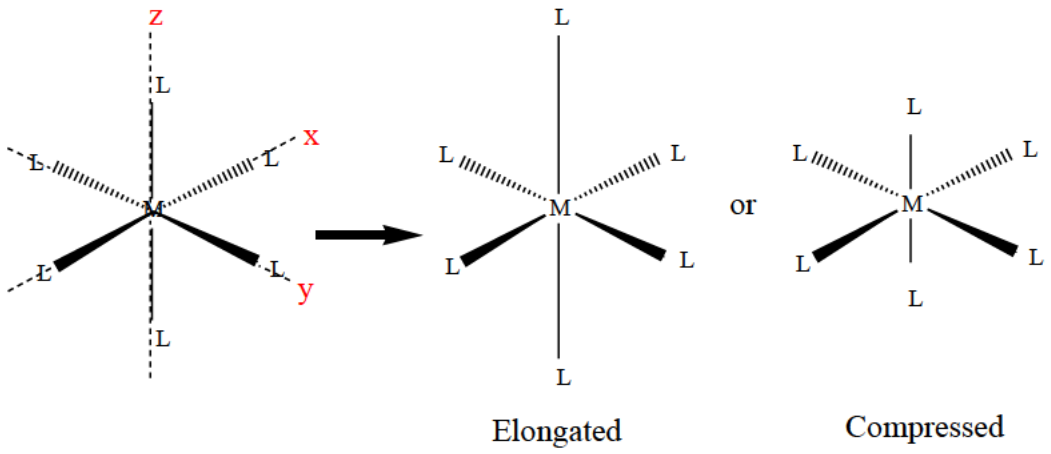

Figure S4. Schematic for tetragonal elongation (positive distortion) and compression (negative distortion) for octahedral complex.

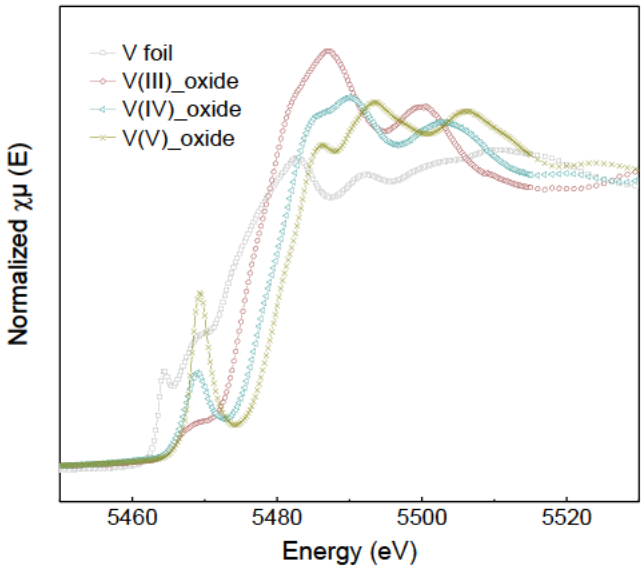

Figure S5. XAS spectra (V K-edge) for vanadium oxide in different valence states and V-foil.

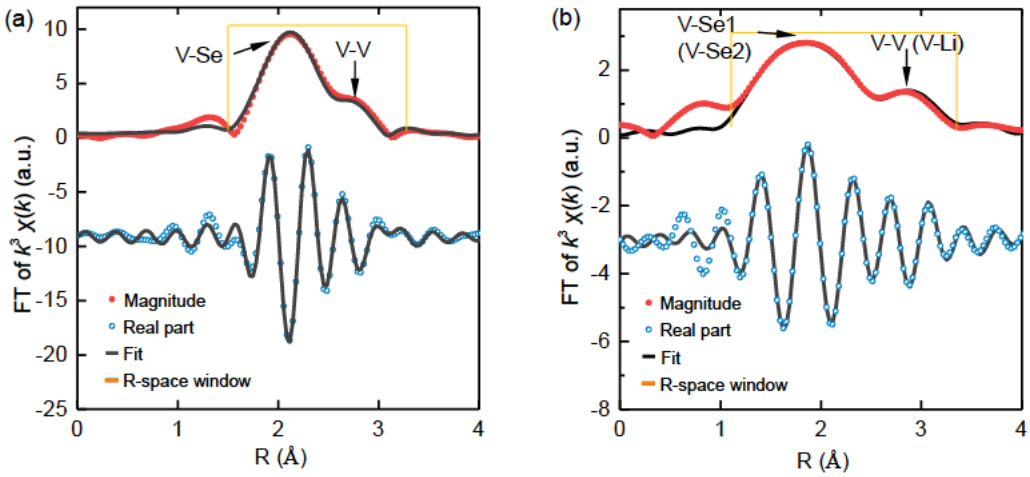

Figure S6. Fourier transform magnitude for experimental and fitted χ(k)*k^3 function for (a) Pristine (L0), and (b) Fully discharged 1T-VSe_2 electrode (L2).

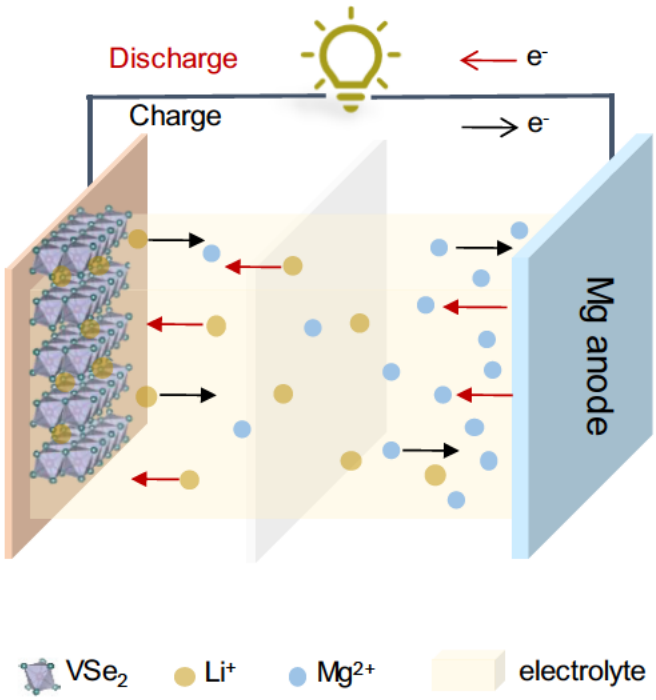

Figure S7. Schematic for working mechanism for Daniell-type Mg^{2+}/Li^{+} hybrid battery.

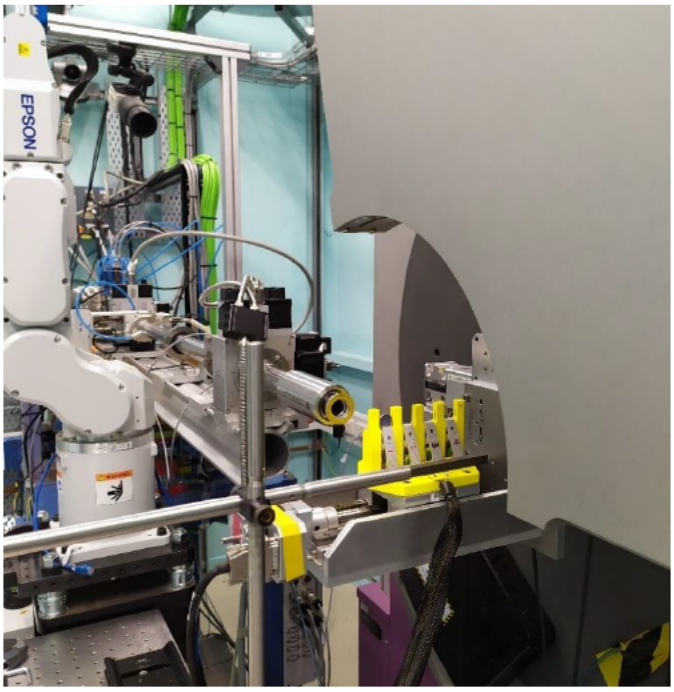

Figure S8. Photo of a synchrotron XRD experimental setup with a four-position modified coin cell battery stage (horizontal) for high throughput operando experiments at Powder Diffraction beamline, Australian synchrotron.

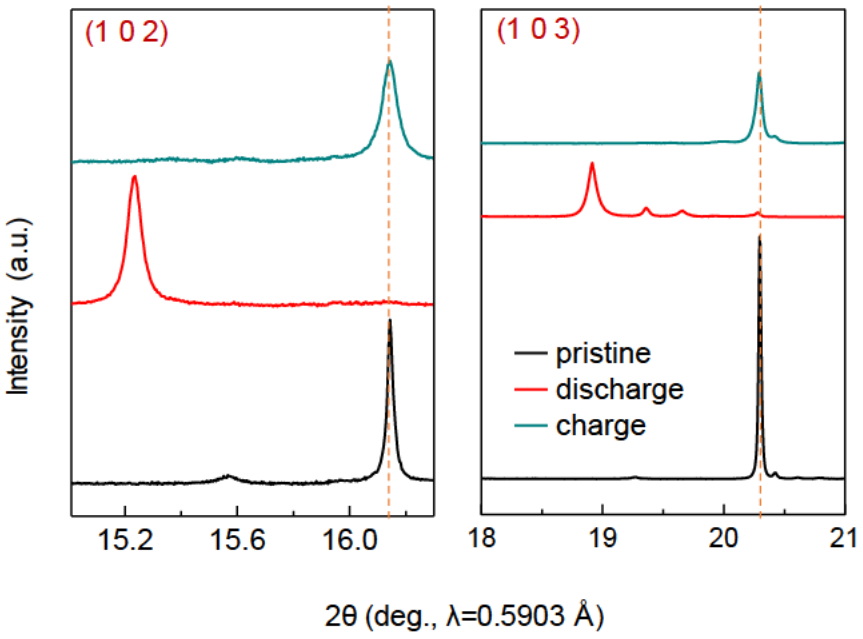

Figure S9. Selected individual synchrotron X-ray diffraction patterns.

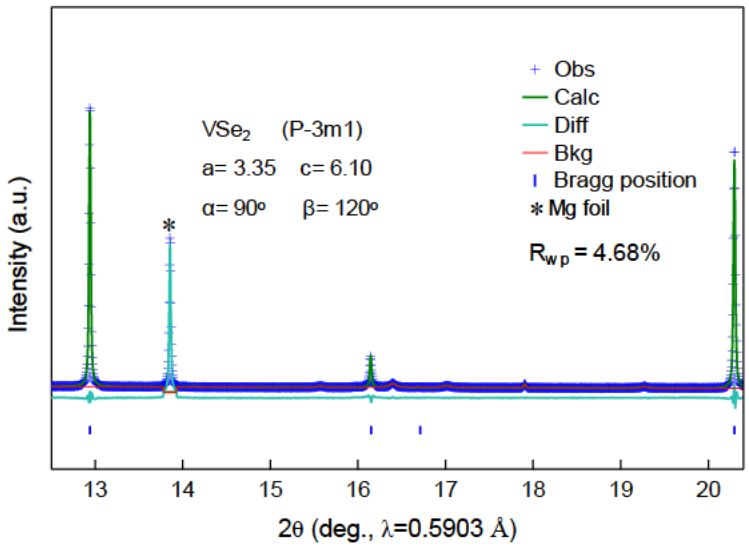

Figure S10. Rietveld refinement of synchrotron X-ray diffraction data for pristine 1T-VSe_2 electrode.

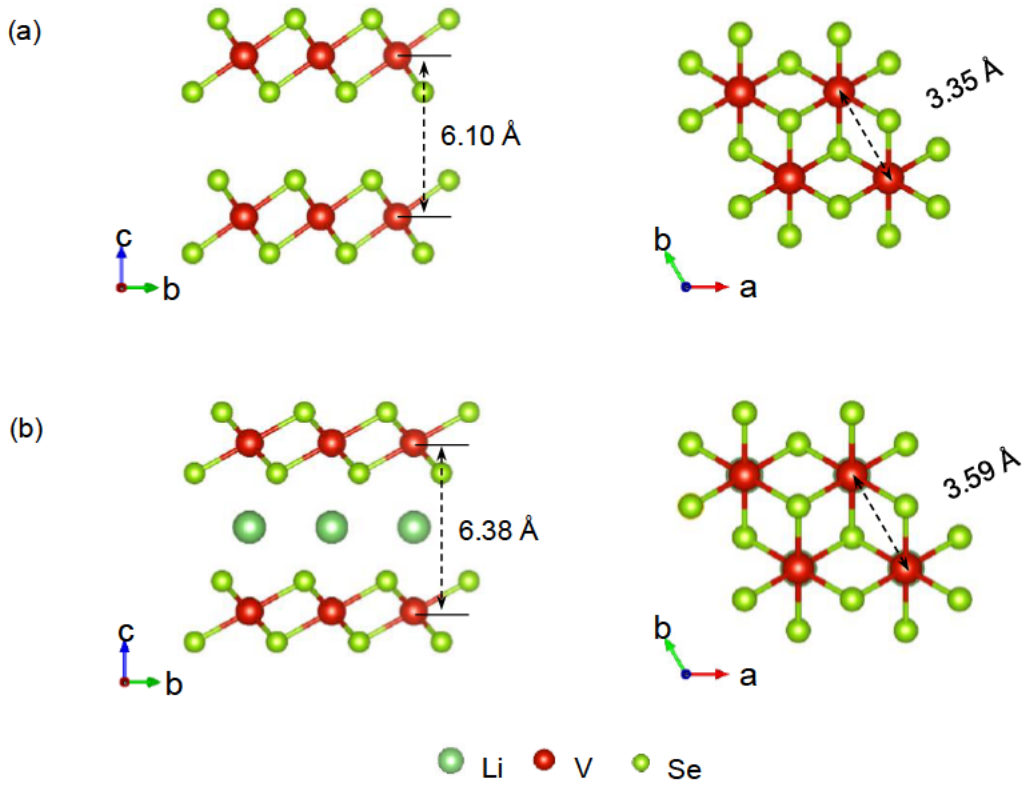

Figure S11. Side (left) and top (right) view of crystal structure of layered (a) 1T-VSe_2 and (b) $LiVSe_2$.

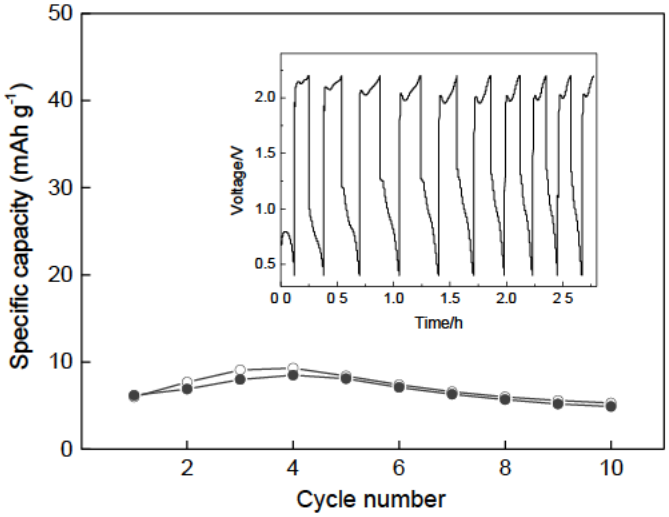

Figure S12. The electrochemical performance of 1T-VSe_2 using electrolyte of MACC without Li-salt. The output capacity is negligible in pure Mg electrolyte. Li^+ intercalation/de-intercalation dominants the cathode reaction.

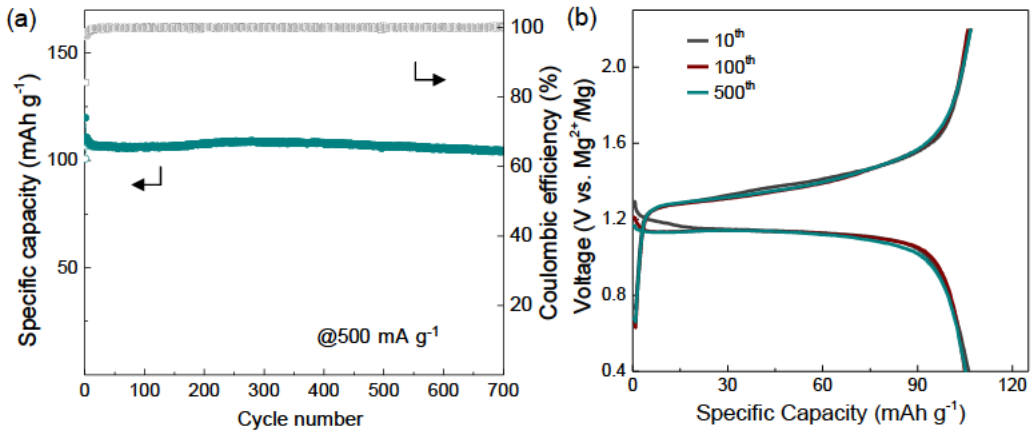

Figure S13. a) Long-term cycling performance at 500 mA g^{-1} at room temperature (RT). (Initial three cycles were activated at a current density 100 mA g^{-1}) exhibiting a low capacity decay of 0.0065 % per cycle (109.2 - 104.2 mAh g^{-1} over 700 cycles). b) Corresponding discharge-charge curves for 1T-VSe_2.

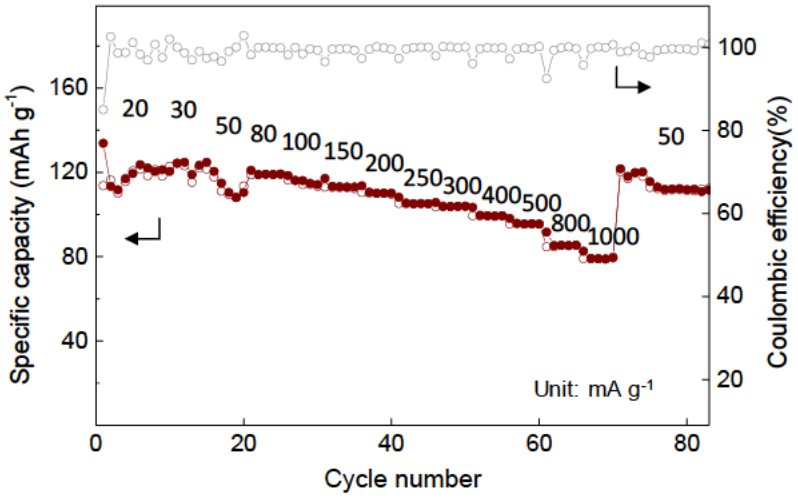

Figure S14. Rate capability for 1T-VSe_2 at RT.

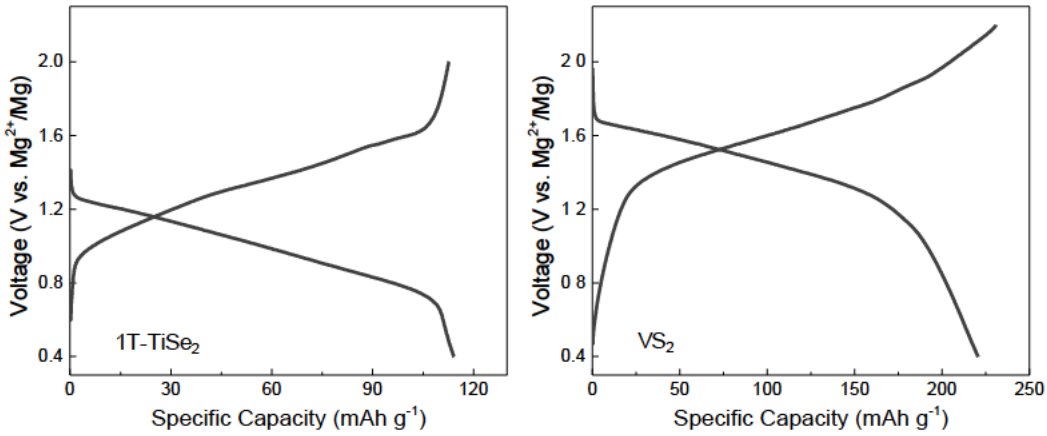

Figure S15. Discharge-charge curves for 1T-$TiSe_2$ and vanadium disulphide (VS_2) at a current density 500 mA g^{-1} in Mg^{2+}/Li^+ hybrid system for the 3th cycle at RT.

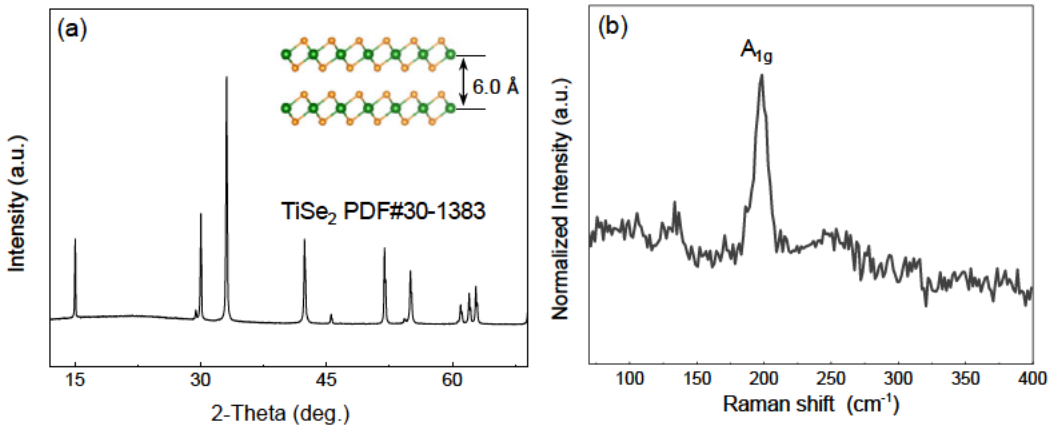

Figure S16. (a) XRD pattern (Inset: corresponding crystal structure), and (b) Raman spectrum for 1T-$TiSe_2$.

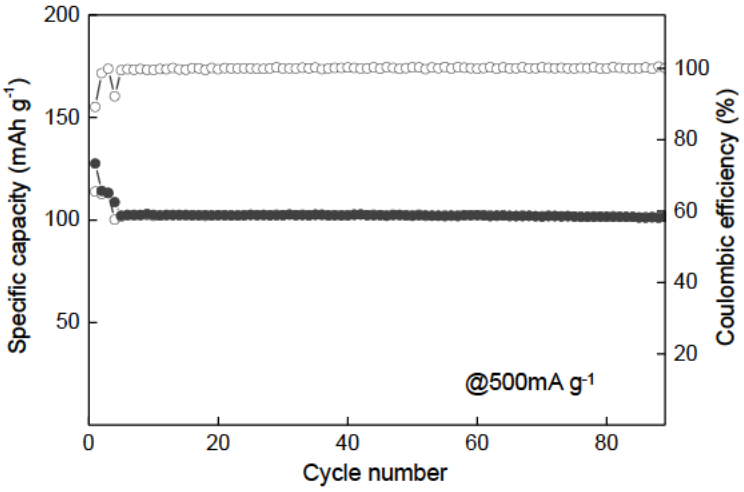

Figure S17. Cycling performance for 1T-$TiSe_2$ at 500 mA g^{-1} at RT. (Initial three cycles were activated at a current density 100 mA g^{-1}).

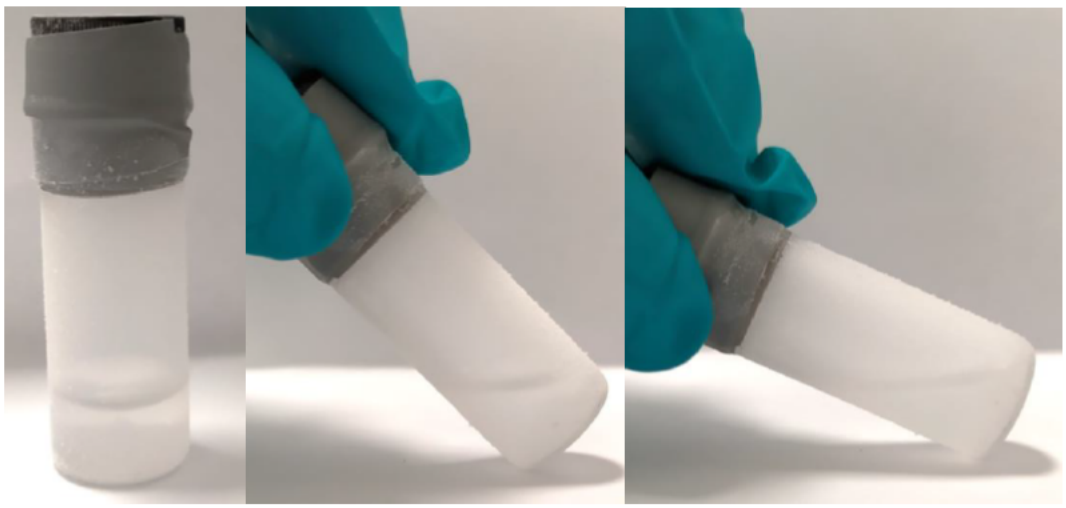

Figure S18. Digital images of prepared Mg^{2+}/Li^{+} hybrid electrolyte at -80 °C. The electrolyte remained fluid.

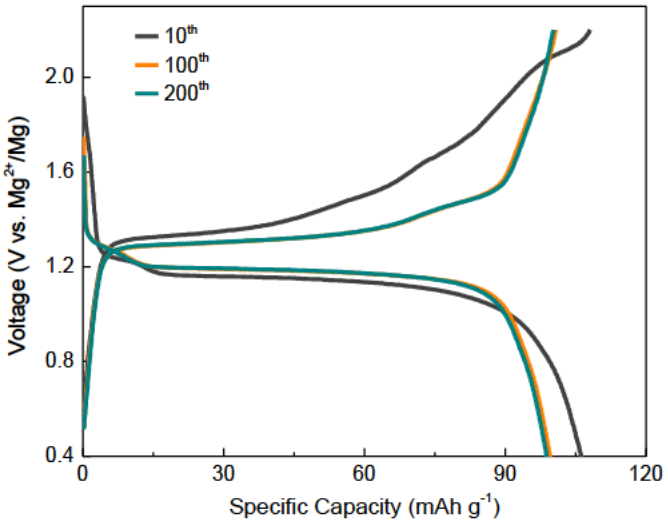

Figure S19. Discharge-charge curves for 1T-VSe_2 at -20 ℃ for different cycles.

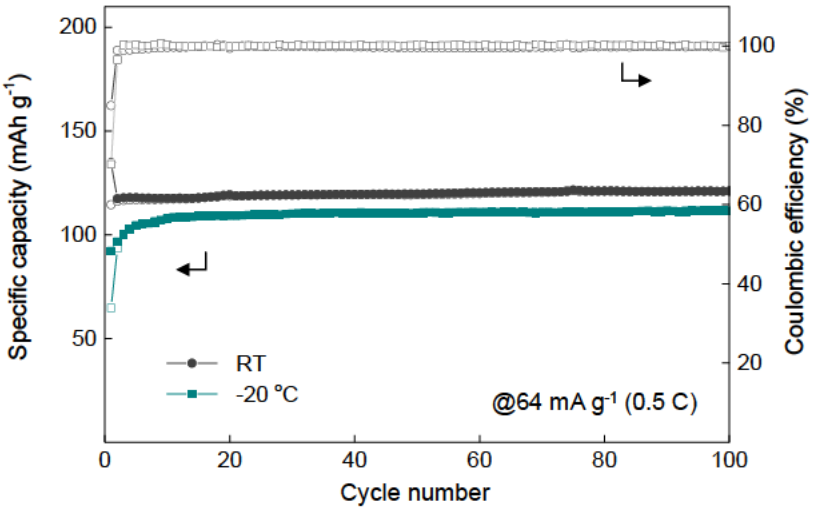

Figure S20. Cycling performance for 1T-VSe_2 at current density 64 mA g^{-1} at -20 ℃ and RT.

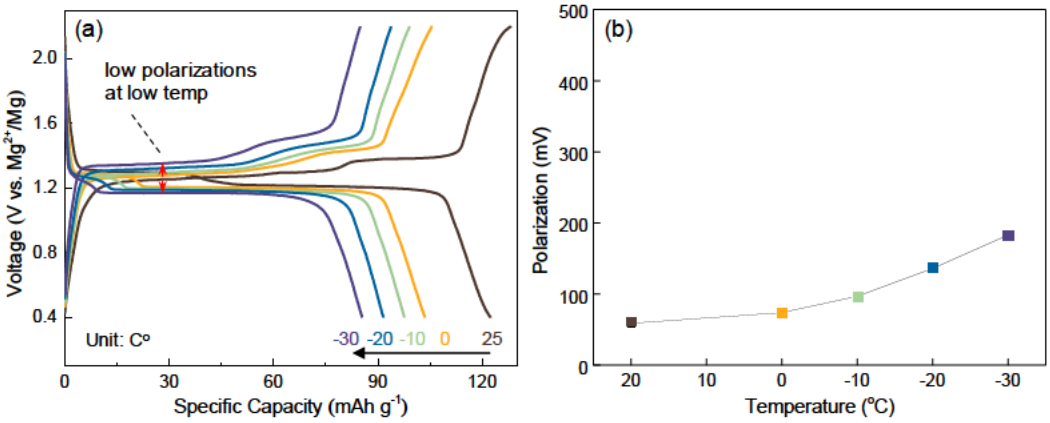

Figure S21. (a) Discharge-charge curves for 1T-VSe_2 at selected temperature. (b) Corresponding polarization value.

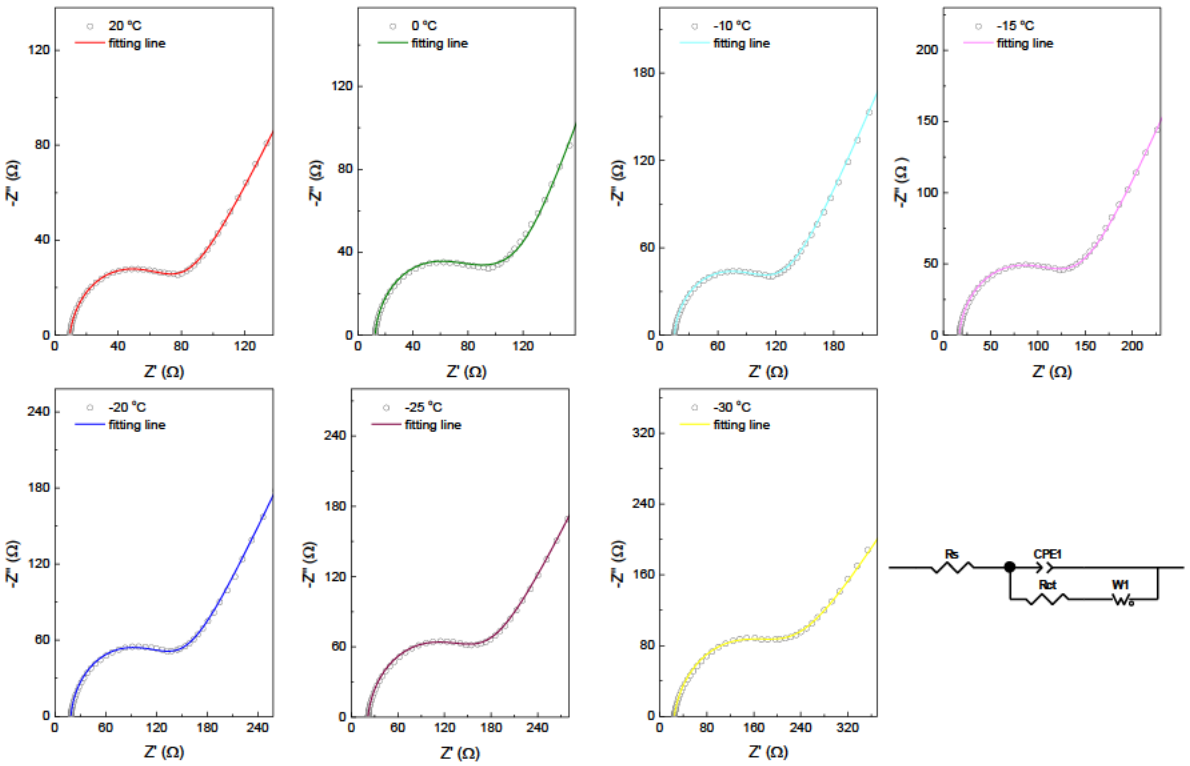

Figure S22. Typical fitted EIS plots for 1T-VSe_2 at differing temperature. R_s and R_{ct} are, respectively, the series ohmic resistance, and charge transfer resistance.

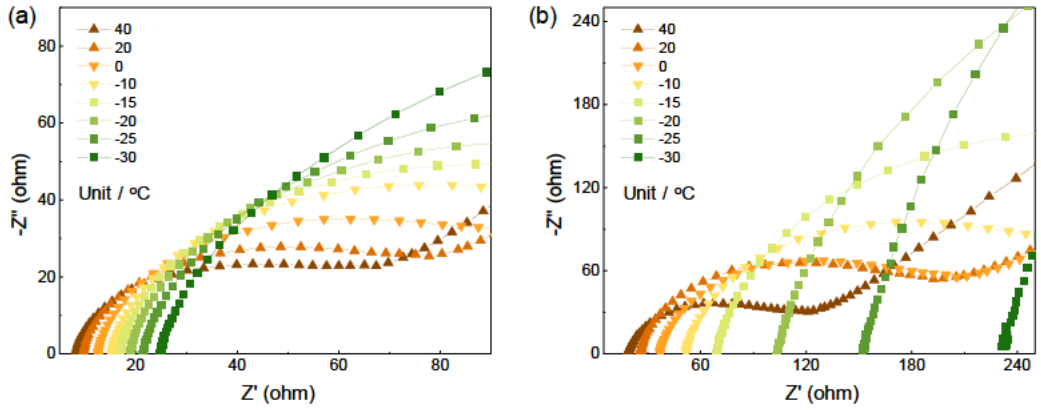

Figure S23. Enlarged electrochemical impedance spectroscopies for high frequency portion of (a) 1T-VSe_2 and (b)1T-$TiSe_2$ at varying temperature.

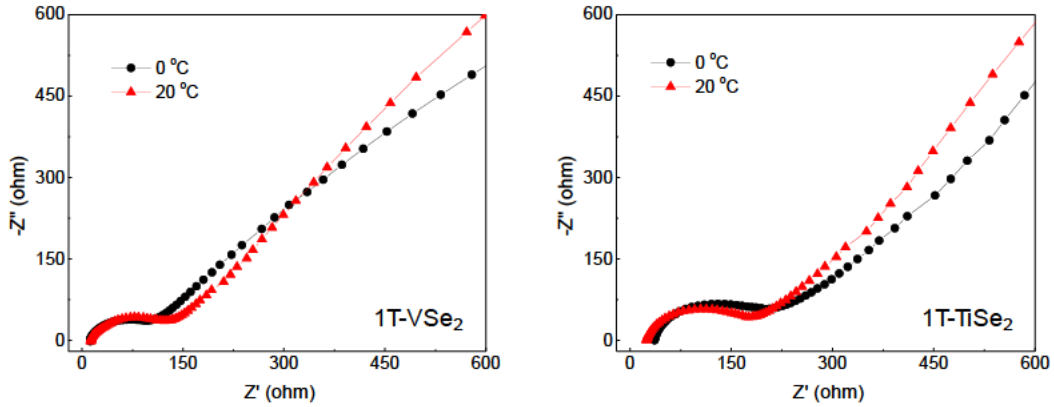

Figure S24. EIS plots for 1T-VSe_2 and 1T-$TiSe_2$ at a rising temperature of 0 and 20 ℃ following testing at -30 ℃.

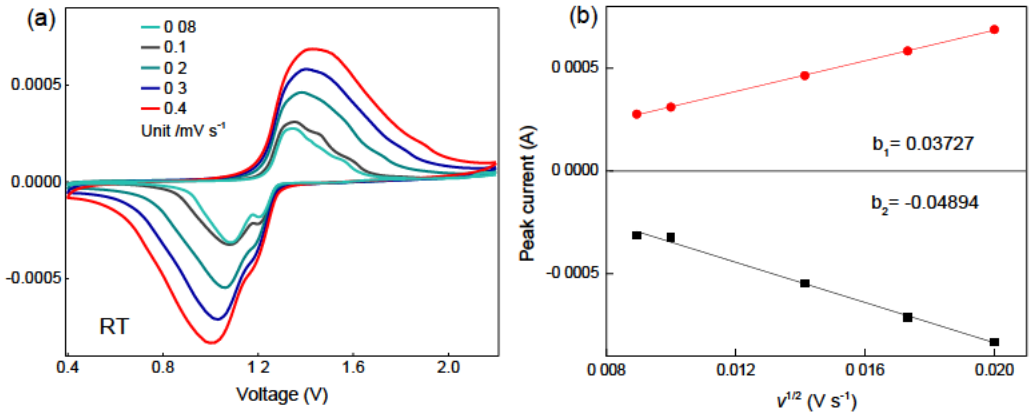

Figure S25. (a) CV curves for 1T-VSe_2 at differing scan rate and RT. (b) Corresponding linear fit for relationship between peak current (I_p) and the square root of scan rate ($v^{1/2}$).

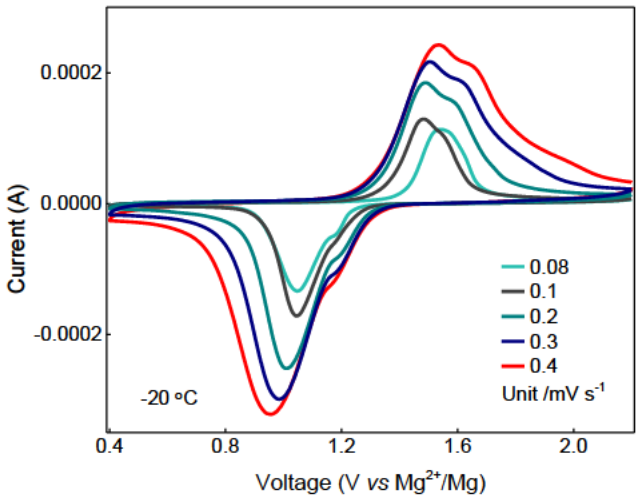

Figure S26. CV curves for 1T-VSe_2 at -20 ºC with differing scan rate.

Table S1. V K-edge structural parameters for pristine 1T-VSe_2 and fully discharged product $LiVSe_2$ derived from least-square fit to FT-EXAFS spectra.

	Path	d / Å	R / Å	σ^2/Å^2
VSe_2	V-Se	2.471	2.47	0.004
$LiVSe_2$	V-Se1	1.963	2.03	0.007
	V-Se2	2.544	2.57	0.006

Table S2. Rietveld refinement results for unit cell parameters from *operando* synchrotron XRD data.

Sample state	Phase name	a (Å)	b (Å)	c (Å)	α	β	γ	Cell volume ($Å^3$)
Discharged phase	$LiVSe_2$	3.59	3.59	6.38	90	90	120	71.3
pristine	1T-VSe_2	3.35	3.35	6.10	90	90	120	59.3

Table S3. Summary for lattice parameters for 1T-VSe_2 prior to and following Li^+ intercalation, and reported TMDs.[7, 8] Red-colour font are results from this work from Rietveld refinement, and; black font is reported values. For MX_2, X is a chalcogen atom (S and Se, etc.) and M transition metal (Ti, V, Mo and W, etc.).

		Lattice parameter (MX_2)			Lattice parameter (Li inserted MX_2)			
		a / Å	c / Å	c/a	a / Å	c / Å	c/a	Δc / Å
1T	VSe_2	3.351	6.101	1.821	3.594	6.380	1.775	0.28
	VSe_2	3.35	6.10	1.821	3.584	6.356	1.773	0.26
	$TiSe_2$	3.535	6.004	1.698	3.644	6.480	1.788	0.48
	TiS_2	3.407	5.696	1.672	3.455	6.195	1.793	0.50
	$ZrSe_2$	3.771	6.129	1.631	3.73	6.66	1.786	0.53
	ZrS_2	3.665	5.835	1.592	3.604	6.25	1.734	0.42
2H	MoS_2	3.16	6.15	1.946	-	6.4	-	0.25
	WS_2	3.16	6.18	1.956	-	-	-	
	TaS_2	3.34	6.04	1.808	3.34	6.475	1.939	0.44
	NbS_2	3.324	5.98	1.799	3.354	6.45	1.923	0.47
	$MoSe_2$	3.30	6.50	1.970	-	-	-	-
	WSe_2	3.3	6.5	1.97	-	-	-	-
	$TaSe_2$	3.463	6.348	1.847	3.477	6.817	1.961	0.47
	$NbSe_2$	3.45	6.27	1.817	3.496	6.772	1.937	0.50

Table S4. Property values for tetrahydrofuran (THF) solvent.

Solvent	Formula	Boiling point (°C)	Melting point (°C)	Density (g ml^{-1})	Dielectric constant	Viscosity (cp)
tetrahydrofuran	C_4H_8O	65	**-108.4**	0.883	7.52	0.48

Table S5. Summary comparison of low-temperature (-20 °C) electrochemical properties for cathode materials for different batteries.

System	Materials	Capacity retention -20°C / RT (%), (Current density, mA g^{-1})	Cycling performance			Ref.
			Capacity (mAh g^{-1})	Current density (mA g^{-1})	Cycle number	
MLIBs	1T-VSe_2	92.2 (64) 87 (100)	97.5	100	500	This work
	$Li_3V_2(PO_4)_3$ (LVP)	69 (100)	93.4	100	100	1[9]
	$LiFePO_4$@GF	86 (Unknown)	88	Unknown	50	2[10]
MIBs	Mo_6S_8	~72.5 (12.8)	~58	12.8	50	3[11]
LIBs	NMC111	~65 (55)	88	55	125	4[12]
	$Li_3V_2(PO_4)_3$@C/CNT	82	77.7	67	200	5[13]
	LISICON-$Li_3V_2(PO_4)_3$	87 (27)	65	1330	900	6[14]
	$LiMn_2O_4$-Ni	90 (28)	~88	28	50	7[2]
	NMC811‘	82 (55)	153	55	100	8[15]
	LiFePO4	Unknown	73	34	100	9[16]
	NMC811	81 (55)	92	55	250	10[17]
	$LiNi_xCo_yMn_zO_2$ (LNCM)	70 (27.5)	113	137.5	1150	11[18]
	$LiNi_{0.8}Co_{0.15}Al_{0.05}O_2$ (NCA)	Unknown	~130	57	450	12[19]
SIBs	$Na_3V_2(PO_4)_2O_2F$	84 (26)	~82	65	600	13[20]
	PB/CNT	85 (17)	82	408	1000	14[21]
	$Na[Ni_xCo_yMn_z]O_2$	79 (27.5)	100	137.5	100	15[22]

MLIBs = Mg^{2+}/Li^+ ion hybrid batteries, MIBs = magnesium ion batteries, LIBs = lithium-ion batteries and SIBs = sodium-ion batteries.

Table S6. EIS fitted results for 1T-VSe_2 electrode at selected temperatures.

Temperature (°C)	20	0	-10	-15	-20	-25	-30
R_s (Ω)	9.5	12.6	15.3	16.7	18.9	21.2	24.6
R_{ct} (Ω)	44.6	55.0	62.5	72.2	78.5	93.1	136

References

[1] B. H. Toby, R. B. Von Dreele, *J. Appl. Crystallogr.* **2013**, 46, 544.

[2] W. Zhang, X. Sun, Y. Tang, H. Xia, Y. Zeng, L. Qiao, Z. Zhu, Z. Lv, Y. Zhang, X. Ge, S. Xi, Z. Wang, Y. Du, X. Chen, *J. Am. Chem. Soc.* **2019**, 141, 14038.

[3] G. Kresse, J. Furthmuller, *Phys. Rev. B Condens. Matter* **1996**, 54, 11169.

[4] G. Kresse, J. Furthmüller, *Comput. Mater. Sci.* **1996**, 6, 15.

[5] J. P. Perdew, *Phys. Rev. Lett.* **1996**, 77, 3865.

[6] A. Tkatchenko, M. Scheffler, *Phys. Rev. Lett.* **2009**, 102, 073005.

[7] M. S. Whittingham, F. R. Gamble, *Mater. Res. Bull.* **1975**, 10, 363.

[8] A. Thompson, J. Scanlon, C. Symon, *Solid State Ion.* **1980**, 1, 47.

[9] M. Rashad, H. Zhang, X. Li, H. Zhang, *J. Mater. Chem. A* **2019**, 7, 9968.

[10] Z. Zhang, H. Xu, Z. Cui, P. Hu, J. Chai, H. Du, J. He, J. Zhang, X. Zhou, P. Han, G. Cui, L. Chen, *J. Mater. Chem. A* **2016**, 4, 2277.

[11] A. Du, H. Zhang, Z. Zhang, J. Zhao, Z. Cui, Y. Zhao, S. Dong, L. Wang, X. Zhou, G. Cui, *Adv. Mater.* **2019**, 31, 1805930.

[12] Y.-G. Cho, M. Li, J. Holoubek, W. Li, Y. Yin, Y. S. Meng, Z. Chen, *ACS Energy Lett.* **2021**, 6, 2016.

[13] L.-H. Tai, Q. Zhao, L.-Q. Sun, L.-N. Cong, X.-L. Wu, J.-P. Zhang, R.-S. Wang, H.-M. Xie, X.-H. Chen, *New J. Chem.* **2015**, 39, 9617.

[14] R. Qin, Y. Wei, T. Zhai, H. Li, *J. Mater. Chem. A* **2018**, 6, 9737.

[15] J. Holoubek, K. Kim, Y. Yin, Z. Wu, H. Liu, M. Li, A. Chen, H. Gao, G. Cai, T. A. Pascal, P. Liu, Z. Chen, *Energy Environ. Sci.* **2022**, 15, 1647.

[16] W. Ren, Y. Zhang, R. Lv, S. Guo, W. Wu, Y. Liu, J. Wang, *J. Power Sources* **2022**, 542, 231773.

[17] C. Wang, B. Nan, L. Chen, N. D. Rodrigo, O. Borodin, N. Piao, J. Xia, T. Pollard, S. Hou, J. Zhang, X. Ji, J. Xu, X. Zhang, L. Ma, X. He, S. Liu, H. Wan, E. Hu, W. Zhang, K. Xu, X.-Q. Yang, B. Lucht, *Angew. Chem. Int. Ed.* **2022**, 61, e202205967.

[18] Z. Sun, Z. Li, L. Gao, X. Zhao, D. Han, S. Gan, S. Guo, L. Niu, *Adv. Energy Mater.* **2018**, 9, 1802946.

[19] X. Fan, X. Ji, L. Chen, J. Chen, T. Deng, F. Han, J. Yue, N. Piao, R. Wang, X. Zhou, X. Xiao, L. Chen, C. Wang, *Nat. Energy* **2019**, 4, 882.

[20] X. Zheng, Z. Gu, J. Fu, H. Wang, X. Ye, L. Huang, X. Liu, X. Wu, W. Luo, Y. Huang, *Energy Environ. Sci.* **2021**, 14, 4936.

[21] Y. You, H. R. Yao, S. Xin, Y. X. Yin, T. T. Zuo, C. P. Yang, Y. G. Guo, Y. Cui, L. J. Wan, J. B. Goodenough, *Adv. Mater.* **2016**, 28, 7243.

[22] J. Y. Hwang, S. M. Oh, S. T. Myung, K. Y. Chung, I. Belharouak, Y. K. Sun, *Nat. Commun.* **2015**, 6, 6865.

Chapter 6: Modulating Solution-Mediated Kinetics for Sodium-Organic Battery Operated at Ultra-Low Temperature

6.1 Introduction and significance

Cycling under ultra-low temperature is a great challenge for rechargeable batteries. Insufficient ionic conductivity of the electrode is considered as one of the main obstacles to this issue. The Organic electrode with kinetically fast surface-controlled reactions can work well at ultra-low temperatures. Here, we propose nanosized disodium rhodizonate/graphene oxide (nDSR/GO) composites as the electrode for sodium-ion batteries, in which the pseudocapacitive electrochemical behaviour of the organic electrode has been fully utilized. More importantly, an intermediate amorphous phase, which is soluble in organic electrolytes, is formed and further enhances the reaction kinetics of the electrode at an ultra-low temperature. By modulating the solution-mediated kinetics of the organic electrode, Na-nDSR/GO battery exhibits a high capacity of 119 mAh g^{-1} at -50 ºC. Prussian blue analogue-nDSR/GO full cell demonstrates an ultra-long lifespan over 2500 cycles with a discharge capacity of 99 mAh g^{-1} at a high current density of 300 mA g^{-1} and -40 ºC. This work sheds light on the unique energy storage behaviour of the organic electrode and provides a new avenue for developing reliable and sustainable ultra-low temperature batteries. The highlights of this work include:

- **In-situ captures an intermediate amorphous phase**. We firstly capture an intermediate amorphous phase for sodium rhodizonate electrode during electrochemical cycling via in-situ Raman spectroscopy. The amorphous intermediate phase is soluble in

organic electrolytes involving a solution-mediated reaction.

- **Proposing a new strategy to enhance kinetics at ultra-low temperature.** By carefully modulating the dissolving and transforming rate of the intermediate amorphous phase, we first utilize kinetically fast solution-mediated reactions to achieve high capacity and long cycling stability of the organic electrode at ultra-low temperatures. This is a viable and universal strategy, which can be extended to other metal-organic battery systems, and even metal-sulfur batteries. This benefits further electrode designs for wide-temperature operation batteries.
- **Excellent ultra-low temperature performance.** The Na-DSR/GO half cell exhibits a high capacity of 119 mAh g^{-1} at -50 ºC. The PBA-DSR/GO full cell demonstrates an ultra-long lifespan over 2500 cycles with a discharge capacity of 99 mAh g^{-1} at a high current density of 300 mA g^{-1} and -40 ºC, which is among one of the best cycling performances for energy storage batteries at ultra-low temperature.

6.2 Modulating Solution-Mediated Kinetics for Sodium-Organic Battery Operated at Ultra-Low Temperature

This Chapter is included as it appears as a journal paper contributed by **Xin Xu**, Huan Li, Shiying Ren, Chao Ye, Han Wu, and Shi-Zhang Qiao. "Modulating solution-mediated kinetics at ultra-low temperature for sodium-organic battery with ultra-long lifespan. " **To be submitted**.

Statement of Authorship

Title of Paper	Modulating solution-mediated kinetics for sodium-organic full battery operated at ultra-low temperature
Publication Status	☐ Published ☐ Accepted for Publication ☐ Submitted for Publication ☑ Unpublished and Unsubmitted work written in manuscript style
Publication Details	

Principal Author

Name of Principal Author (Candidate)	Xin Xu		
Contribution to the Paper	Conducted experiments, data curation, formal analysis, investigation, and writing–original draft.		
Overall percentage (%)	70		
Certification:	This paper reports on original research I conducted during the period of my Higher Degree by Research candidature and is not subject to any obligations or contractual agreements with a third party that would constrain its inclusion in this thesis. I am the primary author of this paper.		
Signature		Date	20 October 2022

Co-Author Contributions

By signing the Statement of Authorship, each author certifies that:

i. the candidate's stated contribution to the publication is accurate (as detailed above);

ii. permission is granted for the candidate in include the publication in the thesis; and

iii. the sum of all co-author contributions is equal to 100% less the candidate's stated contr bution.

Name of Co-Author	Huan Li		
Contribution to the Paper	Conduct computational simulation, writing–review		
Signature		Date	20 October 2022

Name of Co-Author	Shiying Ren		
Contribution to the Paper	Captured microscopic images and assisted with XPS characterization		
Signature		Date	20 October 2022

Name of Co-Author	Chao Ye		
Contribution to the Paper	Supervision, writing–review		
Signature		Date	20 October 2022

Name of Co-Author	Han Wu		
Contribution to the Paper	Help with material synthesis		
Signature		Date	20 October 2022

Name of Co-Author	Shi Zhang Qiao		
Contribution to the Paper	Supervision, resources, conceptualization and writing review and editing		
Signature		Date	20 October 2022

Name of Co-Author			
Contribution to the Paper			
Signature		Date	

Name of Co-Author			
Contribution to the Paper			
Signature		Date	

Name of Co-Author			
Contribution to the Paper			
Signature		Date	

Modulating solution-mediated kinetics for sodium-organic battery operated at ultra-low temperature

Xin Xu,[1] Huan Li,[1] Shiying Ren,[1] Chao Ye,[1] Han Wu,[1] Shizhang Qiao[1]*

ABSTRACT: Ultra-low temperature operation is a great challenge for rechargeable batteries. Insufficient ionic conductivity of the electrode at low temperatures is considered as one of the main obstacles to this issue. The Organic electrode with kinetically fast surface-controlled reactions can work well at ultra-low temperatures. Here, we propose nanosized disodium rhodizonate/graphene oxide (nDSR/GO) composites as the electrode for sodium-ion batteries, in which the pseudocapacitive electrochemical behaviour of the organic electrode has been fully utilized. More importantly, an intermediate amorphous phase, which is soluble in organic electrolytes, is formed and further enhances the reaction kinetics of the electrode at an ultra-low temperature. By modulating the solution-mediated kinetics of the organic electrode, Na-nDSR/GO battery exhibits a high capacity of 119 mAh g^{-1} at -50 ºC. Prussian blue analogue-nDSR/GO full cell demonstrates an ultra-long lifespan of over 2500 cycles with a discharge capacity of 99 mAh g^{-1} at a high current density of 300 mA g^{-1} and a temperature of -40 ºC. This work sheds light on the unique energy storage behaviour of the organic electrode and provides a new avenue for developing reliable and sustainable ultra-low temperature batteries.

Keywords: solution-mediated kinetics, amorphous phase, ultra-low temperature, organic electrode, sodium-ion battery

INTRODUCTION

Organic compounds with distinct advantages such as structural diversity, flexibility, sustainability, and environmental friendliness, have been extensively studied as electrode materials for rechargeable lithium, sodium, potassium, and magnesium batteries.[1-3] Among them, the sodium-organic battery is especially promising because of their natural abundance and low cost of electrode materials comprising only C, O and Na atoms.[4] Compared to inorganic compounds, most organic electrodes exhibit faster kinetics due to their flexible molecular structures and surface-controlled reactions, which bypass the intercalation and solid-state diffusion limitations for the inorganic hosts.[5-7]

Generally, the reduction of unsaturated bonds such as C=C, C=N, and C=O in organic molecules forms radical intermediates producing a negative charge on N or O atoms, and an unpaired electron on C atoms.[8] These organic intermediates are unstable and could readily dissolve in the electrolyte which eventually results in capacity loss, and thus leads to unsatisfactory cycling stability. Over the past decades, various strategies have been proposed to prevent the dissolution and formation of metastable active organic materials.[9] However, solution-mediated reactions, involving the dissolution of metastable solid and nucleation of a stable solid phase, are kinetically fast, which could favor the ultra-low temperature performance of the electrode.[10-11] In this work, we firstly propose the utilization of solution-mediated kinetics in organic electrode materials to advance the ultra-low temperature charge storage performance of Na-ion batteries.

Taking advantage of fast solution-mediated kinetics of organic compounds during cycling requires a balance between dissolution and transformation of the metastable phase to avoid

the loss of active materials. The increased viscosity of organic electrolytes at an ultra-low temperature naturally mitigates the dissolving rate of the metastable phase.[12-13] Therefore, the transforming rate of metastable intermediates dominates the balance and reversibility of the organic electrode. Graphene oxide with abundant functional groups on the surface is capable of anchoring functional molecules via covalent or non-covalent interactions.[14] In this work, the composite of nanosized disodium rhodizonate and graphene oxide (nDSR/GO) offers highly improved electrochemical capacity, rate capability and cycling stability at ultra-low temperatures. The Na-nDSR/GO battery exhibits a high capacity of 119 mAh g^{-1} at an ultra-low temperature of -50 ^{o}C. And nDSR/GO composite electrode in coupling with MnFe-Prussian blue analogue (PBA) cathode for Na-ion batteries exhibits ultra-stable cycling performance with discharge capacity of 99 mAh g^{-1} over 2500 cycles. GO acting as a bridge between the electrolyte and active materials significantly enhances the interfacial kinetics exhibiting low activation energy, and therefore promotes the ultra-low temperature performance of the composite electrode. The in-depth reaction mechanism for nDSR/GO was studied via in-situ Raman and ex-situ synchrotron X-ray absorption spectroscopy. This work significantly promotes the development of ultra-low temperature batteries.

RESULTS AND DISCUSSION

Material characterization and electrochemical performance at room temperature (RT). The self-assembly method via solvent exchange processing was applied to prepare shape-selectable DSR particles, as shown in **S1** and **S2**. Different morphology like prism, butterfly and diamond structures were synthesized through the modification of the solvent mixture ratio and the amount of raw material added. **Fig. 1a** shows the morphology of

nanosized DSR (nDSR) in a diamond shape. The nDSR was used as the control sample for the evaluation of electrochemical performance. The charge storage of the organic electrode depends on the redox centre of carbonyl groups, as depicted in **Fig. 1b**. Na-nDSR half cells were assembled with Na-foil anode, nDSR organic cathode, and 1 M $NaPF_6$ electrolyte. The Na-nDSR electrode shows a rapid capacity loss at RT due to the loss of active materials.[4] To enhance the cycling stability, nDSR was hybridized with GO. **Fig. 1c** exhibits the SEM image of nDSR/GO composites. Following the hybridization, nDSR/GO exhibits a highly improved

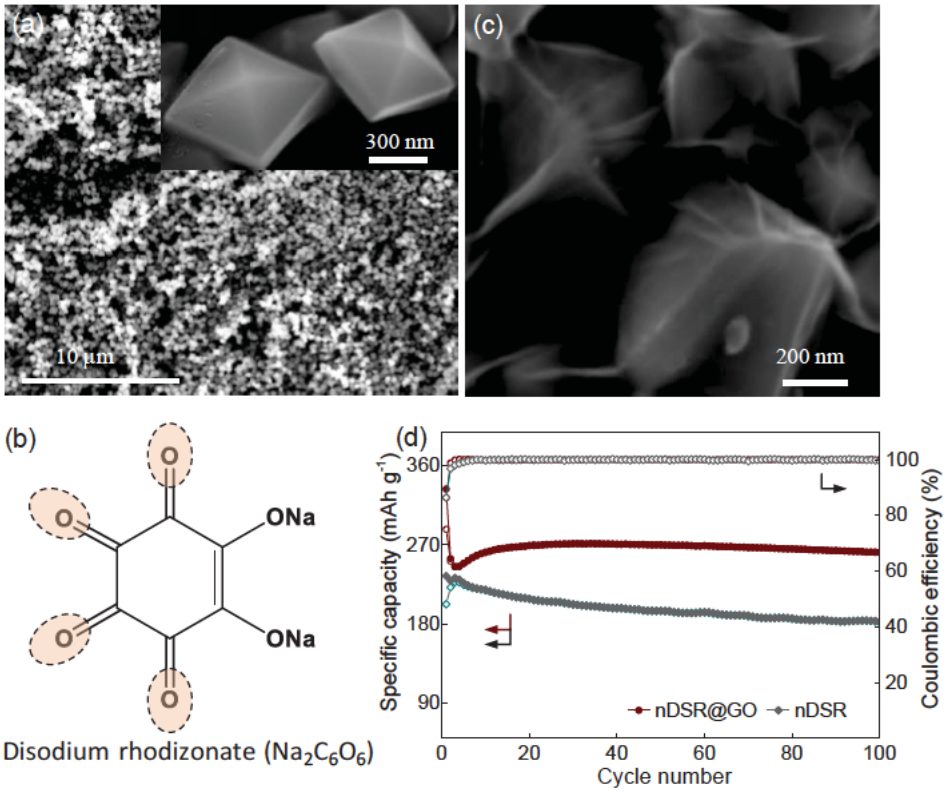

Figure 1. (a) SEM images for nDSR. (b) Molecular structure of DSR (the orange-coloured areas correspond to redox active sites). (c) SEM image of nDSR/GO composite. (d) Cycling performance of nDSR and nDSR/GO in half cells at RT.

capacity of 262 mAh g^{-1} (*vs.* 184 mAh g^{-1} for nDSR) and maintains 98 % capacity over 100 cycles at a current density of 300 mA g^{-1} (**Fig. 1d**). In addition, the nDSR/GO composite

electrode shows an exceptional stability with neglectable capacity lose over 500 cycles at a high current density of 1000 mA g^{-1} (**Fig. S3**), which performs the best cycle life among all reported DSR electrode at RT. **Fig. S4** shows the initial discharge-charge curves of nDSR and nDSR/GO at 1000 mA g^{-1}. nDSR/GO demonstrates more obvious plateaus at 1.7 and 1.3 V and delivers a higher initial capacity of 317 mAh g^{-1} (based on the mass of nDSR/GO composite) than that of the nDSR electrode (257 mAh g^{-1}). The good rate capability of nDSR/GO is shown in **Fig. S5**, indicating a fast reaction kinetics of the electrode. Overall, the composite of nDSR and GO allows the organic electrode to achieve a high capacity and long-cycle life.

Probing solution-mediated reaction via in-situ Raman spectroscopy. The redox reaction of DSR organic electrode occurs between Na^+ and carbonyl groups. The reaction process of Na-organic batteries is monitored at RT via in-situ Raman spectroscopy, ex-situ X-ray absorption spectroscopy (XAS) and X-ray diffraction (XRD). The Raman spectrum of DSR powder has multiple features in the range of 100-1800 cm^{-1} (**Fig. S6**). **Fig. S7-S8** demonstrate the time-dependent evolution of Raman spectra for the initial five cycles of nDSR electrode. After the initial discharging to 1.7 V, all peaks disappear suggesting the formation of intermediate amorphous phase, which is unstable and readily dissolving in the organic electrolyte. The dissolution of the intermediate phase results in the disappearance of Raman activity and loss of active materials, and therefore leads to a poor reversibility for nDSR electrode at RT. **Fig. 2a** and **Fig. S9** show the in-situ Raman spectrum of nDSR/GO composite electrode. Unlike nDSR, the composite electrode exhibits a reversible phase change with obvious Raman features during cycling, indicating a highly reversible

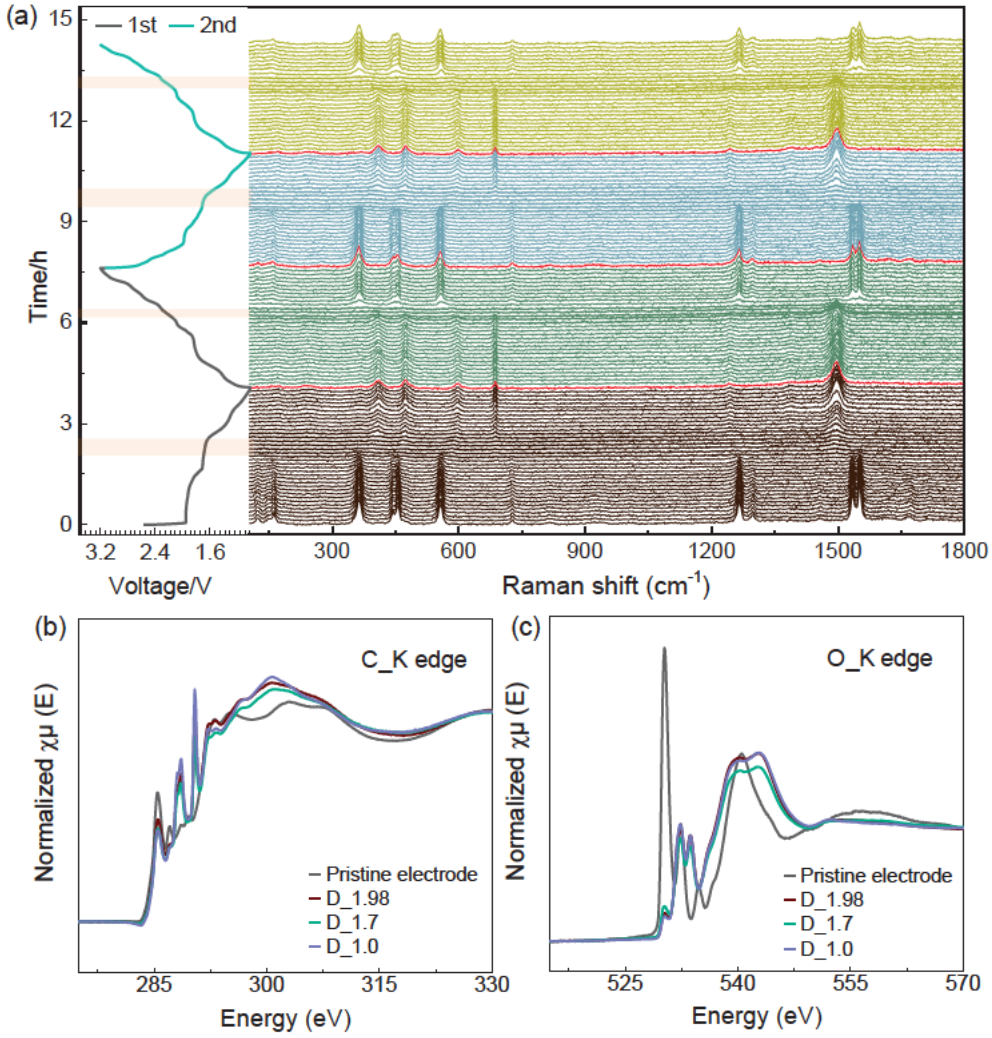

Figure 2. Capturing intermediate amorphous phase. a) In-situ Raman spectroscopy and corresponding discharge-charge profiles for the first and second cycles. X-ray absorption spectroscopy (XAS) of b) C K-edge, and c) O K-edge for electrodes at different discharging cut-off potentials.

electrochemical process. It is noteworthy that a transient and reversible disappearance of Raman peaks occurs at ~1.7 V involving a redox process, which corresponds to the formation of $Na_4C_6O_6$ intermediates.[15-18] The transient disappearance of Raman peaks at ~1.7 V suggests that the formed $Na_4C_6O_6$ is an amorphous phase and soluble in the organic electrolyte. The abnormal change of intensity in XAS spectrum (**Fig. 2b-2c**) and disappearance of peaks in XRD spectrum (**Fig. S10**) for the electrode at ~1.7 V, further

confirm the formation of an amorphous phase.[19] The composite of nDSR and GO can alleviate the dissolving rate of active materials and enhance the reversibility of the electrode. Here, we first capture the intermediate amorphous phase via in-situ Raman, and more detailed investigations will focus on the application of the amorphous phase involved solution-mediated reactions at ultra-low temperatures.

Ultra-low temperature performance in half cells. To take full advantage of the kinetically fast solution-mediated reactions, the organic electrode was evaluated as a cathode for sodium batteries operated at an ultra-low temperature. **Fig. 3a** shows the long-term cycling performance of nDSR and nDSR/GO at a low temperature of -30 ºC and a current density of 200 mA g^{-1}. Both electrodes exhibit good cycling stability at low temperature compared to RT due to the increased viscosity of the electrolyte as temperature decreases. Whilst after hybridizing with GO, the composite electrode delivers a double capacity of nDSR. The Na-nDSR/GO battery delivers a high initial capacity of 318 mAh g^{-1} at a current density of 100 mA g^{-1} with obvious voltage plateaus (**Fig. S11**). The high rate performance of the Na-nDSR/GO battery is shown in **Fig. 3b**. The composite electrode is capable of working at 500 mA g^{-1} with fast reaction kinetics at a low temperature of -30 ºC. The cyclic voltammetry (CV) curves for Na-nDSR/GO batteries are demonstrated in **Fig. S12-S13**, exhibiting a high reversibility. At an ultra-low temperature of -50 ºC, the Na-nDSR/GO battery can still achieve a high capacity of 119 mAh g^{-1} with an average discharging voltage of around 2.0 V at 50 mA g^{-1}. This is among the best ultra-low temperature performance for energy storage batteries. The corresponding galvanostatic discharge-charge curves are demonstrated in **Fig. 3d**, which shows a stable capacity output with clear and flat discharging

plateaus during cycling. The results demonstrate that nDSR/GO is in great potential as an ultra-low temperature electrode material.

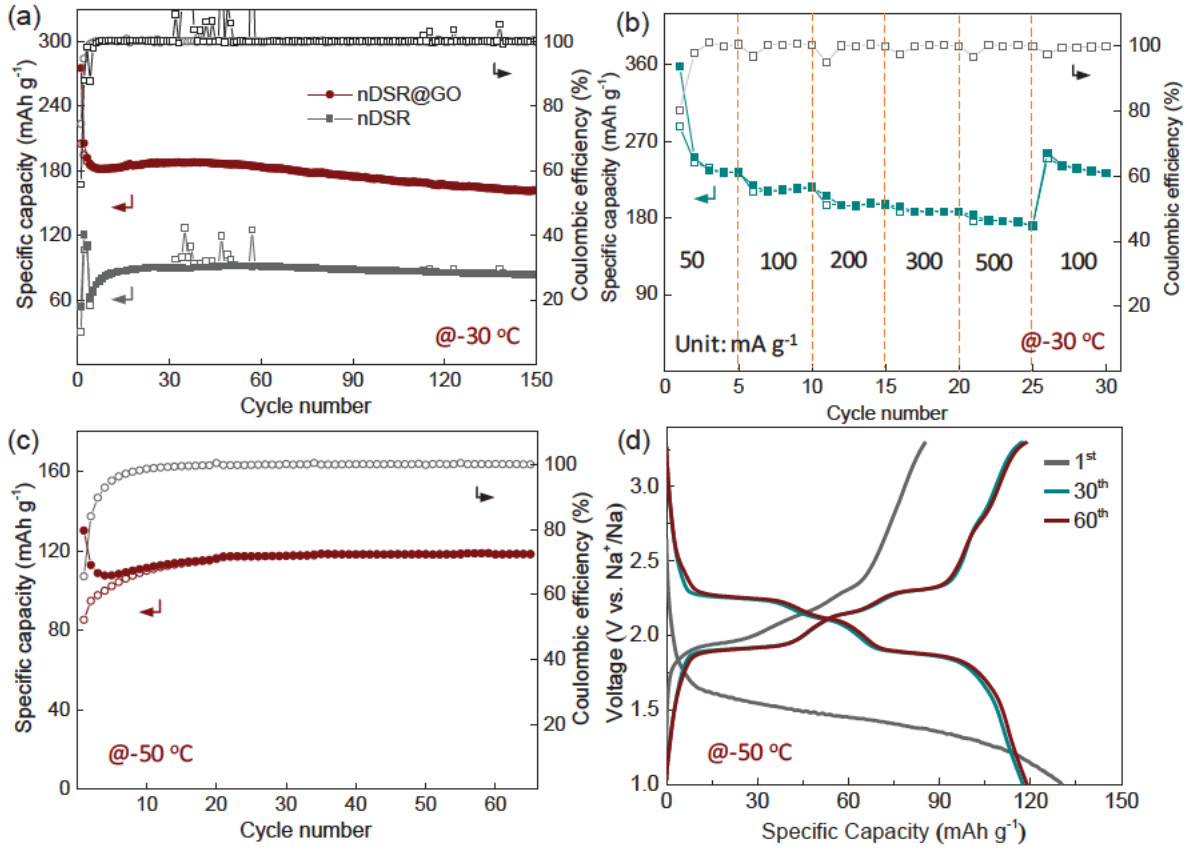

Figure 3. Na-storage properties for nDSR/GO in half cells. a) Cycling performance for nDSR and nDSR/GO at a current density of 200 mA g^{-1} and -30 ℃. b) Rate capability of nDSR/GO at -30 ℃. c) Cycling performance for nDSR/GO at a current density of 50 mA g^{-1} and a low temperature of -50 ℃, and d) corresponding discharge-charge profiles for different cycles at -50 ℃.

To unravel the origin of the excellent electrochemical property of nDSR/GO, we investigated the electronic conductivity and activation energy (E_a) of the electrode. The in-situ electrochemical impedance spectroscopies (EIS) for nDSR and nDSR/GO were conducted during the initial two cycles (**Fig. S14-S15**). The semicircle in EIS corresponds to the charge transfer process of cycling. The resistance at open circuit voltage for nDSR is

larger than of nDSR/GO composite. Whilst after the initial discharging to 1.9 V, the charge transfer resistance (R_{ct}) for nDSR becomes smaller than nDSR/GO, indicating that the hybridization of GO does not enhance the electronic conductivity of the organic electrode. **Fig. 4a-4b** demonstrate the EIS for nDSR and nDSR/GO electrodes at differing temperatures from 25 to -40 ºC. The nDSR electrode shows a smaller R_{ct} than nDSR/GO composite at a temperature above -30 ºC. As displayed in **Fig. 4a**, with the temperature decreasing, the R_{ct} of nDSR undergoes dramatically increasing at a temperature lower than -30 ºC. Whilst the R_{ct} of nDSR/GO exhibits a relatively small and stable increase from 25 to -40 ºC. The change of R_{ct} with temperature is mainly determined by the activation energy. Therefore, the strategy of hybridization of GO has the main influence on activation energy of the electrode, which maintains a stable charge resistance as temperature decreases to ultra-low temperatures. The sessile drop contact angle technique was employed to quantify the effects of GO on the wettability of the electrode. The wettability of organic electrodes will largely influence the energy barrier for surface reactions. After the GO hybridizing, the contact angle is highly significantly decreased from 26.2^{o} to14.5^{o} (**Fig. S16**). A low angle of 14.5 characterizes the composites, which confirms the high wettability of GO composited organic electrodes. The increased wettability inevitably enhances the interfacial kinetics of the composite electrode, which promotes the transforming rate of intermediate amorphous phase and performs a high reversibility.

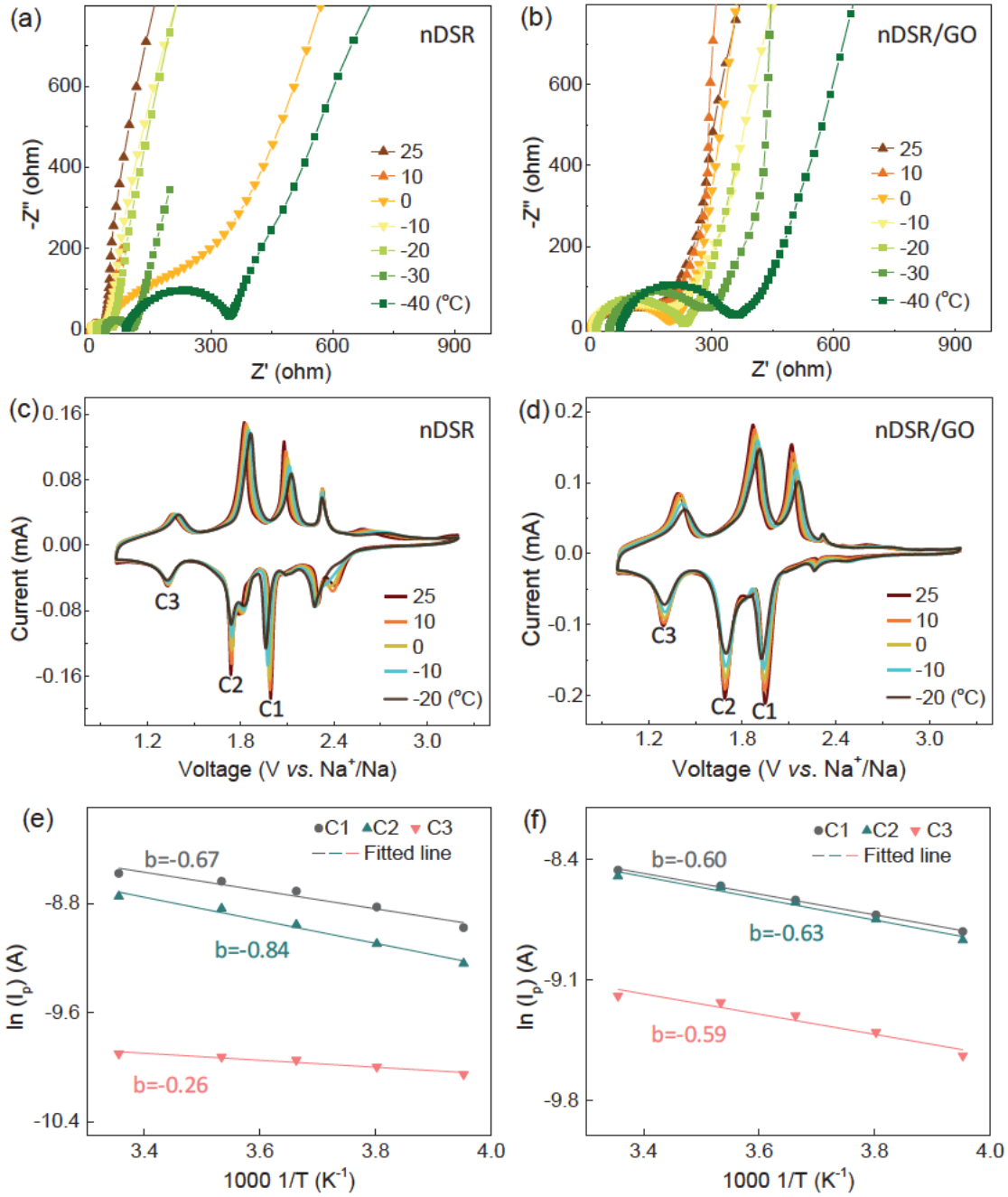

Figure 4. Kinetics investigations for nDSR and nDSR/GO. Electrochemical impedance spectroscopy for a) nDSR, and b) nDSR/GO at differing temperatures. c-d) CV curves at various temperatures. Arrhenius plot for peak current for e) nDSR, and f) nDSR/GO.

CV measurements under different temperatures from -20 to 25 °C were conducted at 0.2 mV s^{-1} for nDSR and nDSR/GO. Our work focuses on two main redox peaks C1 and C2, which corresponds to discharge plateaus of 2.0 and 1.7 V, as marked in **Fig. 4c-4d**. According

to the Arrhenius relationship (eq. S1), the activation energy corresponding to different reduction processes (C1 and C2) for nDSR and nDSR/GO is derived from the slope of peak current (I_p) versus the inverse of temperature (1/T) plot (**Fig. 4e** and **4f**). The calculated Ea for C1 and C2 are listed in Table S1. After GO hybridizing, the Ea for C1 and C2 processes have decreased, and it declines almost 25% of the energy barrier for C2 reduction process. At an ultra-low temperature, the increased wettability after the hybridization of GO largely facilitates Na^+ transport across the electrolyte/electrode interface, and thus exhibits a decreased Ea and fast reaction kinetics. The GO-enhanced kinetics promote the transformation of the intermediate amorphous phase, which well balances the dissolving and transforming rate of active materials, and therefore achieves high discharge/charge capacities and performs excellent reversibility for the organic electrode at ultra-low temperature.

Ultra-low Temperature performance in full cells. We assembled a full cell combining nDSR/GO with MnFe-Prussian blue analogue (PBA) cathode. The cycling performance of PBA-nDSR/GO full cells at -40 ºC is demonstrated in **Fig. 5a-5b**. The full cell delivers a high capacity of 138 mAh g^{-1} at a current density of 100 mA g^{-1} over 650 cycles. And it still shows a capacity of 99 mAh g^{-1} at a high current density of 300 mA g^{-1} over 2500 cycles. The cycling performance of PBA-nDSR full cell at -30 ºC is also demonstrated in **Fig. S17**, exhibiting a stable but much lower capacity of 58 mAh g^{-1} over 1000 cycles. The rate capability of PBA-nDSR/GO at -40 ºC is demonstrated in **Fig. 5c**. The designed full cell can even work at a high current density of 1000 mA g^{-1} with fast kinetics at an ultra-low temperature of -40 ºC. When the temperature was further decreased to -50 ºC, a discharge capacity of 108 mAh g^{-1} can still be obtained. More importantly, following a sudden increase

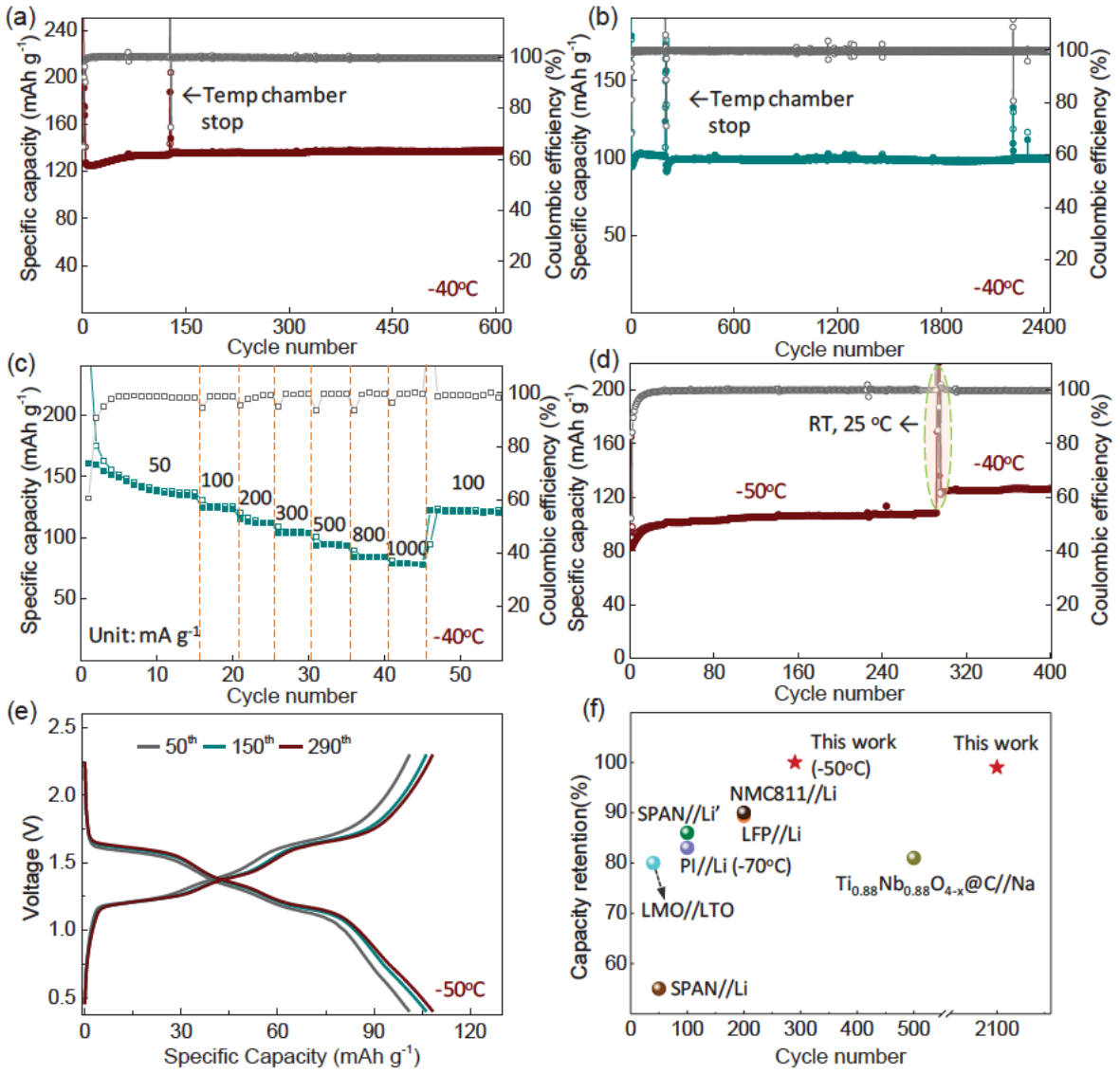

Figure 5. Energy storage performances for PBA-nDSR/GO full cells. Long-term cycling performance at -40 ºC and current density of a) 100, and b) 300 mA g^{-1}. c) Rate capability from 50 to 1000 mA g^{-1} at -40 ºC. d) Cycling performance at an ultra-low temperature of -50 ºC with temperature rising to RT, then dropping to -40 ºC. e) Corresponding discharge-charge profiles for different cycles at -50 ºC) Comparison of cycling stability between this work and previously reported lithium and sodium-ion batteries at ultra-low temperature. (Note: batteries without marking temperature are measured at -40 ºC)

of temperature from -50 ºC to RT and again decreasing to -40 ºC, PBA-nDSR/GO full cells can restore a stable capacity exhibiting an excellent temperature tolerance, as shown in **Fig.**

5d. The discharge-charge curves for different cycles at -50 ºC are demonstrated in **Fig. 5e**, which shows clear voltage plateaus at around 1.62, 1.35, and 1.17 V. The designed PBA-nDSR/GO full cell exhibits the best cycling performance among reported energy storage batteries at ultra-low temperatures, as shown in **Fig. 5f** (**Table S2**). **Fig. S18a** also shows the temperature-dependent rate performance of PBA-nDSR/GO full cell. And corresponding EIS at differing temperatures is shown in **Fig. S18b**. After hybridizing with GO, the full cell exhibits a relatively stable charge transfer resistance as temperature decreases to -40 ºC. The PBA-nDSR/GO takes full advantage of kinetically fast solution-mediate reactions and GO-enhanced interfacial kinetics, achieving a high capacity and long-term cycling performance of designed sodium-ion battery at ultra-low temperatures. We also demonstrate an all-organic full cell, combined an organic salt anode (tetrasodium terephthalate, Na_4TP) and the nDSR/GO cathode, which exhibits a high capacity of 136 mAh g^{-1} at a current density of 100 mA g^{-1} and -30 ºC over 300 cycles (**Fig. S19**). This is a good example of a sustainable battery that comprises only C, O and Na atoms and shows potential in large-scale applications with excellent low-temperature tolerance.

CONCLUSION

In summary, we proposed nanosized disodium rhodizonate (nDSR) as an ultra-low temperature serving organic electrode for sodium-ion batteries. The amorphous phase associated solution-mediated reaction results in a deteriorating capacity of nDSR electrodes at room temperature, but kinetically contributes to an excellent ultra-low temperature performance of the battery. The increased viscosity of the electrolyte and GO-enhanced interfacial kinetics collaboratively work on the balance of dissolving and transforming rate

of intermediate amorphous phase, and thus enhance the rate and reversibility of nDSR/GO composite electrode at ultra-low temperatures. Na-nDSR/GO half cells achieve a high capacity of 119 mAh g^{-1} at -50 ^{o}C. And the PBA-nDSR/GO full cell performs an ultra-stable cycle life of over 2500 cycles. The ultra-low temperature performance of nDSR/GO surpasses reported lithium and sodium batteries. Our findings promote the development of ultra-low temperature batteries, and offer sustainable and cost-efficient approaches to storing renewable energy in a harsh environment.

ACKNOWLEDGEMENT

This work was financially supported by the Australian Research Council (ARC) through discovery projects (FL170100154 and DP220102596). The authors acknowledge support from the soft X-ray Spectroscopy beamline at the Australian Synchrotron, ANSTO, Melbourne. The authors thank Junnan Hao and Shaojian Zhang from The University of Adelaide for the helpful discussion.

REFERENCE

1. Poizot, P.; Gaubicher, J.; Renault, S.; Dubois, L.; Liang, Y.; Yao, Y., Opportunities and Challenges for Organic Electrodes in Electrochemical Energy Storage. *Chem. Rev.* **2020,** *120* (14), 6490-6557.

2. Liang, Y.; Yao, Y., Positioning Organic Electrode Materials in the Battery Landscape. *Joule* **2018,** *2* (9), 1690-1706.

3. Qin, K.; Huang, J.; Holguin, K.; Luo, C., Recent Advances in Developing Organic Electrode Materials for Multivalent Rechargeable Batteries. *Energy Environ. Sci.* **2020,** *13*

(11), 3950-3992.

4. Lee, M.; Hong, J.; Lopez, J.; Sun, Y.; Feng, D.; Lim, K.; Chueh, W. C.; Toney, M. F.; Cui, Y.; Bao, Z., High-Performance Sodium–Organic Battery by Realizing Four-Sodium Storage in Disodium Rhodizonate. *Nat. Energy* **2017,** *2* (11), 861-868.

5. Qin, J.; Lan, Q.; Liu, N.; Zhao, Y.; Song, Z.; Zhan, H., A Metal-Free Battery Working at -80 °C. *Energy Storage Mater.* **2020,** *26*, 585-592.

6. Dong, X.; Lin, Y.; Li, P.; Ma, Y.; Huang, J.; Bin, D.; Wang, Y.; Qi, Y.; Xia, Y., High-Energy Rechargeable Metallic Lithium Battery at -70 ºC Enabled by a Cosolvent Electrolyte. *Angew. Chem. Int. Ed.* **2019,** *58* (17), 5623-5627.

7. Dong, X.; Guo, Z.; Guo, Z.; Wang, Y.; Xia, Y., Organic Batteries Operated at -70°C. *Joule* **2018,** *2* (5), 902-913.

8. Rajagopalan, R.; Tang, Y.; Jia, C.; Ji, X.; Wang, H., Understanding the sodium storage mechanisms of organic electrodes in sodium ion batteries: issues and solutions. *Energy Environ. Sci.* **2020,** *13* (6), 1568-1592.

9. Peng, C.; Ning, G.-H.; Su, J.; Zhong, G.; Tang, W.; Tian, B.; Su, C.; Yu, D.; Zu, L.; Yang, J.; Ng, M.-F.; Hu, Y.-S.; Yang, Y.; Armand, M.; Loh, K. P., Reversible Multi-Electron Redox Chemistry of π-Conjugated N-Containing Heteroaromatic Molecule-Based Organic Cathodes. *Nat. Energy* **2017,** *2* (7), 1-9.

10. Dong, X.; Chen, L.; Liu, J.; Haller, S.; Wang, Y.; Xia, Y., Environmentally-Friendly Aqueous Li (or Na)-ion Battery with Fast Electrode Kinetics and Super-Long Life. *Sci. Adv.* **2016,** *2* (1), e1501038.

11. Wang, Z.; Shen, X.; Li, S.; Wu, Y.; Yang, T.; Liu, J.; Qian, T.; Yan, C., Low-Temperature Li-S Batteries Enabled by All Amorphous Conversion Process of Organosulfur Cathode. *J. Energy Chem.* **2022,** *64*, 496-502.

12. Hubble, D.; Brown, D. E.; Zhao, Y.; Fang, C.; Lau, J.; McCloskey, B. D.; Liu, G., Liquid Electrolyte Development for Low-Temperature Lithium-Ion Batteries. *Energy Environ. Sci.* **2022,** *15* (2), 550-578.

13. Dong, X.; Wang, Y. G.; Xia, Y., Promoting Rechargeable Batteries Operated at Low Temperature. *Acc Chem Res* **2021,** *54* (20), 3883-3894.

14. Lewandowska-Andralojc, A.; Gacka, E.; Pedzinski, T.; Burdzinski, G.; Lindner, A.; O'Brien, J. M.; Senge, M. O.; Siklitskaya, A.; Kubas, A.; Marciniak, B.; Walkowiak-Kulikowska, J., Understanding Structure-Properties Relationships of Porphyrin Linked to Graphene Oxide Through Pi-Pi-Stacking or Covalent Amide Bonds. *Sci. Rep.* **2022,** *12* (1), 13420.

15. Wang, Y.; Ding, Y.; Pan, L.; Shi, Y.; Yue, Z.; Shi, Y.; Yu, G., Understanding the Size-Dependent Sodium Storage Properties of DSR-Based Organic Electrodes for Sodium-Ion Batteries. *Nano Lett.* **2016,** *16* (5), 3329-3334.

16. Yamashita, T.; Momida, H.; Oguchi, T., First-Principles Investigation of a Phase Transition in $Nax C_6O_6$ as an Organic Cathode Material for Na-ion Batteries: Role of Intermolecule Bonding of C_6O_6. *J. Phys. Soc. Jpn.* **2015,** *84* (7), 074703.

17. Chi, X.; Liang, Y.; Hao, F.; Zhang, Y.; Whiteley, J.; Dong, H.; Hu, P.; Lee, S.; Yao, Y., Tailored Organic Electrode Material Compatible with Sulfide Electrolyte for Stable All-Solid-State Sodium Batteries. *Angew. Chem. Int. Ed.* **2018,** *57* (10), 2630-2634.

18. Wang, C.; Fang, Y.; Xu, Y.; Liang, L.; Zhou, M.; Zhao, H.; Lei, Y., Manipulation of Disodium Rhodizonate: Factors for Fast-Charge and Fast-Discharge Sodium-Ion Batteries with Long-Term Cyclability. *Adv. Funct. Mater.* **2016,** *26* (11), 1777-1786.

19. Xiong, H.; Slater, M. D.; Balasubramanian, M.; Johnson, C. S.; Rajh, T., Amorphous TiO_2 Nanotube Anode for Rechargeable Sodium Ion Batteries. *J. Phys. Chem. Lett* **2011,** *2* (20), 2560-2565.

Supporting Information

Modulating solution-mediated kinetics for sodium-organic battery operated at ultra-low temperature

Xin Xu,[1] Huan Li,[1] Shiying Ren,[1] Chao Ye,[1] Han Wu,[1] Shizhang Qiao[1*]

[1]School of Chemical Engineering and Advanced Materials, The University of Adelaide, SA 5005, Australia

EXPERIMENTAL SECTION

Material Preparations.

Synthesis of shape-selected disodium rhodizonate (DSR, $Na_2C_6O_6$) and nanosized DSR /graphene oxide (nDSR/GO) composite: DSR with different morphologies were prepared via molecular self-assembly methods through a solvent exchange processing. For self-assembly, the organic molecule was transferred from a good solvent (H_2O) to a bad solvent (ethanol, EtOH) where the molecule has limited solubility, and thus self-assembly occurs via molecular stacking. The geometrical shape and size of DSR were regulated by the concentration of raw materials, and the volume and volume ratio of H_2O/EtOH. To prepare diamond-shaped nDSR, DSR (40 mg, sigma) was dissolved in 2:1 ratio of H_2O/EtOH (60 ml total) with stirring for 30 min. And then 300 ml EtOH was poured into the solution with a bath sonicated for 12 min. The reddish-purple precipitation was collected by centrifugation and finally dried in a vacuum oven at 60 ^oC overnight. The graphene oxide composited nDSR (nDSR/GO) was prepared in the same method, but with the addition of graphene oxide (GO, 8 mg) during bath sonicated. Similarly, the micro-sized prism was synthesized by adding 40 mg DSR in 2:1 volume ratio of H_2O/EtOH (60 ml total). The butterfly-shaped DSR particles was synthesized by adding 30 mg DSR in 2:1 volume ratio of H_2O/EtOH (60 ml total).

Synthesis of $Na_2MnFe(CN)_6$ (MnFe-PBA): MnFe-PBA was prepared via a typical facile co-precipitation method. Typically, $Na_4Fe(CN)_6$ (1.52 g) and NaCl (15 g) were dissolved in de-ionized (DI) water (100 ml). And $MnCl_2$ (0.63 g) was dissolved in another DI water (50 mL). $MnCl_2$ solution was added dropwise into $Na_4Fe(CN)_6$ solution under stirring. The obtained suspension was aged for 2 h, then separated by centrifugation, washed with DI water three times, and dried under vacuum at 120 ^oC for 10 h. The prepared sample was ground into a fine powder and ready to be used.

Synthesis of sodium terephthalate (Na_2TP)[1]: Na_2TP was prepared via a modified method reported previously. Terephthalic acid (1.73 g) was added into 5 ml hot solution (50 ^oC) of sodium hydroxide (1.38 g) in deionized (DI) water. And then, another 15 ml DI water was added to obtain a clear solution. After stirring for 30 min, 80 ml EtOH was added with stirring for another 6 h at 70 ^oC. The precipitated crystal was collected and dried in a vacuum at 150 ^oC for 1 h. The counter electrode, Na_4TP was prepared via a full discharge of Na_2TP coupling with Na-foil.

Preparation of the electrolyte. All chemicals for electrolyte preparation were purchased from Sigma Aldrich. The diethylene glycol dimethyl ether (DGM, anhydrous, 99.5%) was further dried with activated 4 Å molecular sieves over 12 h before use. The sodium

hexafluorophosphate ($NaPF_6$, 98%) was purchased and used as received. Typically, $NaPF_6$ (1.68 g) was dissolved into 10 ml DGM at room temperature (RT). After overnight stirring, the electrolyte was ready to be used for testing. All the procedures were carried out in an Ar-filled glove box (H_2O< 0.5 ppm and O_2< 0.5 ppm).

Characterization techniques. The morphology of the sample was analyzed by FEI Quanta 450 FEG scanning electron microscopy (SEM). X-ray diffraction (XRD) patterns for sample powders were collected from the X-ray diffractometer (Bruker, D8 ADVANCE ECO) at 40 kV and 25 mA using Cu-Kα radiation (λ=0.15418 nm). Ex-situ synchrotron soft X-ray spectroscopy measurements were conducted at Australian Synchrotron (ANSTO), Melbourne. The obtained data were analyzed and processed with Igor Pro software. All samples for the ex-situ testing were thoroughly rinsed with DGM solvent to remove soluble species on the surface of the electrode.

In-situ Raman spectroscopy. Raman spectroscopy was performed using a confocal Raman microscope (Renishaw, InVia^{TM}) with a 50X objective, and signals were recorded by a 532 nm laser in the range of 100-1800 cm^{-1}. The power of the lasers was kept in 0.1%. We use an 1800 line/mm diffraction grating.

Electrochemical test. The electrochemical performance was evaluated in the 2032 type coin cell. To fabricate the electrode, the synthesized nDSR/GO composite, carbon black (> 99 %, Alfa Aesar) and poly(vinylidene fluoride) (PVDF, Sigma) were mixed with a mass ratio of 60:30:10 in N-methyl-2-pyrrolidone (NMP, Sigma, anhydrous, 99.5%). The mixture was ball milled at 400 rmp for 4 hours and pasted on the aluminium foil with a diameter of 1.2 cm. After drying in vacuum at 80 °C for 12 hours. The weighted mass loading of nDSR/GO was 0.7-1.0 mg cm^{-2}. The nDSR control electrode and Na_4TP counter electrode were prepared in the same method. To prepare the PBA counter electrode, PBA powder, carbon black and polytetrafluoroethylene (PTFE) binder (6% aqueous solution, Sigma-Aldrich) were mixed with a mass ratio of 70:20:10. The mixture was ground in the agate mortar with several drops of ethanol and rolled into a free-standing film. After drying in a vacuum at 80 °C for 12 h. The sample was cut into small pieces and pasted on stainless steel mesh for use. In half cells, the fresh sodium metal and Whatman glass fiber were used as the anode and separator, respectively. In the preparation of full cells, PBA or Na_2TP was used as the counter electrode. All coin cells were assembled in an argon-filled glovebox. Galvanostatic cycling tests were performed on Land CT2001A battery testing system at different rates and temperatures. A thermal test chamber (GWS-MT3065) was applied to carry out variable temperature tests. For all low-temp testing, batteries were kept at a low temperature for 5 h before electrochemical tests. The cyclic

voltammetry (CV) and electrochemical impedance spectroscopy (EIS) data were collected from the electrochemical workstation BioLogic and CHI 760E. EIS tests were conducted in the frequency range from 1 MHz to 0.01 Hz with an amplitude of 5 mV.

Determination of diffusion coefficient and activation energy. The activation energy of the electrode can be calculated based on a thermally activated process.[2]

$$I_p = A_0 \, e^{\frac{-E_a}{RT}} \qquad \text{(eq. S1)}$$

where A_0 is a constant, R is the gas constant, T is the temperature in Kelvin, and E_a represents the activation energy. The peak current (I_p) was obtained from CV profiles at different temperatures.

Supplementary Figures

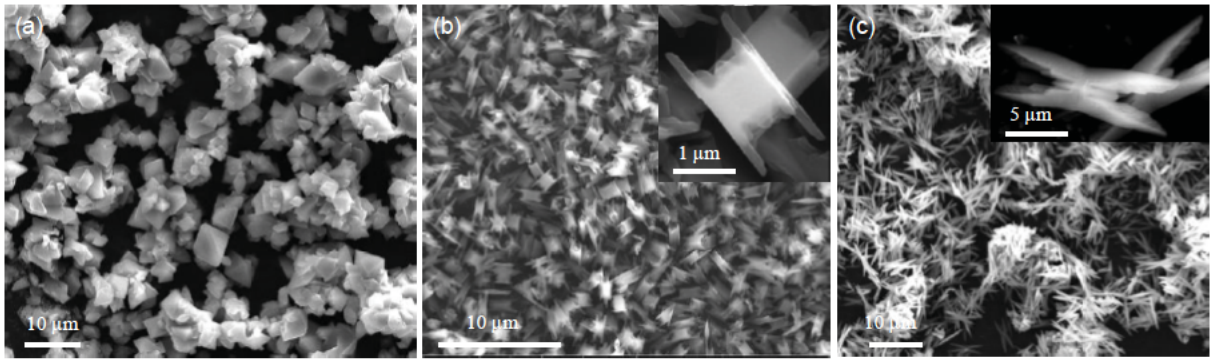

Figure S1. SEM images for (a) commercial purchased DSR powders, (b) prism-shaped, and (d) butterfly-shaped DSR powders.

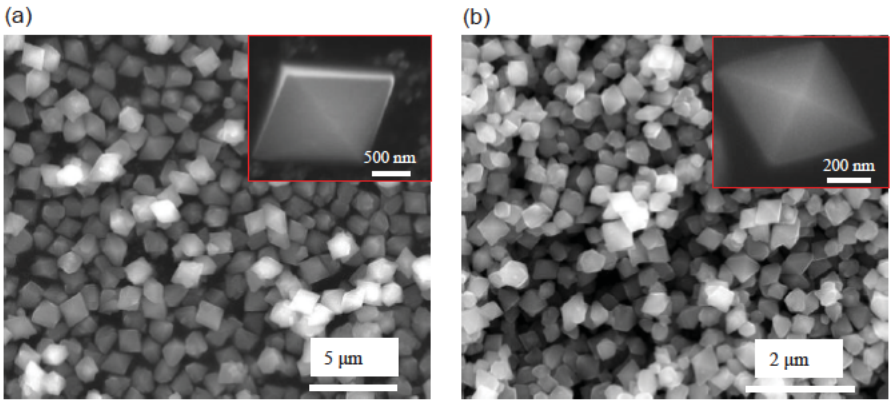

Figure S2. SEM images of DSR with a diamond shape in different sizes, synthesized using different precursor solution volumes (a) 90 ml and (b) 60 ml H_2O/EtOH in a volume ratio of 2:1.

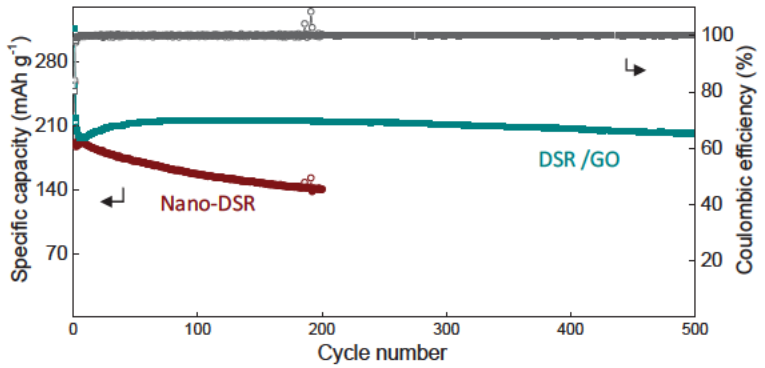

Figure S3. Cycling performance of nDSR and nDSR/GO at room temperature (RT).

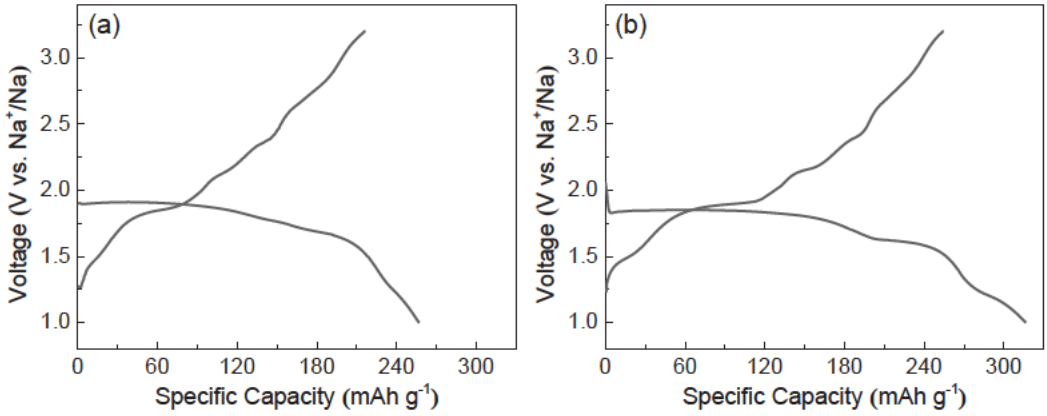

Figure S4. The first discharge-charge curves of (a) nDSR and (b) nDSR/GO at RT and 1000 mA g^{-1}.

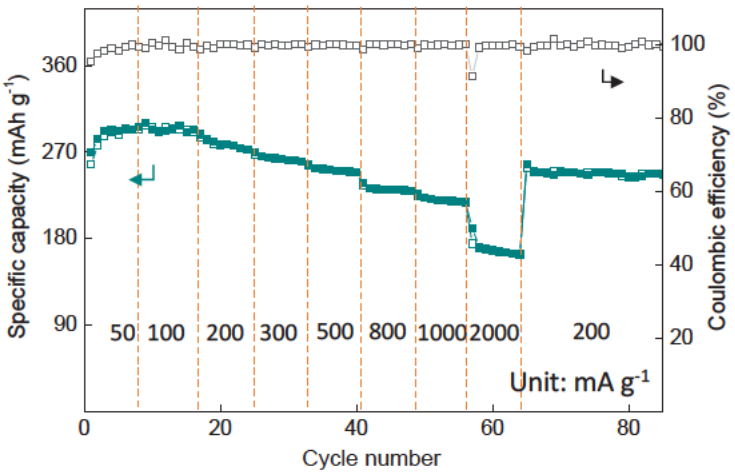

Figure S5. The rate capability of nDSR/GO at RT.

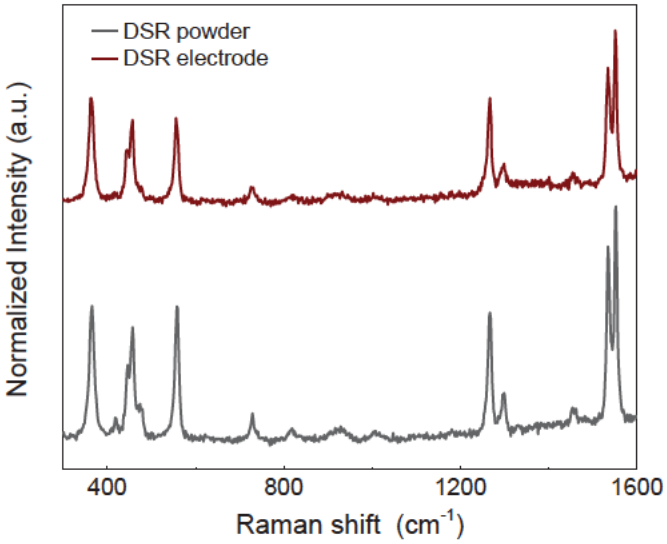

Figure S6. Raman spectra for purchased DSR powders and nDSR/GO composite electrode.

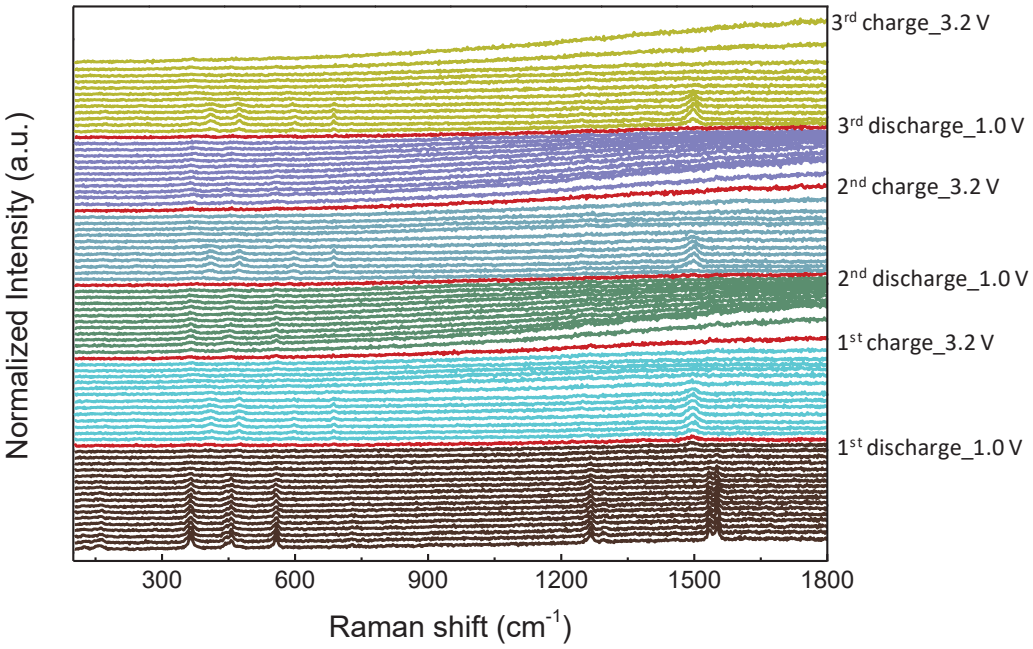

Figure S7. Operando Raman spectra for nDSR for the 1st, 2nd, and 3rd cycle. Cycling in the range of 1.0-3.2 V.

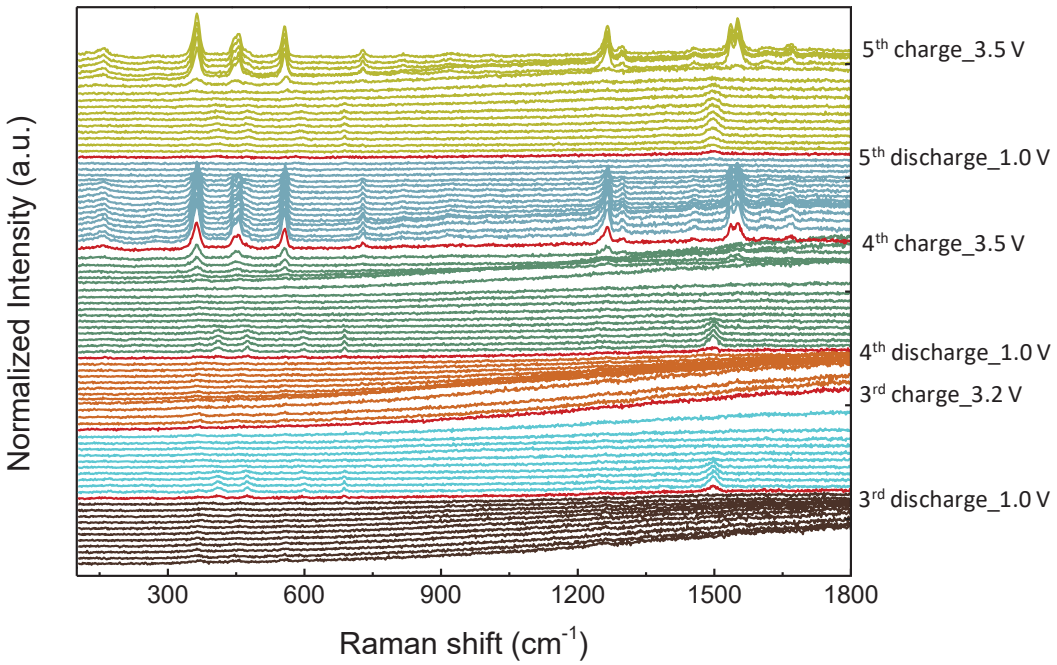

Figure S8. Operando Raman spectra for nDSR for the 3rd, 4th, and 5th cycle. The 4th and 5th cycles were charged to 3.5 V.

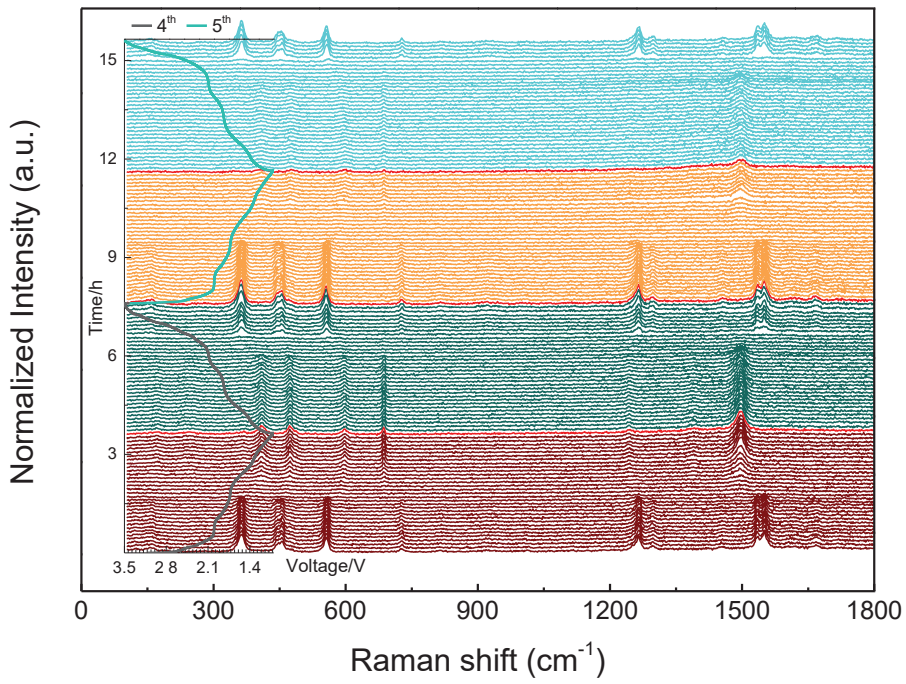

Figure S9. Operando Raman spectra for nDSR/GO for the 4th and 5th cycle, and the corresponding discharge/charge profile. The upper cut-off potential is 3.5 V.

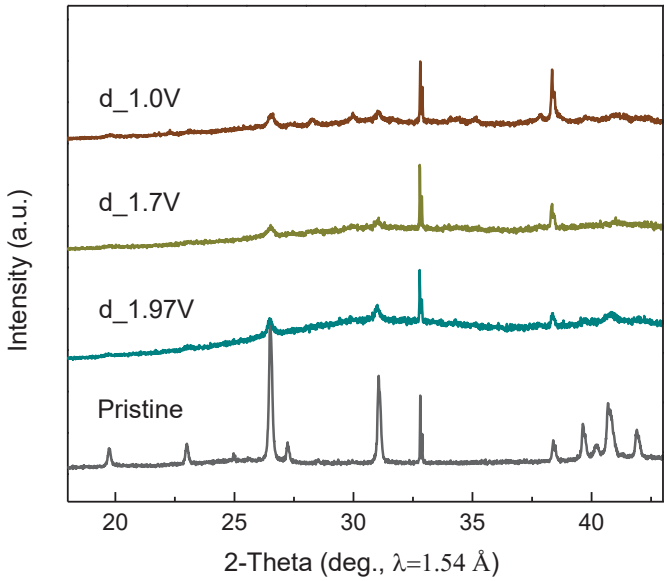

Figure S10. Ex-situ XRD patterns for nDSR/GO electrode at pristine and different discharge states.

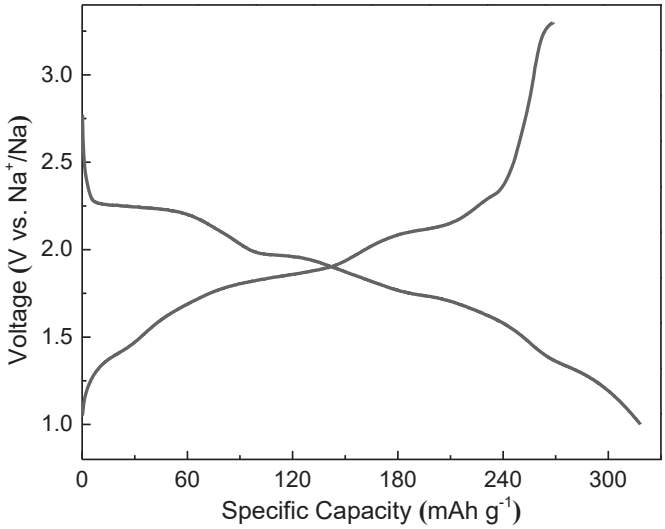

Figure S11. Discharge-charge curves of Na-nDSR/GO at a current density 100 mA g^{-1} and -30 ^{o}C.

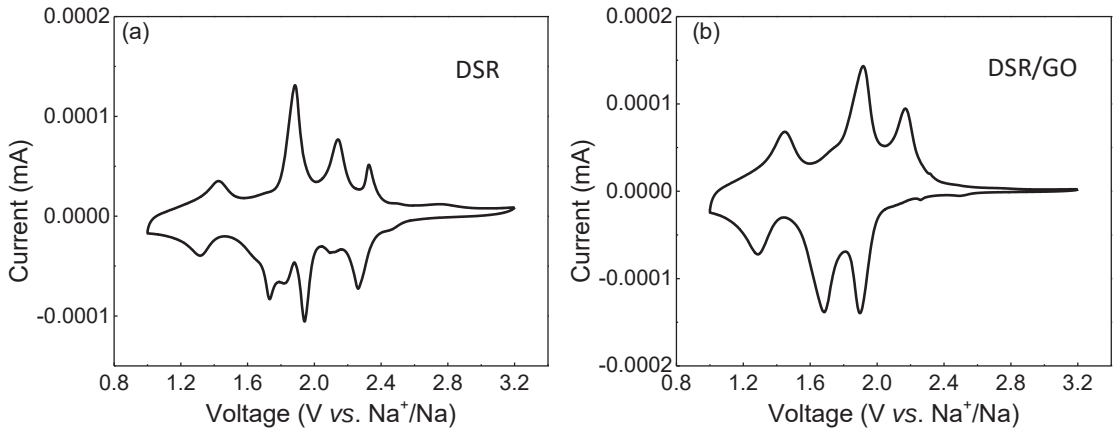

Figure S12. CV curves for (a) nDSR and (b) nDSR/GO at the scan rate 0.2 mV s^{-1} and -30 °C.

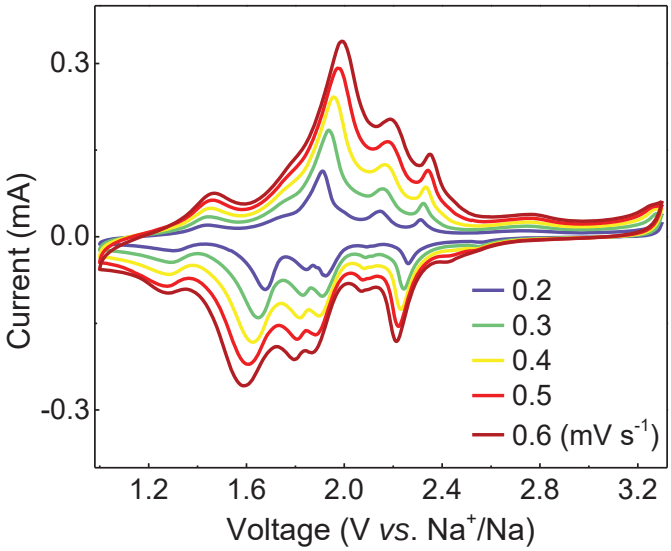

Figure S13. CV curves of Na-nDSR/GO at different scan rates and -30 °C.

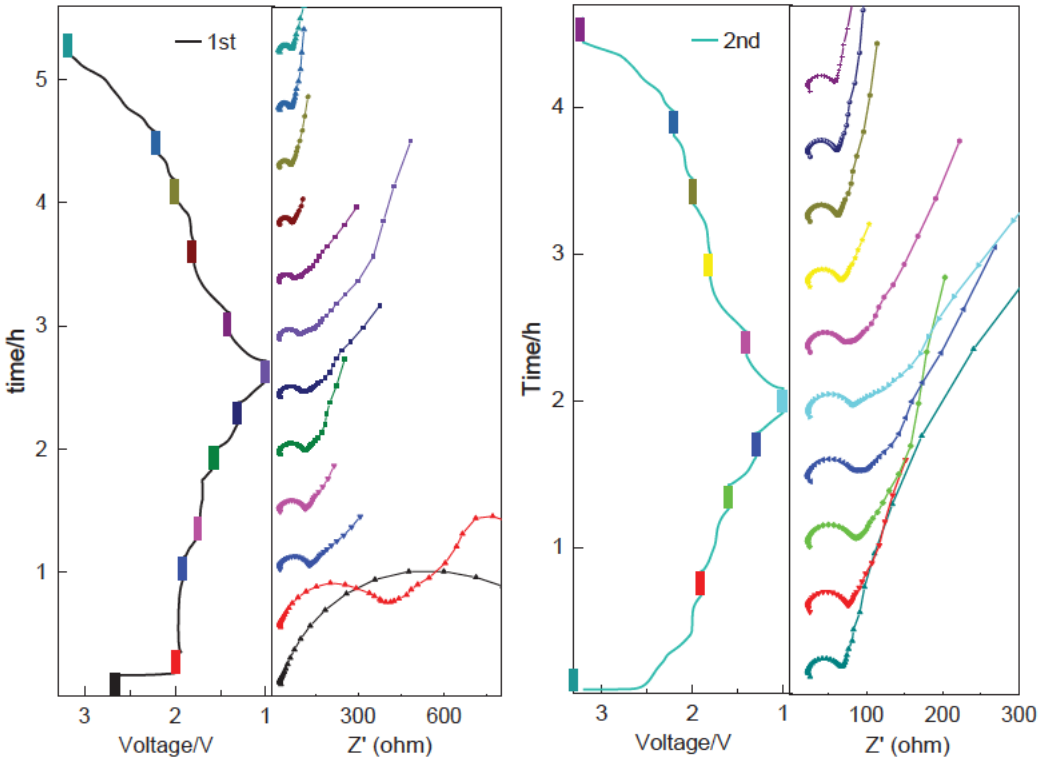

Figure S14. In-situ EIS plots of nDSR for the 1st and 2nd cycle at RT. The discharge-charge range is between 1.0 - 3.2 V at 100 mA g^{-1}.

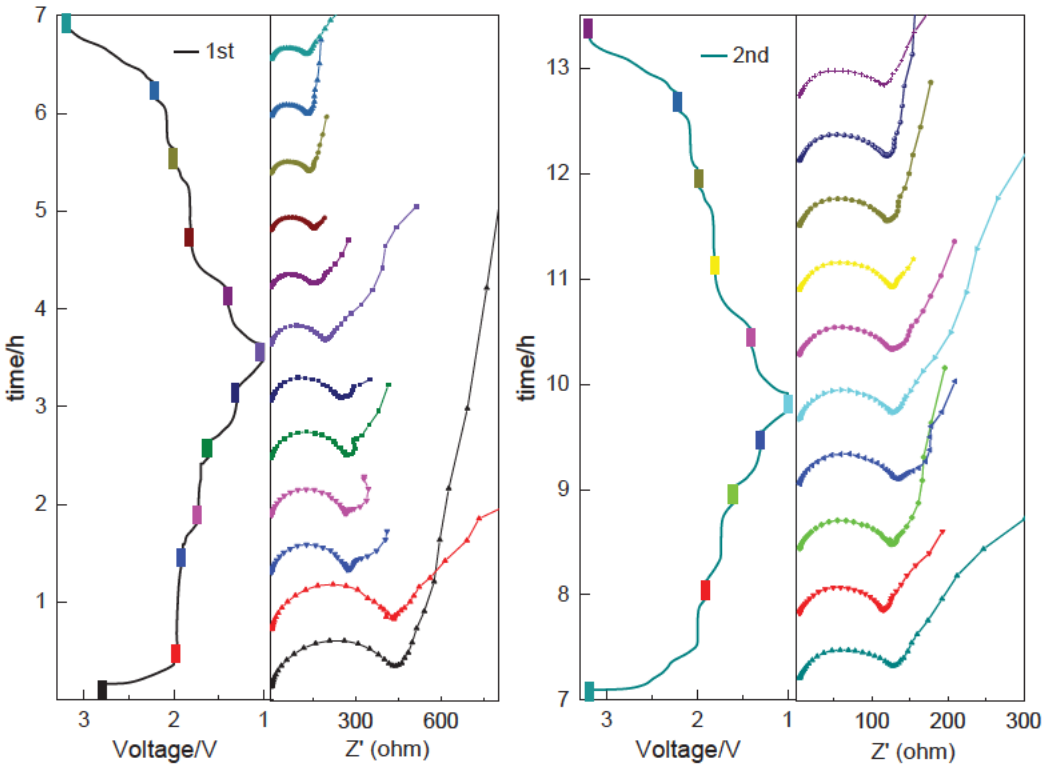

Figure S15. In-situ EIS plots of nDSR/GO for the 1st and 2nd cycle at RT. The discharge-charge range is between 1.0 - 3.2 V at 100 mA g^{-1}.

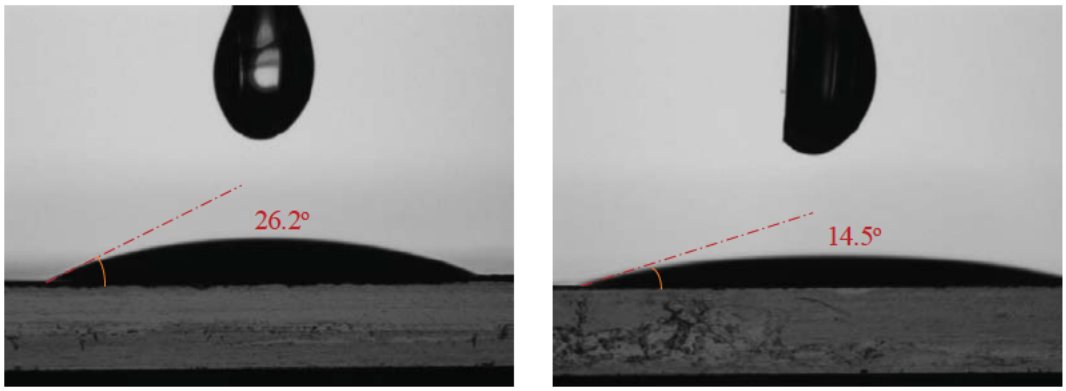

Figure S16. Contact angle measurement on nDSR and nDSR/GO.

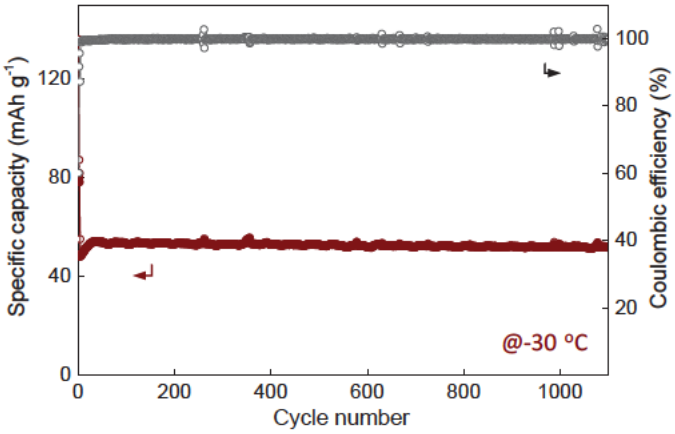

Figure S17. Cycling performance of PBA-nDSR at a current density of 200 mA g^{-1} and -30 °C.

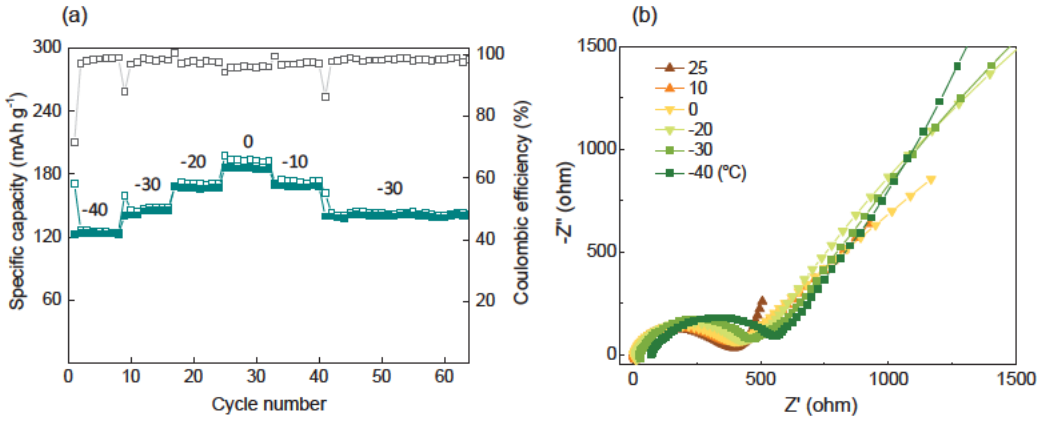

Figure S18. (a) Temperature-dependent rate performance of PBA-nDSR/GO at a current density of 100 mA g^{-1}. (b) Corresponding EIS at different temperatures.

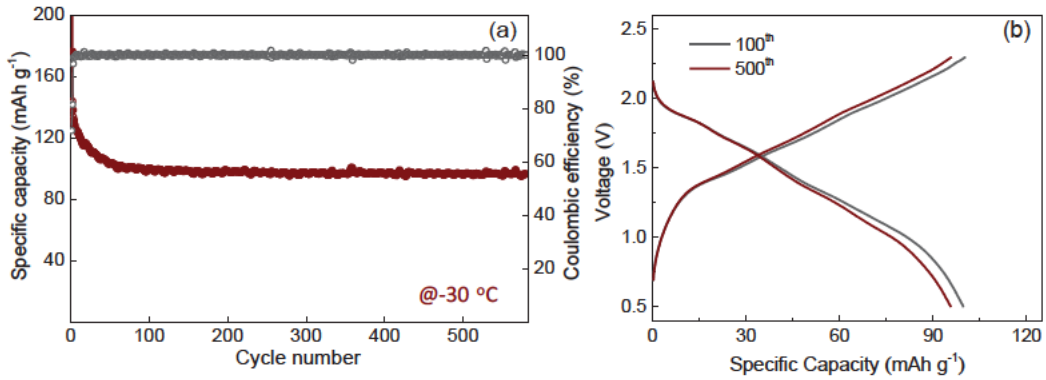

Figure S19. (a) Cycling performance of nDSR/GO-Na_4TP at a current density of 100 mA g^{-1} and -30 ℃. The specific capacity is based on the mass of nDSR/GO. (b) Discharge-charge curves for different cycles.

Table S1. The fitted results of activation energy for nDSR and nDSR/GO for different redox peaks.

Electrode	Activation energy (Ea, kJ mol^{-1})		
	C1	C2	C3
nDSR	5.56	7.02	2.12
nDSR/GO	5.00	5.24	4.87

Table S2. Comparison of the ultra-low temperature (-40 ºC and bellow) properties of different batteries.

Battery systems		Specific capacity	Cycling performance	Average discharge voltage (V)	Operating temperature (ºC)	Ref.
Sodium batteries	nDSR/GO-PBAs	137 mAh g^{-1} at 0.4C	100% retained after 610 cycles	1.22 V	-40	This work
	nDSR/GO-PBAs	98.5 mAh g^{-1} at 1.2C	>99% retained after 2500 cycles	1.18 V	-40	This work
	nDSR/GO-PBAs	109 mAh g^{-1} at 0.2C	100% retained after 290 cycles	1.25 V	-50	This work
	$Ti_{0.88}Nb_{0.88}O_{4-x}$@C-Na	99 mAh g^{-1} at 0.5C	81% retained after 500	~0.7	-40	X[1]
Lithium batteries	$LiFePO_4$(LFP)-Li	~80 mAh g^{-1} at 0.5C	89.4% retained after 200	unknown	-40	X[2]
	NMC811-Li	108 mAh g^{-1} at 0.2C	>90% retained after 200	3.7	-40	X[3]
	$LiMn_2O_4$(LMO)-$Li_4Ti_5O_{12}$ (LTO)	~70 mAh g^{-1} at 0.2C	~80% retained after 40	2.4	-40	X[4]
	SPAN-Li	220 mAh g^{-1} at 0.1C	~55% retained after 50	1.6	-40	X[5]
	SPAN-Li	~300 mAh g^{-1} at 0.2 A g^{-1}	86% retained after 100	~1.4	-40	X[6]
	Polyimide (PI)-Li	~70 mAh g^{-1} at 0.2C	~83% retained after 100	2.3	-70	X[7]
Aqueous batteries	MnO_2@GF-MoO_3	171.8 mAh g^{-1} at 0.2 A g^{-1}	>99% retained after 100	~1.0 (vs. Ag/AgBr)	-70	X[8]
	PI-(LiBr+ TPABr)-PC	56 mAh g^{-1} at 0.5 A g^{-1}	98% retained after 1000 at 1 A g^{-1}	0.8	-40	X[9]
	$NaTi_2(PO_4)_3$@CNTP-AC	~65 mAh g^{-1} at 0.5C	>80% retained after 100	~1.2	-50	X[10]
	αMnO_2-Zn	~40 mAh g^{-1} at 6 A g^{-1}	>99% retained after 1000	~1.3	-50	X[11]

REFERENCE

1. Park, Y.; Shin, D. S.; Woo, S. H.; Choi, N. S.; Shin, K. H.; Oh, S. M.; Lee, K. T.; Hong, S. Y., Sodium Terephthalate as an Organic Anode Material for Sodium Ion Batteries. *Adv. Mater.* **2012,** *24* (26), 3562-3567.

2. Zhang, W.; Sun, X.; Tang, Y.; Xia, H.; Zeng, Y.; Qiao, L.; Zhu, Z.; Lv, Z.; Zhang, Y.; Ge, X.; Xi, S.; Wang, Z.; Du, Y.; Chen, X., Lowering Charge Transfer Barrier of $LiMn_2O_4$ via Nickel Surface Doping To Enhance Li^+ Intercalation Kinetics at Subzero Temperatures. *J. Am. Chem. Soc.* **2019,** *141* (36), 14038-14042.

3. Liang, H.; Liu, L.; Wang, N.; Zhang, W.; Hung, C. T.; Zhang, X.; Zhang, Z.; Duan, L.; Chao, D.; Wang, F.; Xia, Y.; Li, W.; Zhao, D., Unusual Mesoporous Titanium Niobium Oxides Realizing Sodium-Ion Batteries Operated at -40 degrees C. *Adv. Mater.* **2022**, e2202873.

4. Zhang, D.; Zhu, D.; Guo, W.; Deng, C.; Xu, Q.; Li, H.; Min, Y., The Fluorine-Rich Electrolyte as an Interface Modifier to Stabilize Lithium Metal Battery at Ultra-Low Temperature. *Adv. Funct. Mater.* **2022,** *32* (23), 2112764.

5. Holoubek, J.; Kim, K.; Yin, Y.; Wu, Z.; Liu, H.; Li, M.; Chen, A.; Gao, H.; Cai, G.; Pascal, T. A.; Liu, P.; Chen, Z., Electrolyte Design Implications of Ion-Pairing in Low-Temperature Li Metal Batteries. *Energy Environ. Sci.* **2022,** *15* (4), 1647-1658.

6. Zhang, W.; Xia, H.; Zhu, Z.; Lv, Z.; Cao, S.; Wei, J.; Luo, Y.; Xiao, Y.; Liu, L.; Chen, X., Decimal Solvent-Based High-Entropy Electrolyte Enabling the Extended Survival Temperature of Lithium-Ion Batteries to -130 °C. *CCS Chemistry* **2021,** *3* (4), 1245-1255.

7. Holoubek, J.; Liu, H.; Wu, Z.; Yin, Y.; Xing, X.; Cai, G.; Yu, S.; Zhou, H.; Pascal, T. A.; Chen, Z.; Liu, P., Tailoring Electrolyte Solvation for Li Metal Batteries Cycled at Ultra-Low Temperature. *Nat. Energy* **2021,** *6* (3), 303-313.

8. Cai, G.; Holoubek, J.; Xia, D.; Li, M.; Yin, Y.; Xing, X.; Liu, P.; Chen, Z., An Ester Electrolyte for Lithium-Sulfur Batteries Capable of Ultra-Low Temperature Cycling. *Chem. Commun.* **2020,** *56* (64), 9114-9117.

9. Dong, X.; Lin, Y.; Li, P.; Ma, Y.; Huang, J.; Bin, D.; Wang, Y.; Qi, Y.; Xia, Y., High-Energy Rechargeable Metallic Lithium Battery at -70 ºC Enabled by a Cosolvent Electrolyte. *Angew. Chem. Int. Ed.* **2019,** *58* (17), 5623-5627.

10. Yan, L.; Huang, J.; Guo, Z.; Dong, X.; Wang, Z.; Wang, Y., Solid-State Proton Battery Operated at Ultralow Temperature. *ACS Energy Lett.* **2020,** *5* (2), 685-691.

11. Wang, M.; Li, T.; Yin, Y.; Yan, J.; Zhang, H.; Li, X., A -60 °C Low-Temperature Aqueous Lithium Ion-Bromine Battery with High Power Density Enabled by Electrolyte Design. *Adv. Energy Mater.* **2022,** *12* (25) 2200728.

12. Nian, Q.; Wang, J.; Liu, S.; Sun, T.; Zheng, S.; Zhang, Y.; Tao, Z.; Chen, J., Aqueous Batteries Operated at -50 degrees C. *Angew. Chem. Int. Ed.* **2019,** *58* (47), 16994-16999.
13. Yang, G.; Huang, J.; Wan, X.; Liu, B.; Zhu, Y.; Wang, J.; Fontaine, O.; Luo, S.; Hiralal, P.; Guo, Y.; Zhou, H., An Aqueous Zinc-Ion Battery Working at -50°C Enabled by Low-Concentration Perchlorate-Based Chaotropic Salt Electrolyte. *EcoMat* **2022,** *4* (2), e12165.

Chapter 7: Conclusions and Perspectives

7.1 Conclusions

This thesis focuses on the design of advanced electrode materials for both rechargeable Mg and Na-based batteries. It includes in-depth mechanism studies via ex-situ and in-situ/operando spectroscopic techniques. Further work on designing inorganic/organic electrode materials for ultra-low temperature batteries is in progress. According to works in this thesis, conclusions are drawn as follows:

1. I have demonstrated a new alloying reaction mechanism for Mg/Bi batteries via an elaborated electrode design of mesoporous Bi nanosheets. The p-Bi NS with recorded electrochemical performance in the lithium-free electrolyte is ideal for the investigation of Mg charge storage mechanism. MgBi intermediate phase is firstly detected via spectroscopy technologies of synchrotron-based operando X-ray diffraction and near-edge X-ray absorption fine structure. The alloying/de-alloying process can be depicted as a reversible two-step reaction of $Bi \leftrightarrow MgBi \leftrightarrow Mg_3Bi_2$. The ab initio method underscores the energy barrier priority in forming the MgBi intermediate and confirms the high electronic conductivity of MgBi. The intermediate phase accelerates reaction kinetics and acts as a buffer to mitigate disruption of significant volume expansion (204%). The nanoengineering design of p-Bi NS offers a practically new approach for application in corrosive Mg-based electrolyte, and concomitantly to mitigate volume variation.

2. I have constructed a nanostructured Bi anode through an in-situ electrochemical reaction from bismuth selenide. Coupled with Mg^{2+}/Li^{+} hybrid electrolyte, the electrochemical activity and alloy/de-alloy efficiency of the nanostructured Bi anode are exclusively evoked

by Li-salt. The in-situ formed Bi anode with nanosized Bi active crystals exhibits the advantages of short Mg^{2+} diffusion length and extremely high ion-diffusivity. As a result, it demonstrates an excellent rate performance (335 mAh g^{-1} at 1 A g^{-1}) and long cycling stability over 600 cycles, which surpasses the state-of-the-art Bi-based anodes in RMBs. A Li^{+}-driven conversion reaction followed by a reversible Mg alloy/de-alloy process is verified via synchrotron XAS and operando synchrotron X-ray diffraction together with a series of spectroscopic analyses.

3. I have for the first time demonstrated 1T-VSe_2 as a low-temperature cathode in a Mg^{2+}/Li^{+} hybrid cell configuration. A 1T-VSe_2/Mg battery is workable at an ultra-low temperature of -40 ºC. It exhibits a long-term cycling performance with a low capacity decay rate of 0.007 % per cycle over 500 cycles. This performance is better than reported Mg-based batteries. Combined operando synchrotron X-ray diffraction, ex-situ X-ray absorption spectroscopy and DFT computations confirm that Jahn-Teller compression occurs and contributes significantly to fast-overall kinetics and structural stability of 1T-VSe_2 on intercalation /de-intercalation of Li^{+}. Therefore, electrochemical performance is boosted.

4. I proposed nanosized disodium rhodizonate (nDSR) as an ultra-low temperature organic electrode for sodium-ion batteries. The amorphous phase associated solution-mediated reaction results in a deteriorating capacity of nDSR electrodes at room temperature, but kinetically contributes to an excellent ultra-low temperature performance of the battery. The increased viscosity of the electrolyte and GO-enhanced interfacial kinetics collaboratively work on the balance of dissolution and transformation rate of intermediate amorphous phase, and thus enhance the rate and reversibility of nDSR/GO composite electrodes at ultra-low

temperatures. Na-nDSR/GO half cells achieve a high capacity of 119 mAh g^{-1} at -50 ºC. And the PBA-nDSR/GO full cell performs an ultra-stable cycle life of over 2500 cycles. The ultra-low temperature electrochemical performance of nDSR/GO surpasses reported lithium and sodium batteries.

7.2 Perspectives

Although progress has been made in both Mg and Na-based batteries, more efforts in understanding reaction mechanisms and kinetic limitations are still needed to develop them for practical use. These include:

1. High power and energy rechargeable Mg-based batteries. To obtain rechargeable Mg batteries with high energy and power density, efforts should focus on the following aspects: 1) design high-voltage cathode materials with improved Mg^{2+} kinetics, such as layered oxide compound; 2) modify Mg metal anode via artificial SEI to couple with Cl^- free electrolytes, such as single Mg salt or carbonate-based electrolytes; 3) develop Mg-sulfur batteries with high power and energy density.

2. Wide-temperature operated Na-based batteries. Na-based batteries are making strides forward, but the broader and large-scale applications require them to be able to perform wide-temperature tolerance, such as the application in extremely high or low latitudes. Therefore, more works on developing electrode materials and electrolytes that are capable of enduring harsh environments are needed.

3. In-situ/operando spectroscopic studies. To explore new battery systems and to optimize existing battery techniques, in-situ/operando spectroscopic investigations are indispensable because they offer timely information on the change of electrode materials, interfacial layers,

and electrolytes. The current in-situ techniques cannot fully satisfy requirements of time resolution, signal sensitivity, and variable analyses, such as operando characterizations at an ultra-low temperature. It requires the development of instrumental techniques, and the design of in-situ tools and experiments.

To sum up, post-Li batteries (Mg, Na, etc. based batteries) demonstrate strong competitive advantages in certain applications compared to resource-limited LIBs and are promising in practical use. The in-depth fundamental studies of the electrode material via advanced characterization technologies significantly contribute to the rational design and development of high-performance electrodes for the post-Li batteries.

Appendix: Publications during PhD Candidature

[1] **Xin Xu**, Dongliang Chao, Biao Chen, Pei Liang, Huan Li, Fangxi Xie, Kenneth Davey, and Shi-Zhang Qiao. "Revealing the Magnesium-Storage Mechanism in Mesoporous Bismuth via Spectroscopy and Ab-Initio Simulations." ***Angewandte Chemie International Edition*** **2020**, 59(48): 21728-21735.

[2] **Xin Xu**, Chao Ye, Dongliang Chao, Biao Chen, Huan Li, Cheng Tang, Xiongwei Zhong, and Shi-Zhang Qiao. "Synchrotron X-ray Spectroscopic Investigations of In-Situ-Formed Alloy Anodes for Magnesium Batteries." ***Advanced Materials*** **2022**, 34(8): 2108688.

[3] **Xin Xu**, Chao Ye, Dongliang Chao, Kenneth Davey, and Shi-Zhang Qiao. "Initiating Jahn-Teller Effect in Vanadium Diselenide for High Performance Magnesium-Based Batteries Operated at -40 ºC." ***Advanced Energy Materials*****, Under review**.

[4] **Xin Xu**, Huan Li, Shiying Ren, Chao Ye, Han Wu, and Shi-Zhang Qiao. " Modulating Solution-Mediated Kinetics for Sodium-Organic Battery Operated at Ultra-Low Temperature. " **To be submitted**.